UC San Diego
UC San Diego Electronic Theses and Dissertations

Title

Development of Liquefied Gas Electrolytes for Li Metal Batteries

Permalink

https://escholarship.org/uc/item/6wn5t2c4

Author

Yin, Yijie

Publication Date

2023

Peer reviewed|Thesis/dissertation

UNIVERSITY OF CALIFORNIA SAN DIEGO

Development of Liquefied Gas Electrolytes for Li Metal Batteries

A dissertation submitted in partial satisfaction of the requirements for the
degree Doctor of Philosophy

in

Materials Science and Engineering

by

Yijie Yin

Committee in charge:
    Professor Ying Shirley Meng, Chair
    Professor Zheng Chen Co-Chair
    Professor Ping Liu
    Professor Tod Pascal
    Professor Michael Sailor

2023

Yijie Yin, 2023

The dissertation of Yijie Yin is approved, and it is acceptable in quality and form for publication on microfilm and electronically

University of California San Diego

2023

DEDICATION

This dissertation is dedicated to my parents,

Hongbin Yin and *Xiaoqing Sun,*

and my girlfriend, *Yizhen Lou*.

EPIGRAPH

There are things you can't see unless you change your standing.

Eiichiro Oda

TABLE OF CONTENTS

LIST OF FIGURES

LIST OF TABLES

ACKNOWLEDGEMENT

I am especially grateful to my father Hongbin Yin, my mother Xiaoqing Sun, my girlfriend Yizhen Lou, and my cousin Zheng Pan. Without their support, this journey will not be successful.

I would like to acknowledge Prof. Ying Shirley Meng for her guidance and support as the chair of my committee. She instructs me when I know little about the electrochemical energy storage knowledge. She serves as a mentor to provide multiple challenges for myself and consistently require high standard for all academic projects. She provides me the excellent research stage (LESC) and make me learn quickly and grow up. She changed my life.

I would like to acknowledge my co-advisor Prof. Zheng Chen for his strict standard and make me become strong when I face the difficulty. Prof. Chen provides me with a precious opportunity to transit master degree to PhD degree in 2019. Special thanks for his support on the application of dissertation year fellowship.

I would like to acknowledge my committee member, Prof. Ping Liu, Prof. Tod Pascal, Prof. Machiel Sailor for their support and suggestions that have strengthened this thesis.

I would also like to acknowledge Dr. Yangyuchen Yang, Dr. Weikang Li and Dr. Cyrus Rustomji without whom my research would have no doubt taken five times as long. It is their support that helped me in an immeasurable way.

I would like to specially thank the liquefied gas electrolyte subgroup Dr. Daniel Davies, Matt Meyer, Alex Liu, Ganesh Raghavendran for always being with me when I need their help.

I would also like to thank all the Laboratory for Energy Storage and Conversion (LESC) members and Chen's lab members for their unique technical skills that I could learn from and making both labs a great place to work.

Chapter 3 is a reprint of the publication "Yin, Yijie, John Holoubek, Alex Liu, Baharak Sayahpour, Ganesh Raghavendran, Guorui Cai, Bing Han, Matthew Mayer, Noah B. Schorr, Timothy N. Lambert, Katharine L. Harrison, Weikang Li, Zheng Chen, Y. Shirley Meng. "Ultralow-Temperature Li/CFx Batteries Enabled by Fast-Transport and Anion-Pairing Liquefied Gas Electrolytes." Advanced Materials 35, no. 3 (2023): 2207932". The thesis author is the first author of this publication.

Chapter 4 is a reprint of the publication "Yin, Yijie*, Yangyuchen Yang*, Diyi Cheng, Matthew Mayer, John Holoubek, Weikang Li, Ganesh Raghavendran, Alex Liu, Bingyu Lu, Daniel M. Davies, Zheng Chen, Oleg Borodin & Y. Shirley Meng. "Fire-extinguishing, recyclable liquefied gas electrolytes for temperature-resilient lithium-metal batteries." Nature Energy 7, no. 6 (2022): 548-559". The thesis author is the first author of this publication.

Chapter 5 is a manuscript in preparation of "Coulombic Condensation of Liquefied Gas Electrolytes for Li Metal Batteries at Ambient Pressure", co-authored with John Holoubek, Prof. Ping Liu, Prof. Ying Shirley Meng, and Prof. Zheng Chen. The thesis author is the primary author of this section.

VITA

2013-2017 Bachelor of Engineering, Shanghai Jiao Tong University, Shanghai, China

2017-2020 Master of Science, University of California San Diego, U.S.A

2020-2023 Doctor of Philosophy, University of California San Diego, U.S.A

SELECTED PUBLICATIONS

(* authors contributed equally to the work)

Yin, Yijie*, Yangyuchen Yang*, Diyi Cheng, Matthew Mayer, John Holoubek, Weikang Li, Ganesh Raghavendran, Alex Liu, Bingyu Lu, Daniel M. Davies, Zheng Chen, Oleg Borodin & Y. Shirley Meng. "Fire-extinguishing, recyclable liquefied gas electrolytes for temperature-resilient lithium-metal batteries." Nature Energy 7, no. 6 (2022): 548-559.

Yin, Yijie, John Holoubek, Alex Liu, Baharak Sayahpour, Ganesh Raghavendran, Guorui Cai, Bing Han, Matthew Mayer, Noah B. Schorr, Timothy N. Lambert, Katharine L. Harrison, Weikang Li, Zheng Chen, Y. Shirley Meng. "Ultralow-Temperature Li/CFx Batteries Enabled by Fast-Transport and Anion-Pairing Liquefied Gas Electrolytes." Advanced Materials 35, no. 3 (2023): 2207932.

Yin, Yijie*, John Holoubek*, Kangwoo Kim, Ping Liu, Y. Shirley Meng, and Zheng Chen. "Coulombic Condensation of Liquefied Gas Electrolytes for Li Metal Batteries at Ambient Pressure", manuscript in preparation.

Cai, Guorui*, **Yijie Yin***, Dawei Xia*, Amanda A. Chen, John Holoubek, Jonathan Scharf, Yangyuchen Yang, Ki Hwan Koh, Mingqian Li, Daniel M. Davies, Matthew Mayer, Tae Hee Han, Ying Shirley Meng, Tod A. Pascal & Zheng Chen. "Sub-nanometer confinement enables facile condensation of gas electrolyte for low-temperature batteries." Nature communications 12, no. 1 (2021): 3395.

Yang, Yangyuchen, **Yijie Yin**, Daniel M. Davies, Minghao Zhang, Matthew Mayer, Yihui Zhang, Ekaterina S. Sablin, Shen Wang, Jungwoo Z. Lee, Oleg Borodin, Cyrus S. Rustomji, and Y. Shirley Meng. "Liquefied gas electrolytes for wide-temperature lithium metal batteries." Energy & Environmental Science 13, no. 7 (2020): 2209-2219.

Yang, Yangyuchen, Daniel M. Davies, **Yijie Yin**, Oleg Borodin, Jungwoo Z. Lee, Chengcheng Fang, Marco Olgui, Yihui Zhang, Ekaterina S. Sablina, Xuefeng Wang, Cyrus S. Rustomji, Y. Shirley Meng. "High-efficiency lithium-metal anode enabled by liquefied gas electrolytes." Joule 3, no. 8 (2019): 1986-2000.

FIELDS OF STUDY

Major Field: Energy Storage and Nano Engineering
    Studies in Materials Science and Engineering
    Professor Ying Shirley Meng
    Professor Zheng Chen

ABSTRACT OF THE DISSERTATION

Development of Liquefied Gas Electrolytes for Li Metal Batteries

by

Yijie Yin

Doctor of Philosophy in Materials Science and Engineering

University of California San Diego, 2023

Professor Ying Shirley Meng, Chair
Professor Zheng Chen, Co-chair

The increasing demand for electric vehicles and portable devices has revealed the potential of lithium-ion batteries (LIBs). However, conventional graphite-based LIBs fall short in providing sufficient energy density and power density, which hinders the development of electric vehicles and electric aircraft. Lithium metal anode material emerges as one of the most promising candidates for high energy density batteries (> 500 Wh/kg and > 1000 Wh/L) due to its exceptional theoretical specific capacities, lowest reduction potential, and low density. Nonetheless, the commercialization of lithium metal anodes faces challenges such as limited cycle lives caused by continuous dendrite growth and safety concerns arising from porous electrodeposited structures. Electrolyte engineering represents the most efficient approach to establish a compatible anode/electrolyte interphase (SEI) at a fundamental level. Despite significant research on the development of high-concentration electrolytes and localized high-concentration electrolytes, both suffer from reduced ionic conductivities and poor wettability towards thick electrodes. Liquefied gas electrolytes (LGEs) offer a promising alternative to enable high energy density lithium metal anodes due to their low viscosity, inherent pressure, electrochemical stability, and high fluorine content available for donation. However, it is crucial to prioritize addressing challenges related to the pressurized nature, relatively lower Li+/solvent coordination, and the flammability of fluoromethane (FM)-based electrolytes.

To enhance salt solubility and expand the range of compatible salts, we propose replacing FM with the simplest ether, dimethyl ether (Me_2O), due to its similar physical

properties and more polar functional group, which potentially enables stronger Li+ solvation. When integrated with carbon monofluoride electrodes, Me$_2$O-based LGE exhibits excellent performance at ultra-low temperatures, reaching as low as -70°C, and competitive fast-rate capabilities up to 6.25 C.

However, low-concentration Me$_2$O electrolytes face challenges in terms of relatively poor oxidative stability and flammability. To address safety concerns, we enhance the safety features of liquefied gas electrolytes by incorporating Me$_2$O with other fire-extinguishing gas agents. The addition of fluorinated fire-extinguishing gases such as 1,1,1,2 tetrafluoroethane (TFE) and pentafluoroethane (PFE) significantly improves the safety of the formulated electrolytes. By utilizing the concept of localized highly concentrated electrolytes, we have developed a fire-extinguishing TFE-PFE-based LGE that enables stable Li/NMC622 cycling over 200 cycles at a cutoff voltage of 4.2 V. Moreover, these electrolytes can be successfully recollected after use, contributing to the sustainability of the LGE.

In parallel studies, we have observed unique characteristics of Me$_2$O-based electrolytes when high salt concentrations are maintained. Such electrolytes can maintain a liquid state under ambient conditions, facilitating electrolyte preparation and significantly reducing operating pressure, thereby lowering costs. The obtained saturated LiFSI-Me$_2$O electrolyte exhibits excellent stability in Li-metal plating and stripping, achieving over 99.2% Coulombic efficiency for 1000 cycles. When combined with a SPAN electrode, the

electrochemical performance of Li/SPAN demonstrates competitiveness due to the low solubility of polysulfides and the SEI derived from the salt.

In conclusion, by introducing Me_2O-based LGE, we present a promising direction for achieving high energy density, improved safety, ultra-low temperature operation, and sustainability in multiple Li-based batterie

Chapter 1. Motivation

In the **Chapter 1**, I will discuss the motivation of why I choose energy storage and conversion as my PhD research field and why energy storage is an important field for the next decade.

1.1 Urgent Call for Reducing Greenhouse Gas Emission

Since the end of the Cold War, trade liberalization and globalization have greatly promoted economic and social development. However, they have also brought about a surge in resource exploitation and utilization. This has intensified the imbalance between humans and nature, leading to a significant increase in greenhouse gas emissions and impacting the Earth's ecosystem that sustains human life. To address these contradictions, the United Nations, through the Paris Climate Agreement, requires member countries to strive to limit greenhouse gas emissions (GHG) to 2 degrees Celsius, preferably below 1.5 degrees Celsius, during this century. However, such target faced unprecedented challenges owing to the Covid-19 pandemic, Russian-Ukraine War, and the increased tension between Sino-US bilateral relationship. Based on Figure 1.1, it can be observed that the industry and electricity sectors have consistently accounted for over 50% of the total CO_2 emissions since 2008[1]. The popularization of private vehicles has led to a gradual increase in the transport sector's contribution to GHG emissions, rising from 5 to 7 billion metric tons of CO_2 emissions. This trend was influenced by the Covid-19 pandemic, which resulted in fewer people choosing to travel and conduct business activities. However, as the world economy successfully reopens and confronts the challenges posed by Covid-19, it is expected that GHG emissions will rapidly increase. It is crucial to take immediate action to peak GHG emissions before 2030.

a. Total global GHG emissions trends
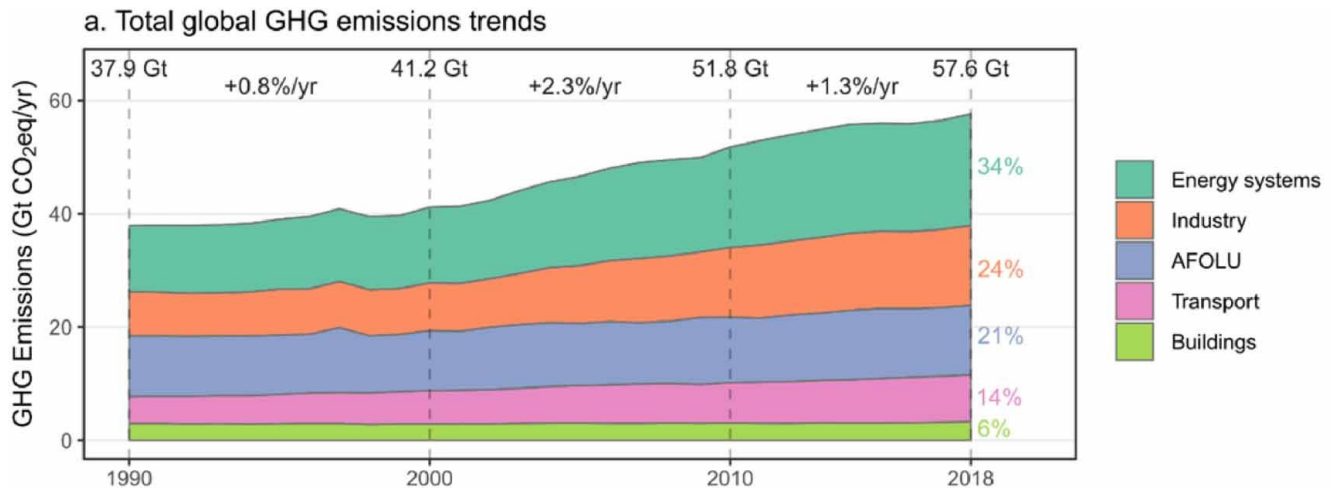
Figure 1.1 Summary of global greenhouse gas emissions by sector from 1990 to 2018

1.2 A Fossil-Fuel Free Economy

To address the increasing consumption of fossil fuels and mitigate climate change, there is significant attention being given to the development of sustainable energy. Renewable energy resources such as wind, solar, geothermal, hydraulic, and nuclear power have been heavily invested in due to their reduced greenhouse gas emissions. However, these energy sources are often location and time-specific. For instance, solar energy is predominantly generated during the daytime when electricity consumption is typically low. On the other hand, electricity usage peaks when people are off work. Efficiently harnessing and utilizing electricity generated by these renewable resources raise critical questions about energy storage and transportation to other areas when needed. Batteries, supercapacitors, hydrogen are considered as the most promising methodology to address the intermittent nature of renewable energy sources and support the integration of clean energy into the grid[2] (Figure 1.2). Among them, by storing and releasing energy electrostatically, supercapacitors can rapidly charge and discharge energy with specific power output up to 104 to 105 Wh Kg-1, making them suitable for applications requiring high power output. However, due to its relatively lower energy density (< 20 Wh Kg-1) compared with batteries (around 220

– 250 Wh Kg-1), supercapacitor cannot store sufficient energy to specific applications required high capacity. In addition, it suffers from the higher self-discharge rate. Hydrogen can offer the highest energy density (> 1000 Wh Kg-1) and serves as the clean fuel to produce zero GHG emissions. Considering the lower energy conversion efficiency, the complicated infrastructure requirements for storage, transportation, and distribution of hydrogen energy, and safety concerns, hydrogen energy has not yet well developed and largely distributed[3]. Compared to them, batteries stand out thanks to higher energy density than supercapacitor, good cycling life, and, flexibility for scale-up, and fast response time for fast discharge applications. It converts the chemical energy contained in their active materials into electric energy through an electrochemical oxidation-reduction reaction. During the daytime, batteries can be charged using renewable energy from fossil fuel-free sources. At night, the stored chemical energy can be released as electric energy and transported to central cities. From the market perspective, batteries are successfully commercialized and will keep booming in the next few decades to rapidly advance the electrification transition.
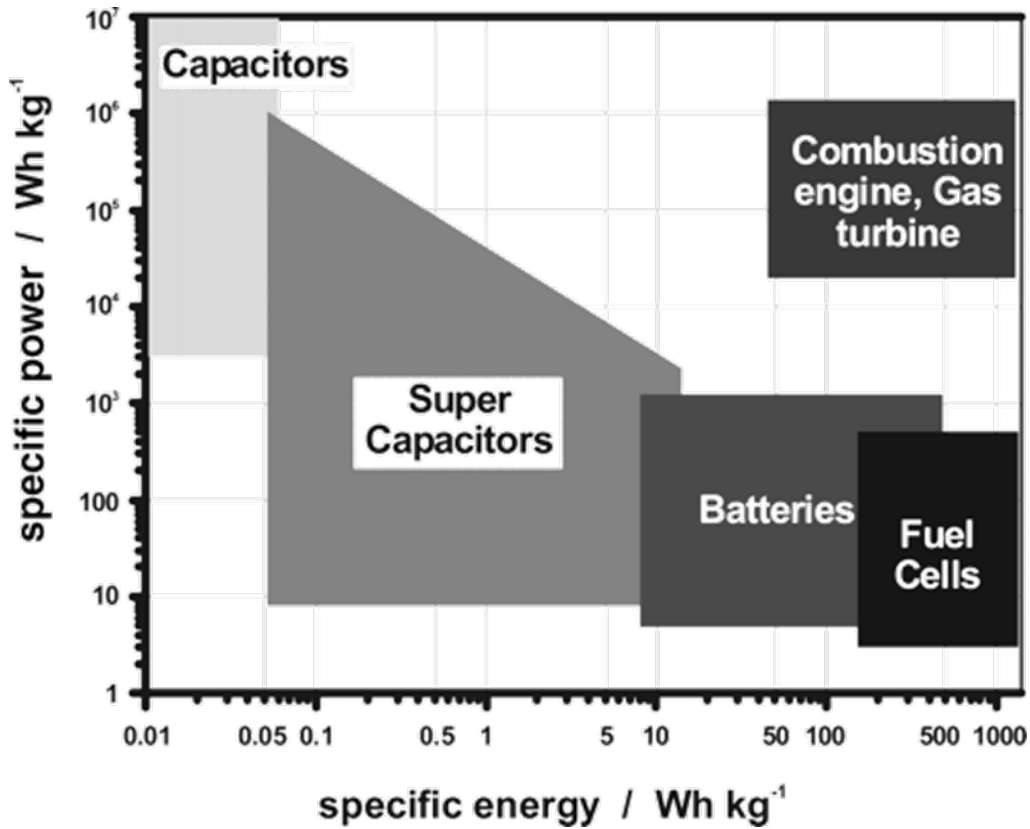
Figure 1.2 Comparison of super capacitors, batteries, and fuel cells.

Batteries play a crucial role in accelerating the transition from petroleum-powered vehicles to battery-powered vehicles, leading to a reduction in greenhouse gas emissions and the elimination of environmental pollution. Figure 1.3 illustrates that the electrification of transportation was relatively limited until 2017(data referred to Rhodium group). However, with advancements in battery technologies, the energy density of batteries has increased. The successful commercialization of Tesla electric vehicles has driven a skyrocketing demand for passenger electric vehicles, which has further grown exponentially since 2020. Projections suggest that this growth trend will continue, with the battery demand reaching over 1400 GWh by 2030. Additionally, we will witness a growth in stationary storage, allowing people to mitigate the reliability issues caused by intermittent power outages resulting from power generation-consumption mismatches.

4

Thanks to improvements in battery manufacturing skills and battery chemistry, the cost of batteries has also significantly decreased. From an early 2000s level of over $8000 per kilowatt-hour (USD/kWh), the cost has now reduced to slightly above $100/kWh by 2020[4]. As the demand for batteries continues to rise, it is anticipated that the cost will further decline. Simultaneously, governmental subsidies are playing an increasingly important role in facilitating the transition from a fossil-fuel-based economy to a sustainable economy powered by renewable resources. These factors contribute to a decrease in pollution and its associated environmental benefits.
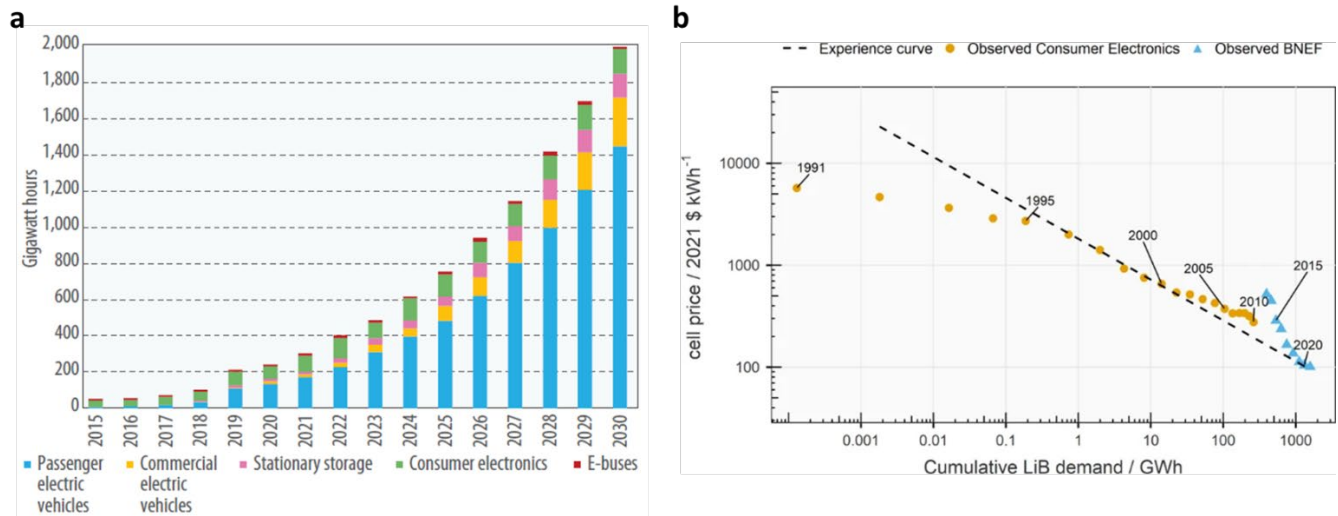
Figure 1.3 Status of Lithium-ion batteries (a) Summary and prospective of uses of lithium-ion batteries (LIB) by sector from 2015 to 2030. (b) Summary of the price change of LIB from 2010 to 2019.

Chapter 2. Introduction of Lithium-ion Batteries

In the **Chapter 2**, I will firstly summarize the history of battery development and introduce the work mechanism of lithium-ion batteries. Specifically, in the chapter 2.2 anode session, graphite-based and lithium metal anode materials will be discussed. In the following chapter 2.3 cathode session, layered oxides and spinel cathodes will be discussed. After that, electrolytes will be extensively discussed in the chapter 2.4 electrolyte sessions. By sectors, design concepts for battery electrolytes, various solvent types, salts for Li-metal batteries will be discussed.

2.1 Lithium-ion Battery Working Mechanism

Lithium-ion batteries are rechargeable energy storage devices commonly used in portable electronics, electric vehicles, and renewable energy systems. They operate based on the movement of lithium ions between two electrodes, typically a graphite anode (negative electrode) and a transition metal oxide cathode (positive electrode), through an electrolyte[5]. During charging, lithium ions (Li^+) are extracted from the transition metal oxide cathode (NMC) and migrate through the electrolyte towards the graphite anode. This movement is driven by a voltage difference created between the cathode and anode. The lithium ions move through the electrolyte solution, typically a lithium salt dissolved in an organic solvent. As the lithium ions reach the anode, they are inserted into the layered structure of the graphite material, commonly referred to as intercalation. This process is reversible, allowing lithium ions to be stored in the graphite anode during charging and released back to the cathode during discharge. Simultaneously, during the charging process, electrons flow through an external circuit from the cathode to the anode. The flow of electrons is driven by the potential difference between the two electrodes, which is maintained by an external power source. As the electrons move through the external circuit, they can perform useful work

such as powering devices or recharging the battery (Figure 2.1). Then, we'd like to describe few definitions which are important for battery.

HOMO stands for Highest Occupied Molecular Orbital, and LUMO stands for Lowest Unoccupied Molecular Orbital. These terms are used to describe the energy levels of electrons in molecules or materials. In the context of Li-ion batteries, the HOMO and LUMO energy levels of the electrolyte and electrode materials play a significant role in the movement of lithium ions during the battery's operation. The energy difference between the HOMO of the electrolyte and the LUMO of the electrode material determines the ease with which lithium ions can be transferred between the electrodes[6].
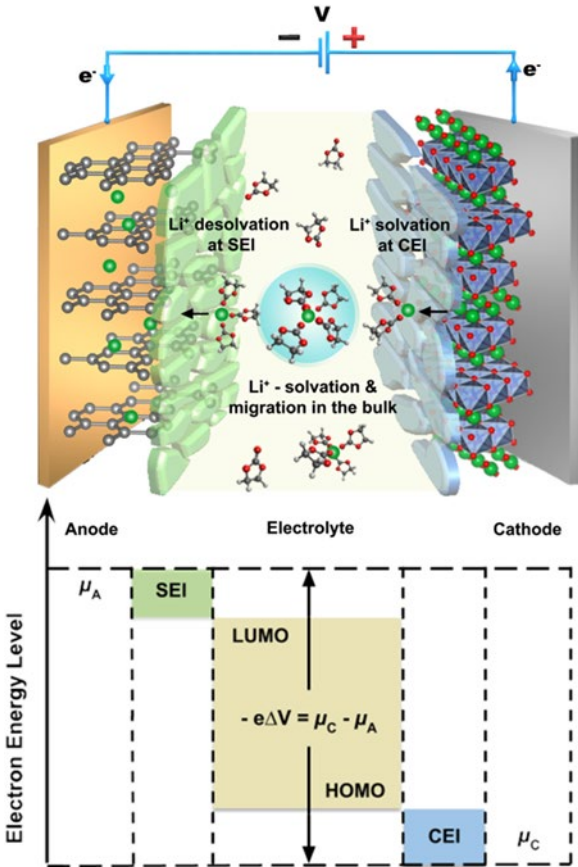
Figure 2.1 Schematic of battery working mechanism

During the initial charging of a Li-ion battery or when exposed to high voltages, a layer called the Solid-Electrolyte Interphase (SEI) forms at the interface between the electrolyte and the electrode

materials[7]. The SEI layer is a thin and stable passivation layer composed of various lithium salts, electrolyte decomposition products, and electrode material components. It acts as a protective layer, preventing further electrolyte decomposition and undesirable reactions between the electrode and electrolyte. The SEI layer also allows the selective transport of lithium ions while blocking the passage of larger and undesired species.

Solvation occurs when the lithium ions dissolve in the electrolyte, which is typically a lithium salt dissolved in an organic solvent[8]. The solvent molecules interact with the lithium ions, stabilizing them and allowing their transport through the electrolyte.

During discharge (or when the battery is in use), as lithium ions move from the anode to the cathode, they undergo desolvation. Desolvation refers to the process in which the lithium ions are released from the solvation structure and become free to move towards the electrode. This desolvation process is crucial for efficient lithium-ion transport and the overall functioning of the battery.

The solvation and desolvation of lithium ions have a significant impact on the performance and behavior of Li-ion batteries. The solvation process affects the solubility and mobility of lithium ions within the electrolyte, while the desolvation process influences the rate of lithium-ion transport and the battery's overall efficiency. The choice of electrolyte solvent and the solvation/de-solvation behavior of lithium ions are important considerations in battery design and optimization.

2.2 Anodes

2.2.1 Graphite-based materials

Graphite anode materials are commonly used in various electrochemical devices, including lithium-ion batteries. They possess several notable characteristics that make them ideal for such applications. Graphite anode materials are composed of stacked layers of graphene sheets. Each graphene sheet consists

of a hexagonal lattice of carbon atoms. These sheets are held together by weak van der Waals forces, allowing for easy intercalation of lithium ions during charging and discharging cycles (Figure 2.2). Graphite exhibits good electronic conductivity due to its unique layered structure[9]. The π-electrons in the carbon-carbon bonds within each graphene sheet can move freely, facilitating electron transfer during electrochemical processes. However, the lithium ions' diffusion through the graphite lattice is relatively slow, limiting the rate at which the battery can charge and discharge. Graphite anode materials are also relatively inexpensive compared to other anode materials like silicon or metal alloys. The availability of graphite and the well-established manufacturing processes contribute to its affordability.

However, graphite anodes have a relatively low theoretical capacity of around 372 mAh/g. This means that the amount of lithium ions that can be stored in graphite is limited, resulting in lower energy density compared to some alternative materials. It also suffers from lower lithium-ion diffusion rates compared to some alternative anode materials, resulting in limitations on the charging and discharging rates of the battery. This can affect the overall power performance of the device[10].
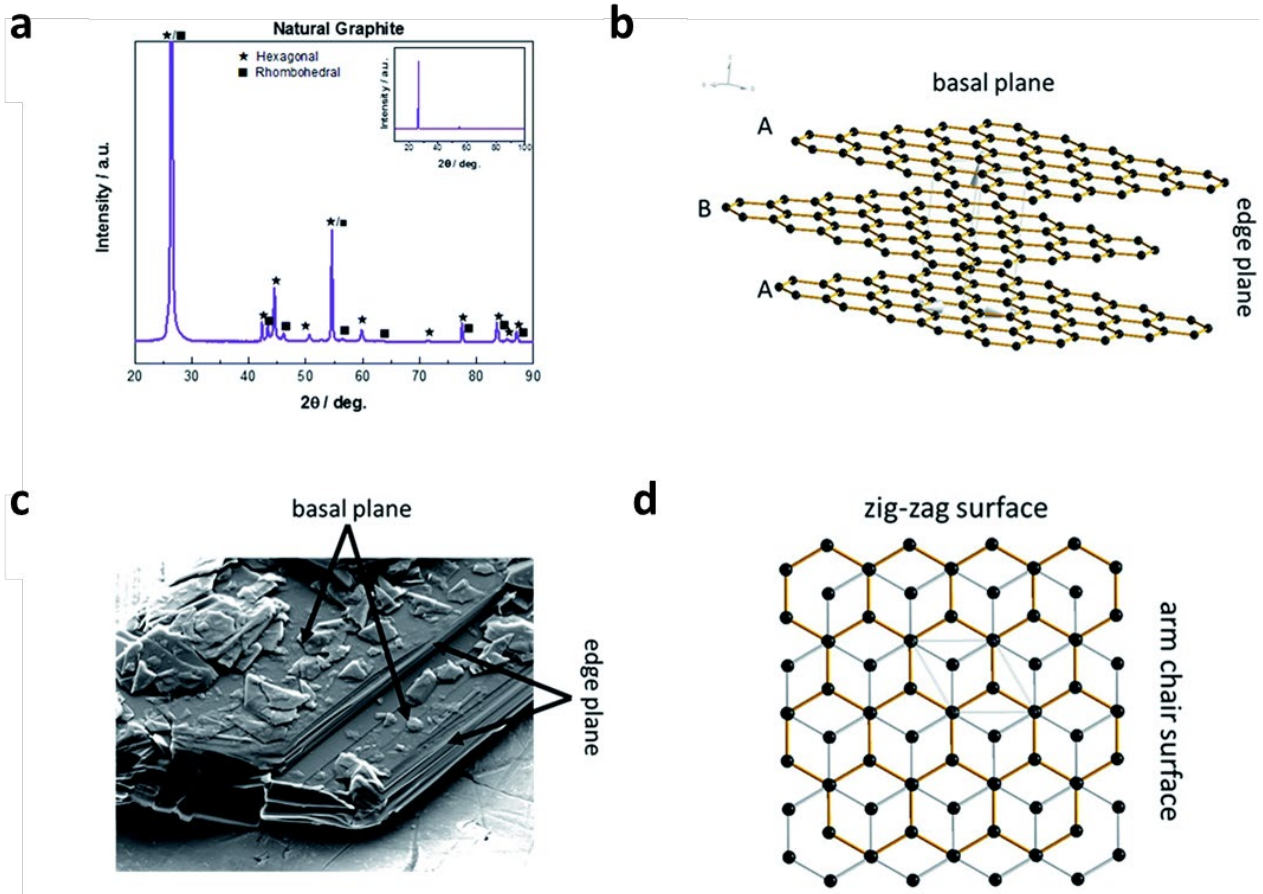
Figure 2.2 Basic properties of graphite electrode. (a) X-ray diffraction of natural graphite. (b) Schematic illustration of the layered structure. (c) Exemplary SEM micrograph (d) Schematic illustration of the layered graphite structure in bird's eye view

2.2.2 Lithium-based materials

Li-Metal Anodes:

Lithium (Li) metal is ideal for use in battery anodes (Figure 2.3), given its highest theoretical specific capacity (3860 mAh g–1), exceedingly low standard reduction potential (−3.04 V relative to the standard hydrogen electrode), and one of the lowest solid densities (0.534 g cm–3)[4]. However, the high reactivity of lithium partially restricts the widespread implementation of lithium metal batteries (LMBs). The primary obstacle with the lithium metal anode is the decline in Coulombic efficiency (CE), a consequence of side reactions that persistently erode the active lithium pool and use up the electrolyte.

Ideally, electrolytes should create a shielding solid electrolyte interphase (SEI) to curb further reactions between lithium and the electrolyte. Unfortunately, the significant volume change of the lithium anode during cycling undermines the SEI, allowing newly exposed lithium to react with the electrolyte. This issue is magnified by the unevenness in the SEI, which encourages dendritic lithium plating. These lithium dendrites with high aspect ratios can readily lead to the development of non-functional or "dead" lithium during long-duration cycling. Besides, the byproducts from these reactions result in a buildup of a thick SEI layer and "dead lithium", enhancing cell overpotential and accelerating cell failure. Recently, more developments are performed to address above issues[11].

Researchers are exploring the use of solid-state electrolytes and fluorinated electrolytes in Li-metal batteries to replace the conventional liquid electrolytes. Solid-state and fluorinated electrolytes can enhance safety by reducing the risk of dendrite formation, improve cycling stability and improve the system thermal stabilities. Various protective coatings and additives are being investigated to mitigate the reactivity of the lithium metal anode with the electrolyte. These coatings and additives aim to suppress dendrite growth, improve Coulombic efficiency, and prolong battery life. Some studies have explored the use of composite anodes, combining lithium metal with other materials like carbon or metal oxides. These composite anodes aim to improve cycling stability, promote uniform lithium deposition, and enhance the overall performance of Li-metal batteries.
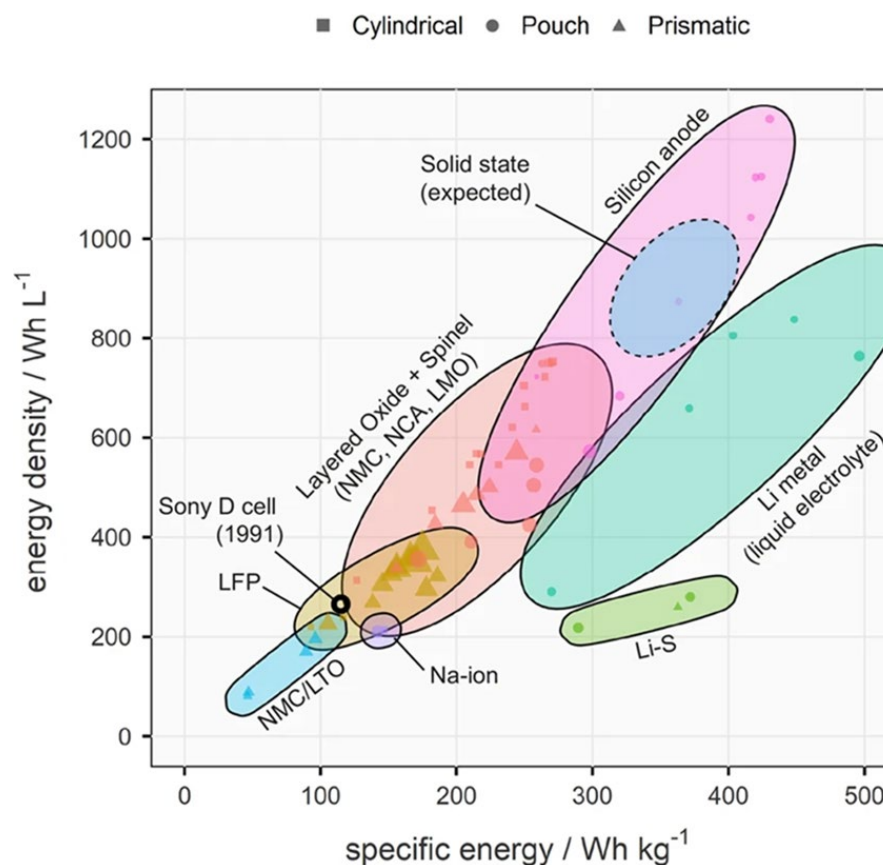
Figure 2.3 Summary of energy density for different battery chemistries

2.3 Cathodes

In the entire time frame of LIBs, the overarching goal has always been high energy density, long cycle life, and high safety. To that end, extensive screening, and development of practical electrode materials for LIBs remains a core process in innovating the LIB landscape.

Ideally cathode materials for LIBs should possess: 1) A higher standard reduction potential relative to the anode for a high cell voltage; 2) Sufficient electronic conductivity and Li-ion diffusion; 3) High reversible capacity; 4) High chemical/electrochemical stability against electrolytes. Development of cathode materials satisfying the requirements can mainly be categorized into intercalation and conversion regarding their reaction mechanism with Li[12].

2.3.1 Intercalation-type

Intercalation cathodes are widely utilized in commercialized LIBs where Li ions are intercalated/deintercalated in the electrode without severe volumetric expansion. On the other hand, conversion cathodes undergo a phase conversion reaction during the charge/discharge process, effectively increasing the specific capacity at the cost of structural and cycling stability. While the high specific capacity of conversion-type cathodes is promising for next-generation battery technologies[13], issues with cycle life, rate capability, and other shortcomings must be first addressed to enable their practical applications. As such, research efforts have predominantly been focused on intercalation cathodes for practical applications despite their lower specific capacities compared to conversion type cathodes.

Starting in the 1970s, Whittingham demonstrated the first rechargeable lithium metal battery based on a TiS2 cathode, capable of the chemical intercalation of one lithium per TiS2 molecule[14]. Although good reversibility was enabled, the low cell voltage (< 2.5V) limited the energy density with further Li-metal issues, raising serious safety concerns. Future development of cathodes to increase cell voltage and circumvent utilization of the Li-metal anode led to exploration of lithiated transition metal oxide cathodes in the 1980s by Goodenough's group[15].

Fundamentally, the switch from transition-metal disulfides (MS2) to transition-metal oxides as cathode materials is based on the understanding that the O2-:2p band lies at a lower energy than the S2-:3p band. As the difference between the redox energies of the cathode and anode dictates cell voltage, transition-metal oxides enable cell voltages as high as 4V since higher oxidation states of transition metals such as Co3+/4+ may be accessed (Figure 2.4)[16]. Whereas attempts to access higher oxidation states in sulfides will result in oxidation of the S2- ions. This paradigm shift resulted in the discovery of three classes of oxide cathodes by Goodenough's group in the 1980s which will be further discussed.
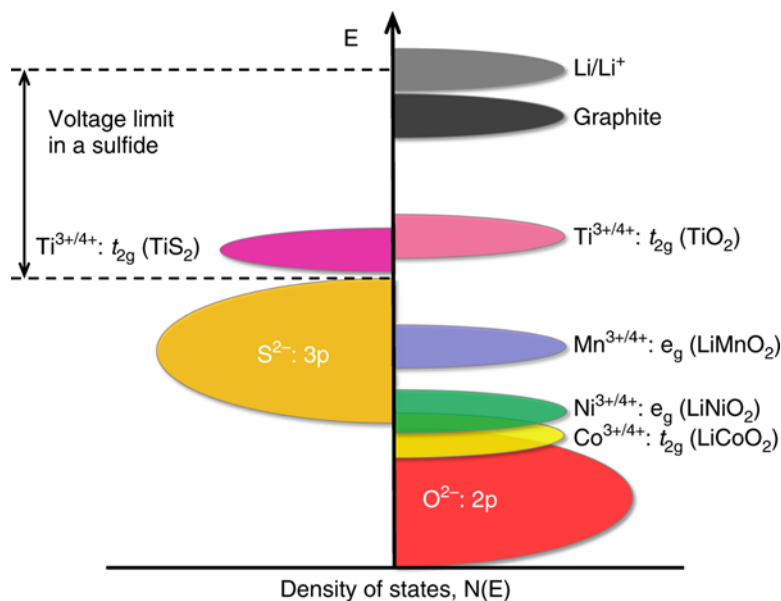
Figure 2.4 Redox energy bands relative to anion: p bands. The lower energy of the O^{2-}: 2p band allows for access to higher oxidation states of transition metals, enabling transition-metal oxides to operate at substantially higher voltages (~4V) than transition-metal disulfides (<2.5V)

Primarily, LiCoO2 (LCO), LiMn2O4 (LMO), and LiFePO4 (LFP) will be discussed as representative materials for the layered, spinel, and olivine classes of transition-metal oxides due to the high volume of reported literature behind their applications in rechargeable LIBs.

As the first-generation cathode in commercialized LIBs, the layered LCO possesses excellent two-dimensional lithium-ion diffusion owing to the good cation ordering of the Li+ and Co3+ within its alternate (111) planes (Figure 2.5a). Coupled with high electronic conductivity, LCO offers fast charge-discharge characteristics with high reversibility. Therefore, it continues to see prevalent usage for portable consumer electronics. However, irreversible capacity loss occurs during excessive charging or Li-ion extraction (x > 0.5) from the Li1-xCoO2 layered crystal lattice [17], explaining the variance in practical specific capacity (~140 mAh g-1) from the theoretical specific capacity (274 mAh g-1).

Further development of layered transition-metal oxides as cathodes aimed to address the high cost from Co and limited capacity of LCO, mainly involving either elemental doping or surface modifications to reduce capacity loss[18]. A big breakthrough in this regard was the synthesis of layered ternary transition-

metal oxides such as LiNi1-y-zMnyCozO2 (NMC) in 2001[19] with the design principle being that each individual transition metal perform a specific function. Specifically, the introduction of Ni allows for a higher Li extraction and capacity.x However, the synthesis of LiNiO2 (LNO), an analogue to the layered LCO, typically sees the reduction of Ni3+ which makes a well-ordered structure difficult to achieve[20]. Meanwhile, incorporation of Mn can maintain the structural stability as Ni2+ is stable in the presence of Mn4+. Consequently, recent trends have been to progressively increase the Ni content and decrease the Co content in NMC such that higher capacity and lower costs may be achieved simultaneously. Nonetheless, rational design of NMC cathodes for next-generation battery systems must consider the individual characteristics of Mn, Co, and Ni such as chemical/structural stability, electrical conductivity, abundance, and environmental benignity.
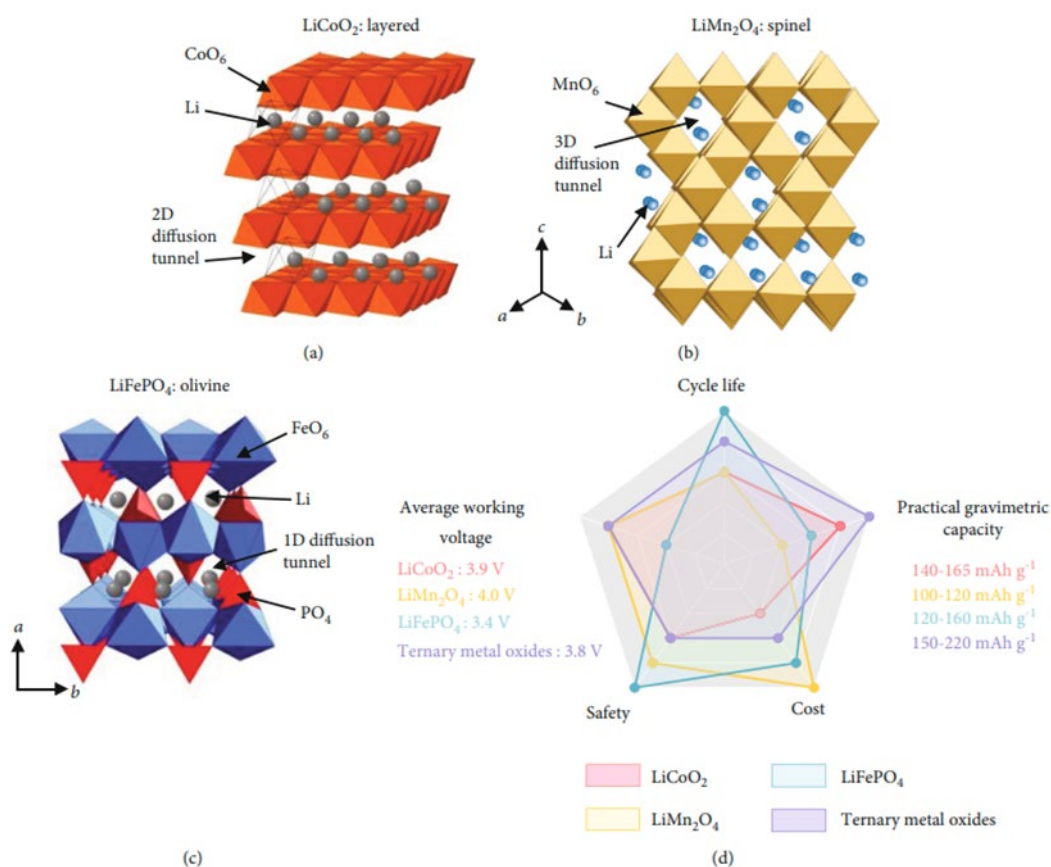
Figure 2.5 Commercial transition-metal oxide cathode materials. Crystal structures of (a) LiCoO₂, (b) LiMn₂O₄, (c) LiFePO₄, and (d) radar summary chart for commercial cathode materials

As opposed to the layered class of oxides, spinel LMO offers three-dimensional lithium-ion diffusion where Mn vacancies allow for Li-ion transportation within the spinel framework and a cubic close-packed structure of oxide-ions. Compared to layered LCO as a cathode material, LMO has even faster charge-discharge characteristics with good reversibility, making it a promising candidate for high powered batteries. Albeit the practical specific capacity of LMO (120 mAh g-1) is relatively low amongst cathode materials and Mn dissolution with trace H+ (acidity) in electrolytes leads to capacity fading[21]. Presently, research efforts have been made to partially substitute Mn with other transition metals such as Ni with similar working concepts as NMC, resulting in the $LiMn_{1.5}Ni_{0.5}O_2$ (LNMO) spinel[22]. Subsequently, the stabilization of the Ni2+ in the presence of Mn4+ in LNMO provides a higher operating voltage at ~4.7V.

Firstly, proposed as a cathode material by Goodenough's group in 1997[23], olivine LFP contrasts the layered and spinel class oxides by having slow one-dimensional lithium-ion diffusion and relatively low electronic conductivity. These issues, however, are mostly remedied by reducing the particle size or additional carbon coating. Moreover, olivine LFP intrinsically possesses higher thermal stability and safety compared to the layered and spinel oxide cathodes as the oxygen is bounded strongly to P by covalent bonds[24]. This makes olivine LFP highly appealing for grid-storage applications where volumetric energy density is less crucial of a parameter.

2.3.2 Conversion-type

Besides layered oxides, there are increasing attentions to revisit conversion-type cathode materials due to their high specific capacity, low cost. Here, we take an example of iron trifluoride (FeF3). The conversion-type FeF_3 electrode is a promising material for use in lithium-ion batteries (LIBs). FeF3 undergoes a conversion reaction during the charging and discharging processes, leading to the reversible insertion and extraction of lithium ions (Li+). In the initial discharging stage, FeF3 acts as the cathode material. As the battery discharges, lithium ions (Li+) are extracted from the anode (typically Li metal)

and migrate through the electrolyte toward the cathode. When the lithium ions reach the FeF3 cathode, a conversion reaction occurs. Based on Figure 2.6, a transition phase of A-LixFeyF3 will firstly form. When the state of discharge further goes, the A-LixFeyF3 will be reduced to FeF3 and B-LixFeyF3. Then the discharge voltage reaches to around 1 V, FeF3 will finally be reduced to Fe and the formation of LiF happens. The FeF3 compound reacts with the lithium ions, resulting in the reduction of FeF3 to form iron (Fe) and lithium fluoride. This conversion reaction involves the breaking and formation of chemical bonds within the FeF3 lattice. There will be some irreversible capacity loss during discharging and not 100 % capacity can be charged back. During charging, Fe will be oxidized to FeF3 and A-LixFeyF3. This reconversion allows the FeF3 cathode to store and release lithium ions reversibly (Figure 2.6)[25].
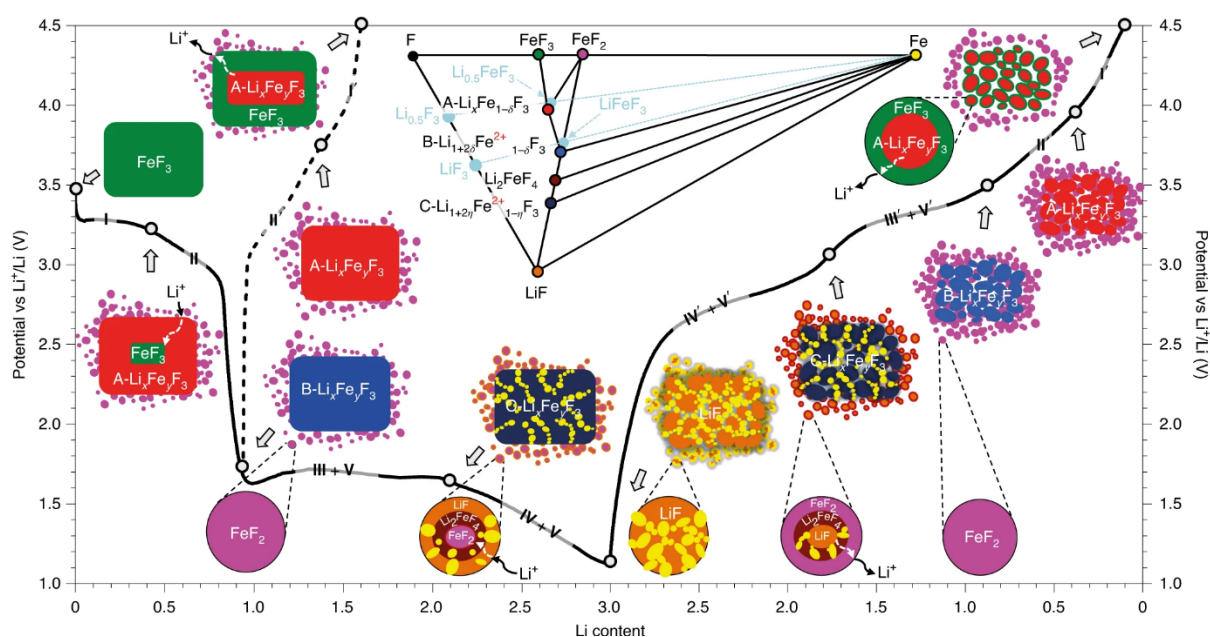
Figure 2.6 Proposed discharge and charge process for Li/FeF3 system

It's important to note that the conversion-type FeF3 electrode typically experiences significant volume changes during the conversion reaction, which can cause mechanical stress and particle pulverization. To address this issue and maintain electrode integrity, various strategies, such as nano-structuring, carbon

coating, or the use of conductive additives, can be employed to improve the electrode's performance and stability.

The conversion-type FeF3 electrode has gained attention as a potential high-capacity cathode material for LIBs due to its high theoretical capacity and environmentally friendly nature. However, challenges remain, including issues related to electrode reversibility, cycling stability, and capacity fade, which researchers are actively addressing through material design and optimization approaches.

2.4 Electrolytes

2.4.1 Design concepts

The battery electrolyte plays a critical role in the functioning of lithium-ion batteries (LIBs) by providing sufficient ion transport, stabilizing the interface between the anode and cathode, and influencing overall battery safety[26].

Conventional carbonate electrolytes easily cause dendritic lithium (Li) growth and porous solid electrolyte interphase (SEI) formation due to their incompatibility with Li metal and undesirable SEI chemical compositions. While ethers have been proposed for better Li metal compatibility, their oxidative stability remains questionable when coupled with high-voltage layered oxides. To address this issue, new electrolyte concepts have been developed.

High salt concentration (HCE) electrolytes have been developed to improve oxidative and reductive stabilities[27]. At diluted concentrations, Li+ ions are surrounded by solvents, resulting in a solvent-separated ion pair solvation structure. As the salt concentration increases, the anions participate in the solvation structure, forming contact ion pairs. Simultaneously, the presence of free solvents in the solvation structure decreases. When the salt concentration reaches its saturation state, clusters of Li+ ions with anions and solvents form, resulting in aggregate solvation structures. It has been demonstrated that

18

the anion-pair rich solvation structure facilitates the decomposition of the salt anions and typically forms an organic outer layer and an inorganic inner layer SEI. This salt-derived SEI effectively passivates the Li metal and prevents corrosion from the electrolytes (Figure 2.7)[28]. However, HCE electrolytes also suffer from reduced ionic conductivity and reduced wettability on separators and electrodes. To address these issues, localized highly concentrated electrolytes (LHCE) have been introduced and developed[29]. These LHCEs maintain the local salt/solvent molar ratio while adding diluents to lower the overall salt concentration of the electrolyte. This approach enhances Li+ ion diffusivity and improves wettability towards electrodes and separators.
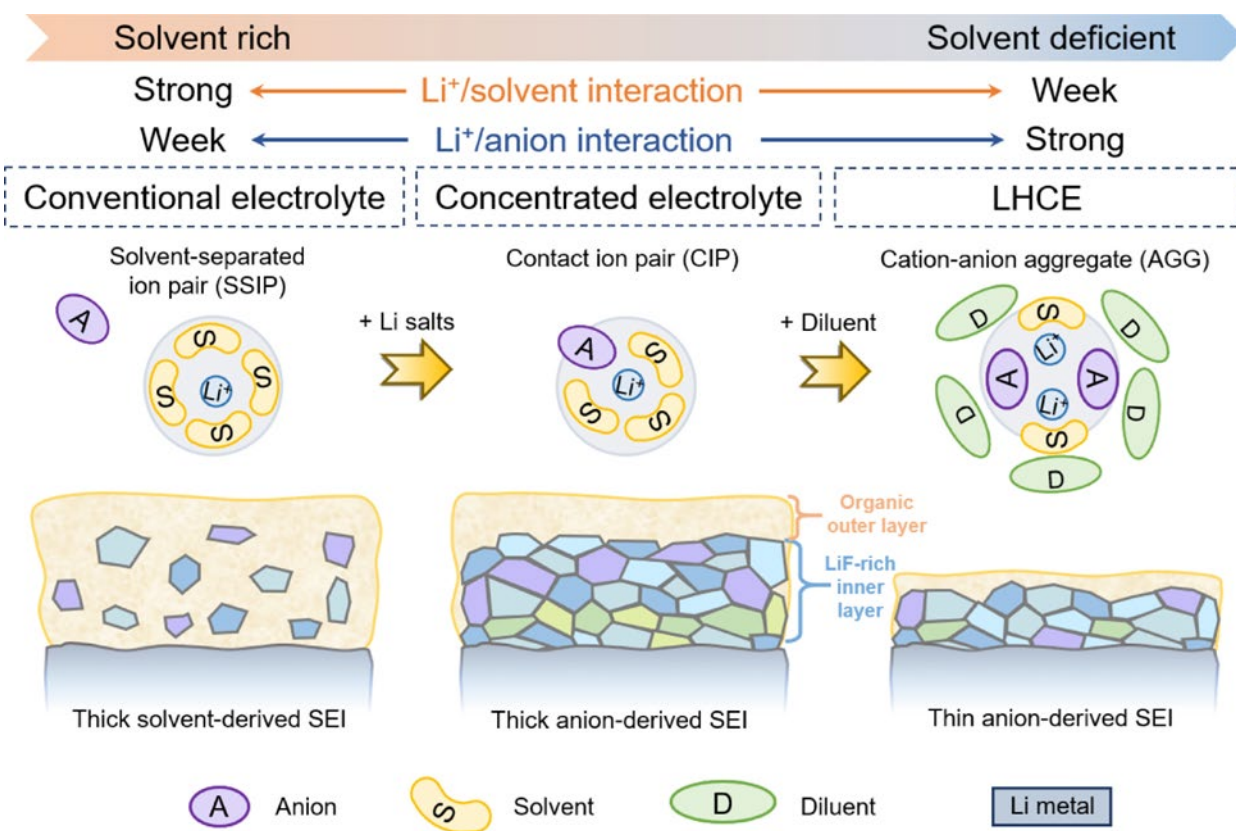
Figure 2.7 Illustration of different electrolytes based on the solvation structures

Besides the design parameters based on solvation structures, searching for physical properties to design different solvents are also considered. To overpass the physical limit of liquid solvents, a new type of liquefied gas solvents has been proposed. In 2017, the first demonstration of fluoromethane (FM) based

liquefied gas electrolytes (LGE) showcased its attractive properties, including a low melting point (-141 °C), low viscosity (0.085 cP), high dielectric constants, and a wide HOMO/LUMO gap[30]. These properties made FM a promising candidate for high-performance electrolytes. The initial generation of FM-based LGE enabled good Li/LCO and moderate Li/Cu cycling (~97.2 % C.E.), which were attributed to the favorable properties of FM.

However, FM suffers from poor salt solubilities. To address this issue, the addition of Tetrahydrofuran (THF) as a cosolvent was demonstrated to improve salt solubility. The THF-FM LGE combination resulted in an average Li C.E. of 99.6% over 500 cycles, surpassing the state-of-the-art performance[31].

Nevertheless, the THF-FM based LGE exhibits poor oxidative stability due to the ether characteristics of THF. To improve the situation, THF was replaced with Acetonitrile (ACN), which increased the salt concentration from 0.3 M to 1.2 M. The resulting ACN-FM based LGE enabled good Li/NMC cycling over 500 cycles and expanded the temperature window to 55°C, providing a wider operational temperature range[32].

Subsequently, difluoromethane (DFM) was explored as an alternative to FM, as it showed slightly improved safety features. However, DFM has lower salt solubility compared to FM, and the performance of DFM based LGE was found to be less competitive, particularly in terms of oxidative stability[33].

In summary, LGE systems show promising to improve the lithium-metal cyclability, low-temperature operation, and oxidative stability. However, there is an urgent need for a comprehensive understanding of the fundamental strategies required to improve safety.
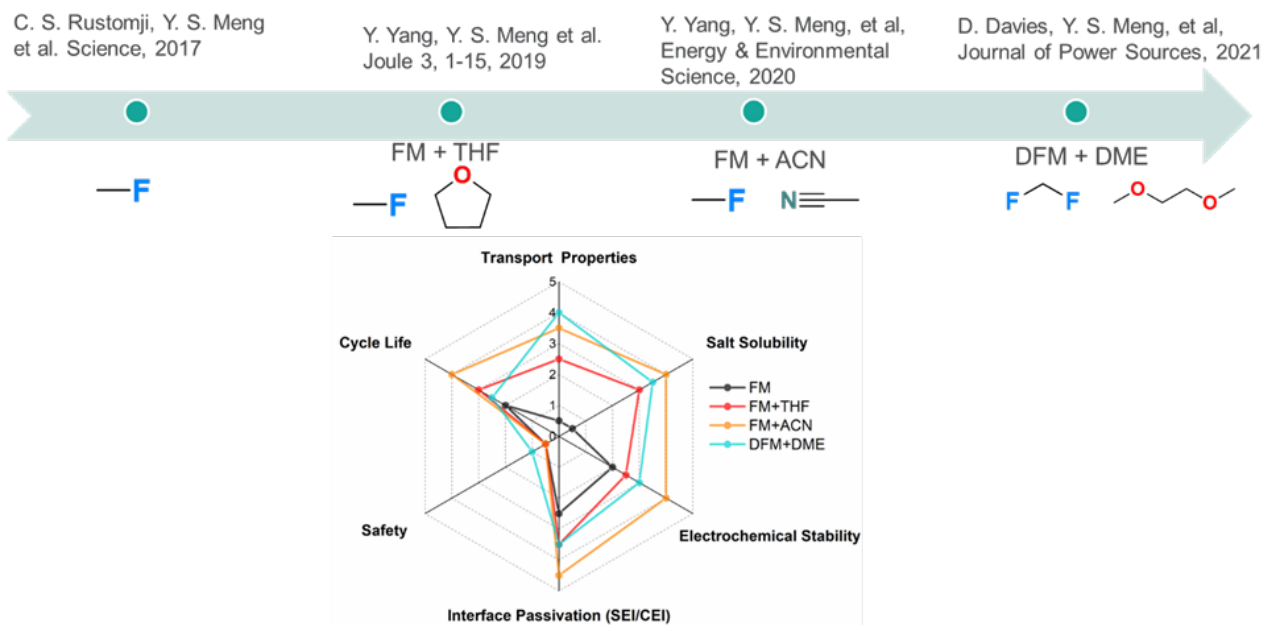
Figure 2.8 Timeline and summary of developed LGEs for enabling lithium metal anode

2.4.2 Different Functional Groups for Battery Solvents

Ether electrolytes have gained attention as a viable alternative to conventional carbonate electrolytes in lithium metal batteries. Unlike carbonate electrolytes, ethers exhibit lower reactivity towards lithium metal, thereby reducing the risk of dendrite formation and the growth of the solid electrolyte interphase (SEI) layer. However, it is important to note that ether electrolytes also have certain limitations, particularly concerning their oxidative stability when paired with high-voltage cathode materials like layered oxides. The elevated voltage levels can trigger side reactions that degrade the ether electrolyte and compromise its stability, leading to diminished battery performance and potential safety concerns.

To address these concerns, recent proposals have suggested the use of fluorinated ether solvents to enhance the oxidative stability while preserving the compatibility of ethers with Li-metal[34]. Figure 2.9 demonstrates that partially fluorinated solvents like F4DEE and F5DEE show promising potential for improved oxidative resistance. Additionally, these fluorinated solvents exhibit higher boiling points compared to 1,2 DEE. It is worth noting, however, that there may be a slight decrease in reduction

resistance due to the fluorination process. Nevertheless, the presence of pre-stored fluorine within the solvent molecules allows for the formation of LiF, which can serve as a protective layer on the Li-metal surface to offset the reduction resistance reduction[35]. Although limited publications are available on the topic[34], the strategies involving fluorinated ethers hold promise for enhancing the oxidative stability of ethers while maintaining excellent cycling stability for Li-metal.

a

Molecular Structures	Name	Melting Point (°C)	Boiling Point(°C)
	DME	−58	85
	1,2 DEE	−74	121.4
	F4DEE	-	186
	F5DEE	-	186
	BTFE	25	63

b
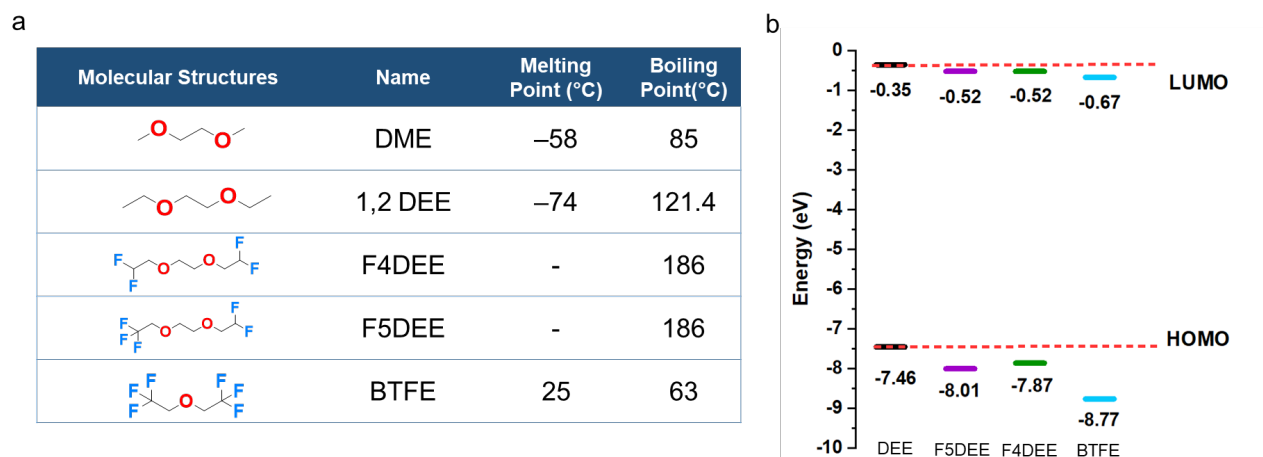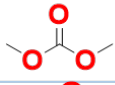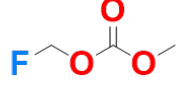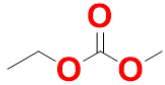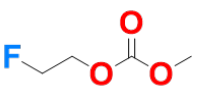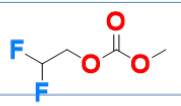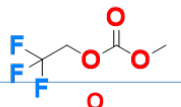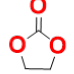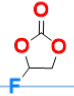
Figure 2.9 Summary of ether solvents and its related simulated LUMO and HOMO values

Carbonate solvents, such as EC and EMC, have been widely utilized in traditional lithium-ion batteries due to their ability to form a stable solid electrolyte interphase (SEI) with graphite, as well as their balanced physical properties, including dielectric constant, viscosity, melting point, and boiling point, when compared to ethers and esters (Table 2.1). However, when applied to lithium-metal systems, carbonated electrolytes have shown limited performance due to issues such as dendritic growth and the formation of a thick SEI layer.

Nevertheless, these challenges can be effectively addressed by incorporating high salt concentrations or utilizing localized highly concentrated carbonated electrolytes. These approaches mitigate the incompatibility with lithium metal and promote the formation of a salt-derived SEI, resulting in a denser lithium morphology. Particularly noteworthy is the use of high concentrations of FEC, as the

decomposition of the FEC solvent leads to the formation of an SEI enriched with LiF. This LiF-rich SEI has the potential to improve Li-metal cyclability and enhance high-voltage endurance up to 5 V[36].
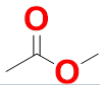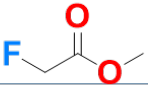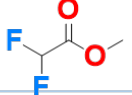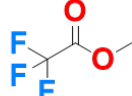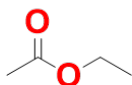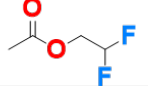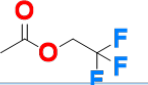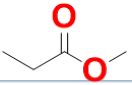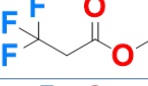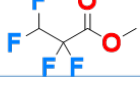
Table 2.1 List of different carbonates for potential battery solvents

Molecular Structures	CAS	Name	Melting Point (°C)	Boiling Point(°C)
	616-38-6	DMC	2	90
	207804-61-3	F1DMC	-	108
	623-53-0	EMC	−55	101
	627-43-0	F1EMC	-	93
	916678-13-2	F2EMC	-	-
	156783-95-8	F3EMC	-	90
	96-49-1	EC	35	243
	114435-02-8	FEC	18	212

Esters and propionates are commonly employed as cosolvents to enhance ionic transport in low-temperature lithium-ion batteries[37]. Their reduced freezing point and viscosity compared to carbonates make them favorable choices. Moreover, esters and propionates exhibit improved thermodynamic compatibility with lithium metal when compared to carbonates. However, their application in lithium-metal anodes has received limited attention due to challenges such as their low boiling point and relatively poor salt solubility, which hinder the formation of an anion-rich solvation structure necessary for facilitating the salt-derived solid electrolyte interphase (SEI).
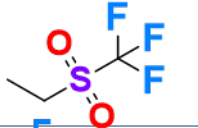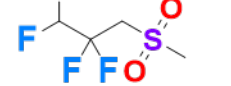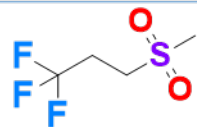
In a recent study by John et al.[38], fluorination of propionates was performed, resulting in the utilization of F3MP in combination with FEC, which demonstrated excellent stability of the lithium metal anode. This fluorinated system exhibited enhanced oxidative stability and resilience at low temperatures, attributed to the formation of fluorine-rich interphases. Apart from F3MP, there are other potential fluorinated esters and propionates worth exploring for their potential to enhance Li-metal stability. Conducting systematic investigations into fluorination strategies for esters and propionates represents an interesting direction for battery electrolyte design.

Table 2.2 List of different acetates and propionates for potential battery solvents

Molecular Structures	CAS	Name	Melting Point (°C)	Boiling Point(°C)
	79-20-9	MA	−98	57
	453-18-9	F1MA	−40	104
	433-53-4	F2MA	-	85
	431-47-0	F3MA	−78	43
	141-78-6	EA	−83	77
	1550-44-3	F2EA	-	106
	406-95-1	F3EA	-	78
	554-12-1	MP	−88	80
	18830-44-9	F3MP	-	96
	1893-38-5	T4FMP	-	93

Fluorinated sulfones have mainly been studied for graphite systems, due to their fluorination features of generating LiF SEI and enhanced oxidative stabilities. However, rare studies have been performed for lithium metal batteries. Considering some successful demonstration of fluorinated sulfones in the graphite/high-voltage cathodes[39], preferrable fluorinated features and relatively low Li solvating power, it is hypothesized to generate LiF-rich SEI and CEI and retain anion-pair solvation structures. Thus, it might be worthing to explore their potential in the lithium metal systems. Physical properties for some reported fluorinated sulfones[39] are summarized and listed in the table 2.3.

Table 2.3 List of different fluorinated sulfones for potential battery solvents

Molecular Structures	Name
	TFEMS
	FMES
	TFPMS
	FPMS

2.4.3 Battery Salts
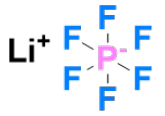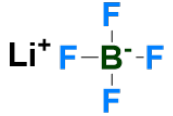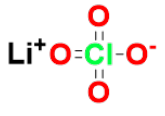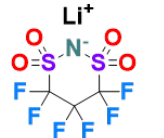
Lithium salt is an essential component of electrolytes in lithium-ion batteries. It not only provides free-shuttling ions and facilitates ion transport within the battery but also participates in the formation of solvation structures and plays a crucial role in the chemical composition of the solid electrolyte interphase (SEI) film. Commonly used lithium salts in battery electrolytes include $LiPF_6$ (lithium hexafluorophosphate), LiFSI (lithium bis(fluorosulfonyl)imide), and $LiBF_4$ (lithium tetrafluoroborate)[6].

$LiPF_6$ is widely used in commercial graphite-based lithium-ion batteries. It offers good stability, high ionic conductivity, and a wide electrochemical stability window. LiPF6-based electrolytes have been extensively studied and optimized for high-performance battery applications, compatible with graphite, NMC, LFP, and other materials. However, concerns exist regarding the safety and stability of LiPF6 electrolytes at elevated temperatures or in the presence of moisture. Under certain conditions, LiPF6 can decompose, releasing toxic and corrosive gases, which poses safety risks.

LiFSI has gained attention as a promising lithium salt electrolyte additive for advanced rechargeable batteries, particularly for lithium metal anodes. LiFSI exhibits improved thermal stability compared to LiPF6 and high ionic conductivity. LiFSI-based electrolytes have demonstrated enhanced stability when in contact with lithium metal and effectively suppress dendrite growth at high salt concentrations. However, recent studies have raised concerns about its thermal stability, as the LiFSI-based system may undergo exothermic decomposition above 210°C.

$LiBF_4$ is another lithium salt used as an electrolyte additive in lithium-ion batteries. It offers good thermal stability and a wide electrochemical stability window. LiBF4-based electrolytes have been investigated for their compatibility with various electrode materials and their impact on battery performance, particularly in low-temperature applications. However, LiBF4 exhibits lower ionic conductivity compared to LiPF6, limiting its suitability for high-performance battery systems.

Table 2.4 List of different salts for battery electrolytes

Molecular Structures	CAS	Name	Melting Point(°C)
	171611-11-3	LiFSI	124-128
	90076-65-6	LiTFSI	234
	21324-40-3	$LiPF_6$	200
	14283-07-9	$LiBF_4$	296.5
	7791-03-9	$LiClO_4$	236
	33454-82-9	LiOTf	>300
	189217-62-7	LiHFDF	-

Chapter 3. Ultra-Low Temperature Li/CF$_x$ Batteries Enabled by Fast-transport and Anion-pairing Liquefied Gas Electrolytes

Lithium fluorinated-carbon (Li/CF$_x$) is one of the most promising chemistries for high-energy density primary energy storage system in applications where rechargeability is not required. Though Li/CF$_x$ demonstrates high energy density (>2100 Wh kg^{-1}) under ambient conditions, achieving such a high energy density when exposed to subzero temperatures remains a challenge, particularly under high current density. Here, we report a liquefied gas electrolyte with an anion-pair solvation structure based on dimethyl ether with a low melting point (−141 ^{o}C) and low viscosity (0.12 mPa×S, 20 ^{o}C), leading to high ionic conductivity (> 3.5 mS cm^{-1}) between −70 and 60 ^{o}C. Besides that, through systematic X-ray photoelectron spectroscopy integrated with transmission electron microscopy characterizations, we evaluate the interface of CF$_x$ for low-temperature performance. We conclude that the fast transport and anion-pairing solvation structure of the electrolyte brings about reduced charge transfer resistance at low temperatures, which resulted in significantly enhanced performance of Li/CF$_x$ cells (1690 Wh kg^{-1}, −60 ^{o}C based on active materials). Utilizing 50 mg cm^{-2} loading electrodes, the Li/CF$_x$ still displayed 1530 Wh kg^{-1} at −60 ^{o}C. This work provides insights into the electrolyte design that may overcome the operational limits of batteries in extreme environments.

3.1 Introduction

Primary batteries serve an indispensable role in providing sustainable power in extreme environments which require long storage and operation life. Thus, there is an escalating demand for primary batteries with high energy/power density and extreme-temperature adaptability. Amongst the well-known primary batteries, Li/CF_x presents itself as one of the most promising candidates for satisfying the above requirements. At the same time, other chemistries, e.g., Li/Manganese oxide (Li/MnO_2), Li/Sulfur dioxide (Li/SO_2), and Li/Thionyl chloride ($Li/SOCl_2$), suffer from swelling[40], gas venting, and toxicity. Li/CF_x is a lightweight, safe, and highly stable system with a low self-discharge rate of < 0.5 % per year at room temperature with the highest theoretical energy density up to 2180 Wh kg^{-1} (CF_1 based on active materials). However, the Li/CF_x batteries suffer inferior rate and low-temperature (Low-T) performance due to the sluggish bulk electrolyte transport and increased charge transfer impedance. To overcome the above challenges, the kinetic limitations of Li/CF_x must be understood and addressed. These include (1) Li^+ diffusion through the solid electrolyte interface (SEI) and cathode electrolyte interface (CEI) layers; (2) Li^+ solvation and de-solvation processes; (3) Li^+ diffusion through bulk electrolytes; (4) Li^+ insertion and/or diffusion in CF-CF layers; (5) C-F bond breaking. Of the steps above, 1-4 are directly related to the electrolyte, indicating that the electrolyte plays a major role in governing the low-T behavior. However, current electrolyte research prioritizes the pursuit of performance rather than comprehensive understanding of the dominating factors governing low-T behavior.

Historically, electrolyte design for low-temperature Li/CF_x batteries have prioritized low freezing point and low viscosity solvents to optimize the Li^+ transport. Tracing back to the effective conventional electrolytes for Low-T CF_x batteries, NASA's Jet Propulsion Laboratory firstly reported an electrolyte formula consisting of 1 M lithium tetrafluoroborate ($LiBF_4$) coupled with 4:1 dimethoxyethane (DME): propylene carbonate (PC), which could deliver more than 600 mAh g^{-1} capacity at C/40 rate under −40ºC[41].

The optimized salt concentration and tris(2,2,2-trifluoroethyl) borate (TTFEB) additive further enhanced the specific capacity to around 300 mAh g^{-1} at C/5 rate under −60 ºC. Additionally, the utilization of acetonitrile outperformed the DME system at both power capability (C/10) and low-temperature discharge performance (−60 ºC). This was due to its improved ionic conductivity (5 mS cm^{-1} to 11 mS cm^{-1}), facilitating bulk electrolyte transport at low temperatures. However, recent reports detailing the insertion of solvated Li$^+$ into the CF$_x$ lattice and the formation of a ternary intermediate C-(solvated Li$^+$-F) imply that the electrolyte solvation structure directly influences the charge-transfer resistance as well, which is known to be crucial at low-temperature. To this end, replacing strongly solvating DME with relatively weak solvating methyl butyrate (MB), which enabled an anion-pairing solvation structure, has been shown to improve both the high rate and low-temperature performance of Li/CF$_x$ cells. The authors demonstrated an improved rate performance (1 C, 834 mAh g^{-1}) and a 240 mAh g^{-1} discharge capacity under −70 ºC at 0.5 V cutoff voltage, although the formulated electrolyte delivered less than 1 mS cm^{-1} ionic conductivity at −70 ºC. Therefore, the design criteria of low-T electrolytes for CF$_x$ batteries are either fast bulk ionic transport or formulating anion-pair solvation structure or integrating both parameters, where more recent studies demonstrated the anion-pair solvation structure may predominate the low-T discharge kinetics. However, the pursuit of both factors is mostly contradictory and rarely reported in the battery field. The formation of anion-pair structure requires the increase of salt concentration or the addition of inert diluents to form a locally high salt-to-solvent ratio, which reduces the ionic conductivity of the electrolyte and increases viscosity. On the contrary, the dilute concentration electrolytes often offer the higher ionic conductivities, but they may suffer from the sluggish de-solvation process due to stronger Li$^+$-solvent coordination at reduced temperatures especially when using solvents with high solvating power[42-43]. Apart from the above discussions, electrolytes also determine the properties of anode/electrolyte interphase (SEI) and cathode/electrolyte interface (CEI). For example, SEI formed on lithium metal vary at different

temperature and is proven to affect the low-T lithium metal cycling efficiency. Given the sensitivity of the CEI formed at CF_x and the significant volume expansion after CF_x discharge, there is no clear report on the chemical composition of the CEI at sub-zero temperature and its correlation with low-T performance.

Owing to the ultra-low melting point and viscosity of gaseous molecules, transformative liquefied gas electrolytes (LGE) based on hydrofluorocarbons (e.g. fluoromethane) were reported to deliver a superior electrochemical performance with Li/CF_x at −40 °C although it offers < 1 mS cm^{-1} ionic conductivity. When paired with co-solvents, the formulated LGE improves the salt solubility and enables an anion-pairing solvation structure while maintaining a rapid transport at reduced temperature. These unique features of LGE strongly indicate a promising candidate for Low-T Li/CF_x batteries.

Herein, we formulated a new LGE based on dimethyl ether (Me_2O) and PC, maintaining an ionic conductivity > 3.5 mS cm^{-1} from −70 to 60 °C. Due to the weakly solvating power of Me_2O, the formulated electrolyte enables improved rate and low-temperature performance. The Li/CF_x cell utilizing a 4.3 mg cm^{-2} loading CF_x cathode, delivered 780 mAh g^{-1} (91 % room-temperature capacity retention) under 10 mA g^{-1} at −60 °C. Moreover, when 50 mg cm^{-2} CF_x is utilized, the cell still displays 706 mAh g^{-1} (84 % room-temperature capacity retention) at −60 °C and the average discharge voltage can be maintained above 2.1 V. Furthermore, a systematic study combining different advanced characterizations was conducted to figure out the improving mechanism, including both the bulk and interphase aspects.

3.2 Results

3.2.1 Physical properties and electrochemical transport properties

An ideal electrolyte for ultra-low temperature and high-rate Li-CF_x primary batteries should offer the lowest possible melting point (< −100 °C) and low viscosity. Besides, the electrolyte should easily de-solvate from its solvation shell, which brings about reduced charge transfer resistance[44]. The Me_2O shows

31

an ultra-low melting point of −141 ℃ and a viscosity of 0.12 mPa×S at 20 ℃, which outperforms DME

with −58 ℃ and 0.46 mPa×S, acetonitrile (ACN) with −45 ℃ and 0.343 mPa×S, tetrahydrofuran (THF)

with −108 ℃ and 0.456 mPa×S, and the recently reported methyl butyrate (MB) with −95 ℃ and 0.526

mPa×S **(Figure 3.1a)**. Among gaseous solvents, Me_2O endows higher salt solubility than fluoromethane

(FM) and difluoromethane (DFM) owing to the higher Lewis basicity of the C-O-C than C-F[45], further

enhancing electrolyte's ionic conductivity. In addition, Me_2O has been proved to offer excellent lithium

metal compatibility at a wide temperature range. Considering the above features, Me_2O is introduced to

replace DME in the conventional $LiBF_4$-DME-PC formulations. We first optimized the ratio between

Me_2O and PC to maximize transport properties and discharge performance. As shown in **Figure 3.6**, when

the volume ratio reaches 6.5:1, the optimized electrolyte delivered the highest ionic conductivity of 3.54

mS cm^{-1} at −70 ℃ and the highest room-temperature discharge capacity and nominal voltage. Furthermore,

different lithium salts in 6.5:1 volume ratio of Me_2O:PC electrolytes have been evaluated, and we found

$LiBF_4$ exhibited optimal CF_x capacity utilization and discharge overpotential over lithium

bis(fluorosulfonyl)imide (LiFSI) and lithium bis(trifluoromethanesulfonyl)imide (LiTFSI) salts at room

temperature **(Figure 3.7)**, which is in alignment with previously reported results that $LiBF_4$ could reduce

the activation energy for the charge transfer process. Thus, the 1 M $LiBF_4$ in Me_2O: PC at a 6.5:1 volume

ratio was formulated as the optimized electrolyte, hereby denoted as 1 M $LiBF_4$-Me_2O-PC. 1 M $LiBF_4$ in

DME: PC with 6.5:1 volume ratio (denoted as 1 M $LiBF_4$-DME-PC), 1 M $LiBF_4$ in DME (denoted as 1

M $LiBF_4$-DME) and 1 M $LiBF_4$ in Me_2O (denoted as 1 M $LiBF_4$-Me_2O) are chosen as control systems for

the mechanism study.

The ionic conductivities were measured to investigate the transport properties, as shown in **Figure

3.1b**. Owing to the superior physical properties of Me_2O, the 1 M $LiBF_4$-Me_2O-PC and 1 M $LiBF_4$-Me_2O

demonstrate stable ionic conductivity from −70 to +60 °C. Among them, 1 M $LiBF_4$-Me_2O-PC invariably

displayed > 3.5 mS cm^{-1}, higher than the electrolyte without PC. In contrast, although the conventional 1 M LiBF$_4$-DME-PC exhibits an ionic conductivity of > 4 mS cm^{-1} before −10 °C, a large drop is observed (< 1 mS cm^{-1}) below −20 °C, which is due to the salt precipitation from the electrolyte (**Figure 3.8**). Similarly, severe ionic conductivity drops were observed for the other liquid 1 M LiBF$_4$-PC and 1 M LiBF$_4$-DME systems at reduced temperatures, mainly caused by the salt precipitation or the freezing of the electrolytes.

a

Solvent	Melting Point (°C)	Boiling Point(°C)	Critical Point(°C)	Viscosity (mPa·s)
Dimethyl Ether	−141	−24	127	0.12
Propylene Carbonate	−48.8	242	377	2.5
Tetrahydrofuran	−108	66	268	0.456
Acetonitrile	−45	82	272	0.343
1,2- Dimethoxyethane	−58	85	263	0.46
γ-Butyrolactone	−43.5	204	436	1.7
Methyl butyrate	−95	102	281	0.526
Fluoromethane	−142	−78	44	0.085
Diflüromethane	−136	-52	78	0.12

b
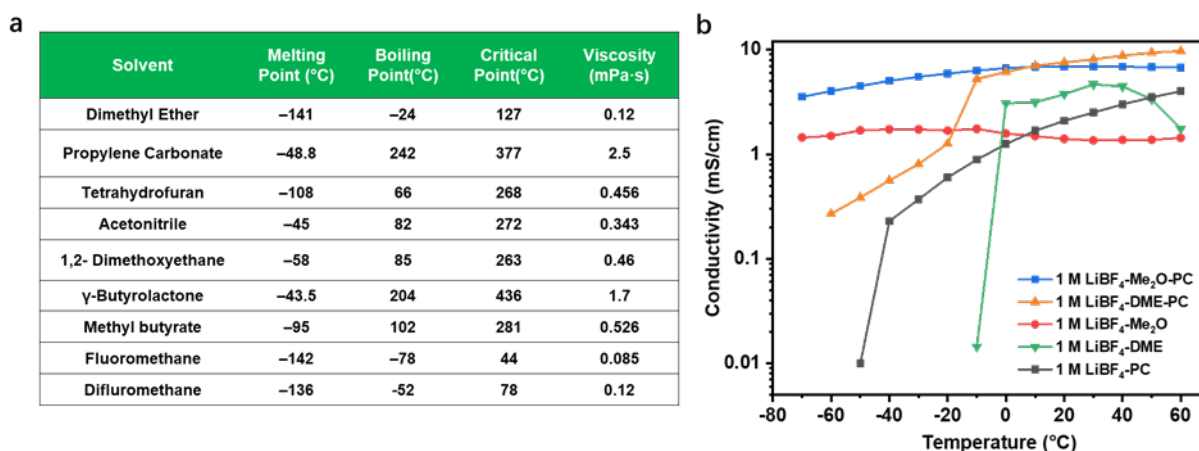
Figure 3.1 Design of the Low-T Electrolytes (a) Summary of physical properties of different solvents, data extracted from published works[6, 46] (b) Measured ionic conductivity of the investigated electrolytes at different temperatures.

3.2.2 Solvation structure

The solvation structure of the electrolyte influences the Li$^+$ de-solvation process, as commonly depicted by Molecular dynamics (MD) simulation and Raman spectroscopy. Here, both techniques were applied to understand the effect of solvent selection on anion-pairing. 1 M LiBF$_4$-Me$_2$O-PC, 1 M LiBF$_4$-DME-PC, 1 M LiBF$_4$-PC, and 1 M LiBF$_4$-Me$_2$O were directly compared with the individual solvents and salt. Based on the Raman spectra in **Figure 3.2a**, the solvated BF$_4^-$ (B-F stretching) in the 1 M LiBF$_4$-Me$_2$O-PC exhibits a blue shift compared with the DME-PC counterpart, indicating more anions participate

in the solvation shell.   As for the C-O-C stretching of Me_2O (**Figure 3.2b**), there is no obvious peak shift or peak broadening observed for C-O-C stretching of Me_2O after dissolving 1 M $LiBF_4$ salt, indicating the low ratio of solvated Me_2O. As a comparison, the DME solvent exhibited an obvious blue shift of C-O-C stretching when 1 M $LiBF_4$ salt was added (**Figure 3.9**). This indicated higher solvated DME represented in the 1 M $LiBF_4$-DME-PC. In addition, the DFT calculations suggest weaker binding between the Me_2O molecule and Li^+ of -1.76 eV than the DME molecule and Li^+ of -2.84 eV, which is consistent with the Raman observation (**Figure 3.2b**). As shown in **Figure 3.2c**, the stretching mode of the C=O from PC also varies in different electrolytes, both 1 M $LiBF_4$-DME-PC and 1 M $LiBF_4$-Me_2O-PC showed an obvious blue shift compared with pure PC, where the latter spectrum show slightly larger shifting, demonstrating the increased coordination between PC and Li^+ inside 1 M $LiBF_4$-Me_2O-PC. Similar observations can also be found that more solvated PC appear in the 1 M $LiBF_4$-Me_2O-PC at the PC ring bending position (**Figure 3.9**). Based on the above observations, the anion-pairing solvation structure of 1 M $LiBF_4$-Me_2O-PC is demonstrated in **Figure 3.2d,** which differs from the solvent coordinated solvation structure of 1 M $LiBF_4$-DME-PC.

MD simulations confirmed the observations from Raman spectroscopy. The simulation boxes contain 1 M $LiBF_4$-DME-PC (**Figure 3.2e**) and 1 M $LiBF_4$-Me_2O-PC (**Figure 3.2h**). After equilibration, the radial distribution functions (RDFs) for Li^+ in 1 M $LiBF_4$-DME-PC and 1 M $LiBF_4$-Me_2O-PC were computed at both 20 °C and 0 °C, and the related results are shown in **Figure 3.2f** and **3.2i**. In terms of probability at 20 °C, it was found that DME predominates the solvation shell, whereas BF_4^- anion and PC accounted for lower but comparable percentages (**Figure 3.2f-g**), resulting in an average Li coordination environment consisting of 2.3 DME (two oxygen atoms per DME), 0.39 PC, and 0.38 BF_4^-. On the other hand, the most probable coordinating species in 1 M $LiBF_4$-Me_2O-PC is BF_4^-, followed by PC and Me_2O (**Figure 3.2i-j**), resulting in an average Li coordination environment consisting of 0.81 Me_2O, 1.1 PC and

2.4 BF_4^-. It is noteworthy in both cases that although the probability of PC coordination is high, its sparing volumetric composition yields relatively low coordination numbers. In terms of the Me_2O, although the coordination number of Me_2O is around 0.81, the relative ratio between solvated and un-solvated Me_2O is extremely low due to the high volumetric ratio of total Me_2O amount. At 0 °C, it was observed that the solvation structure of the 1 M $LiBF_4$-DME-PC electrolyte shifts slightly away from DME (2.3 to 2.0) and towards PC (0.39 to 0.52), whereas the 1 M $LiBF_4$-Me_2O-PC shows negligible shift for all molecules (**Figure 3.2i-g**), still maintaining anion-pair solvation structure. Importantly, such anion-pairing solvation structure demonstrated improved Li^+ diffusivity of the 1 M $LiBF_4$-Me_2O-PC at 20 and 0 °C compared with that of the 1 M $LiBF_4$-DME-PC ((**Figure 3.10**). Integrated with the increased transport properties, the anion-paired solvation structure has also been proved to significantly benefit the Li^+ de-solvation portion of charge transfer, resulting in facile kinetics and an improved low-temperature performance.
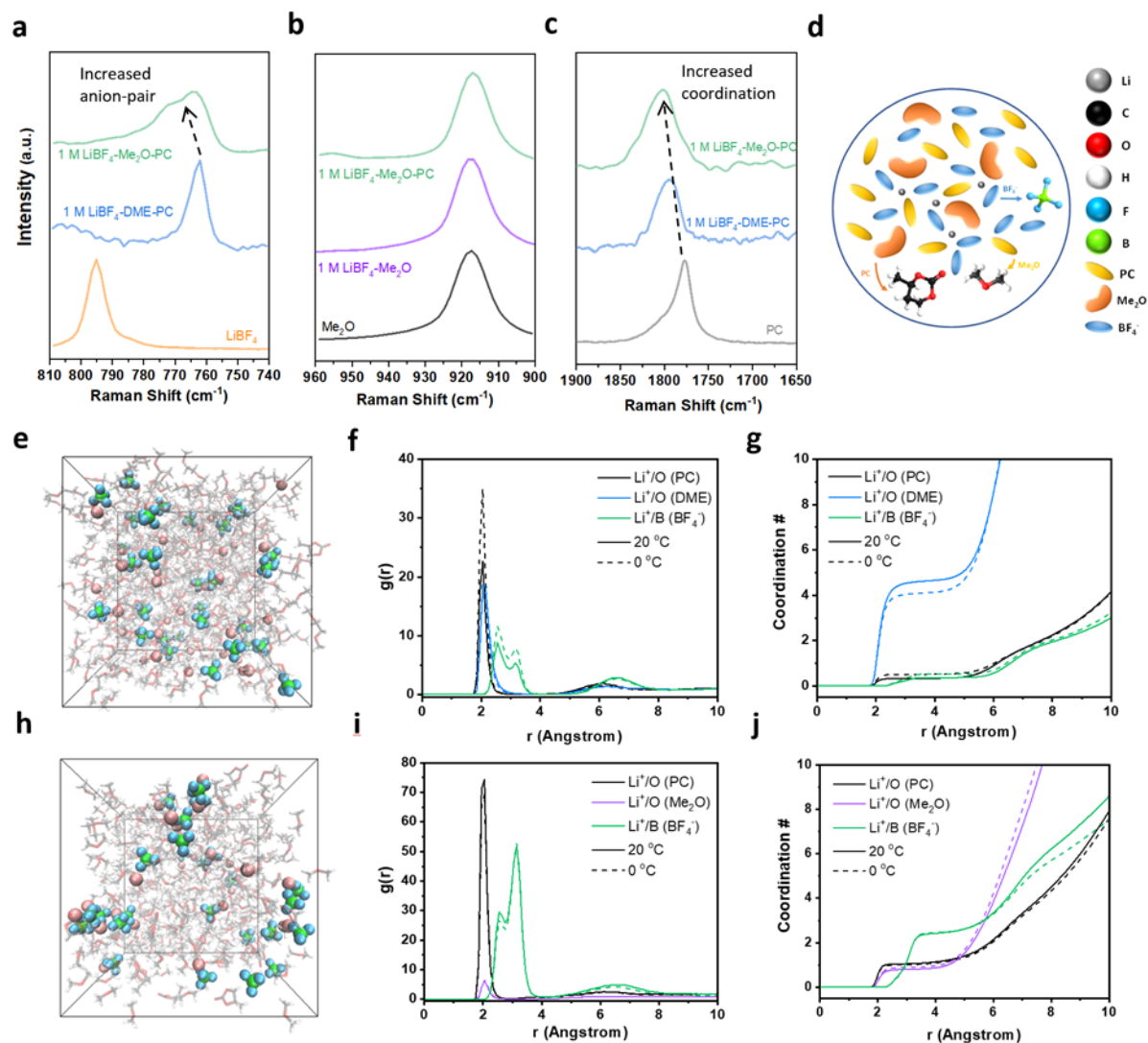
Figure 3.2 Raman spectra and simulated results of formulated and reference electrolytes. Raman spectra for (a) LiBF$_4$ salt (b) Me$_2$O solvent and (c) PC solvent in different electrolytes. (d) Proposed solvation structure of formulated electrolyte. (e-j) MD simulation results containing 1 M LiBF$_4$-DME-PC and 1 M LiBF$_4$-Me$_2$O-PC.

3.2.3 Electrochemical performance of Li/CFx batteries

Four operating temperatures (−70, −60, +23, +55 °C) were performed to evaluate the temperature-dependent discharge performance of Li/CF$_x$ cells in the formulated electrolytes. The discharge profiles of the cells with the 1 M LiBF$_4$-Me$_2$O-PC and 1 M LiBF$_4$-DME-PC electrolytes are shown in **Figure 3.3a** and **Figure 3.3b**, respectively. Under the current density of 10 mA g^{-1}, the two electrolytes delivered

similar performances at 23 °C where 1 M LiBF$_4$-DME-PC shows slightly higher discharge capacity and voltage platform at 55 °C. However, the 1 M LiBF$_4$-Me$_2$O-PC electrolyte produced substantially improved performance than 1 M LiBF$_4$-DME-PC, providing 780 mAh g^{-1} and 603 mAh g^{-1} at −60 and −70 °C, respectively, with higher discharge voltage plateaus. In comparison, the 1 M LiBF$_4$-DME-PC electrolyte demonstrates reduced discharge capacities of 431 mAh g^{-1} at −60 °C and 267 mAh g^{-1} at −70 °C, respectively. This difference can be attributed to the higher ionic conductivities of the 1 M LiBF$_4$-Me$_2$O-PC electrolyte with higher Li$^+$ diffusivity and a facile de-solvation process enabled by anion-pair solvation structure, which further gives rise to the utilization of CF$_x$ at such low temperatures, as confirmed by the more prominent LiF peaks from X-ray diffraction of the discharged CF$_x$ (**Figure 3.11**). Interestingly, the cell employing 1 M LiBF$_4$-Me$_2$O delivered 708 mAh g^{-1} capacity at −60 °C (**Figure 3.12**), which was lower than the cell using the 1 M LiBF$_4$-Me$_2$O-PC, but still outperformed both cells discharged in the 1 M LiBF$_4$-DME and 1M LiBF$_4$-DME-PC, indicating Me$_2$O is more crucial than PC for the low-T performance.

To further evaluate the rate performance, Li/CF$_x$ cells were discharged at increased current densities of 1000 and 5000 mA g^{-1} at room temperature. As shown in **Figure 3.3c**, the two electrolytes deliver similar capacities at a current density of 1000 mA g^{-1}. However, under 5000 mA g^{-1}, the 1 M LiBF$_4$-Me$_2$O-PC demonstrates a higher discharge capacity of 645 mAh g^{-1} when compared to 603 mAh g^{-1} in the 1 M LiBF$_4$-DME-PC. The electrolyte performance at reduced temperatures was also evaluated under increased current densities, as shown in **Figure 3.3d** for −60 °C and **Figure 3.13** for −70 °C. At −60 °C, the 1 M LiBF$_4$-Me$_2$O-PC retained 63.6% of the CF$_x$ theoretical capacity at a high current density of 300 mA g^{-1} while the 1 M LiBF$_4$-DME-PC failed to discharge at 100 mA g^{-1}. At −70 °C, the 1 M LiBF$_4$-Me$_2$O-PC electrolyte again demonstrates improved performance against the reference electrolyte which failed to discharge at 100 mA g^{-1}. When using 50 mg cm^{-2} CF$_x$ with 409 μm thickness (**Figure 3.14**), the 1 M LiBF$_4$-

Me$_2$O-PC can discharge at 100 mA g^{-1} with a higher voltage drop (down to 1.57 V) at room temperature (**Figure 3.3e**). When the cells are exposed to −60 °C, the 1 M LiBF$_4$-Me$_2$O-PC maintains 35.3 mAh cm^{-2} capacity (706 mAh g^{-1}) at such extreme conditions (**Figure 3.3e**). By contrast, the 1 M LiBF$_4$-DME-PC delivered 855 mAh g^{-1} capacity at room temperature but almost no capacity at −60 °C even with predischarge step (**Figure 3.15**). Even under 100 mA g^{-1} current density at −60 °C, the cell using 1 M LiBF$_4$-Me$_2$O-PC still deliver 203 mAh g^{-1} capacity with predischarge condition (**Figure 3.16**). In conclusion, the 1 M LiBF$_4$-Me$_2$O-PC enabled Li/CF$_x$ cells with high energy density at ultra-low temperatures when compared with other reported electrolytes, further reinforcing its promise to enable next-generation primary batteries in extreme environments (**Figure 3.3f**).
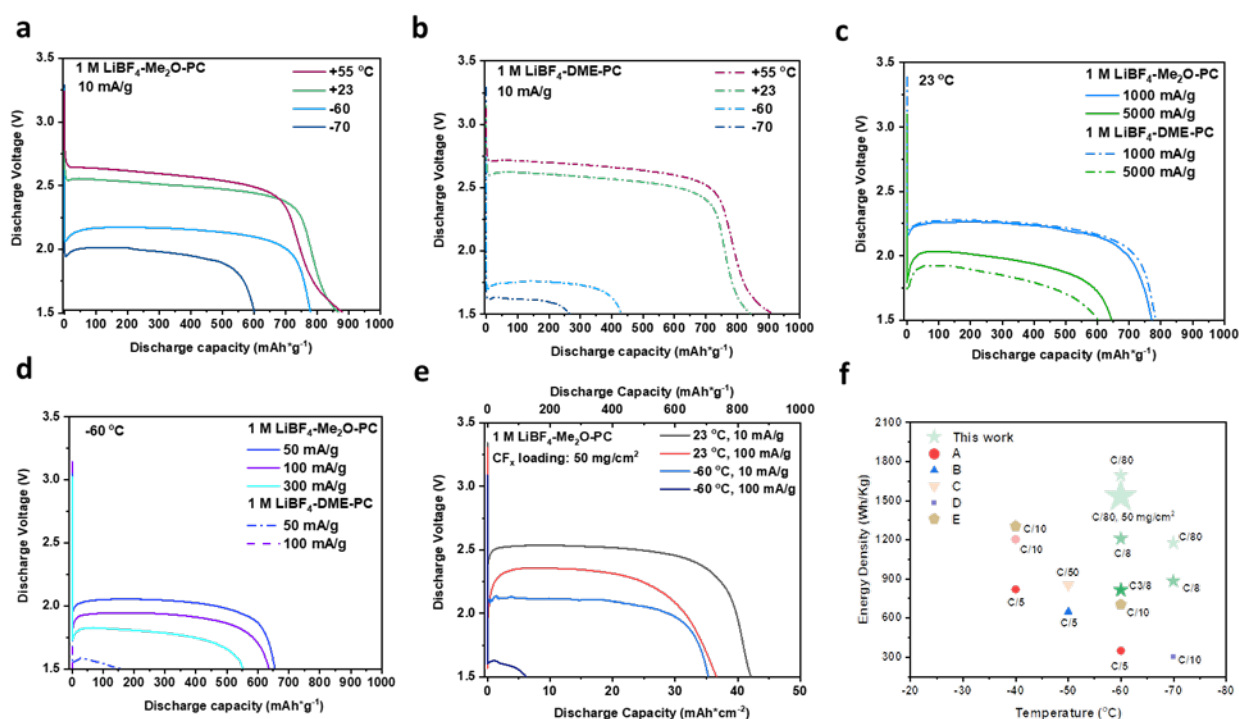
Figure 3.3 Electrochemical performance of CFx (a-b) Measured electrochemical performance at a wide-temperature range of 1 M LiBF4-Me2O-PC and 1 M LiBF4-DME-PC. (c) Different current density discharge at room temperature. (d-e) Discharge profiles under different current densities, temperatures. (f) Summary of energy density at different temperatures.

3.2.4 Interfacial Analysis

To comprehend the outstanding performance delivered by 1 M $LiBF_4$-Me_2O-PC, we performed electrochemical impedance spectroscopy (EIS) to monitor the overall impedance during the different depths of discharge in both electrolytes. As shown in **Figure 3.17** and **Figure 3.18**, the EIS spectra are fitted following graphite/electrolyte interface model. The bulk resistance (R_b) of solvated Li^+ in 1 M $LiBF_4$-Me_2O-PC remains stable over different depth of discharge states and is consistently lower than the 1 M $LiBF_4$-DME-PC (**Figure 3.18**), which aligns with the ionic conductivity results in **Figure 3.1**. In terms of the charge transfer impedance (R_{ct}) which represents the breakup of the solvation shell of Li^+, 1 M $LiBF_4$-Me_2O-PC has a R_{ct} 2-4 times lower than that of 1 M $LiBF_4$-DME-PC before reaching the 20-hour discharge, where the turning points occur between the 10-hour and 20-hour discharge state. After the 20-hour discharge, the charge transfer resistance is significantly reduced in the 1 M $LiBF_4$-DME-PC but still higher than its counterpart. During the entire discharge, 1 M $LiBF_4$-Me_2O-PC possessed lower interfacial impedance (R_{int}), which indicates lower Li^+ diffusion barriers through the SEI/CEI. It is well-known that the interface plays an important role in the charge transfer kinetics, which is correlated to the de-solvation process of the electrolytes near the interface, the diffusion through CEI, and the chemistry and structure of CEI. Considering the complexity in de-convoluting each step, X-ray photoelectron spectroscopy (XPS) was performed on the 10-hour discharged CF_x at −60 °C to investigate if the chemical composition of CEI determines the charge transfer impedance difference, and the data are shown in **Figure 3.4a-f**. Given that both samples were stopped at the same discharge capacity, the formed LiF and carbon should be the same in quantity. Based on the global survey of discharged CF_x, similar F, B, and O atomic concentrations can be observed over different etching times (**Figure 3.4b, c**). This indicates the similarity of interfacial chemistry in both electrolytes. We further examined the fine spectra of different elements. The C 1s from the pristine CF_x electrode shows the characteristic structure of CF_x materials, mainly containing C-C, C-

F, and C-F$_2$ bonds (**Figure 3.4d**). After discharge, C-F/C-F$_2$ peaks decreased drastically, indicating the electrochemical reaction. Apart from that, CEI information can be depicted by O1s signal because the ether electrolytes are the source of extra oxygen. After 10-hour discharge, a new C=O appeared in both C 1s and O 1s spectra with a relatively weak intensity over different etching conditions, implying a thin CEI formed in both electrolytes. Interestingly, there is no obvious difference from both electrolytes in all XPS spectra, in addition to the more predominated C and F 1s signal (**Figure 3.4e, f**). When fully discharged to 1.5V, higher Li-F, less carbonyl group, and C-C signal can be observed in CF$_x$ discharged in 1 M LiBF$_4$-Me$_2$O-PC due to higher CF$_x$ utilization (**Figure 3.19**). Based on the above analysis, we can conclude the CEI chemistry exerts nonobvious influence on low-T performance.
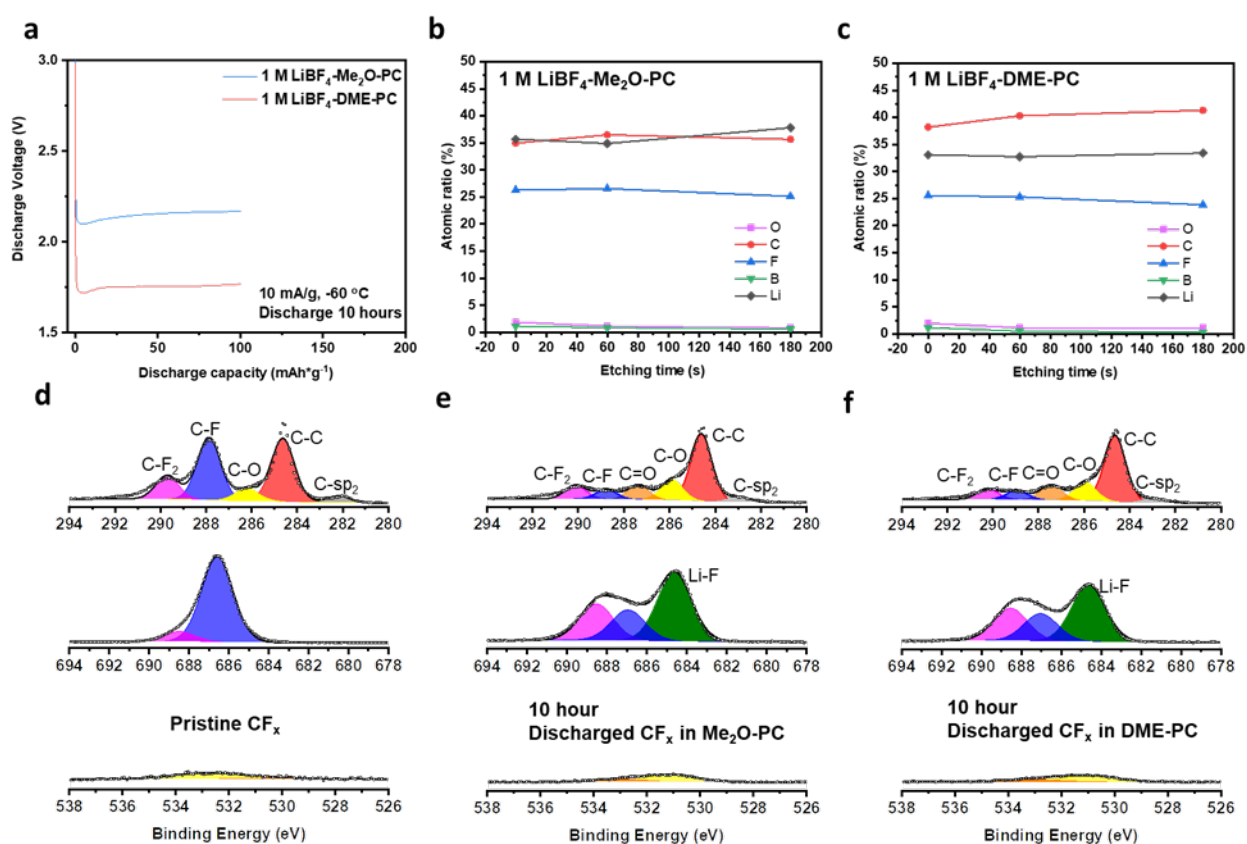
Figure 3.4 Global and local XPS analysis of the CF$_x$ at different states. (a) Voltage profiles of 10-hour discharged CF$_x$ in both electrolytes. (b-c) Summary of atomic concentration of CF$_x$ discharged in 1 M LiBF$_4$-Me2O-PC and 1 M LiBF$_4$-DME-PC (c). (d-f) Local survey of pristine CF$_x$,10-hour discharged CFx in 1 M LiBF4-Me$_2$O-PC and 10-hour discharged CF$_x$ in 1 M LiBF$_4$-DME-PC.

To understand the local CF_x structure change during low-T discharge, scanning transmission electron microscopy-electron energy loss spectroscopy (STEM-EELS), high resolution transmission electron microscopy (HRTEM), and selected areal electron diffraction (SAED) were performed on CF_x samples discharged at −60 °C in different electrolytes under 10 mA g^{-1} (**Figure 3.5a-e, Figure 3.20-21**). Based on the STEM images and elemental mappings of discharged CF_x, a greater prevalence of Li was observed in 10-hour discharged CF_x in the 1 M LiBF$_4$-Me$_2$O-PC compared to the 1 M LiBF$_4$-DME-PC at selected areas (**Figure 3.5a-b**). Both samples demonstrate the C and F elements with the new appearance of Li elements, where the Li distribution is more homogeneous in the discharged CF_x in 1 M LiBF$_4$-Me$_2$O-PC. Coupled with EELS spectra (**Figure 3.5c-e**), both samples show Li-F feature as standard LiF sample, indicating the breaking of C-F bond and the formation of Li-F and graphitic carbon after 10-hour discharge. The inhomogeneity of LiF formation and scattered distribution of unreacted CF_x from the CF_x discharged in 1 M LiBF$_4$-DME-PC confirmed the sluggish transport / de-solvation properties of the 1 M LiBF$_4$-DME-PC electrolyte, which, in contrast, highlighted the superior performance enabled by the 1 M LiBF$_4$-Me$_2$O-PC with the homogeneous distribution of the discharged products. The fully discharged CF_x were also evaluated, and the results were consistent with the observations from the 10-hour discharged samples (**Figure 3.20-21**). Considering the significantly reduced interfacial resistance obtained from the 1 M LiBF$_4$-Me$_2$O-PC electrolyte (**Figure 3.17**) for Li/CF_x cell, the LGE should benefit the Li metal side as reported before, where Me$_2$O-based LGE demonstrates improved SEI structure compared with DME-based liquid electrolyte for lithium metal cycling at both room temperature and reduced temperature. Integrated with the above analysis, we can conclude that the structure of discharge products (LiF and graphitic carbon) appears similarly in both electrolytes and also places unimportant influences on low-T performance. Instead, bulk ionic transport and Li$^+$ de-solvation are more critical factors affecting the utilization of CF_x and the distributions of discharge products.
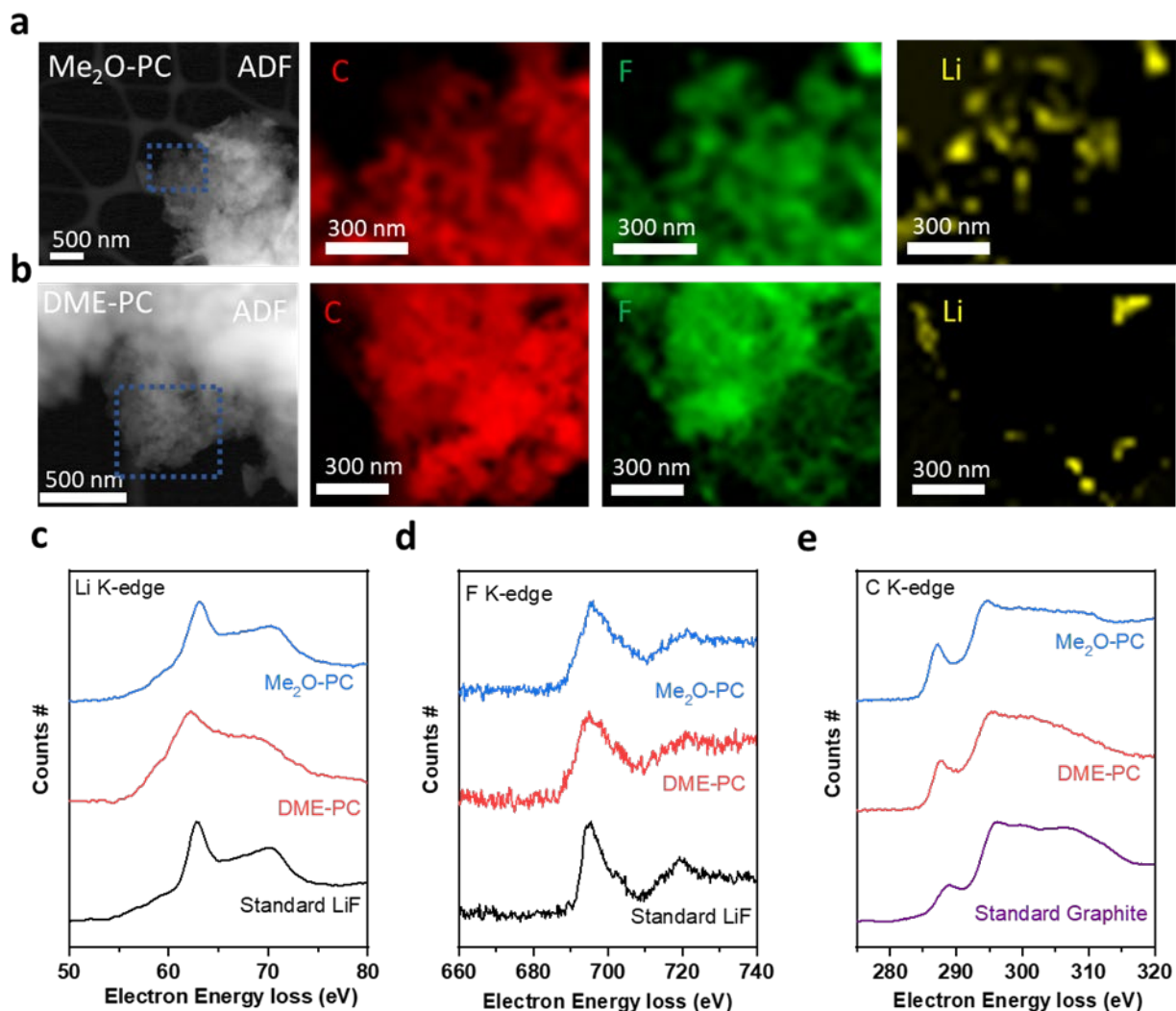
Figure 3.5 STEM-EELS, HRTEM and SAED of the 10-hour discharged CFx at −60 °C. (a) STEM image and EELS mappings of discharged CFx in (a) 1 M LiBF$_4$-Me$_2$O-PC and (b) 1 M LiBF4-DME-PC. EELS spectra of (c) Li K-edge, (d) F K-edge, and (e) C K-edge.

3.3 Experimental Methods

3.4.1 Materials

Dimethyl ether (99%) was obtained from Sigma-Aldrich. The salts lithium bis(fluorosulfonyl)imide (99.9%) and lithium bis(trifluoromethane)sulfonimide (99.9%) were purchased from BASF and lithium tetrafluoroborate was purchased from Sigma-Aldrich. 1,2-dimethoxyethane (99.5%) and propylene

carbonate were purchased from Sigma-Aldrich and stored over molecular sieves more than two days before formulating the electrolytes. The CF_x powders were purchased from ACS material (GT1FS012). The CF_x electrodes were made with an 8:1:1 ratio between active materials: PVDF:C65 and casted on Al foils. All casted electrodes were dried at 80 ^oC overnight before use. The CF_x electrode loading is approximately 4.3 mg cm^{-2}.

Fabrication of 50 mg cm^{-2} CF_x cathodes was accomplished by forming and rolling a dough. First carbon black (Super-P) was mixed with a commercial carbon fluoride (Advanced Research Chemicals, ARC-5-R-175) in a 5:95 wt% ratio by using a mortar and pestle. Once thoroughly mixed, 5.6 wt% Teflon (60 wt% suspension in H_2O, Sigma-Aldrich) was added dropwise to the powder and mixing via mortar and pestle continued. With addition of binder the powder began to agglomerate, although not all powder adhered into one mass. To ensure a proper dough another 6.5 wt% of Teflon (wt% including previous Teflon addition) was mixed in with mortar and pestle. A small amount of isopropyl alcohol was used to wet the mixture and facilitate spread of Teflon among the carbon and CFx powders. Approximately 10 min of hand mixing after the second Teflon addition a dough formed that was free standing and did not shed powder. The dough was then rolled on a glass slab with a glass rolling pin to a thickness of ~0.5 mm and then dried at 80°C for 12 hr.

3.4.2 Electrochemical measurements

Ionic conductivity of different electrolytes was performed in custom fabricated pressurized stainless-steel cells with polished stainless-steel (SS 316L) as both electrodes. OAKTON standard conductivity solutions (0.447 to 80 mS cm^{-1}) were utilized to frequently calibrate the cell constant for the cells.

Electrochemical impedance spectroscopy was collected by a Biologic SAS (SP-200) system and the spectra were then fitted using ZView 4 software.

Battery discharging tests were performed using an Arbin battery test station (BT2043) from Arbin Instruments in custom designed pressurized stainless-steel cells. Li metal (FMC Lithium, 1 mm thickness, 3/8-inch diameter), separators and CF_x electrodes were sandwiched, where Li metal serves as counter electrode and the CF_x serves as working electrode. A three-layer 25μm porous PP/PE/PP membrane (Celgard 2325) was used for all the electrochemical tests. The electrolyte amount is flooded (> 50 g Ah^{-1}) for all electrolytes mentioned in this work.

For Li/CF_x discharge tests in different temperatures, the cells were soaked at the testing temperature in a temperature chamber (Espec) for at least 2 hours before discharge. All room temperature discharge tests are performed without controlling the temperature. The pre-discharge of Li/CF_x with 50 mg cm^{-2} cathodes is performed at room temperature for 2-hour discharge using 10 mA g^{-1}.

3.4.3 Material characterization

The X-Ray Diffraction (XRD) measurements were done by a Bruker APEX II Ultra diffractometer with Mo Kα ($\lambda = 0.71073$ Å) radiations to check the crystal structures. The samples were prepared by scratching the cathode electrode and filling the capillary tubes inside an Ar-filled glovebox. All the cathode samples were not washed before these measurements.

Super-low-dose TEM/EELS techniques were developed for characterizing CF_x structures. The discharged CF_x cathodes were rinsed with DME to remove residual salt and dried at 80 °C under vacuum on a hotplate prior to analysis. The cathode powders were scratched from electrodes and put on a Cu TEM grid for all measurements. HRTEM samples were transferred into the TEM (ThermoFisher Talos 200X TEM operated at 200 kV), which is equipped with a CETA camera and low-dose system. The HRTEM images in panel D&F are acquired with an electron dose rate of ~200 e $Å^{-2}$ s^{-1} for ~1s. The STEM (EELS Mapping) samples were also transferred into the ThermoFisher Talos 200X TEM. The TALOS microscope

is equipped with a high-resolution Gatan imaging filter (Gatan Continuum 1069) for EELS mapping. The probe current utilized for EELS maps on the TALOS was approximately 140 pA.

Raman spectra of liquefied gas electrolytes were carried on Renishaw inVia confocal Raman microscope with an excitation wavelength of 532 nm. All spectra were calibrated with Si (520 nm) and analyzed by Wire 3.4 software developed by Renishaw Ltd. The Raman spectra measurements of Me_2O-based electrolytes were performed in a custom-built pressurized cell[33].

X-Ray photoelectron spectroscopy (XPS) was performed using a Kratos AXIS Supra DLD XPS with monochromatized Al Kα radiation (λ= 0.83 nm and hυ=1486.7 eV) under a base pressure $<10^{-8}$ Pa. To avoid moisture and air exposure, samples were transferred to the XPS chamber directly from a glovebox via air-tight transfer. All spectra were calibrated with hydrocarbon C-H C 1s (284.6 eV) and analyzed by CasaXPS software. To remove residual salt on the surface, all samples were rinsed with DME and dried in glovebox antechamber before analysis. The etching condition was set as an Ar1000+ cluster at 5 keV. The etching times were 60 s and 180 s.

3.4.4 Computational Analysis

Classical, fixed-charge Molecular Dynamics (MD) simulations were performed in LAMMPS using the General Amber forcefield for solvents and Li^+ with the anion described with the potentials of Doherty et al. Liquid simulation boxes were constructed from random, amorphous distributions of the molecules, with compositions corresponding to the volume ratios and salt concentrations described above. In all cases the charges of the Li^+ and FSI^- molecules were scaled to the optical dielectric of the solvents present in the system as employed by Park et al[47], which is 0.72 for DME/PC and 0.76 for Me_2O/PC. Periodic boundary conditions were applied in all directions.

For each system, the step size for all simulations was 1 fs. First, an initial energy minimization at 0 K (energy and force tolerances of 10^{-4}) was performed, after which the system was slowly heated from 0 K

to 298 K at constant volume over 0.01 ns using a Langevin thermostat, with a damping parameter of 100 ps. The system was then subjected to 5 cycles of quench-annealing dynamics in an effort to eliminate the existence of meta-stable solvation states, where the temperature was cycled between 298 K and 894 K at a ramp period 0.025 ns followed by 0.1 ns of dynamics at either temperature extreme with a total of 1.25 ns for all 5 cycles. After annealing, the system was equilibrated in the constant temperature, constant pressure (NpT ensemble) for 1.5 ns. The applied pressure was the 1 atm for DME/PC and 4.83 atm for Me_2O/PC, which was the experimental electrolyte pressure measured with Honeywell FP5000 pressure sensor at room temperature. The stresses in the system were isotropically resolved using the Andersen barostat at a pressure relaxation constant of 1 ps). Finally, we performed 10 ns of constant volume, constant temperature (NVT) production dynamics. Radial distribution functions and solvation snapshots sampled from the MD trajectory were obtained using the Visual Molecular Dynamics (VMD) software.

DFT binding energy calculations were performed using the Q-Chem 5.1 package. First, a geometry optimization step at the B3LYP//6-31+G(d,p) level of theory followed by single point energy calculations at the B3LYP//6-311++G** level of theory. Solvent binding energies were calculated as:

$$\Delta E = E_{Li^+ + solvent} - (E_{Li^+} + E_{Solvent})$$

3.4 Supplementary Information
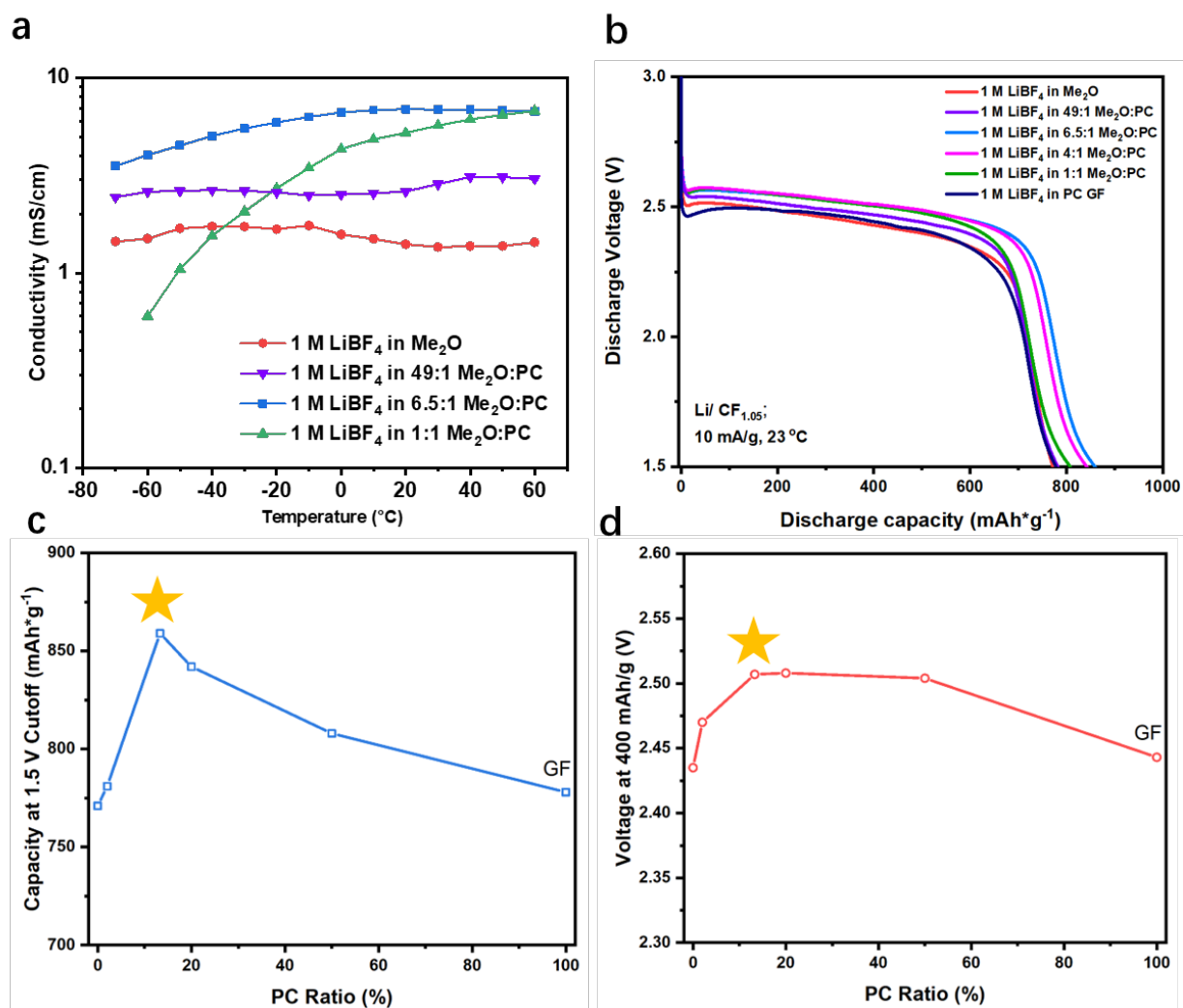
Figure 3.6 Investigation of different Me$_2$O:PC ratio influence on transport and performance (a) Measured conductivities at wide temperature range (b) Electrochemical performance at room temperature (c) Summary of discharge capacity at 1.5 V cutoff vs PC ratio (d) Summary of voltage at 400 mAh g^{-1} specific capacity vs PC ratio
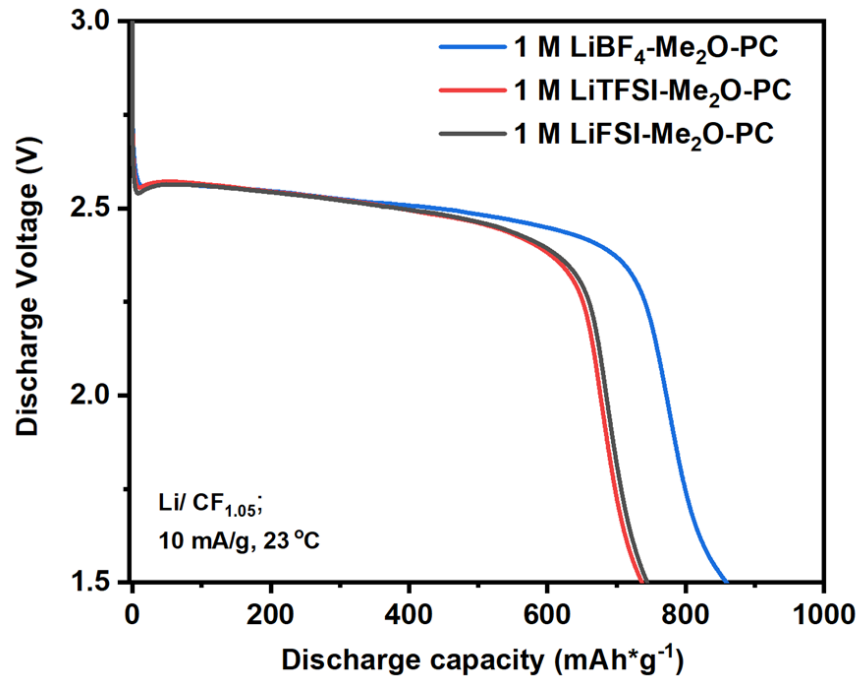
Figure 3.7 Salt influence on electrochemical performance in Me$_2$O-PC solvent mixture with a 6.5:1 volume ratio
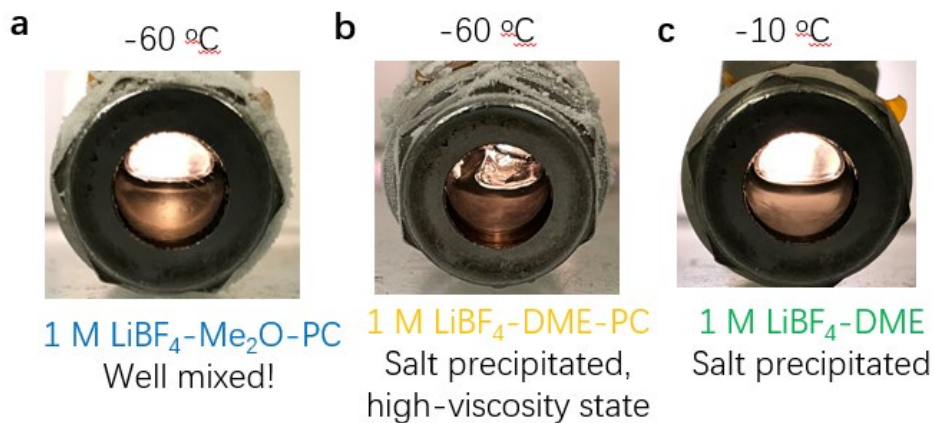
Figure 3.8 Investigation of salt solubility for studied electrolytes at low temperature (a) 1 M LiBF$_4$-Me$_2$O-PC (b) 1 M LiBF$_4$-DME-PC (c) 1 M LiBF$_4$-DME
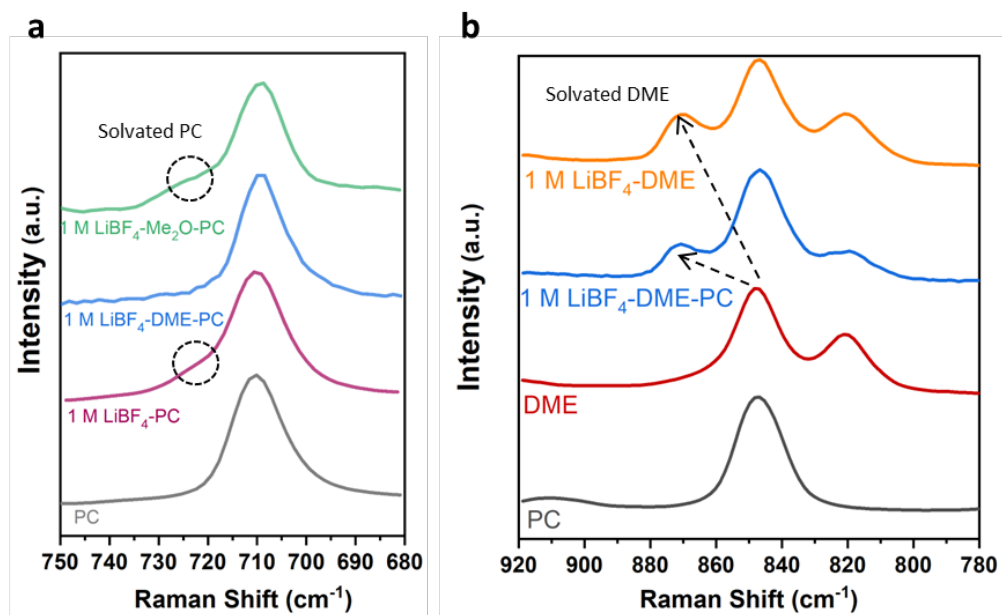
Figure 3.9 Raman spectra of (a) bending mode of the PC ring and (b) C-O-C stretching of DME
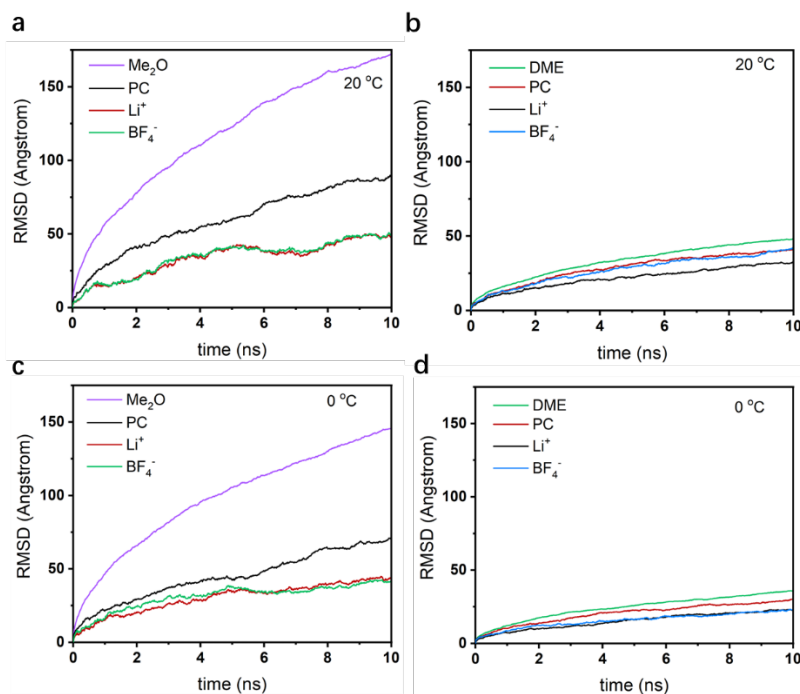
Figure 3.10 Root mean-square displacement of different compounds inside electrolytes of (a,c) 1 M LiBF$_4$-Me$_2$O-PC, (b,d) 1 M LiBF$_4$-DME-PC at 20 and 0 °C, respectively
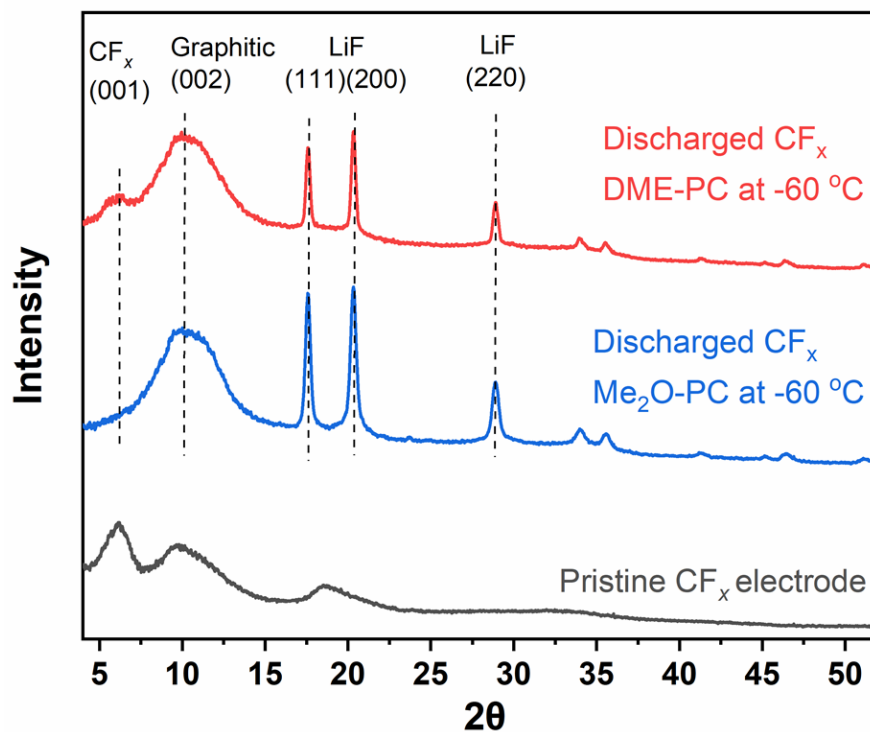
Figure 3.11 Summary of X-ray diffraction of discharged CF_x in different electrolytes and pristine CF_x
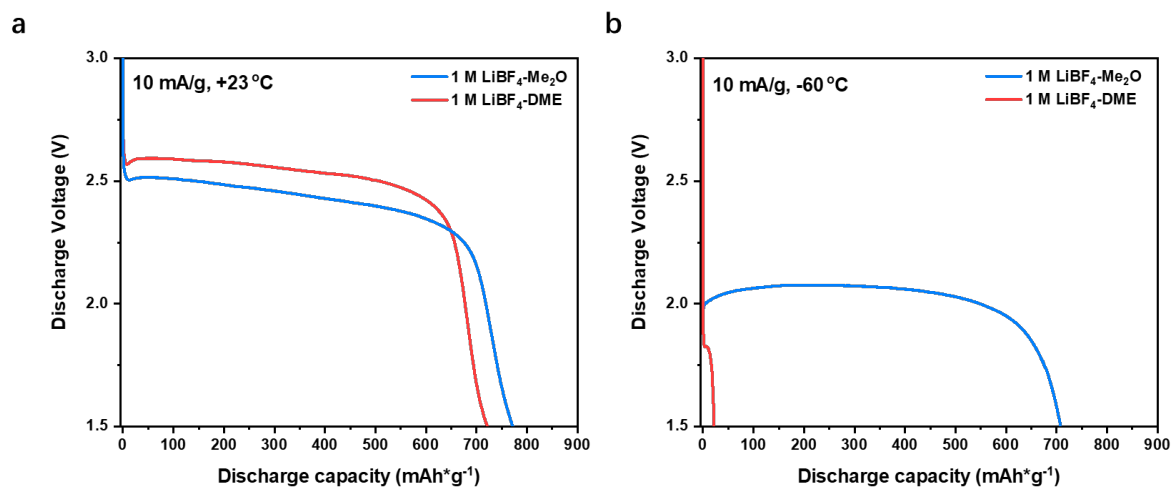
Figure 3.12 Electrochemical performance comparison without PC influence (a) room temperature (b) −60 °C
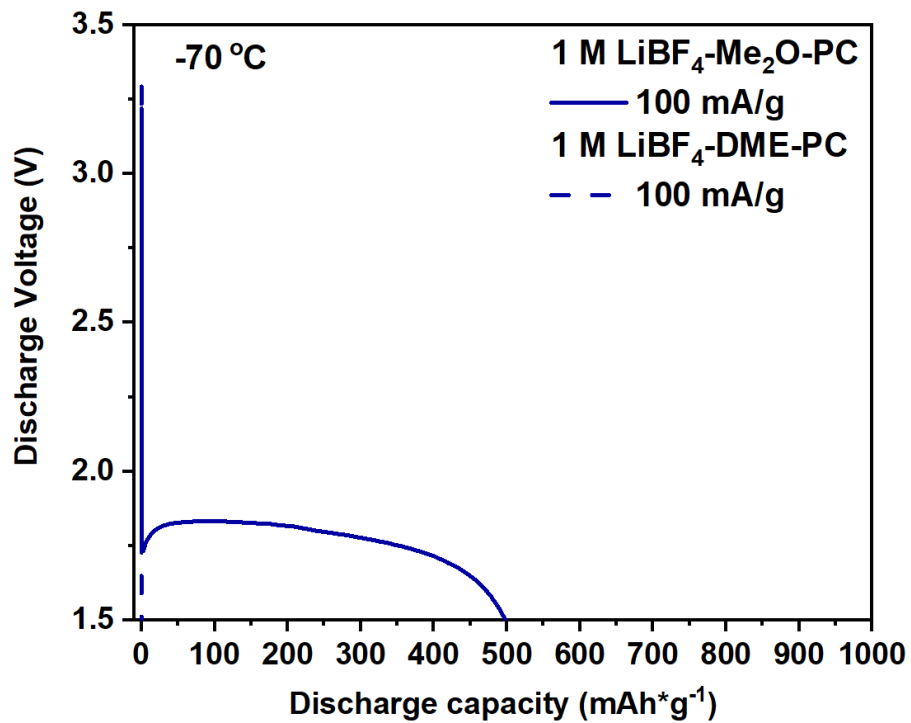
Figure 3.13 Electrochemical performance comparison of Li/CF$_x$ discharge at -70 °C under 100 mA g^{-1}
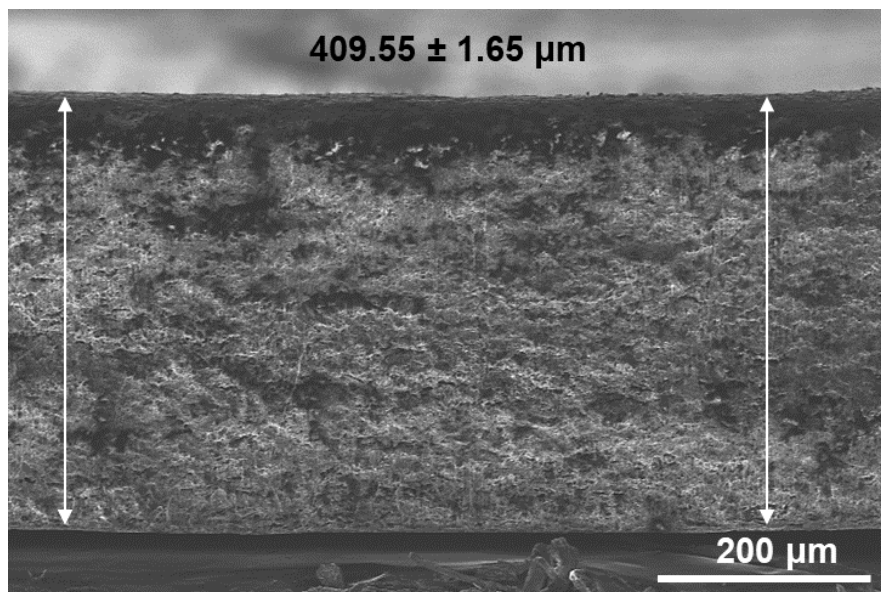
Figure 3.14 Cross-sectional scanning electron microscopy image of pristine CF$_x$ with 50 mg cm^{-2} loading
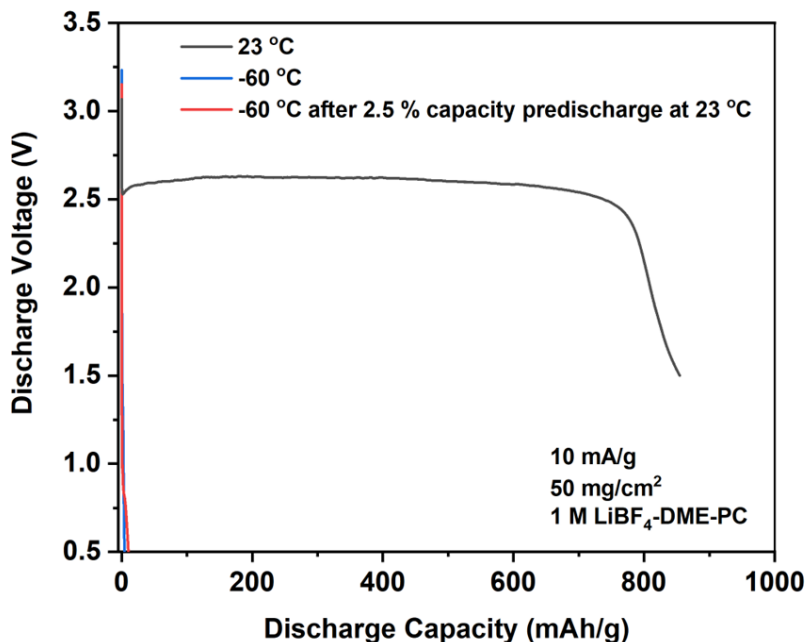
Figure 3.15 Electrochemical performance comparison of 50 mg cm^{-2} Li/ CF$_x$ discharge in the 1 M LiBF$_4$-DME-PC
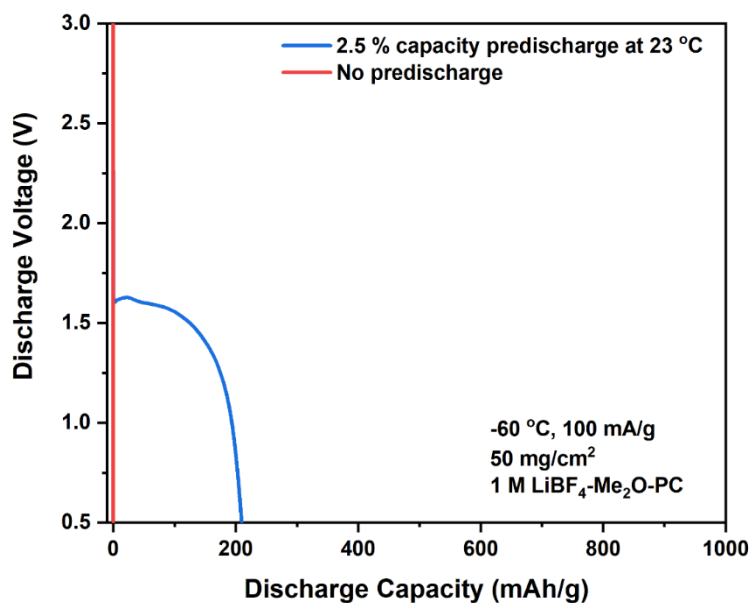
Figure 3.16 Electrochemical performance of Li/CF$_x$ discharge at −60 °C under 100 mA g^{-1} in the 1 M LiBF$_4$-Me$_2$O-PC using 50 mg cm^{-2} CF$_x$. The blue data extends the Figure 3e to 0.5 V cutoff voltage.
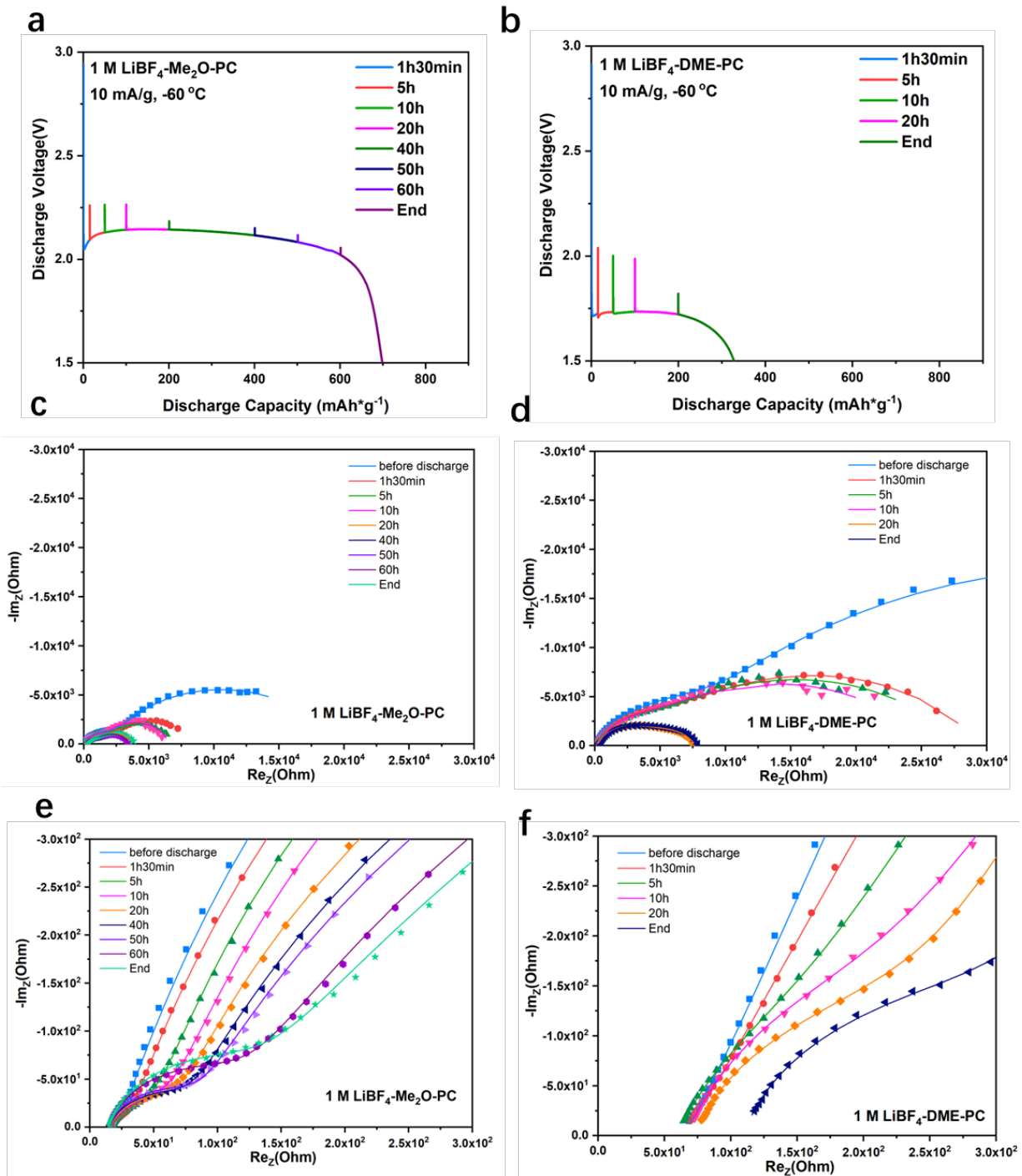
Figure 3.17 Discharge voltage profiles of (a) 1 M LiBF$_4$-Me$_2$O-PC and (b)1 M LiBF$_4$-DME-PC under EIS monitoring over discharge. EIS spectra at different depth of discharge of (c,e) 1 M LiBF$_4$-Me$_2$O-PC and (d,f) 1 M LiBF$_4$-DME-PC at −60 ºC. Figure (e) and (f) are zoomed in areas from (c) and (d) respectively. The fitting curves are in solid lines, and the raw data is shown in points
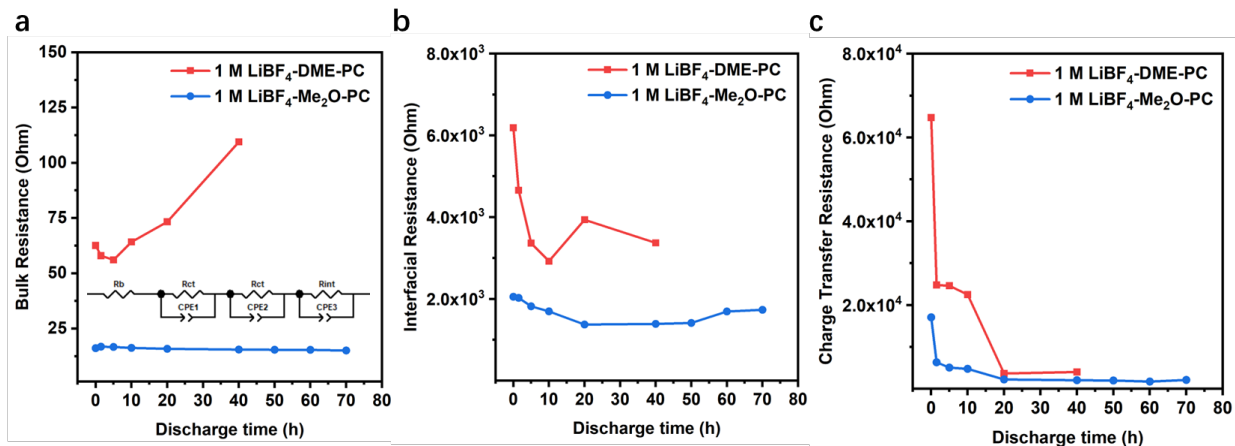
Figure 3.18 Summary of (a) bulk resistance, (b) interfacial resistance and (c) charge transfer resistance. The inset of (a) shows the fitting model
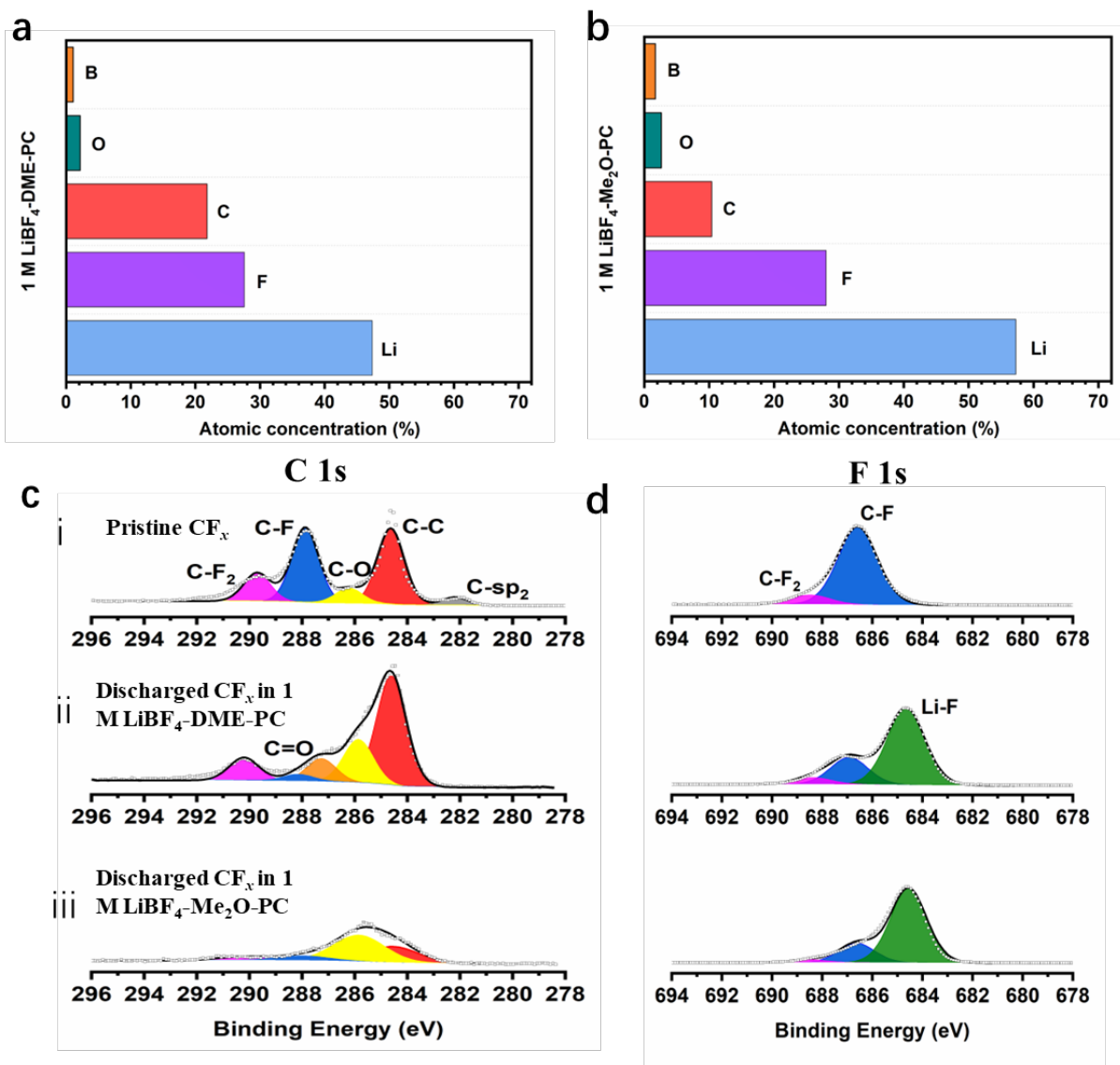
Figure 3.19 Global and local XPS analysis of the CF_x at pristine and fully discharged at −60 °C using 10 mA g^{-1}. (a-b) Summary of atomic concentration of CF_x fully discharged in 1 M LiBF$_4$-Me$_2$O-PC and 1 M LiBF$_4$-DME-PC. (c) Local survey of pristine CF_x and fully discharged CF_x in the 1 M LiBF$_4$-Me$_2$O-PC and the 1 M LiBF$_4$-DME-PC.
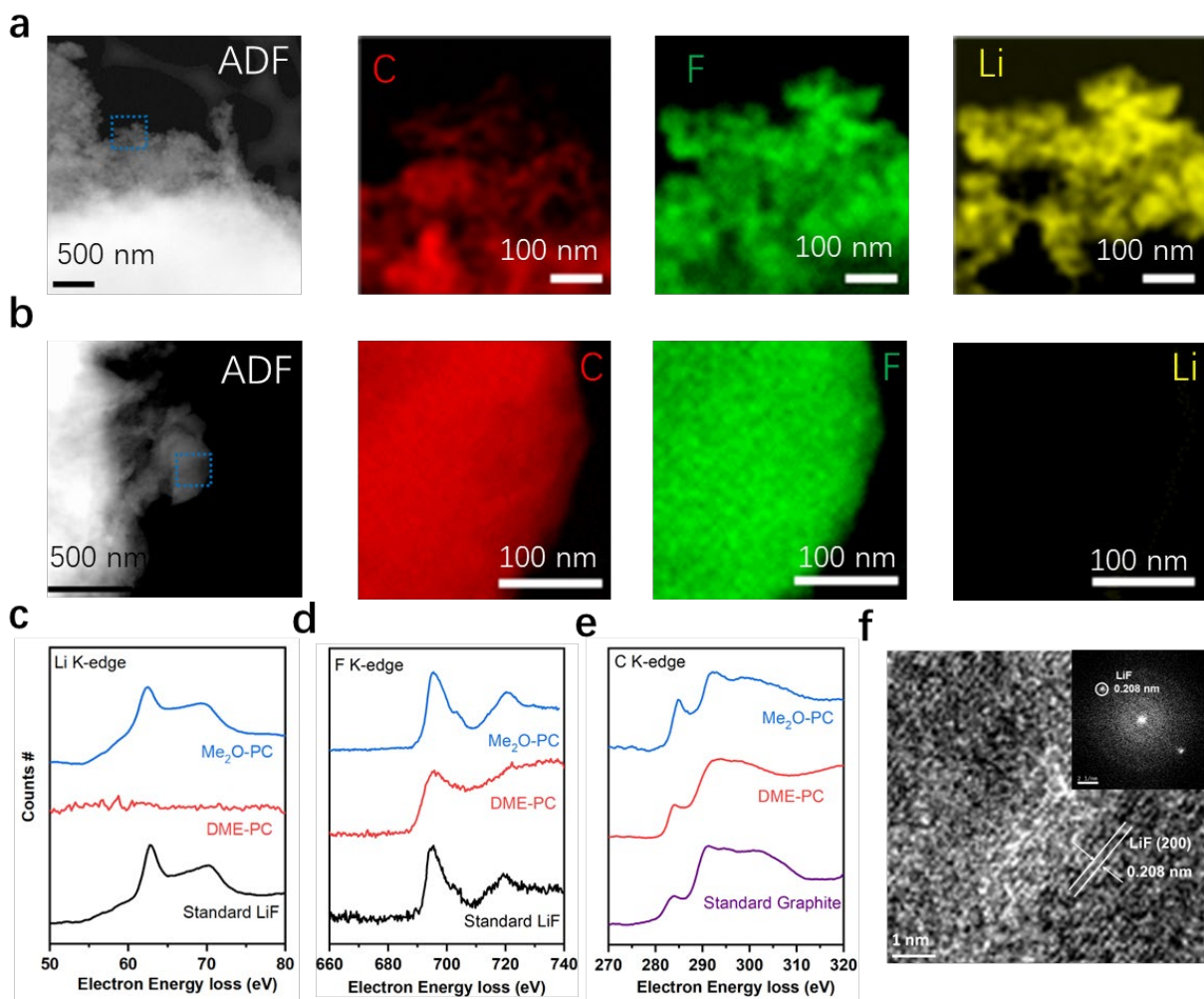
Figure 3.20 STEM-EELS, HRTEM and SAED of fully discharged CF_x at −60 °C using 10 mA g^{-1}. (a-b) STEM image and elemental mappings of discharged CF_x in 1 M LiBF$_4$-Me$_2$O-PC and 1 M LiBF$_4$-DME-PC (c-e) EELS spectra of Li K-edge, F K-edge, and C K-edge (f) HRTEM (top) and SAED (bottom) of discharged CF_x in the 1 M LiBF$_4$-Me$_2$O-PC.
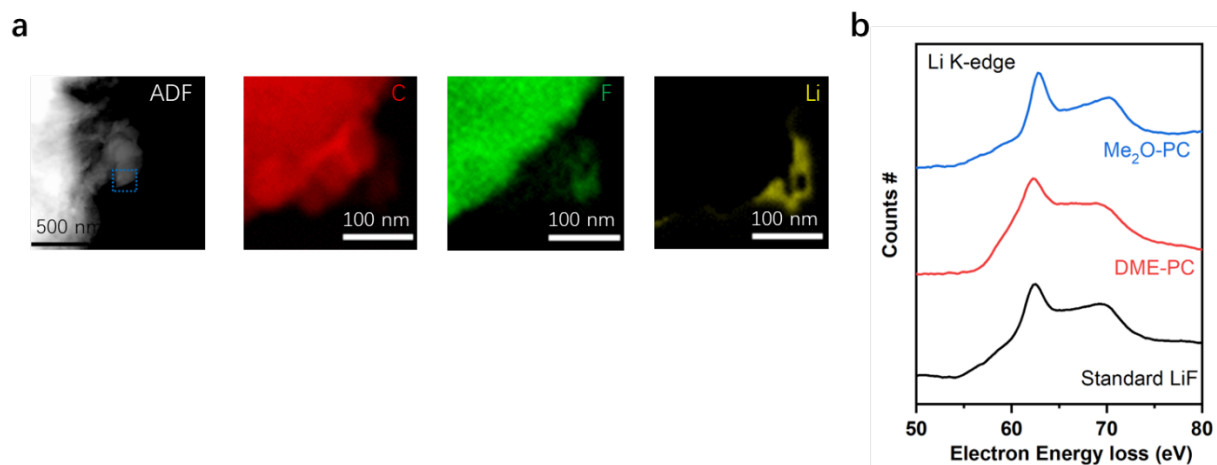
Figure 3.21 (a) STEM image and elemental mappings of discharged CF_x in the 1 M $LiBF_4$-DME-PC at different location based on Figure S16. (b) Corresponding EELS spectra of Li K-edge.

3.5 Conclusions

In conclusion, 1 M $LiBF_4$-Me_2O-PC electrolyte has been well-formulated to improve the temperature-dependent and rate-dependent performance of Li/CF_x primary battery. The optimized electrolyte demonstrated > 3.5 mS cm^{-1} ionic conductivity through a wide temperature range of −70 to 60 $^{\circ}$C. Raman, MD, and DFT simulations suggested the formulated electrolyte features an anion-pairing solvation of which the predominating Me_2O molecules have weak affinity with Li^+, facilitating the rate capability and low-temperature operation by affecting the de-solvation process while maintaining decent transport. Benefitting from the fast kinetics of the de-solvation and bulk transport, the optimized electrolyte enables high utilization of CF_x, demonstrating excellent rate performance at both room temperature and −60 $^{\circ}$C and high energy over an extended operating temperature window (−70°C ~ +55°C). XPS and STEM-EELS revealed that the CEI chemistry had little impact on the low-T performance, highlighting the importance of electrolyte de-solvation and bulk transfer features. This work provides a route to enable high power and high energy density Li/CF_x batteries operated in the extreme low-T environment, which may enlighten advanced primary battery designs with high energy and power in the future.

Chapter 3, in full, is a reprint of the material "Yin, Yijie, John Holoubek, Alex Liu, Baharak Sayahpour, Ganesh Raghavendran, Guorui Cai, Bing Han, Matthew Mayer, Noah B. Schorr, Timothy N. Lambert, Katharine L. Harrison, Weikang Li, Zheng Chen, Y. Shirley Meng. "Ultralow-Temperature Li/CFx Batteries Enabled by Fast-Transport and Anion-Pairing Liquefied Gas Electrolytes." Advanced Materials 35, no. 3 (2023): 2207932". The dissertation author was the primary investigator and first author of the paper.

Chapter 4. Fire-extinguishing, Recyclable Liquefied Gas Electrolytes for Temperature-resilient Lithium Metal Batteries

High energy density, improved safety, temperature resilience and sustainability are desirable properties for lithium battery electrolytes, yet these metrics are rarely achieved simultaneously. Inspired by the compositions of clean fire extinguishing agents, we demonstrate inherently safe liquefied gas electrolytes (LGE) based on 1,1,1,2-tetrafluoroethane (TFE) and pentafluoroethane (PFE) that maintain > 3 mS cm^{-1} ionic conductivity from –78 to +80 $^{\circ}$C. As a result of beneficial solvation chemistry and a fluorine-rich environment, Li cycling at > 99% Coulombic efficiency for over 200 cycles at 3 mA cm^{-2} and 3 mAh cm^{-2} was demonstrated in addition to stable cycling of Li/NMC622 full batteries from –60 to +55 $^{\circ}$C. Additionally, we demonstrate a one-step solvent recycling process based on the vapor pressure difference at different temperatures of LGE, which promises sustainable operation at scale. This work provides a route to sustainable, temperature resilient lithium metal batteries with fire-extinguishing properties that maintain state-of-the-art electrochemical performance.

4.1 Introduction

In recent decades, the demand for high-energy secondary batteries has increased exponentially, with their applications expanding from portable electronics to electric vehicles and grid storage[48]. The Li metal anode is considered as the most promising candidate for high energy density rechargeable battery due to its highest theoretical specific capacity (3,860 mAh·g^{-1}) and lowest electrochemical potential (–3.04 V versus the standard hydrogen electrode). However, safety concerns associated with dendrite growth along with the limited cycle life and capacity decay at subzero temperature hampers their practical application. As the above issues are highly contingent on the physical and chemical properties of the battery electrolyte, the development of novel chemistries and design strategies are crucial to solving them.

To this end, a relatively limited number of battery electrolytes have demonstrated highly reversible lithium metal performance capable of producing hundreds of cycles at the full-cell level[49-50,51]. The progress is limited due to parasitic reactions of Li metal with electrolytes from solid electrolyte interphase (SEI) cracking, porous plating morphologies, and dendrite formation, leading to irreversibility of Li cycling[52,53]. Furthermore, atypical cycling temperatures introduce additional design complexity, where low-temperatures have been demonstrated to result in dendritic morphologies and poor reversibility, and increased temperatures tend to exacerbate parasitic reactivity of all kinds[54]. Even if these metrics were to be obtained in a single system, the inherent flammability of common solvents with desirable reductive stability (e.g., ethers) is sub-optimal[50, 55]. Although non-flammable solvents exist, their long-term electrochemical stability is often problematic, mainly caused by their instability with the Li metal anode[56]. To further complicate these already stringent design considerations, the widespread production of Li metal batteries is also highly dependent on the economic and environmental sustainability of the cells, where the recyclability of every component including the electrolyte is highly desirable[57,58]. Given all of these factors, the design of electrolyte systems that consist of temperature resilient reversibility, inherently safe

physical properties, and a viable route to environmentally and economically sustainable application is a seemingly insurmountable challenge.

Extensive efforts have been devoted to developing non-flammable electrolytes, but all of them fail to satisfy the aforementioned requirements simultaneously. Solid-state electrolytes are regarded as promising candidates owing to their non-flammable nature and high packing density that can potentially boost the energy density of batteries[59]. However, the ionic conductivity of solid-state electrolytes suffers even at moderately low temperatures (< 0°C), which casts doubts on their practical use where a wide temperature window is needed. Ionic liquid electrolytes with molten salts present low volatility and low, or non-flammability, however their high viscosity (particularly at low temperatures) and cost limit their applications[60]. Besides that, little to no reports of solid-state electrolytes or ionic liquids have demonstrated viable Li metal performance in full cells without the introduction of additional cell components[61]. In commonly used liquid electrolytes, organic non-flammable phosphates solvents such as trimethyl phosphate (TMP) and triethyl phosphate (TEP) have been explored to obtain enhanced safety[62,63]. Although such solvents are unable to produce stable solid electrolyte interphases (SEI) on either graphite or Li metal anodes[64,65], increasing the salt concentration of TMP-based electrolytes has been shown to promote salt-derived inorganic SEI layers and consequently improve the interface stability as well as maintain safe operation[66]. Yet cost, viscosity, electrode wetting, and low-temperature performance are sacrificed in these high-concentration systems. More recently, localized high-concentration electrolytes (LHCE) were formulated by adding inert dilutes to lower the viscosity of the whole electrolyte, improving upon the above-mentioned issues while maintaining all the desired properties for battery performance[67,68]. Based on this concept, non-flammable LHCEs were developed by coupling inert dilutes like bis(2,2,2-trifluoroethyl) ether (BTFE) with non-flammable solvents such as TMP or TEP[69,70]. Fire-retardant LHCEs were also formulated by using non-flammable dilutes, for example 2,2,2-trifluoroethyl 1,1,2,2-

tetrafluoroethyl ether (HFE) with flammable solvents[71]. Although these LHCE delivered a higher CE for Li metal and better capacity retention over long-term cycling, the diluents are often flammable or decrease conductivity of the electrolyte, with relatively low boiling points (BTFE, +62°C; HFE, +57°C) hindering their operation at higher temperature. Though the vast array of previously explored chemistries have made significant progress either improving electrochemical performance, safety or renewability metrics, an electrolyte chemistry which comprehensively addresses all of them has yet to be demonstrated[72].

To circumvent the conventional liquid phase temperature window, a transformative concept of using a variety of hydrofluorocarbon liquefied gas as the main solvents was proposed[73]. Owing to ultra-low viscosity and freezing point, these LGE display improved performance at low temperature. To expand on the original LGE systems, another advancement in performance was also made through the addition of other co-solvents such as tetrahydrofuran and acetonitrile respectively, which resulted in stable Li plating and stripping over 500 cycles with an average CE of 99.6% and Li/NMC cycling with more than 96.5% capacity retention after 500 cycles[31-32]. However, the utilization of high pressure and flammable gasses cannot satisfy the previously discussed safety and environmental concerns.

Here, we report a versatile liquefied gas electrolyte for wide-temperature lithium metal batteries with intrinsic fire-extinguishing properties and economical recollection after utilization. By rationally designing TFE, PFE-based electrolytes, we show a self-fire-extinguishing effect and demonstrate a simple one-step solvent recycling process. Due to sufficiently high ionic conductivity over wide temperature range, favorable solvation structure, and SEI formation, the designed LGE showed stable Li metal cycling with a CE of 99% and long-term Li/NMC622 cycling up to 4.2 V from –60 °C to +55 °C.

4.2 Results

4.2.1 Rational design of liquefied gas electrolytes

The desired liquefied gas solvents need to satisfy several potentially conflicting criteria. Ideally, the liquefied gas solvent should possess solvation ability sufficient to achieve >1M salt solubility in addition to having sufficiently low vapor pressure, low- or non-flammability, low viscosity, and low freezing point. As no single solvent satisfies all criteria, we utilize a mixture of non-flammable, low viscosity, low vapor pressure hydrofluorocarbons and Li^+ coordinating ethers to achieve a balanced electrolyte. Compared with different ethers' properties (**Figure 4.1a**), dimethyl ether (Me_2O) exists in the gaseous state at ambient conditions. Of the ethers, it has the lowest freezing point and viscosity combined with high solvating power, reductive stability and good compatibility with Li metal. By comparison with the previously reported FM solvent, Me_2O has a higher critical point at 127 °C and lower vapor pressure - down to 75 psi at room temperature (**Table 4.1**)[74,75]. Despite its flammability, Me_2O generates non-toxic and noncorrosive (e.g. H_2O) products after combustion[76], whereas the combustion of flammable fluorinated solvents such as fluoromethane and the widely used BTFE results in the generation of hydrogen fluoride[77].

Table 4.1 Physical properties of the different solvents.

Solvent	Melting Point (°C)	Boiling Point(°C)	Critical Point(°C)	Flash Point(°C)	Vapor Pressure (psi)	Dipole (Debye)	Dielectric Constant	Viscosity (mPa·s)
1,2-Dimethoxyethane	−58	85	263	−2	0.93	1.71	7.2	0.46
Diethyl Ether	−117	35	194	35	10.28	1.3	4.33	0.224
Dimethyl Ether	−141	−24	127	−41	75	1.3	5.02	0.12
1,1,1,2-Tetrafluoroethane	−103	−26.3	101	250	82	2.06	9.7	0.207
Pentafluoroethane	−103	−48.5	66	None	175	1.56	4.5	0.15
1,1,1,2,3,3,3 - Heptafluoropropane	−131	−15.6	102	None	65.7	1.46	2.0	0.244
Fluoromethane	−144	−78	44	-	494	1.85	9.7	0.085

All data values are extracted from published works26,29,30,33. The vapour pressure, dipole moment, relative dielectric constant and viscosity values were obtained for solvents in a saturated liquid state at +20 °C.

To tackle the flammability issues, a non-flammable solvent needs to be a majority component in a mixture. The ideal non-flammable cosolvent would keep the aforementioned physical properties as well as a broad electrochemical window, and low solvation ability to maintain an ion-pairing solvation structure. Based on these principles and inspired by the fire-extinguishing agents FS 49 C2 (**Figure 4.1b, Figure 4.8 and Note 1**), TFE and PFE were identified as potential liquefied gas cosolvents. With a high flash point (TFE, T_{flash} = +250 °C), non-flammability of PFE and high fluorine atomic ratios[78,79], these molecules also exhibit moderate vapor pressure, low melting point (down to –103 °C), and low HOMO (Highest Occupied Molecular Orbital) energy (**Table 4.1, Figure 4.9**)[80]. The proposed electrolyte system is shown in **Figure 4.1c** after combining Me_2O with TFE/PFE and salt. Due to the strong bonding energy and low polarity of the C-F bond, TFE and PFE are expected to have low solvation ability with lithium salts and largely serve as inert agents. Nearly all Me_2O solvents are coordinated to Li^+ and its aggregates resulting in an enhanced oxidative stability of Me_2O. Owing to the fire-extinguishing characteristics of TFE and PFE, the battery operation under harsh situations would significantly suppress flames. By comparison, batteries using conventional flammable carbonated solvents would result in severe thermal runaway and easily cause fires. Furthermore, the moderate vapor pressure would also enable a simple separation and recycle process to collect used solvents, which is discussed in a later session.

As for the salt selection, lithium bis(fluorosulfonyl)imide (LiFSI) and lithium bis(trifluoromethanesulfonyl)imide (LiTFSI) are considered appropriate salt candidates due to their lower dissociation energy over lithium hexafluorophosphate ($LiPF_6$) and lithium tetrafluoroborate ($LiBF_4$) and the formation of high fluorine content interfaces[81]. After performing the solubility tests on LiFSI/LiTFSI-

Me$_2$O-TFE/PFE mixture (**Figure 4.10-11 and Note 2**), 1 M LiFSI in Me$_2$O (Salt: Me$_2$O molar ratio of 1: 1.7) coupled with TFE (labeled as 1 M LiFSI-Me$_2$O-TFE) and 1 M LiFSI in Me$_2$O (Salt: Me$_2$O molar ratio of 1: 1.5) coupled with TFE: PFE 7:1 volume ratio (labeled as 1 M LiFSI-Me$_2$O-TFE-PFE) which have high fluorine atomic ratio are selected for this work. A detailed comparison of the LiFSI-based and LiPF$_6$-based LGE is presented in the **Supplementary Note 3** combined with **Figure 4.12** and **4.13.**
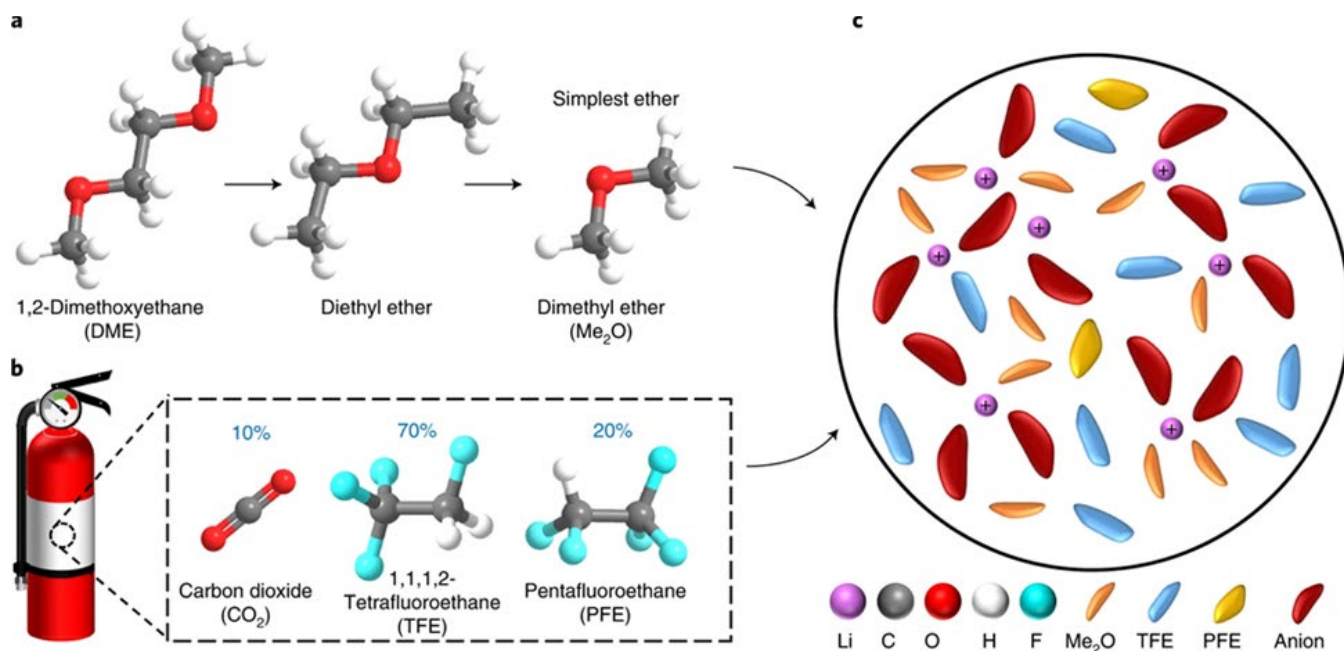
Figure 4.1 Design of liquefied gas electrolytes (a) Selected dimethyl ether, as the simplest ether with the fast transport, strong Li$^+$ solvation and high salt solubility (b) Composition with clean extinguishing agent FS 49 C2. (c) Proposed solvation structure of designed liquefied gas electrolytes.

4.2.2 Transport and safety properties

The electrolytic conductivities of the liquefied gas electrolytes were measured and shown in **Figure 4.2a**. In contrast with a sharp conductivity drop observed for traditional electrolytes such as 1 M LiPF$_6$ in ethylene carbonate/ethyl methyl carbonate with a 3:7 weight ratio (labeled as 1M LiPF$_6$ in EC-EMC) or 1 M LiFSI in 1,2-dimethoxyethane (labeled as 1 M LiFSI-DME), liquefied gas electrolytes 1 M LiFSI-Me$_2$O, 1 M LiFSI-Me$_2$O-TFE, and 1 M LiFSI-Me$_2$O-TFE-PFE exhibit near constant conductivity >1 mS/cm over a wide temperature range (–78 to +80 °C). The enhanced ionic conductivity at low

temperature for the liquefied gas electrolytes is attributed to the low viscosity and low melting point. Notably, conductivities measured in the 1 M LiFSI-Me$_2$O and 1 M LiFSI-Me$_2$O-TFE electrolytes exceed 14.1 mS/cm and 4.5 mS/cm respectively, in the temperature range of –78 °C to +70 °C which aligns with molecular dynamics (MD) simulation predictions. The conductivity of as-obtained electrolytes at low temperature compares favorably to most other electrolyte systems[82,83], which experience severe conductivity drop at low temperature. The changes in vapor pressure over a range of temperature for different liquefied gas solvents and electrolytes are shown in **Figure 4.2b**. In contrast to the previously proposed FM-based liquefied gas electrolytes, the Me$_2$O, TFE, and PFE-based electrolyte and its components have significantly lower vapor pressure. Specifically, vapor pressure of Me$_2$O, TFE and PFE is only 15%, 17%, and 35% of FM's vapor pressure at +20 °C, respectively. Me$_2$O and TFE have similar vapor pressures over a wide temperature range with high critical points. We utilize a TFE: PFE volume ratio of 7:1 to closely follow the composition of the fire-extinguisher FS 49 C2. This mixture has a lower operation pressure than pure PFE solvent.   The resulting 1 M LiFSI-Me$_2$O-TFE-PFE electrolyte possesses both improved safety and wide temperature operation window.

We then validated the fire extinguishing effectiveness of the 1 M LiFSI-Me$_2$O-TFE-PFE electrolyte by fire douse test (**Figure 4.14**). Tests were conducted by blowing an ignited candle with various types of gases and gas mixtures at a constant gas flow rate. Air gas is used as a reference to demonstrate the flow rate set in the tests doesn't influence the flame (**Figure 4.2c**). CO$_2$ gas shows a suppression of the fire after a relatively long time of around 25 seconds, by gradually decreasing the local oxygen concentration (**Figure 4.2d, Supplementary Video 2**). Meanwhile, due to the strong chemical C-F bond and faster heat adsorption, the individual TFE and PFE components effectively extinguish fire within 1.4 seconds. This occurs as the agent changes from liquid to gas phase during venting in addition to the presence of C-F bonds that block the chain reactions (**Figure 4.15**). As expected, Me$_2$O gas demonstrates high

flammability that leads to a stronger flame (**Figure 4.2e**). To verify the fire-extinguishing features of the proposed 1 M LiFSI-Me$_2$O-TFE-PFE electrolyte, the formulated electrolyte (**Figure 4.2f**) itself is directly released to the flame. We observed robust fire suppression in a much shorter time than observed for pure CO$_2$ (**Figure 4.2d**) despite the small content of Me$_2$O present in the electrolyte (**Figure 4.2e**). Based on the above results, we prove that the 1 M LiFSI-Me$_2$O-TFE-PFE electrolyte is self-flame-extinguishing.
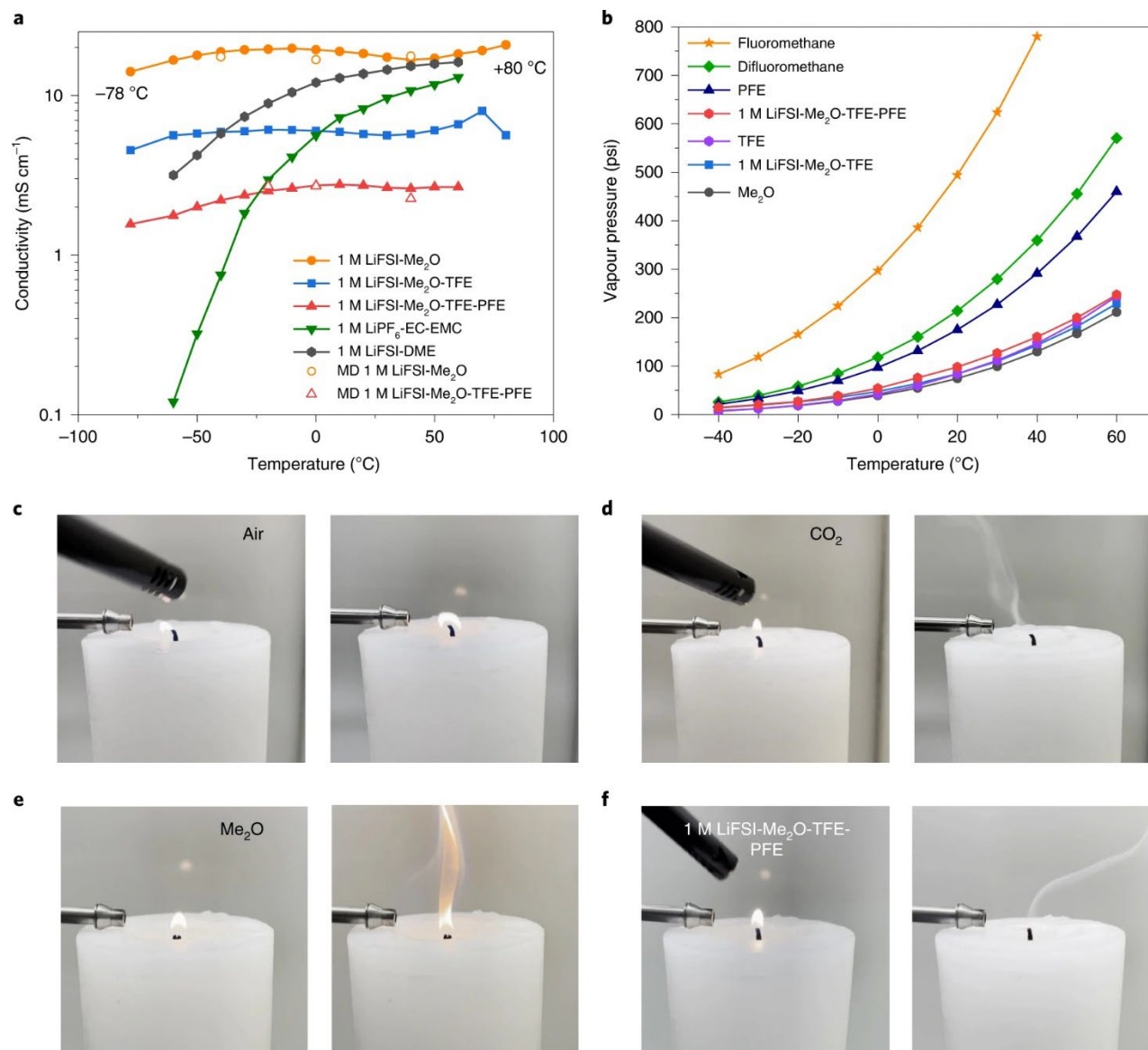
Figure 4.2 Properties of LGEs. (a-b) Ionic conductivity and vapor pressure of the LGEs over a wide temperature range. (c–f), Fire-douse tests with different pure gases or gas mixtures demonstrated using ignited candles.

4.2.3 Bulk structure of electrolyte

The solvation structure of the liquefied gas electrolytes was investigated by Raman spectroscopy using customized high-pressure cells[84]. To understand the solvation structure evolution with the increase of salt/ether ratio, Raman spectra of 1 M, 4 M, saturated concentrations (around 7 M) of LiFSI in Me_2O and formulated 1 M LiFSI-Me_2O-TFE-PFE electrolyte were obtained (**Figure 4.3a-c**). **Fig. 3a** shows that the S-N-S bending peak is blue-shifted from 730 to 748 cm^{-1} due to formation of the $FSI^-(Li^+)_n$ contact ion pairs and aggregates with increasing salt concentration. The saturated 7 M LiFSI in Me_2O and 1 M LiFSI-Me_2O-TFE-PFE electrolytes have the same S-N-S bending peaks at 748 cm^{-1} indicating similarity of salt aggregation and cluster formation, which is consistent with the similarity of the salt-to-solvent ratios for these electrolytes. The peak appearing at 721 cm^{-1} for 1 M LiFSI-Me_2O-TFE-PFE was assigned to the characteristic peak of C-F_3 symmetric deformation, which is consistent of pure PFE spectra. Raman spectra for the TFE co-solvent are shown in **Figure 4.3b**. A slight blue shift of TFE molecules at 838 cm^{-1} (C-C stretching vibration) is attributed to the weak interaction between Li^+ and F-CH_2, which is verified by the MD simulations discussed below. For the C-O-C stretching band of Me_2O, a red shift for center position from 918 to 916 cm^{-1} was observed due to the increasingly solvated Me_2O in the electrolytes from low salt concentration to saturated salt concentration (**Figure 4.3c**). In short, solvated FSI^- and Me_2O dominate the solvation structure, which is believed to reduce the free Me_2O solvent amount leading to the improvement of oxidative stability. This facilitates the salt decomposition to form a LiF-rich SEI on the anode.
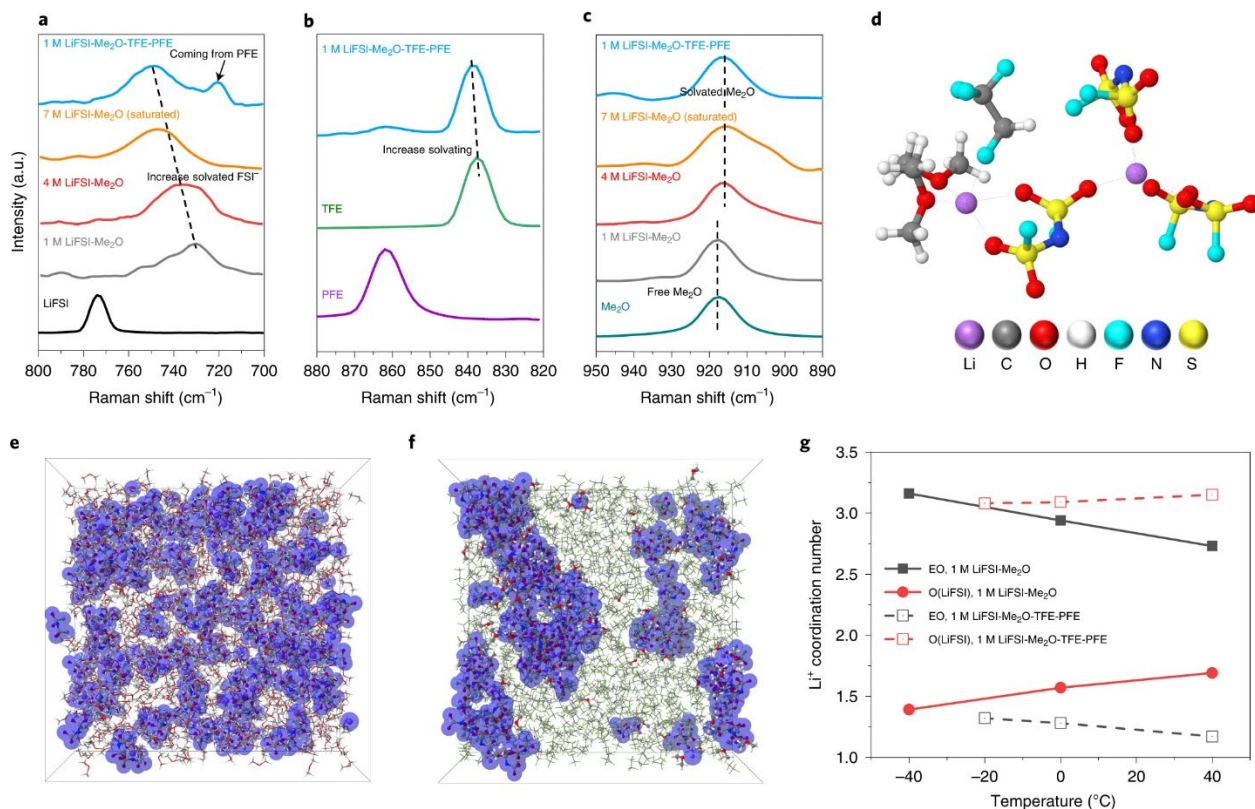
Figure 4.3 Bulk structure and MD simulation results (a-c) Raman spectra of different LiFSI concentrations in Me$_2$O and Me$_2$O-TFE-PFE mixture (d-g) MD results of (d) representative Li$^+$ solvates, (e) 1 M LiFSI-Me$_2$O and (f) 1 M LiFSI-Me$_2$O-TFE-PFE at 273 K. (g) Li$^+$ coordination numbers of Li-EO (Ether Oxygen) bonding and Li-O from LiFSI bonding at different temperatures.

The bulk structure of 1 M LiFSI-Me$_2$O and 1 M LiFSI-Me$_2$O-TFE-PFE electrolytes were examined via MD simulations using APPLE&P force fields after validating its ability to predict the solvent-Li$^+$ binding energy obtained in quantum chemistry (QC) calculations (**Figure 4.16, Note 4**). The Li$^+$ binding to Me$_2$O is the strongest, followed by Li$^+$-TFE and Li$^+$-PFE indicating that TFE is more effective at salt dissociation than PFE. MD simulations reveal a dominance of short well-dispersed ionic aggregates in 1M LiFSI-Me$_2$O, while much larger aggregates were found in 1 M LiFSI-Me$_2$O-TFE-PFE (**Figure 4.3d-f, Figure 4.17-19**). A clear trend of increasing the extent of aggregation with increasing temperature is observed. It is consistent with increasing the Li$^+$-FSI$^-$ coordination and decreasing the Li-ether oxygen coordination with increasing temperature (**Figure 4.3g**). Dilution of 1M LiFSI-Me$_2$O with TFE and PFE solvents decrease a fraction of "free" Li$^+$ and TFSI$^-$ from (12-24%) to well below 0.1%, making charge

transport by free ions negligible in the 1 M LiFSI-Me$_2$O-TFE-PFE electrolyte. Through analysis of the radial distribution functions (RDFs), representative solvates and coordination numbers (**Figure 4.20-21, Figure 4.3g**) reveal the strongest propensity for a Li$^+$ to coordinate to ether oxygen (EO) atoms of Me$_2$O followed by oxygens of FSI$^-$ and fluorine of TFE. No coordination of Li$^+$ to fluorine of PFE is observed in alignment with QC results, indicating the weakest binding of Li$^+$ to PFE solvent in agreement with Raman data (Fig. 3b). The Li$^+$(Me$_2$O) (FSI)$_2$ and Li$^+$(Me$_2$O) (FSI)$_3$ are the most probable local Li$^+$ environments allowing formation of the extended aggregates (**Figure 4.22**). Nearly all (>94%) Me$_2$O are bound to Li$^+$ in 1 M LiFSI-Me$_2$O-TFE-PFE resulting in improved oxidation stability due to a low fraction of "free" ether solvent that is known to undergo H-transfer on the LiNiO$_2$-like cathode surfaces[85].

MD simulations accurately predict electrolyte conductivity (**Figure 4.2a**). Conductivity decreases by a factor of 6 with the addition of TFE and PFE to 1 M LiFSI-Me$_2$O. This is attributed to the decrease of ion diffusion by a factor of 2.3-2.6 times and the increased ion aggregation and elimination of free ions. A near constant conductivity with temperature variation is due to the compensation of slowing down of ionic motion with decreasing temperature with an increasing fraction of charge carriers due to the breakdown of the larger ionic aggregates resulting in increasing ionicity at reduced temperatures that is consistent to being closer to ideal line in the Walden plot (**Figure 4.23-24**).

4.2.4 Electrochemical performance

Li metal soak tests were first performed to examine the compatibility of electrolytes with Li metal (**Figure 4.25 and Note 5**). It was observed that the Li metal retained a clean and polished appearance after soaking in the 1 M LiFSI-Me$_2$O, 1 M LiFSI-Me$_2$O-TFE and 1 M LiFSI-Me$_2$O-TFE-PFE electrolytes for 15 days. For Li metal plating/stripping tests, the ether-based liquid electrolyte could cycle well under mild conditions (0.5 mA cm^{-2},1 mAh cm^{-2}). However, under a current density of 3 mA cm^{-2} with a practical capacity of 3 mAh cm^{-2}, the performance of Li metal anode in 1 M LiFSI-DME quickly drops after 9

cycles. (**Figure 4.4a**). The cell using 1 M LiFSI-Me$_2$O cycles with a 96.4% average CE in the first 100 cycles, suggesting an improved Li metal compatibility with Me$_2$O over DME, although CE fades in subsequent cycles. On the contrary, the liquefied gas electrolytes using 1 M LiFSI-Me$_2$O-TFE-PFE and 1 M LiFSI-Me$_2$O-TFE deliver first cycle CEs of 94.8% and 96.8%, respectively. Average CEs of 98.8% and 99.0% are achieved in the subsequent 200 cycles (**Figure 4.4a**), demonstrating their electrochemical compatibility with Li metal anodes and indicating the robustness of the salt-derived SEI. The 1 M LiFSI-Me2O-TFE-PFE is further investigated in a wide temperature range, where it retains average CEs of 97.3%, 97.2%, 95.2% and 91% at 0, –20, –40 and –60 °C respectively, under the same current density of 3 mA cm^{-2} and plating capacity of 3 mAh cm^{-2}. In comparison, the low concentration counterpart delivers an average CE of 73.7 % at -40 °C and the cell malfunctions at –60 °C with severe CE fluctuation. Although the reference 1 M LiFSI-DME liquid electrolyte cycles under a mild 1 mA cm^{-2} and 1 mAh cm^{-2} condition, the cell CEs fades dramatically at subzero temperature due to the solvent-dominated solvation structure and low transference number (**Figure 4.4b**).
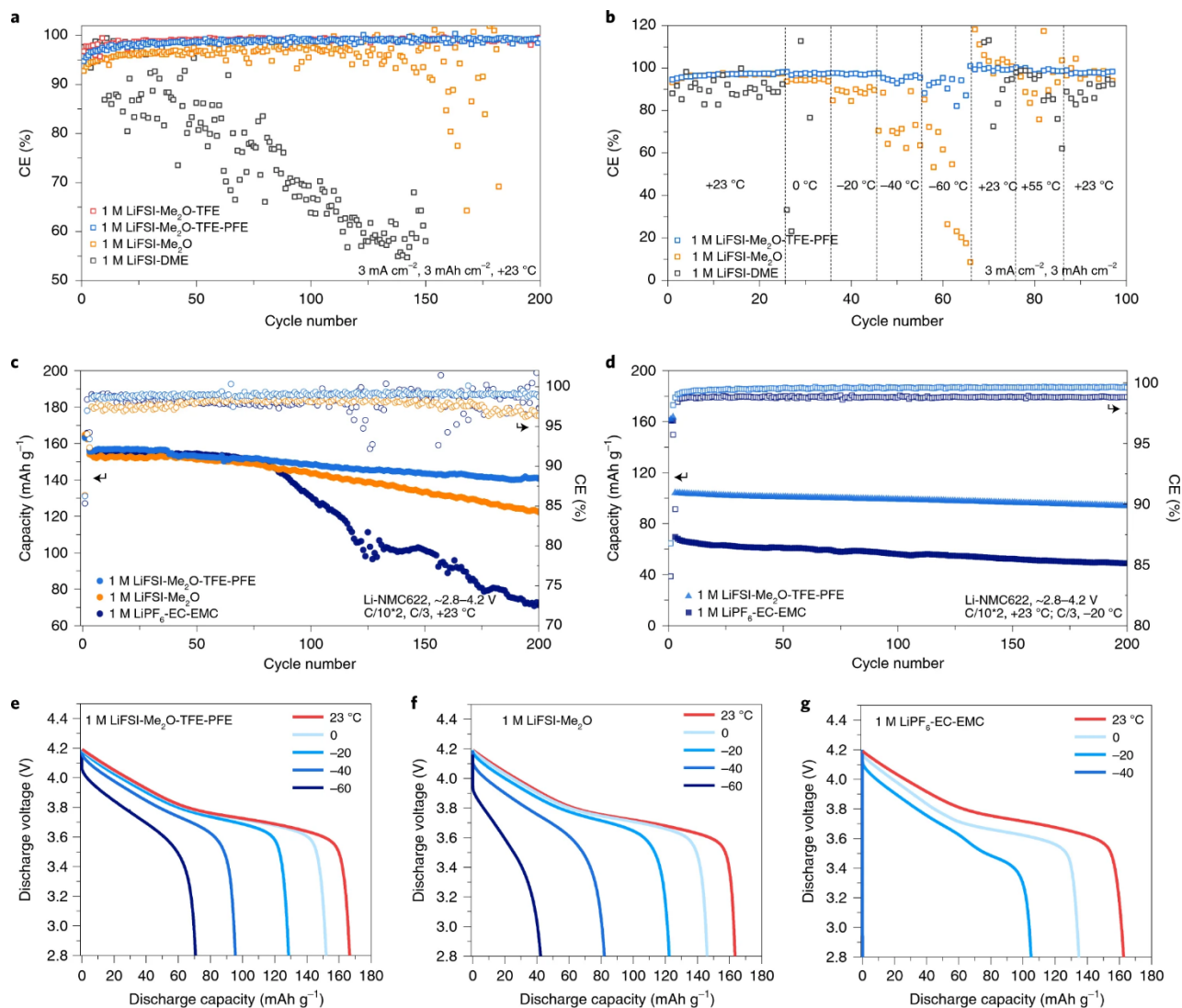
Figure 4.4 Electrochemical performance of lithium metal anode and Li-NMC622 cells in liquefied gas electrolytes (a) The CE of Li metal plating/stripping over 200 cycles in various electrolytes at +23 °C and (b) different temperatures. (c-g) Li-NMC622 long-term cycling at different temperatures.

Cells comprising of a Li metal anode and a $LiNi_{0.6}Mn_{0.2}Co_{0.2}O_2$ cathode (NMC622) with an average loading of ~1.8 mAh·cm^{-2} were fabricated to investigate the oxidative stability of the liquefied gas electrolyte. A widely used commercial electrolyte consisting of 1 M $LiPF_6$ in ethylene carbonate/ethyl methyl carbonate with a 3:7 weight ratio (Gen2) was selected for the reference cell. Based on a Li-NMC622 voltage hold test (**Figure 4.26**), 1 M LiFSI-Me₂O-TFE and 1 M LiFSI-Me₂O-TFE-PFE electrolytes exhibit oxidation stability up to 4.4 V. At room temperature and 4.2 V upper voltage, the Li-

NMC622 cells in 1 M Me$_2$O-TFE-PFE provides average CE of > 99.0 % with capacity retention of 90.4 % over 200 cycles (**Figure 4.4c**). In comparison, the carbonate-based electrolyte shows a quicker capacity fade. With a limited 20 μm Li metal resources corresponding to a N/P ratio of 2.3:1, the formulated LGE maintains a 153 mAh g^{-1} discharge capacity over 50 cycles (**Figure 4.27**). At reduced temperature (–20 °C) the 1 M LiFSI-Me$_2$O-TFE-PFE electrolyte exhibits a high average CE of 99.6 % and a capacity retention of > 90.0 % after 200 cycles while carbonate-based electrolyte demonstrates lower average CEs and reduced (70.1%) capacity retention (**Figure 4.4d**). Furthermore, the 1 M LiFSI-Me$_2$O-TFE-PFE electrolyte displays improved long-term cycling at +55 °C with a capacity retention of 80% after 50 cycles compared with Gen2 (**Figure 4.28**). Owing to the high conductivity and high transference number of 0.59 (**Figure 4.29**), it also shows an outstanding rate capability, with a 90% capacity retention under a C-rate of 1C and no obvious capacity decay under a C rate of C/2 over 100 cycles (**Figure 4.30**). Besides Li metal anode, the formulated LGE enables reversible intercalation and de-intercalation of Li$^+$ in graphite with CEs of 99.75% over 30 cycles (**Figure 4.31**), indicating the LGE compatibility with graphite anode.

To further evaluate the 1 M LiFSI-Me$_2$O-TFE-PFE electrolyte performance across a wide temperature window, the Li-NMC 622 cells were cycled with both carbonate and ether-based electrolytes as references. Under the same charge and discharge rate of C/15 and a cutoff voltage of 4.2 V, the discharge capacities are approximately the same across all three electrolytes at room temperature. At –60 °C, the 1 M LiFSI-Me$_2$O and 1 M LiFSI-Me$_2$O-TFE-PFE electrolytes demonstrate discharge capacities of 43 and 71 mAh g^{-1} respectively (**Figure 4.4e, f**). On the contrary, the carbonate-based electrolyte is incapable of charging and discharging at –40 °C. (**Figure 4.4g**). Based on the above results, we have successfully demonstrated the formulated LGE can maintain stable long-term cycling at room temperature and enhanced low temperature performance as well as steady rate capability. Compared with other works utilizing nonflammable fluoro-ether solvents, the resulting LGE maintains state-of-the-art performance

with enhanced safety (**Supplementary Table 1, 2**), which paves the way to development of next-generation lithium metal batteries.

4.2.5 Morphology and interface chemistry characterizations

To understand the electrolytes' influence on the surface and cross-sectional morphology of the deposited Li metal, cryogenic focused ion beam/scanning electron microscopy (cryo-FIB/SEM) was applied to mitigate potential beam damage on Li metal[86]. The lithium samples were plated onto a Cu foil with a 3 mAh cm^{-2} capacity using a current density of 0.5 mA/cm^{-2}, which corresponds to an electrodeposition thickness of approximately 15 μm.

Electrolyte formulations exert a crucial influence on the electrodeposited Li metals. Here, we compare the Li metal morphology and the thickness of SEI formed in LGE with the control electrolytes. Consistent with the literature[27], plating in a 1 M LiFSI-DME electrolyte shows a locally dense and relatively large granular Li metal, however a high structural tortuosity at the cross-section area is also apparent (**Figure 4.5a, d**). Moreover, the global distribution of the plated Li turns out to be inhomogeneous (**Figure 4.5a**), which explains the inferior cycling stability of the DME-based electrolyte at a high current density. On the contrary, both the dilute Me$_2$O and Me$_2$O-TFE-PFE electrolytes deliver a dense Li metal morphology with large granular sizes and uniform global coverage (**Figure 4.5b, c**). Although small voids are observed for the dilute Me$_2$O, Li metal plated from the 1M LiFSI-Me$_2$O-TFE-PFE electrolyte has significantly fewer voids and a dense morphology (**Figure 4.5e, f**), indicating a lower nucleation barrier and homogeneous deposition of Li metal. In accord with cryo-FIB/SEM images, the Li anode after extended cycling also demonstrates a more compact morphology when cycled in 1 M LiFSI-Me$_2$O and 1M LiFSI-Me$_2$O-TFE-PFE electrolytes, compared to the samples cycled in 1M LiFSI in DME. To visualize the SEI thickness of the deposited Li in 1 M LiFSI-DME and 1 M LiFSI-Me$_2$O-TFE-PFE electrolytes, cryogenic transmission electron microscopy (Cyro-TEM) was performed (**Figure 4.5g-h** and

Figure 4.32). Clear differences in the SEI thickness on the deposited Li are observed for the two electrolytes. The SEI formed in the 1 M LiFSI-DME electrolyte showed a thickness over 155 nm (**Figure 4.5g**), whereas the SEI formed in the 1 M LiFSI-Me$_2$O-TFE-PFE electrolyte was much thinner, only 22 nm thick **(Figure 4.5h)**. Although the Li deposited in each electrolyte has a bulky structure (**Figure 4.32**), the ultra-thick SEI on the Li deposited might deteriorate the Li||Cu cycling behavior of the 1 M LiFSI-DME electrolyte. However, the thin and dense SEI formed on a Li deposited in 1 M LiFSI-Me$_2$O-TFE-PFE electrolyte is thought to give rise to the improved cycling stability. These results further illustrate that Me$_2$O is a promising ether solvent that has electrochemical compatibility with Li metal. With the increase of the salt-to-solvent ratio, the reductive stability is further strengthened as demonstrated in 1 M LiFSI-Me$_2$O-TFE-PFE.
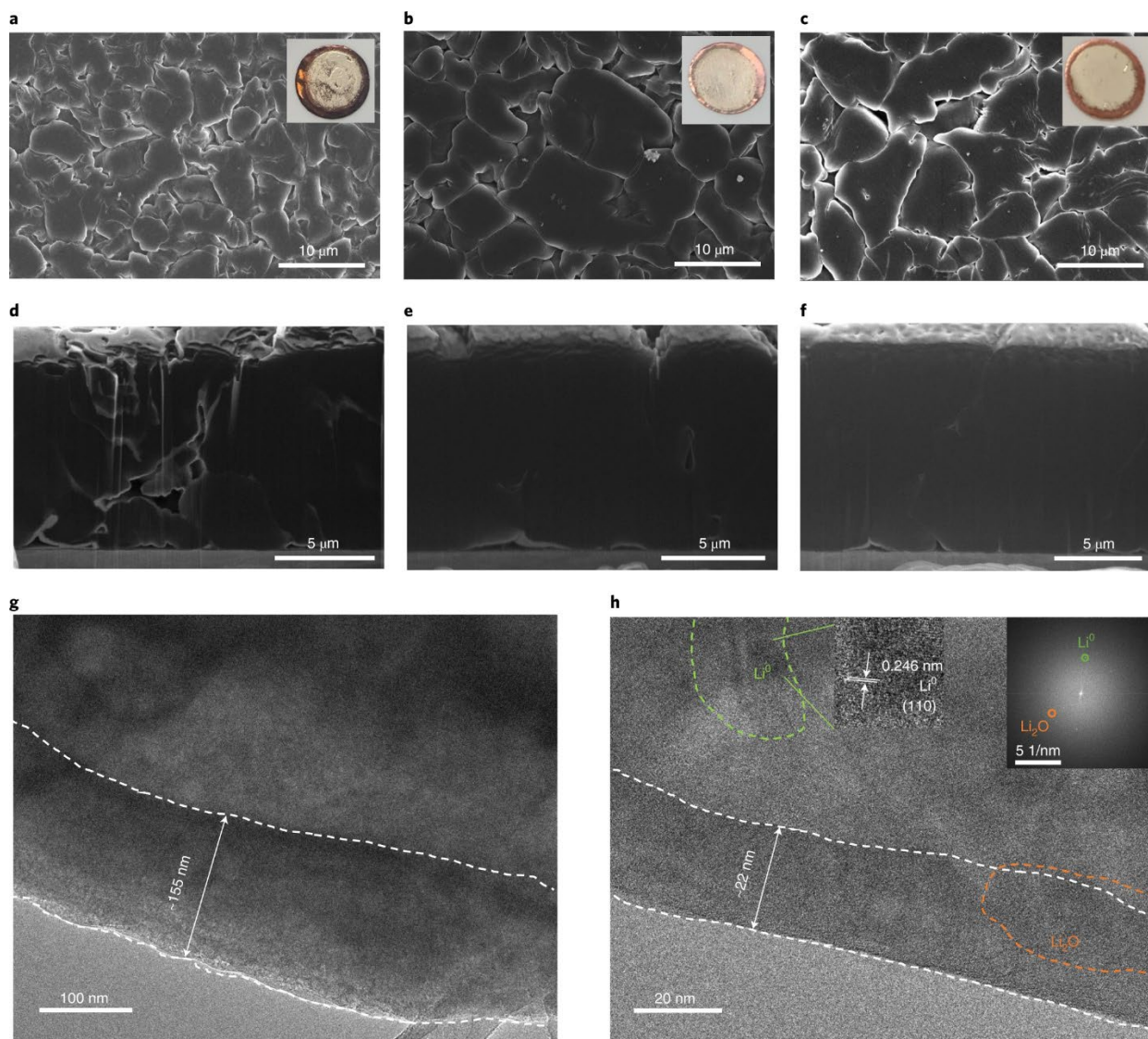
Figure 4.5 Visualization of Li morphology and SEI. Cryo-FIB/SEM images of surface and cross-section area of deposited lithium metal after first plating on the Cu foil using (a,d)1 M LiFSI-DME (b,e) 1 M LiFSI-Me$_2$O (c,f) 1 M LiFSI-Me$_2$O-TFE-PFE respectively. Cryo-TEM images of the deposited Li (g,h).

Along with the Li morphology difference, the improved cycling performance of the formulated electrolyte compared with the reference dilute ether electrolytes can also be explained by different chemical compositions of the respective SEI layers as characterized by X-ray photoelectron spectroscopy (XPS) with depth profiling. C signal including C-C/C-H, C-O and C=O represents organic species of SEI. From global survey of C 1s atomic concentrations (**Figure 4.6a-c**), it can be observed that the SEI formed in 1 M LiFSI in DME (**Figure 4.6a**) has the highest carbon ratio, while the SEIs formed in 1 M LiFSI in

Me$_2$O (**Figure 4.6b**) and 1 M LiFSI-Me$_2$O-TFE-PFE (**Figure 4.6c**) show gradually descending carbon ratios. Li atomic concentration mostly represents inorganic ratio inside SEI. As shown in **Fig. 6a-c**, the SEI formed in 1 M LiFSI-Me$_2$O-TFE-PFE contains the highest Li concentration around 60%, whereas the SEI formed in 1 M LiFSI-DME and 1 M LiFSI-Me$_2$O shows 39% and 48%, respectively. Interestingly, with increasing etching time, the two predominating Li, O and secondary F, S and N atomic concentrations in the SEI formed in 1 M LiFSI-Me$_2$O-TFE-PFE vary in a narrow range. Coupled with the observation of a homogeneously thin layer of SEI by Cryo-TEM, it shows similar structure of monolithic SEI reported by Cao, et al[87]. Overall, the global survey results are consistent with MD and Raman results showing less free ether solvent in the solvation structure and further strengthening the conclusion that there is less solvent decomposition on the Li-metal surface in the 1 M LiFSI-Me$_2$O-TFE-PFE electrolyte.

As for local survey of specific chemical information, since all electrolytes are ether-based systems, they maintain similar types of chemical compositions at each individual spectrum (**Figure 4.6d-f**, **Figure 4.33**). However, their difference can be dictated in their relative ratio, where there are more salt-decomposed compounds such as LiF, Li$_2$O and Li$_2$S generated in the 1 M LiFSI-Me$_2$O-TFE-PFE from the F 1s, O 1s and S 2p spectra (**Figure 4.6f**). The observation of rich-Li$_2$O, Li$_2$S SEI have also been reported by some localized highly concentrated ether-based electrolytes, which might be the favorable SEI components for lithium metal anode[87,88,89]. For the two references, it clearly indicates more organic C-O, C=O compounds. The appearance of the organic compounds suggests that there is more decomposition of DME (**Figure 4.6d**) or Me$_2$O solvents (**Figure 4.6e**), leading to the relatively poor electrochemical stability with lithium metal.
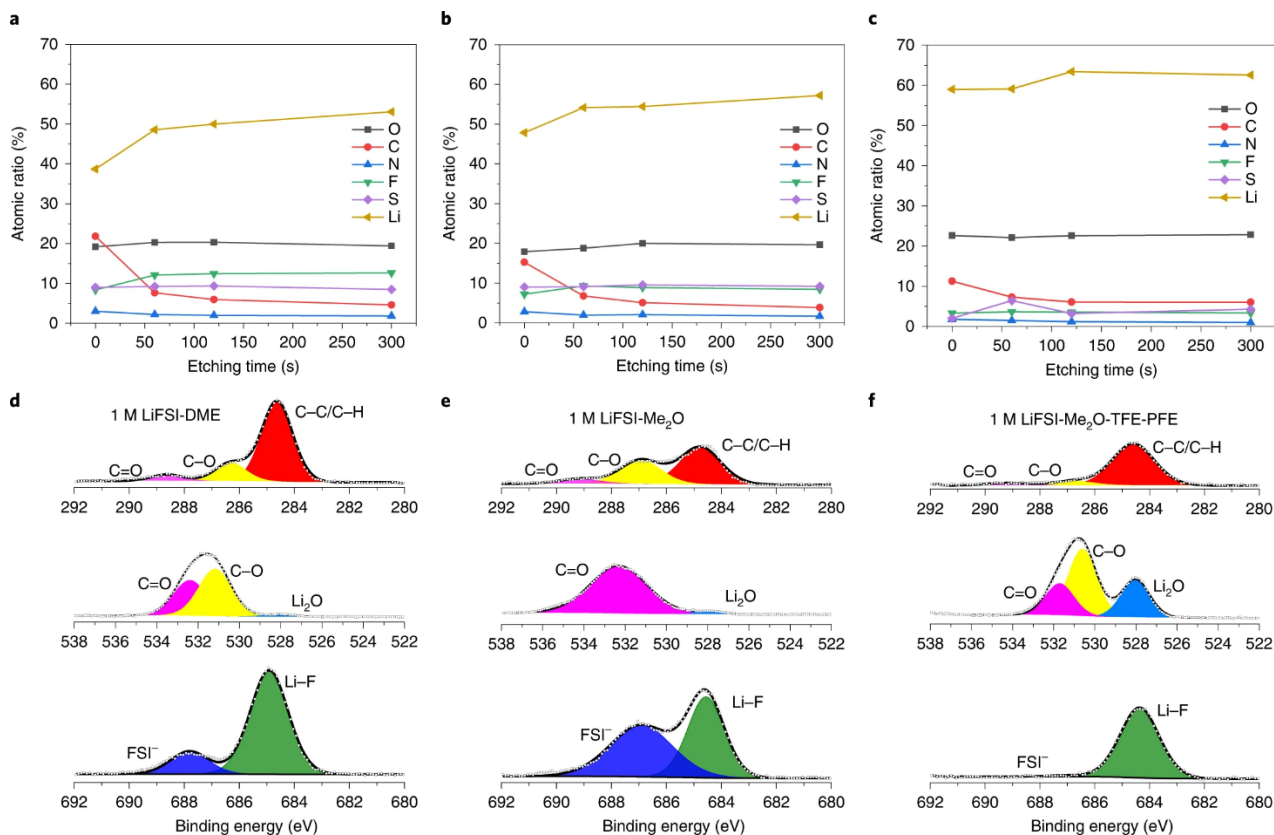
Figure 4.6 SEI information obtained by XPS measurement with electrolytes. Quantified atomic elemental ratios of the SEI at different sputtering times(**a-c**), as well as surface spectra from cycled lithium (**d-f**) for 1M LiFSI-DME (**a, d**), 1M LiFSI-Me$_2$O (**b, e**) and 1M LiFSI-Me$_2$O-TFE-PFE (**c, f**).

4.2.6 Recyclability of liquefied gas solvent

Battery recycling is crucial to reducing cost and removing the potential risks that battery components pose to the environment. To better understand the bottleneck of the battery recycling process, a closed loop of Li metal batteries recycling is illustrated in **Figure 4.7a**. Even with a lean electrolyte condition, the electrolyte still occupies a large ratio by weight (24%)[70] in Li-NMC pouch cells. The electrolyte ratio would be even higher for more porous electrodes, such as sulfur. However, the electrolyte is not recovered but simply disposed of during the electrolyte handling process or not mentioned in most published work[90,91]. To efficiently collect the spent electrolytes, the primary challenge is to separate the electrolyte from electrodes considering the porous, high surface area of the electrodes and high viscosity of the

electrolyte[92]. Conventionally, supercritical CO_2 is employed for electrolyte extraction from both separators and electrode materials owing to its enhanced dissolution characteristics. In addition, the electrolyte salt and solvents can all be recovered when the extractant CO_2 is supplemented with some functional additives (eg. ACN, PC)[93]. However, considering the intrinsic high-pressure nature of supercritical CO_2, the cost of this technique limits its wide application. By comparison, owing to the low viscosity, low boiling point of LGE systems, the ease of evaporation controlled by temperature changes would not require a complicated separation process. Furthermore, commercialization of LGE technology on large scales will require recycling of hydrofluorocarbon gases, otherwise the stable C-F bond from these F gases would cause a noticeable global warming effect (**Figure 4.34**).
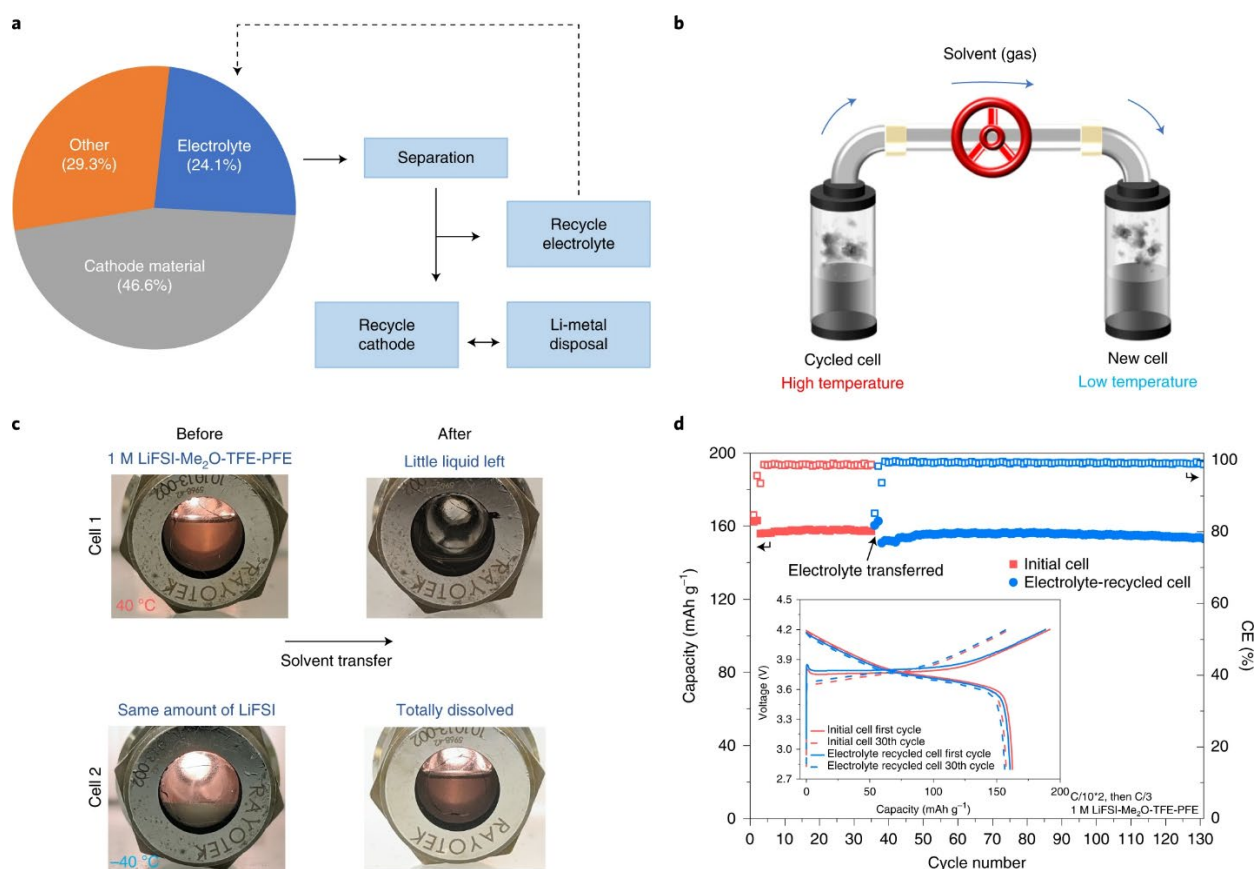
Figure 4.7 Recycling concept and demonstration of liquefied gas electrolytes (a-b) Schematic of potential closed loop direct recycling process and practical process of liquefied gas solvent collection and recycling. (c) Demonstration of solvent transfer. (d) Electrochemical performance comparison of Li/NMC622

To overcome the above issues, a practical LGE recycling process is proposed by using the vapor pressure-temperature relationship in liquefied gas solvents (**Figure 4.7b**). If a temperature difference is generated between two connected containers with a liquefied solvent inside, the solvent will transfer and liquefy in the low-temperature container. This solvent transfer is driven by the pressure gradient generated by the temperature difference. The proposed method is a simple approach to collect and reuse the liquefied gas solvent. Tests using window cells were performed first as a control to directly observe the solvent transport (**Figure 4.7c**). A window cell with 1 M LiFSI-Me$_2$O-TFE was placed in a temperature chamber with a higher temperature (+40 °C, P$_{vapor}$ =143 psi), which was connected to a second window cell with the same amount of LiFSI in a chamber with lower temperature (–40 °C, P$_{vapor}$ = 13.9 psi). Driven by the large pressure difference, most of the solvents in the high-temperature cell were transferred and liquefied in the lower temperature end. This resulted in a well-mixed, new 1 M LiFSI-Me$_2$O-TFE-PFE electrolyte, proving the capability to recycle LGE. Using the same process, the solvent of 1 M LiFSI-Me$_2$O-TFE-PFE in a cycled Li-NMC coin cell was successfully transferred into a newly assembled Li-NMC cell without adding any extra solvent. Notably, the performance for the recycled cell showed nearly identical capacity, efficiency, and a similar voltage profile in comparison to the original cell (**Figure 4.7d**). These results demonstrate the effectiveness of this simple solvent recycling process and is easily integrated to the standard assembling process of liquefied gas cells (**Supplementary Note 6 and Figure 4.35**). With further optimizations, this is a promising process for practical LGE recycling. The successful recycling of dimethyl-ether and hydrofluorocarbons co-solvents in the electrolyte solution not only creates new applications for the by-products synthesized from the conventional petroleum industry, but also endow them with sustainable energy.

4.3 Methods

4.3.1 Materials

Dimethyl ether (99%) was obtained from Sigma-Aldrich. 1,1,1,2-tetrafluoroethane (99%), Pentafluoroethane (99%) and 1,1,1,2,3,3,3-Heptafluoropropane (98%) were purchased from SynQuest Labs. The salts Lithium bis(fluorosulfonyl)imide (LiFSI) (99.9%) and lithium bis(trifluoromethane)sulfonimide (LiTFSI) (99.9%) were purchased from BASF. 1M $LiPF_6$ in EC/EMC 3:7 was obtained from BASF. 1,2-dimethoxyethane (DME, 99.5%) were purchased from Sigma-Aldrich and stored with molecular sieves. The NMC622 (A-C023) was supplied by Argonne national laboratory, which was casted on Al foil, and was heated and rolled before use. 20 μm Li foils were donated from Applied Materials.

4.3.2 Electrochemical measurements

Conductivity of electrolytes was measured in a custom fabricated high-pressure stainless-steel cell setup, with polished stainless-steel (SS 316L) as the electrodes. Calibration of the cell constant was performed by using OAKTON standard conductivity solutions (0.447 to 80 mS cm^{-1}).

Transference number of Li^+ in the electrolyte was measured using potentiostatic polarization method with an applied voltage of 5 mV. The cell setup consisted of two lithium metal foils sandwiched between 500-micron glass fiber separators. Electrochemical impedance spectroscopy (EIS) data was collected by a Biologic SAS (SP-200) system and ZView software was utilized to fit the spectra.

Customized high-pressure SS (316L) cells were used for battery cycling with Arbin battery test station cycler (BT2043). Li metal (FMC Lithium, 1 mm thickness, 3/8-inch diameter, counter electrode) and a polished SS316L (working electrode) with a single 25 μm porous polypropylene separator (Celgard

2075) were used for all the electrochemical tests. Flooded electrolytes with more than 50 g/Ah were added to all cells. The initial stacking pressure is around 200-400 kPa. The testing temperature is at an average 23 °C without specific control.

For the plating and stripping experiments of Li/SS, a discharge current density of 0.5 mA·cm^{-2} was applied until 0 V vs. Li and the voltage was held for 5 hours to form a stable SEI on the current collector. Plating was started after the SEI formation followed by stripping until a 1 V vs. Li cut off voltage. The Coulombic efficiency of the cycling was calculated as the Li stripping capacity divided by the Li plating capacity during each cycle. For the test in different temperatures, the cells were soaked at the testing temperature in a temperature chamber (Espec) for several hours before cycling. Two activation cycles using C/10 rate at room temperature was performed for Li/NMC cells and then cycled at a selected rate and temperature.

4.3.3 Material characterization

The pressure measurements of different pure gases or formulated LGE are performed in a Honeywell FP5000 pressure sensor from –40 to +60°C.

Lithium metal soak tests are performed in a custom-built SS cell withstanding up to 2000 psi. All Lithium are soaked in the corresponding electrolytes for half months. The optical images were taken after dissembling the soak cells.

Fire extinguishing experiments are conducted in a fume hood with the following fixed parameters: gas flow at 150 standard cubic centimeters per minute (SCCM), relative height and distance of safety cell and candle, and an open system within the fume hood (**Figure 4.14**). The experiments are set up with a safety cell connected to a mass flow controller (MFC) and a stainless-steel tube with a valve for precise control of the gas flow. The cell serves to isolate the gas tanks from the ignited candle for a safe operating environment. A constant gas flow is maintained by the MFC while the relative height and distance between

the cell and candle are fixed with two utility clamps. Subsequently, various different gas types are utilized in this experimental setup to demonstrate their fire extinguishing efficacy.

Renishaw inVia confocal Raman microscope was used for obtaining the Raman spectra of the liquified gas electrolytes, with a green laser of excitation wavelength 532nm. Si (520nm) was employed to calibrate all spectra with subsequent analysis performed through Wire 3.4 software developed by Renishaw Ltd.

The surface and cross-section morphology of the deposited lithium was observed by a FEI Scios Dual Beam FIB/SEM. The operating voltage and emission current of the electron beam were 5 kV and 0.1 nA. A gallium ion beam source was used to mill the sample. The operating voltage of the ion beam source was 30 kV. Different emission currents of ion beam were chosen for different purposes, i.e. 5 nA for pattern milling, 10 pA for imaging by ion beam and 0.3 nA for cross-section cleaning. During ion beam milling, the stage temperature was maintained at -175 °C to prevent beam damage on the Li metal sample.

The cryo-TEM samples were prepared by electrochemically depositing Li onto TEM grids in the Li∥Cu cells. The cells were tested at a current density of 2mA cm^{-2} to plate Li for 5min. After Li deposition, the TEM sample grids were lightly rinsed with DME to remove trace Li salts in an Ar-filled glove box. Once dried under vacuum, the sample grids were sealed in airtight bags before being transferred to the TEM facility. The sample grids were mounted onto a TEM cryo-holder (Gatan) via a cryotransfer station. In short, the whole TEM sample preparation and transfer process prevented any air exposure to the Li metal at room temperature. TEM characterizations were carried out on JEM-2100F at 200 kV. High-resolution TEM images were taken at a magnification of ×300K with a Gatan OneView Camera (full 4K×4K resolution) when the temperature of the samples reached about 100K. Fast Fourier transform patterns were analyzed using Digital Micrograph software.

X-Ray photoelectron spectroscopy (XPS) samples were prepared by electrochemically cycling in Li‖Cu cells. The cells were tested at a current density of 1 mA cm^{-1} and a capacity of 1 mAh cm^{-1} over 50 cycles. Then, the deposited Li samples on Cu side were lightly washed by DME solvent to remove trace Li salts in an Ar-filled glovebox and dried inside glovebox antechamber. To avoid moisture and air exposure, sealed samples were transferred to the XPS chamber directly from a nitrogen-filled glovebox via vacuum transfer. Then experiments were performed using a Kratos AXIS Supra DLD XPS with monochromatized Al Kα radiation (λ= 0.83 nm and hυ=1486.7 eV) under a base pressure <10^{-8} Pa. CasaXPS software was utilized to perform the XPS analysis, which all spectra were calibrated with hydrocarbon C 1s (284.6 eV).   The etching condition is set as Ar500+ cluster at 5 keV. The etching time are 60s, 60s and 180s.

4.3.4 Simulations

HOMO and LUMO energies were obtained from Density Functional Theory (DFT) calculations performed in Q-Chem 5.2. Single molecules were assembled and subjected to gas-phase DFT geometry optimization using the 6-31+G* basis set from Pople and coworkers[94] and the B3LYP[95] functional, a well-balanced level of theory providing a reasonable compromise between speed and accuracy. To obtain the final orbital energies, single point energy calculations were performed on the molecules post optimization at the B3LYP//6-311++G** level of theory.

Molecular dynamics (MD) simulations were performed using a revised many-body polarizable APPLE&P force field (FF) that utilized atomic induced dipoles to describe polarization[96-97]. A complete set of force field parameters, connectivity files and MD simulation code are provided as an archive file in Supporting Information. We evaluated ability of the force field to describe the gas-phase binding energies of the Li$^+$ cation to Me$_2$O, TFE and PFE solvents obtained from quantum chemistry (QC) calculations as shown in **Figure 4.16**. Basis set superposition error (BSSE) correction was applied to all Møller–Plesset

perturbation theory of second order (MP2) by using aug-cc-pvTz (abbreviated as Tz) basis set. Binding energies from MD using FF are in good agreement with MP2/Tz and composite G4MP2 results, accurately describing the order of the Li-solvent binding.

MD simulation cells of 1 M LiFSI-Me$_2$O contained 100 LiFSI and 1292 Me$_2$O, while 1 M LiFSI-Me$_2$O-TFE-PFE simulation cells contained 100 LiFSI, 136 Me$_2$O, 946 TFE, 115 PFE. Simulation times, densities, transport and structural properties are summarized in **Supplementary Tables 3-4**. Multiple replicas were simulated at a select temperature to estimate error bars. Simulations were performed in constant volume – temperature (NVT) ensemble using Nose – Hover thermostat. Multiple timestep integration was employed with timestep of 0.5 fs for bonded interactions, time step of 1.5 fs for all non-bonded interactions within a truncation distance of 8.0 Å. and an outer timestep of 3.0 fs for all non-bonded interactions between 8.0 Å and the nonbonded truncation distance of 14 Å. Because the heterogeneous structure of electrolyte with large ionic aggregates surrounded by the relatively low-density solvent, a number of additional simulations were performed with a shorter nonbonded truncation distance of 12 Å instead of 14 Å to ensure that predicted properties are not influenced by the choice truncation distance as shown **Supplementary Table 3**. The Ewald summation method was used for the electrostatic interactions between permanent charges with permanent charges or induced dipole moments with $k = 8^3$ vectors. The reciprocal part of Ewald was calculated every 3.0 fs. Induced dipoles were found self-consistently with the convergence criteria of 10^{-9} (electron charge $*$ Å)^2.

Despite fast solvent and ion diffusion, the residence times of Li$^+$ near Me$_2$O solvent and FSI$^-$ are rather long, 7ns and 10 ns, respectively, at 0 °C for 1 M LiFSI-Me$_2$O-TFE-PFE electrolyte compared to 0.5ns and 2.7 ns for 1 M LiFSI-Me$_2$O at 0 °C. The increased residence time for Li-Me$_2$O in 1 M LiFSI-Me$_2$O-TFE-PFE compared to 1 M LiFSI-Me$_2$O electrolyte is attributed to the formation of a much longer aggregates and lack of "free" Me$_2$O that is needed for an efficient exchange of the "complexed" Me$_2$O

with the "free" Me_2O. The Li-FSI residence time is the slowest relaxation time scale in both electrolytes and requires MD simulations to be longer by a factor of 5-10 than the relaxation time in order to properly average the Li^+ environments and obtain an accurate estimate for the degree of ion dynamic correlation that is often call ionicity as shown in **Figure 4.23**.

4.4 Supplementary Information

Supplementary Note 1

Clean Agent FS 49 C2 (Figure 4.8) is a clean fire extinguishing gas mixture that effectively suppresses fires while sustaining breathable concentrations of oxygen in the air. Furthermore, it is environmentally friendly with components of TFE and PFE characterized by an Ozone Depletion Potential (ODP) of 0.

Supplementary Note 2

A series of salt solubility tests were performed to check the salt dissolution in different solvents or their mixtures (Figure 4.10). 1 M LiTFSI/LiFSI can immediately dissolve in Me_2O. When mixed with TFE, both LiTFSI and LiFSI can formulate a solution with a maximum 1:1.7 Salt: Me_2O ratio. When switched to PFE or 1,1,1,2,3,3,3-Heptafluoropropane (HFP), LiFSI systems will observe phase separations. By comparison, LiTFSI can obtain a well dissolved solution with a maximum 1:1 Salt: Me_2O ratio. This can be explained by the lower bond dissociation energy of LiTFSI over LiFSI, which makes LiTFSI more dissolvable. Interestingly, these principles are verified for LiTFSI in pure PFE and HFP system. Both of them can dissolve less than 0.1 M LiTFSI, however, they cannot well mix with LiFSI. TFE can dissolve less than 0.1 M LiTFSI or LiFSI.

Supplementary Note 3

The $LiPF_6$-based analog of LGE was investigated by measuring salt solubility, Li metal corrosion, ionic conductivity, Li metal anode cycling performance (Figure 4.12 and 4.13). Figure 4.12, shows that a lower

Salt: Me$_2$O ratio of 1:2 (vs. Salt: Me$_2$O ratio of 1:1.5 for the LiFSI-based LGE) is required to fully dissolve 1 M LiPF$_6$ in the same mixture of Me$_2$O with TFE:PFE 7:1 volume ratio. There is no salt precipitation observed at –78 and 60 °C (Figure 4.12a-d). Besides, the formulated LiPF$_6$-based LGE electrolyte maintains good stability with Li metal after soaking for half a month and more than 3 mS cm^{-1} conductivity over wide-temperature range (Figure 4.12e-f). However, during Li metal plating and stripping (Figure 4.13a-b), cells deliver poor cycling stability at standard 0.5 mA cm^{-2}, 1 mAh cm^{-2} and higher current density at 3 mA cm^{-2}, 3 mAh cm^{-2}. This inferior cycling of the LiPF$_6$-based LGE is largely attributed to the less robust SEI.

Supplementary Note 4

Methodology for extracting transport properties from MD simulations follows previous work[98], and is described below for completeness. Solvent and ion self-diffusion coefficients were extracted using the Einstein relation from linear fits to mean-square displacements divided by six. Due to the finite size of the simulation cells, long range hydrodynamic interactions restrict the diffusion and generally slows the ion diffusion. The leading order finite size correction (FSC) to the self-diffusion coefficient is given by Eq. S1,

$$\Delta D^{FSC} = \frac{2.837 k_B T}{6 \pi \eta L}$$

(S1)

where k_B is the Boltzmann constant, T is temperature, L is a linear dimension of the simulation periodic cell and η is viscosity. Solvent and ion diffusion coefficients were corrected for the finite size using eq. S1. Viscosity was calculated using the Einstein relation including both diagonal and non-diagonal elements to enhance the statistics using eqs S2-S4:

$$\eta = \lim_{t \to \infty} \eta(t) = \lim_{t \to \infty} \frac{V}{20 k_B T t} \left(\left\langle \sum_{\alpha,\beta} \left(L_{\alpha\beta}(t) - L_{\alpha\beta}(0) \right)^2 \right\rangle \right) \text{(S2)}$$

$$L_{\alpha\beta}(t) = \int_0^t P_{\alpha\beta}(t')\,dt' \quad (S3)$$

where k_B is the Boltzmann constant, T is temperature, t is time, V is the volume of the simulation box, P_{ab} is the stress sensor given by:

$$P_{\alpha\beta} = \frac{\sigma_{\alpha\beta} + \sigma_{\beta\alpha}}{2} - \frac{\delta_{\alpha\beta}}{3} tr(\sigma) \quad (S4)$$

where σ_{ab} is the stress tensor with $\delta_{ab} = 1$ for $\alpha = \beta$ and $\delta_{ab} = 0$ for $\alpha \neq \beta$. The dynamic degree of ion uncorrelated motion (α_d) was calculated eqs. 5-S7:

$$\alpha_d = \frac{\kappa}{\kappa_{uncorr.}} \quad (S5)$$

$$\kappa_{uncorr} = \frac{e^2}{Vk_BT}(n_+ D_+ + n_- D_-) \quad (S6)$$

$$\kappa = \lim_{t \to \infty} \frac{e^2}{6tVk_BT} \sum_{i,j}^N z_i z_j < ([\mathbf{R}_i(t) - \mathbf{R}_i(0)])([\mathbf{R}_j(t) - \mathbf{R}_j(0)]) > \quad (S7)$$

where e is the electron charge, V is the volume of the sample, k_B is Boltzmann's constant, T is the temperature and n_+ and n_- are the number of cations and anions, respectively. κ_{uncorr} is the "ideal" conductivity that would be realized if ion motion were uncorrelated. The degree of ion uncorrelated motion (α_d) was extracted from the plateau that is reached around 3-6 ns following discussion in the previous work.

Supplementary Note 5

Li metal soak tests were performed to check the compatibility of liquefied gas solvents and electrolytes (Figure 4.25). After soaking Li metal for half month, the Li metals in TFE or PFE maintained their shape but decolored, indicating incompatibility with Li metal. The compatibility for Me_2O is improved in

comparison to TFE and PFE. For the 1 M LiFSI-Me$_2$O, 1 M LiFSI-Me$_2$O-TFE and 1 M LiFSI-Me$_2$O-TFE-PFE electrolytes, the Li metals retained a clean and shinning appearance due to the stable interface.

Supplementary Note 6

For a typical LGE cell fabrication, the details are demonstrated below:

1. The Li metal, separators and electrodes are assembled and fixed between two high-density polyethylene (HDPE) parts with SS316 centers, as shown in the Figure 4.35a.

2. HDPE parts are kept in position using two SS316 screws, and the stacking pressure is adjusted by tightening the screws.

3. The stacked setup is then placed in a stainless-steel cell, in which the salts/liquid and co-solvents are pre-loaded inside the cells. Then the cell is sealed before removing from Ar-filled glovebox.

4. After removing from glovebox, the LGE cells are connected to a gas filling system which is accurately controlled by mass flow controllers (MFC) and pressure sensors (Figure 4.35b).

5. Before filling, gas supply lines are vacuumed to remove the remaining gas from the previous fillings and the pressure sensors are actively monitoring any potential pressure changes in order to get rid of any leakages.

6. After leakage checking, cells to be filled are soaked in a temperature chamber set at certain low temperatures (such as –20 ~ –60°C) for certain amount of time to generate enough vapor pressure difference for filling.

7. After turning on the valves of the cell and the gas tank, the solvent will transfer from the gas tank through MFC to the cell soaked at lower temperature and liquifies inside. During filling, MFC calculates

the amount of gas transferred. Once reaching the target mass of gases, MFC is automatically shut down and pressure sensors stop recording.

8. After that, filled cells are disconnected from gas supply lines and ready for electrochemical testing after warmup.

This is a detailed process of how to fabricate the LGE cell at a lab-scale. Figure 4.35b shows a commercialized gas filling system which can support 10-20 LGE cells assembling simultaneously from South 8 Technologies, Inc. With the expansion of the current system, it is possible to manufacture LGE cell in large quantities.

Component	Composition (%)
TFE	60-80
PFE	10-30
CO_2	10-30

Figure 4.8 The compositions of clean agent of FS 49 C2[99]
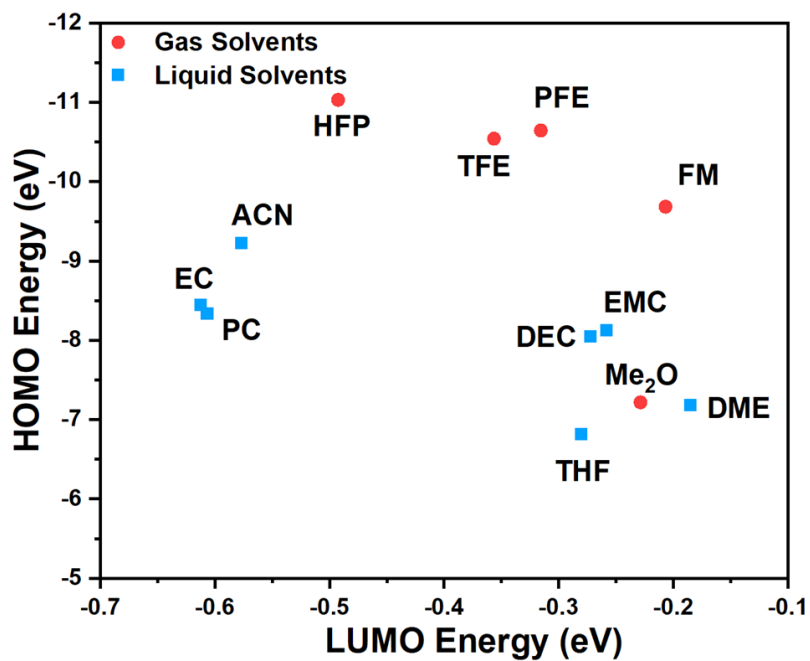
Figure 4.9 Calculated LUMO and HOMO energy of different individual solvents

Mixed(M)
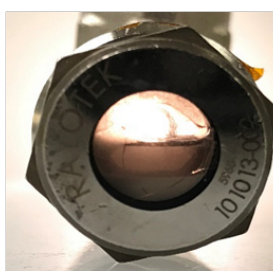
Salt Precipitation(P)
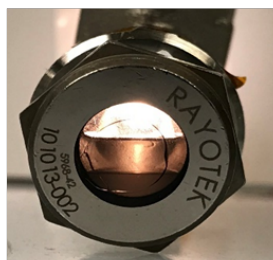
Phase Separation(S)

	1 M LiTFSI	1 M LiFSI
Me$_2$O	M	M

In TFE		
LiTFSI	Li$^+$:Me$_2$O: 1:1.5	Li$^+$:Me$_2$O: 1:1.7
1 M	P	M
LiFSI	Li$^+$:Me$_2$O: 1:1.5	Li$^+$:Me$_2$O: 1:1.7
1 M	P	M

In PFE		
LiTFSI	Li$^+$:Me$_2$O: 1:1	Li$^+$:Me$_2$O: 1:1.5
1 M	M	M
LiFSI	Li$^+$:Me$_2$O: 1:1	Li$^+$:Me$_2$O: 1:1.5
1 M	S	S

In HFP		
LiTFSI	Li$^+$:Me$_2$O: 1:1	Li$^+$:Me$_2$O: 1:1.5
1 M	M	M
LiFSI	Li$^+$:Me$_2$O: 1:1	Li$^+$:Me$_2$O: 1:1.5
1 M	S	S

	LiTFSI	LiFSI
TFE	< 0.1 M	< 0.1 M
PFE	< 0.1 M	P
HFP	< 0.1 M	P

Figure 4.10 Solubility of electrolytes for various LiFSI/LiTFSI (Li$^+$) salt: Me$_2$O ratios in TFE/PFE/HFP diluents at +23 ºC and solubility of electrolytes for LiFSI/LiTFSI in pure Me$_2$O/TFE/PFE/HFP solvents. "M" denotes mixed, "P" denotes salt precipitation, "S" denotes phase separation
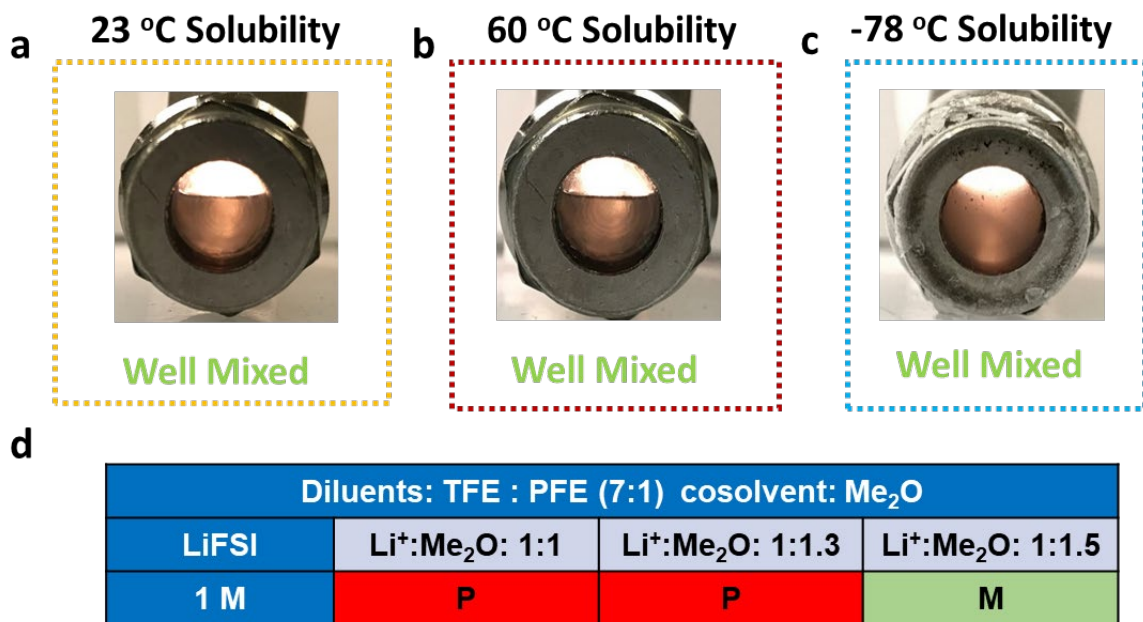
Figure 4.11 Solubility test on 1 M LiFSI-Me$_2$O-TFE-PFE at different temperatures (a) +23 ^{o}C (b) +60 ^{o}C and (c) –78 ^{o}C. (d) Solubility of electrolyte for various LiFSI (Li$^+$) salt: Me$_2$O ratios at 23 ^{o}C, "P" denotes salt precipitation, "M" denotes well-mixed
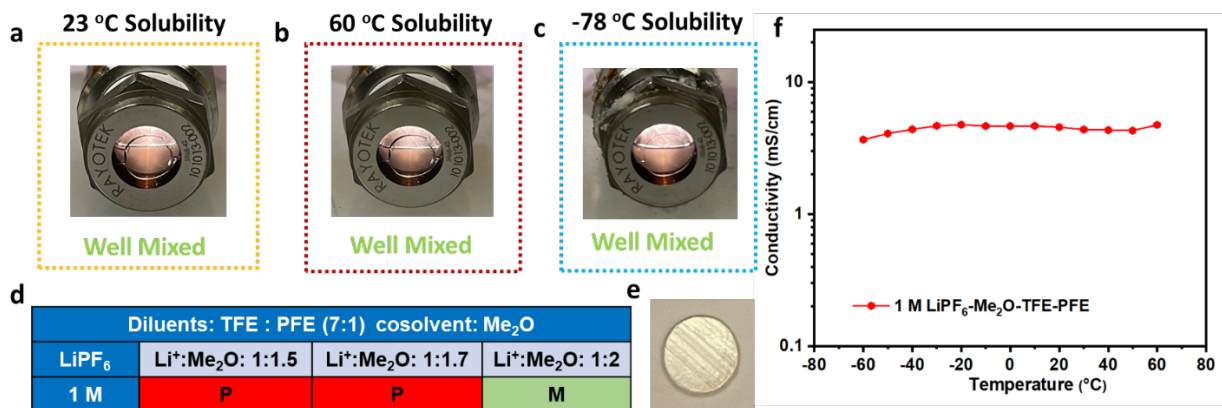
Figure 4.12 Solubility test on 1 M LiPF$_6$-Me$_2$O-TFE-PFE at different temperatures (a) +23 ^{o}C (b) +60 ^{o}C and (c) –78 ^{o}C. (d) Solubility of electrolyte for various LiPF$_6$ (Li$^+$) salt: Me$_2$O ratios at +23 ^{o}C, "P" denotes salt precipitation, "M" denotes well-mixed (e) Li metal soaked in formulated electrolyte for half months (f) Measured ionic conductivities of LiPF$_6$-based electrolyte
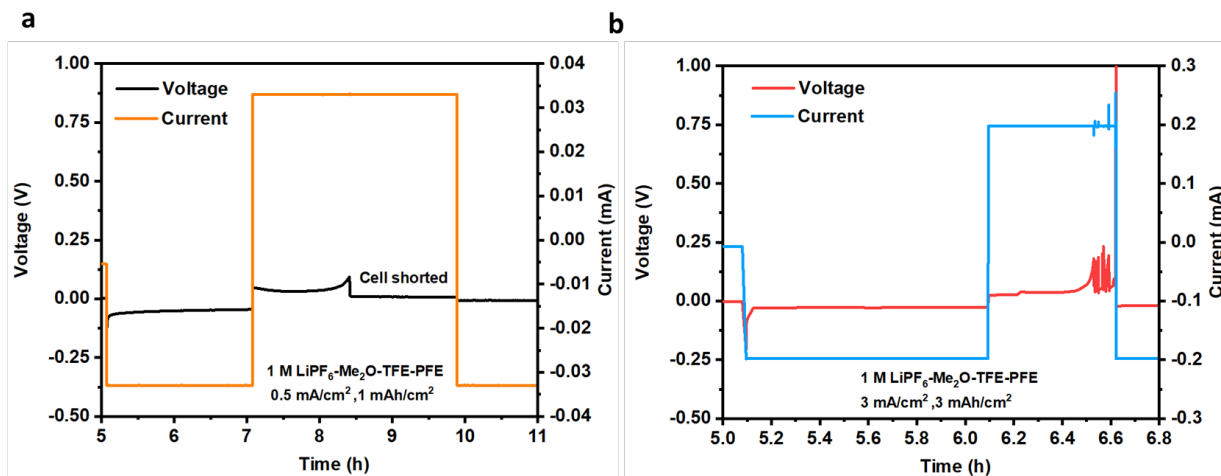
Figure 4.13 Li metal plating and stripping in electrolyte using LiPF$_6$ salt at 0.5 mA cm^{-2}, 1 mAh cm^{-2} (a) and 3 mA cm^{-2}, 3 mAh cm^{-2} (b)
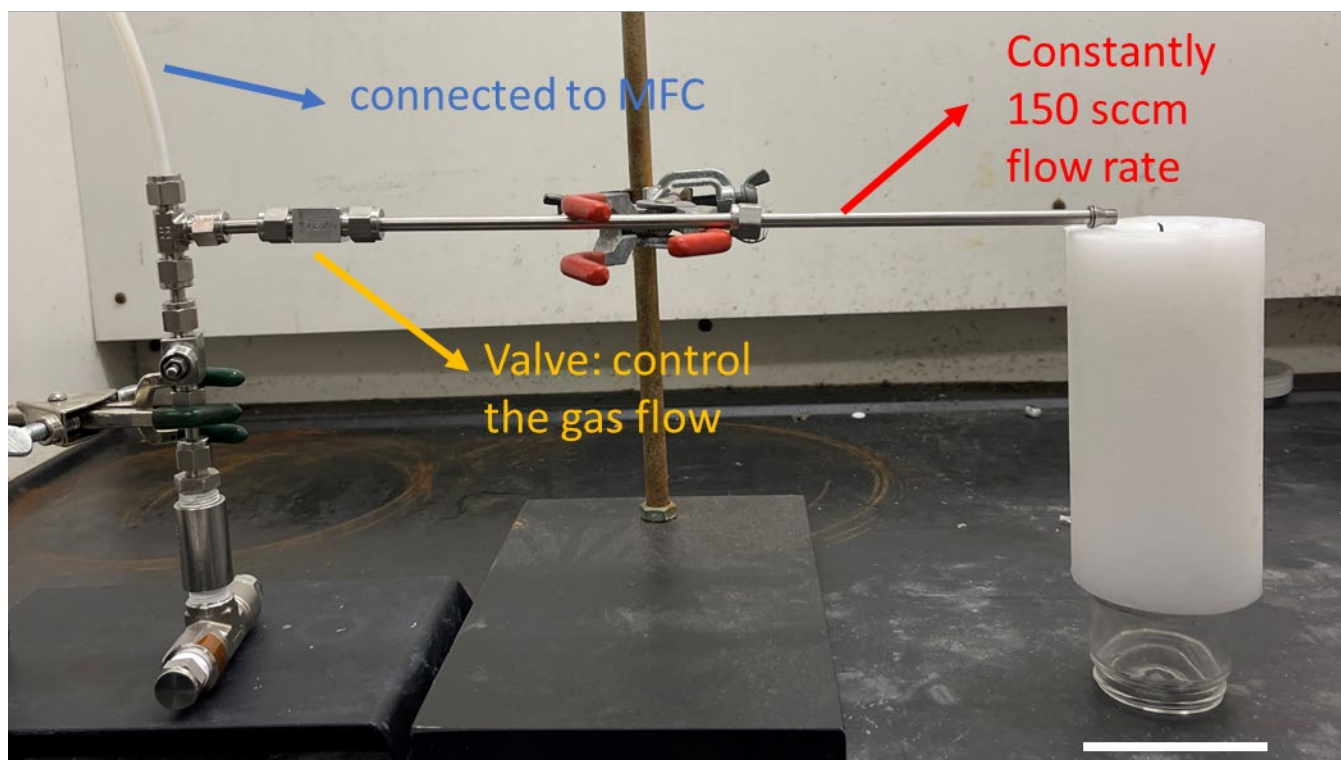
Figure 4.14 Device setup for candle tests. The flow rate is controlled by mass flow control (MFC) at a fixed 150 sccm for different gases. The scale bar is 8 cm.
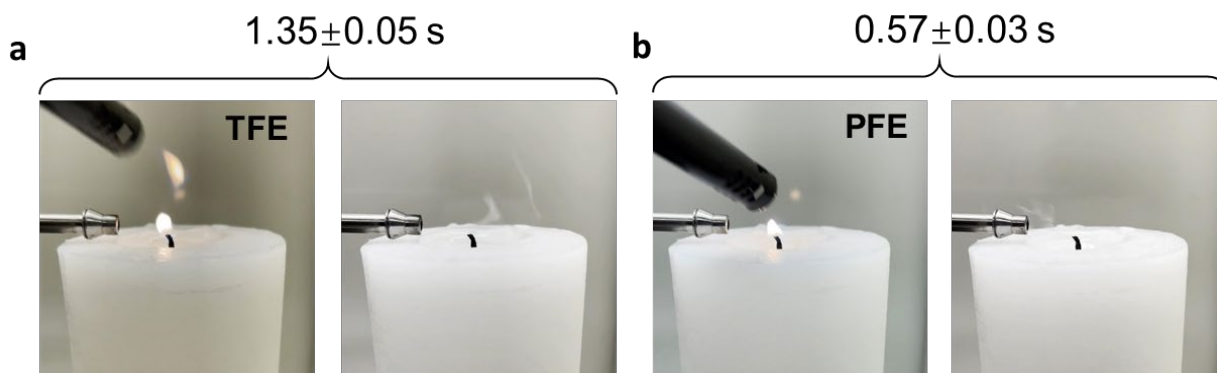
Figure 4.15 Fire douse tests of different pure gases demonstrated by ignited candles with extinguishing times (a) TFE, 1.35±0.05 s and (b) PFE, 0.57±0.03 s
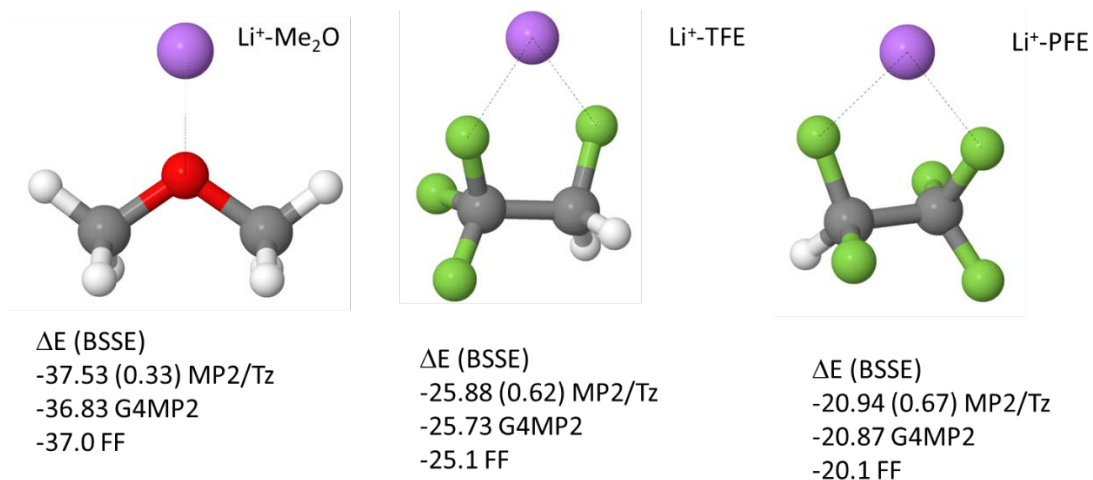
Figure 4.16 Binding energy of Li^+ to solvents (ΔE, in kcal mol^{-1}) from QC and FF, basis set superposition error (BSSE). Color: Li^+, purple; C, grey; O, red; H, white; F, green.
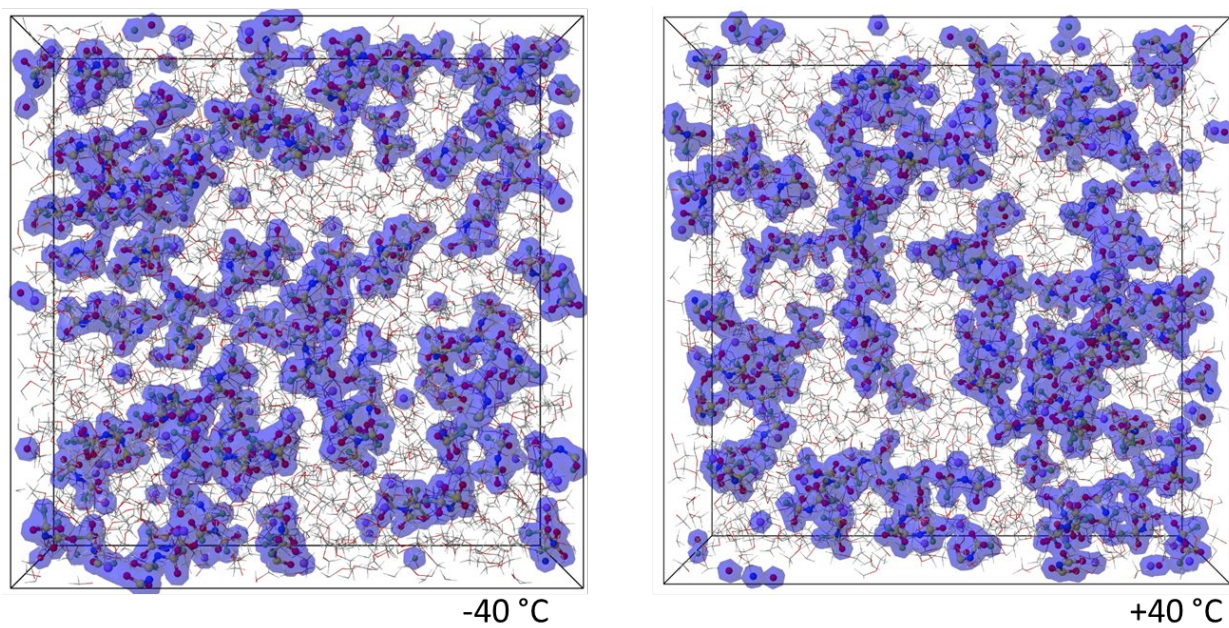
Figure 4.17 Snapshots of the MD simulation cells containing 1 M LiFSI-Me$_2$O. Blue isosurfaces highlight the locations of Li and FSI$^-$
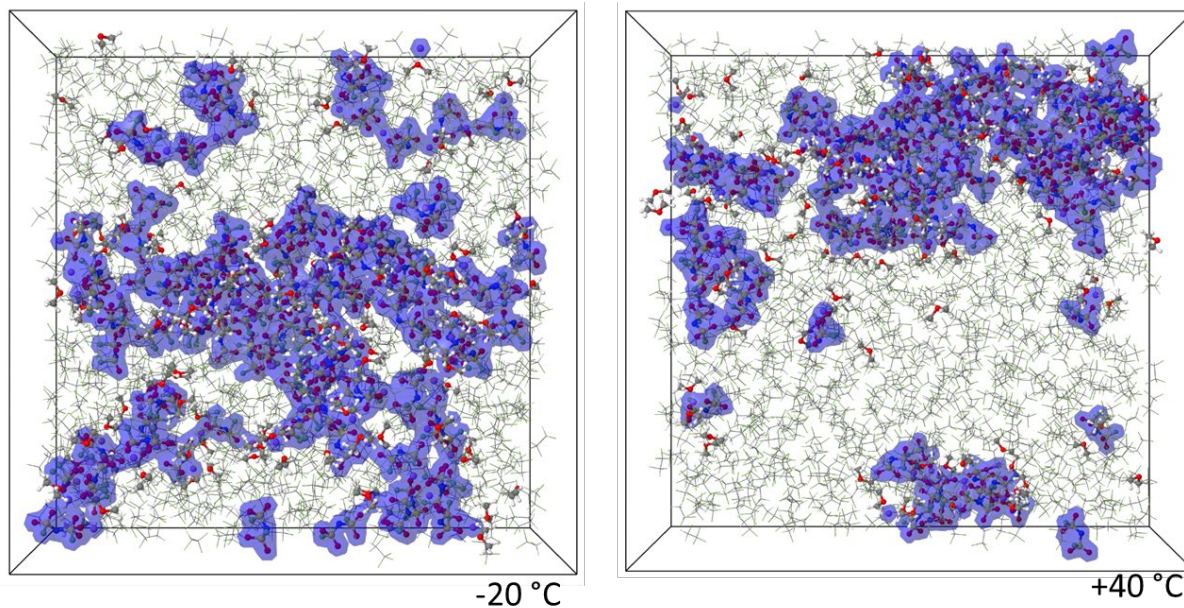
Figure 4.18 Snapshots of the MD simulation cell containing 1M LiFSI in Me$_2$O-TFE-PFE. Blue isosurfaces highlight the locations of Li and FSI$^-$
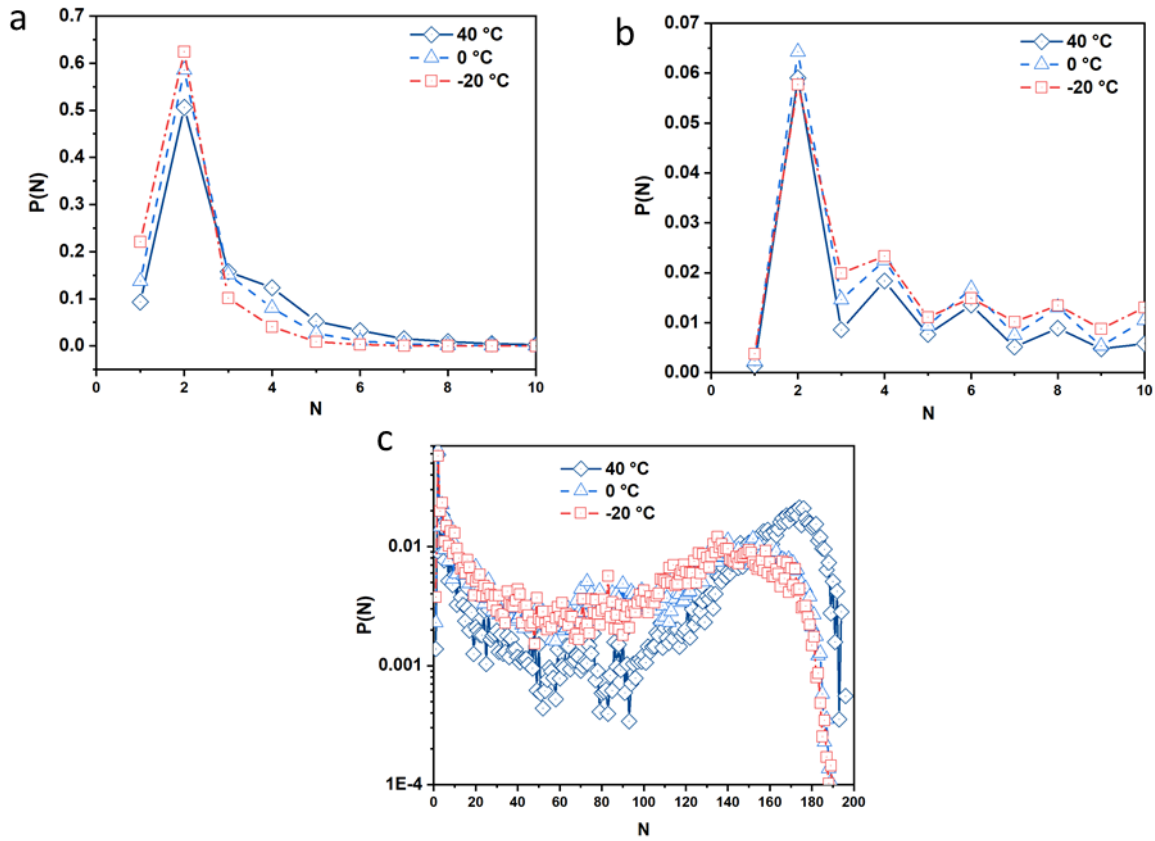
Figure 4.19 Probability of an ion to belong to an aggregate of size N for 1M LiFSI in Me$_2$O (a) and 1M LiFSI in Me$_2$O-TFE-PFE (b-c). Note (c) shows the distribution using a semi-log scale. There are 200 ions in a simulation box
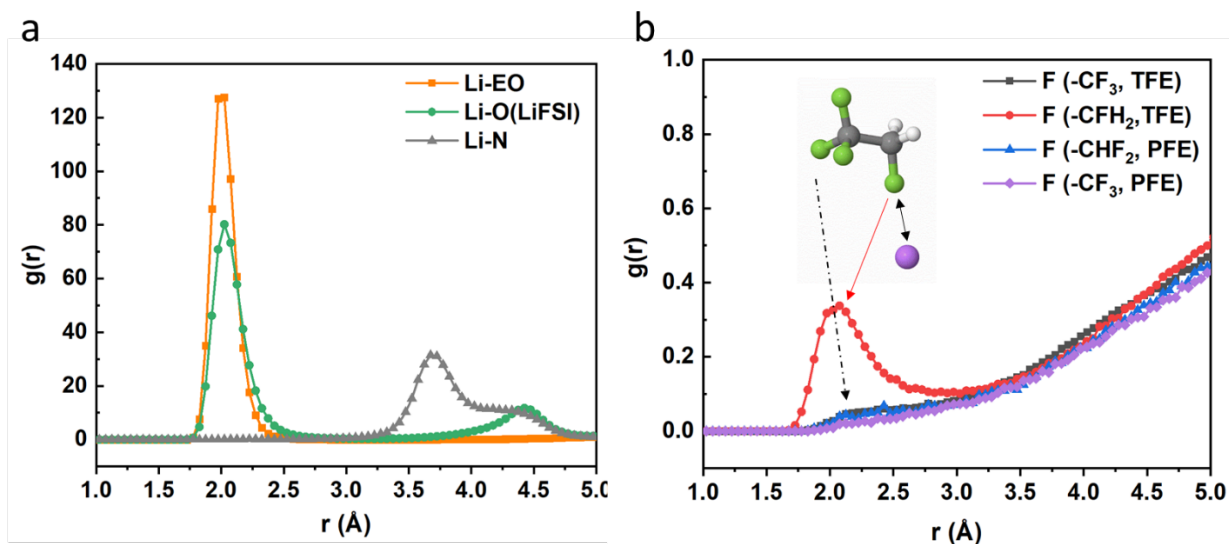
Figure 4.20 (a) Radial distribution functions (RDFs) for the Li$^+$ cations with oxygen of Me$_2$O and LiFSI, nitrogen of LiFSI. (b) Fluorine of –CF$_3$, -CFH$_2$ from TFE and –CHF$_3$, -CF$_3$ from PFE in the simulations for 0 °C. Color: Li, purple; C, grey; H, white; F, green.
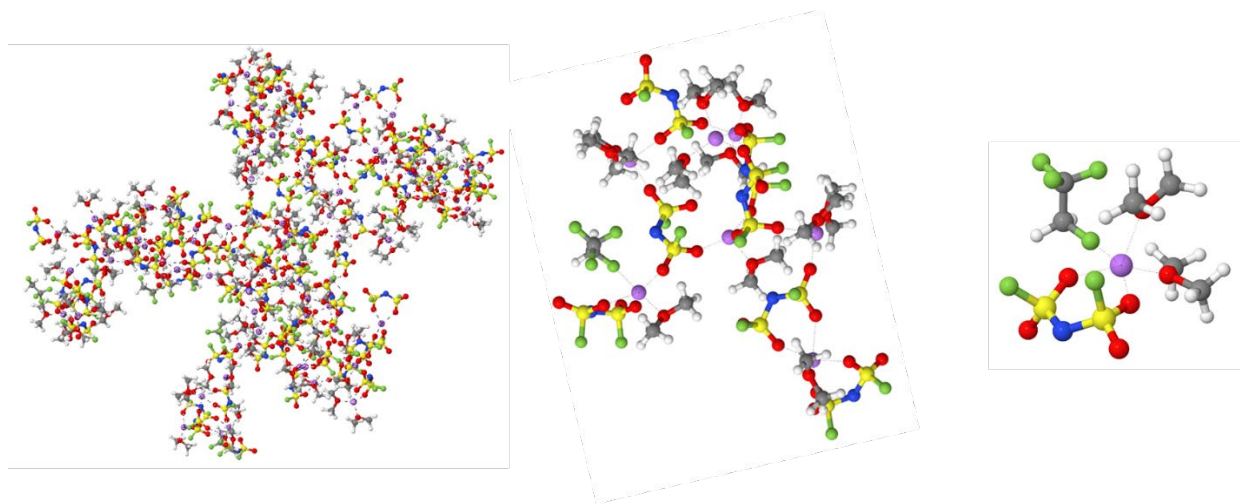
Figure 4.21 The representative Li$^+$ solvates observed in MD simulations of 1 M LiFSI-Me$_2$O-TFE-PFE at 0 °C. Color: Li, purple; C, grey; O, red; H, white; F, green; N, navy; S, light yellow.
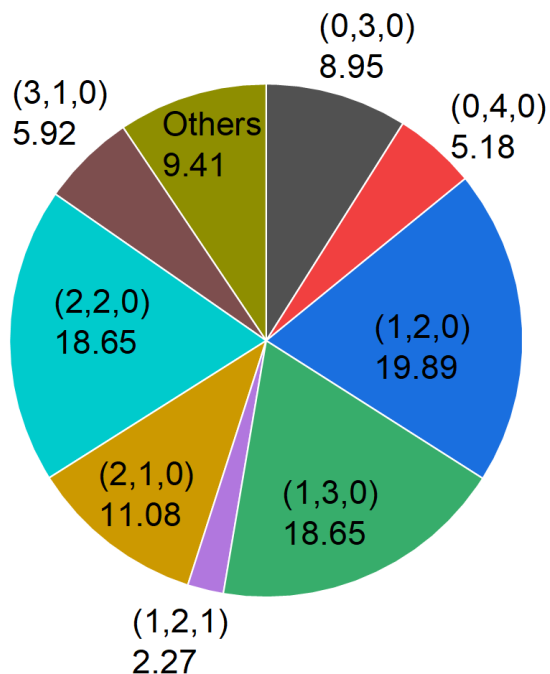
Figure 4.22 Probability of the most probable Li^+ solvates (in %) for triads (EO of Me_2O, FSI, F (from TFE) for 1M LiFSI-Me_2O-TFE-PFE from MD simulations at 273 K. Only solvates with populations more than 2% are shown
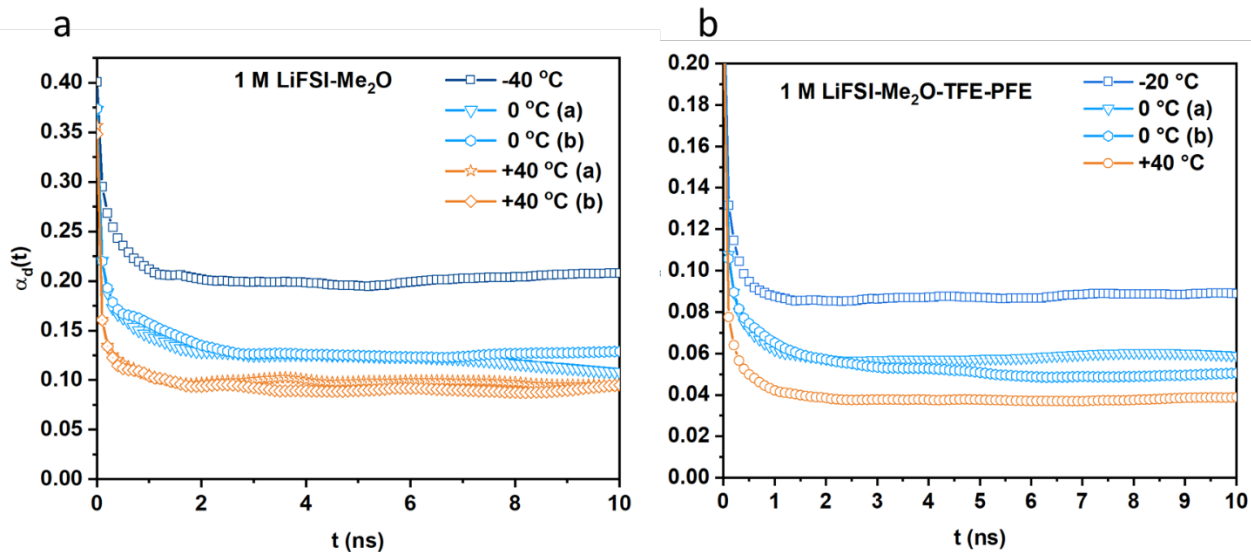
Figure 4.23 Ionicity $a_d(t)$ vs. MD simulation time for 1 M LiFSI-Me_2O (a) and for 1 M LiFSI-Me_2O-TFE-PFE (b) at three temperatures. Two independent replicas were simulated for 1 M LiFSI-Me_2O at 0°C and +40 °C and at 0 °C for 1 M LiFSI-Me_2O-TFE-PFE denoted as (a) and (b)
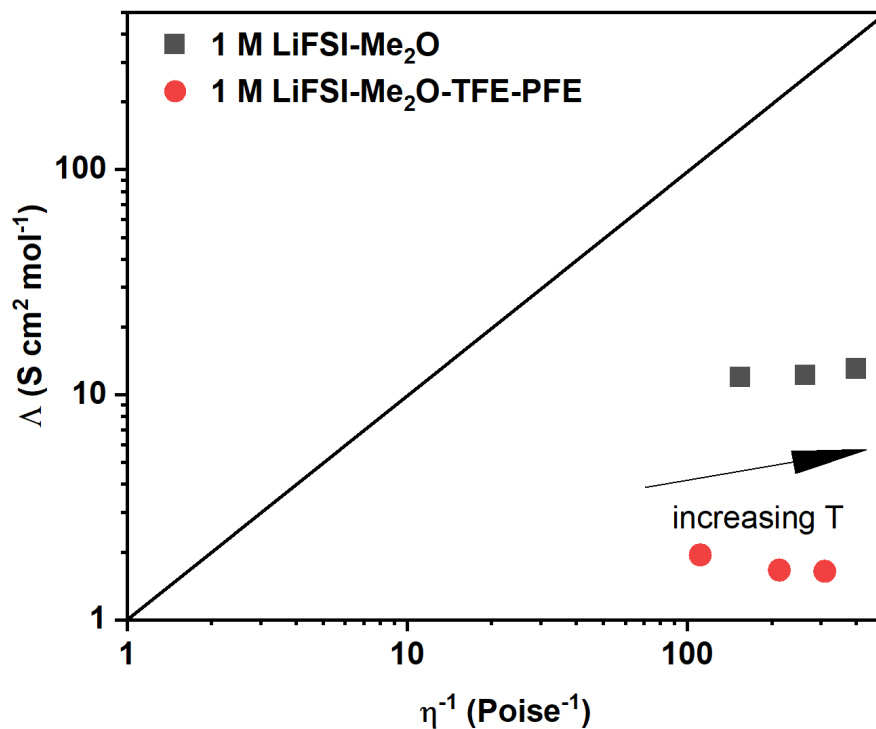
Figure 4.24 Walden plot for electrolytes at –40, 0 and +40 ºC from MD simulations
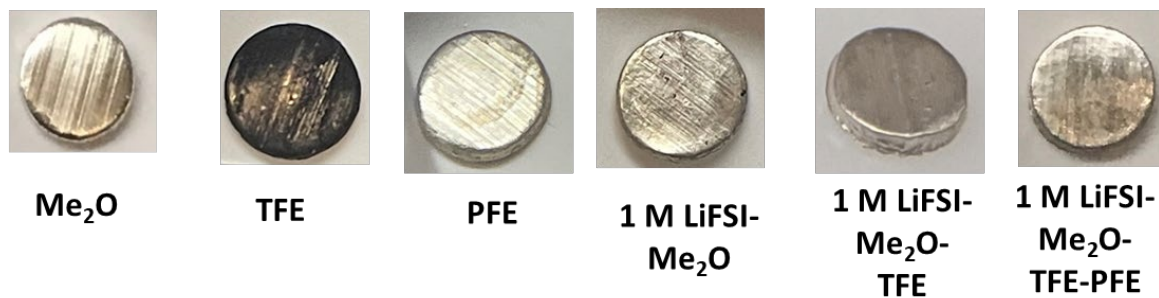
Figure 4.25 Optical images of lithium metals soaked in liquefied gas solvents and electrolytes for 14 days
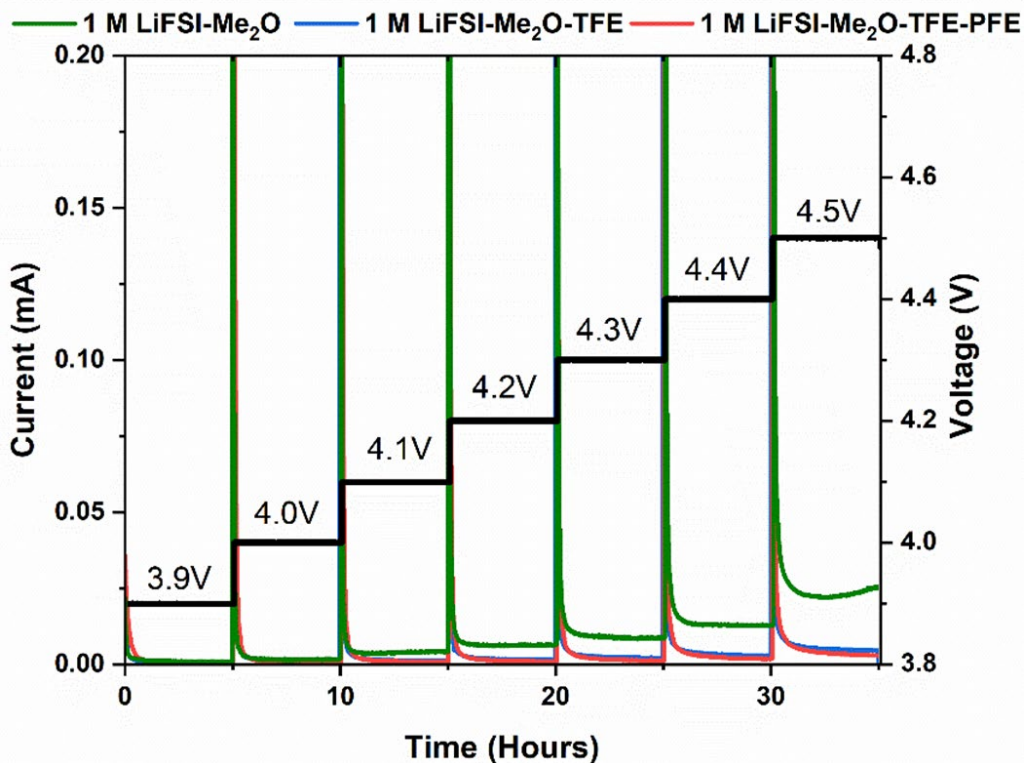
Figure 4.26 Li-NMC622 voltage hold test in the liquefied gas electrolytes.
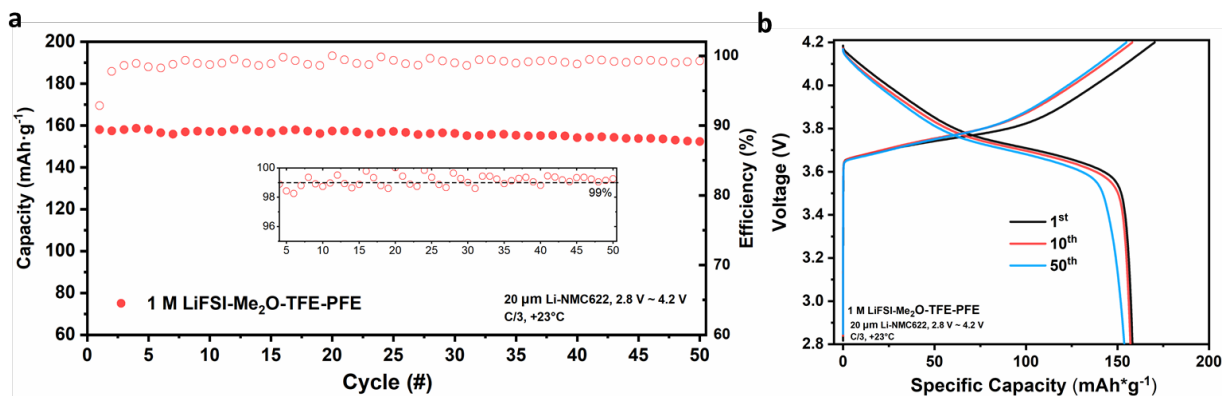
Figure 4.27 20 µm Li/NMC cycling over 50 cycles under C/3 rate at room temperature (a). Detailed voltage plateau at specific cycles (b)
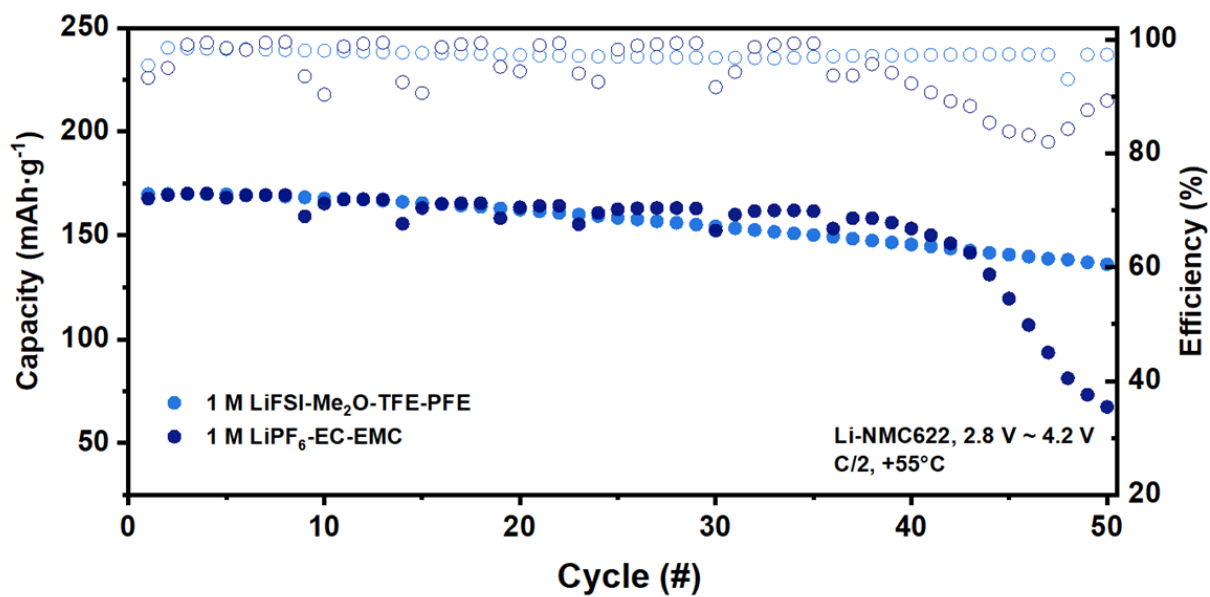
Figure 4.28 Li/NMC cycling over 50 cycles at +55 °C
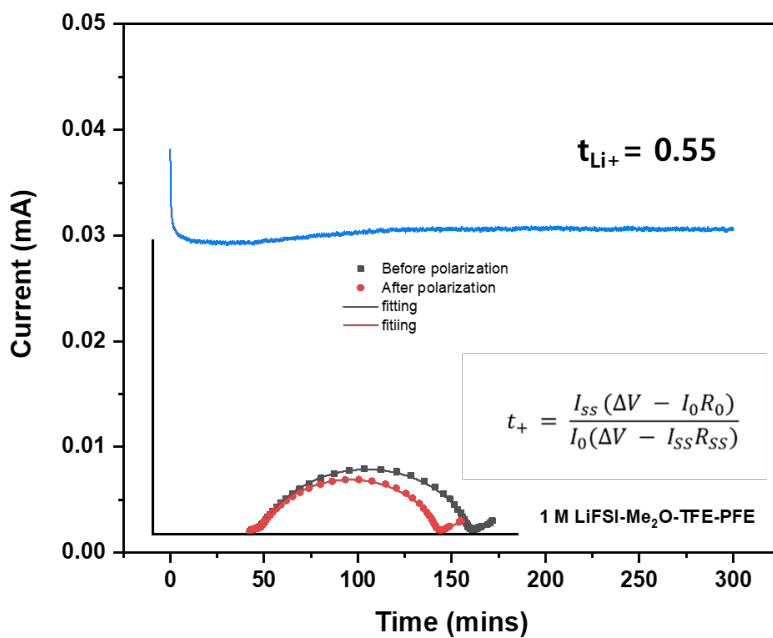
Figure 4.29 Transference number measurement of designed electrolyte
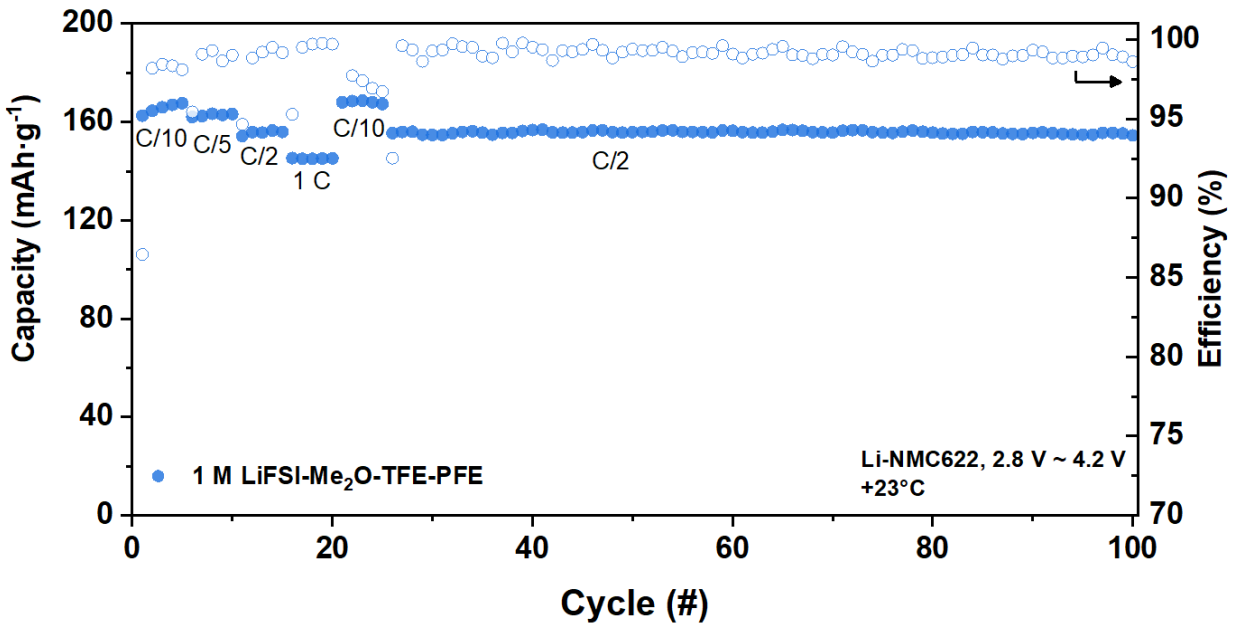
Figure 4.30 Li/NMC cycling at different current rate
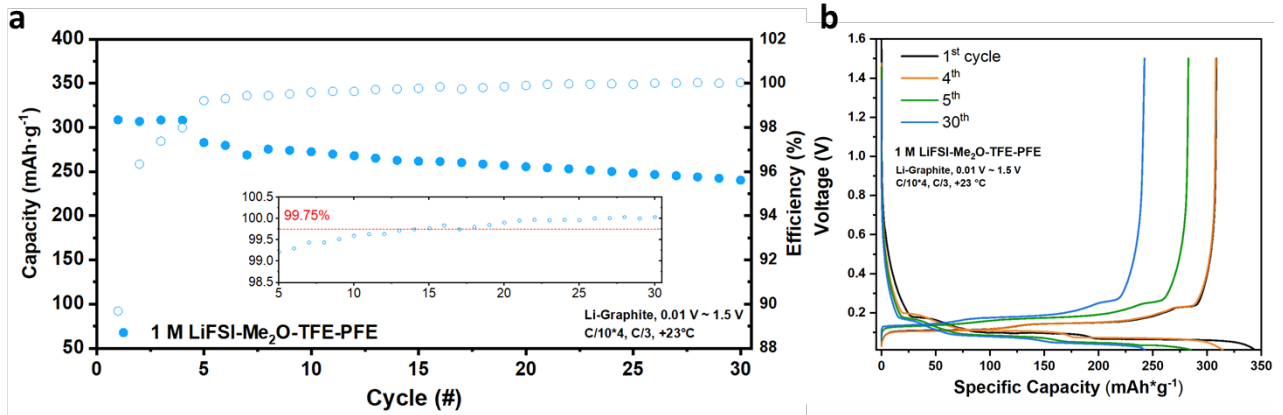
Figure 4.31 Li/graphite half-cell cycling (a). Detailed voltage plateau at specific cycles (b)
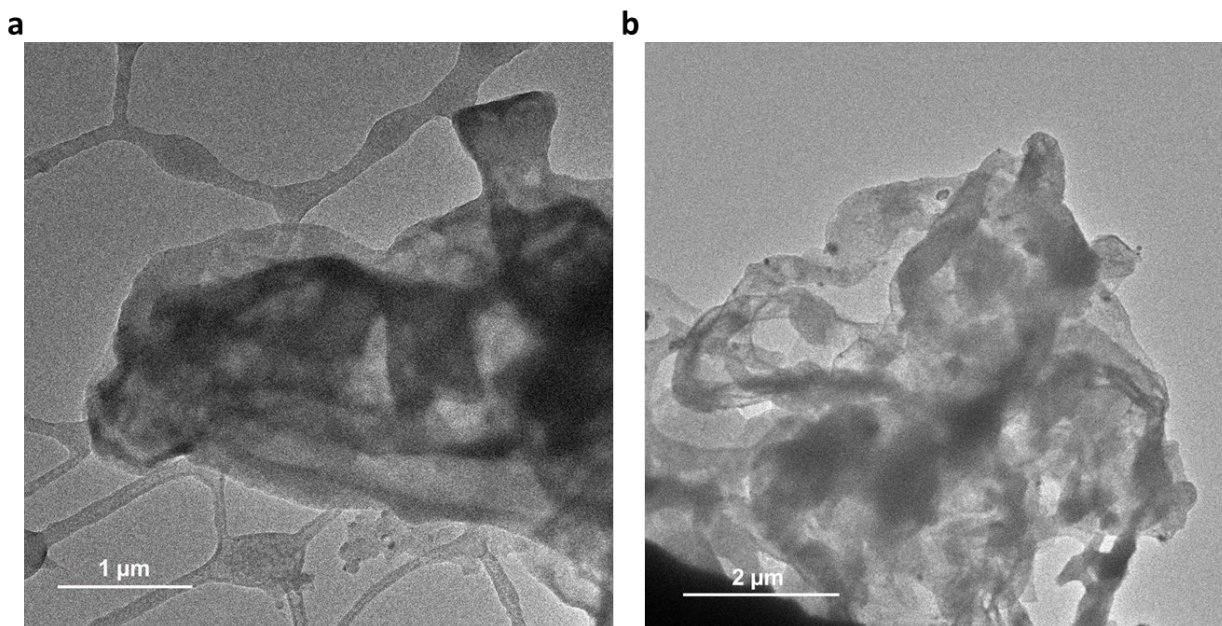
Figure 4.32 Cryo-TEM images of the deposited Li by 1 M LiFSI-DME (a) and 1 M LiFSI-Me$_2$O-TFE-PFE (b) at micron scale
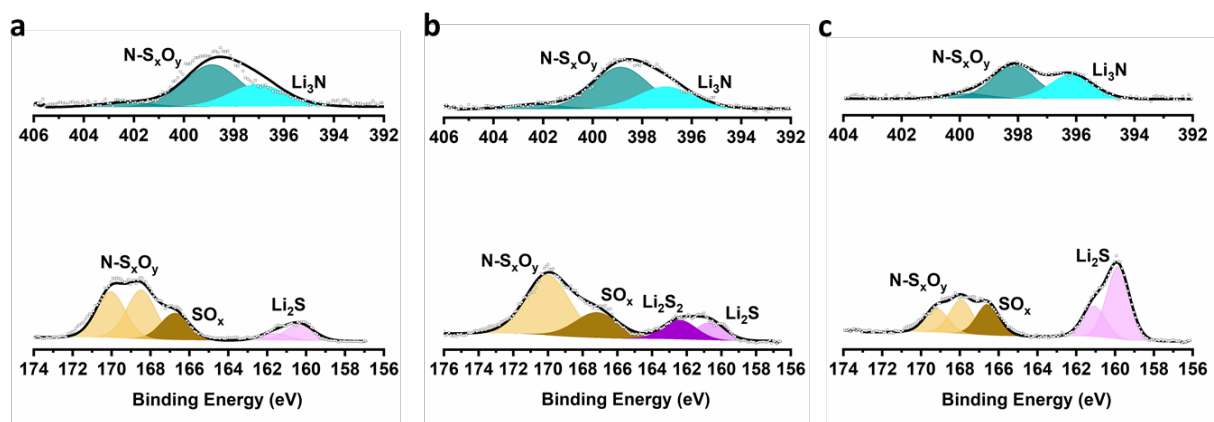
Figure 4.33 Surface spectra from cycled lithium (a-c) for 1M LiFSI-DME (a), 1M LiFSI-Me$_2$O (b) and 1M LiFSI-Me$_2$O-TFE-PFE (c). As for the surface spectra, those represents N 1s spectra, and S 2p spectra from top to bottom view

Industrial Designation or Chemical Name	Chemical Formula	Lifetime (years)	Global Warming Potential for Given Time Horizon		
			20-yr	100-yr	500-yr
Dimethyl Ether	CH_3OCH_3	0.015	1	1	<<1
Pentafluoroethane, R-125	CF_3CHF_2	136	6,350	3,500	1,100
1,1,1,2-Tetrafluoroethane, R-134a	CF_3CH_2F	14	3,830	1,430	435
1,1,2,3,3,3-Heptafluoropropane, HFC-227ea	CF_3CHFCF_3	34.2	5,310	3,220	1,040
Fluoromethane, HFC-41	CH_3F	3.1	490	150	45
Difluoromethane, HFC-32	CH_2F_2	5.6	3600	650	200

Figure 4.34 Summary of the global warming potential for different gases. Data are extracted from IPCC Second Assessment Report[100]
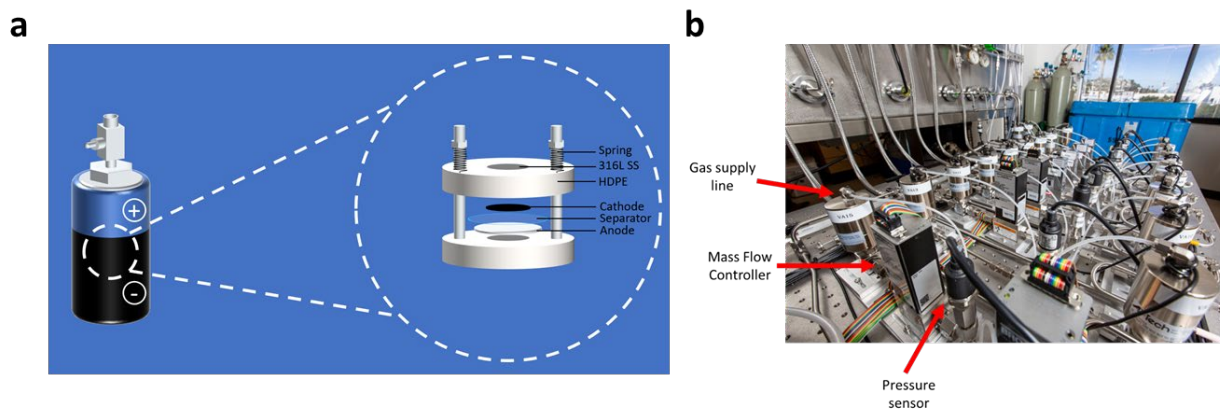
Figure 4.35 (a) LGE cell setup; (b) Filling system for liquefied gas technology. South 8 Technologies Inc. holds the copyright. (https://www.south8technologies.com)

Table 4.2 Summary of inert fluoro-ether solvents used in the electrolytes
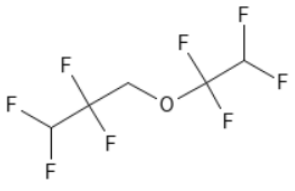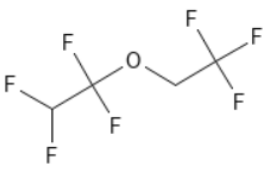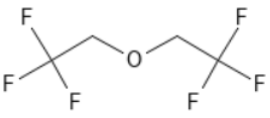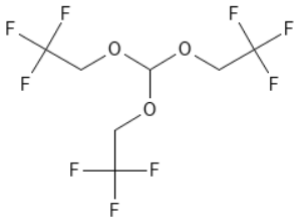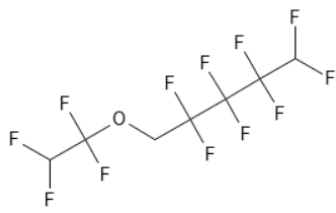
Chemical Formula	Name	Flash point	Boiling point
	1,1,2,2-Tetrafluoroethyl 2,2,3,3-tetrafluoropropyl ether (TTE)	27.5 °C	93.2°C
	2,2,2-Trifluoroethyl 1,1,2,2-tetrafluoroethyl ether (HFE)	None	56.7°C
	Bis(2,2,2-trifluoroethyl)ether (BTFE)	1°C	62-63°C
	Tris(2,2,2-trifluoroethyl)orthoformate (TFEO)	60°C	144-146°C
	1H,1H,5H-Octafluoropentyl 1,1,2,2-tetrafluoroethyl ether (OFE)	None	133°C

Table 4.3 A summary of liquid electrolytes for lithium metal batteries with a focus on fluoro-ethers

Electrolyte	Transport properties	Flammability	C.E. of Li/Cu cycling	Low-T performance
1 M LiPF$_6$-FEC/FEMC-HFE[101]	5.1 mS cm^{-1} at 25 °C	Non-flammable	0.5 mA cm^{-2}, 2 mAh cm^{-2}, around 99% over 560 cycles	Not reported
1.28 M LiFSI-FEC/FEMC-HFE[102]	2.3 mS cm^{-1} at 25 °C >0.01 mS cm^{-1} at -80 °C	Non-flammable	0.5 mA cm^{-2}, 2 mAh cm^{-2}, around 99.4% from 20 to 100 cycles	Li/NCA half-cell. C/3 around 82% capacity retention over 450 cycles at -20 °C
5 M LiTFSI-EA-DCM[85]	0.6 mS cm^{-1} at -70 °C	Flammable	0.2 mA cm^{-2}, 0.5 mAh cm^{-2}, 96.5% from over 50 cycles	Li/organic polyimide half-cell. C/5 around 80% capacity retention over 100 cycles at -70 °C
1 M LiFSI-DME-OFE[103]	1.24 mS cm^{-1} at 25 °C	Non-flammable	1 mA cm^{-2}, 1 mAh cm^{-2}, 99.3% over 250 cycles	Not reported
1.2 M LiFSI-TEP-BTFE[104]	1.3 mS cm^{-1} at 25 °C.	Non-flammable	3 mA cm^{-2}, 98.5% over 10 cycles	Not reported
1 M LiTFSI-DME-HFPN[105]	0.2 mS cm^{-1} at 25 °C	Non-flammable	Not reported	Not reported
4 M LiFSI-PC/FEC[106]	Around 0.7 mS cm^{-1} at 25 °C	Non-flammable	0.2 mA cm^{-2}, 4 mAh cm^{-2}, >99.2% over 20 cycles	Not reported
1 M LiFSI-Me$_2$O-TFE-PFE (Our work)	2.7 mS cm^{-1} at 20 °C 1.6 mS cm^{-1} at -78 °C	Fire-extinguishing	3 mA cm^{-2}, 3 mAh cm^{-2}, 99% over 200 cycles	Li/NMC622 half-cell. C/3 90.5% capacity retention with average 99.6% CE over 200 cycles at -20 °C

Table 4.4 A summary of MD simulations of 1 M LiFSI-Me$_2$O

	313	313	273	273	273	233
Temp (K)	313	313	273	273	273	233
Non-bonded cutoff (Å)	14	14	14	14	12	14
Length of equilibration (ns)	49.4	25.6	15.1	23.0	32.0	12.8
Length of production runs (ns)	39.6	49.2	82.0	57.6	37.8	106.1
box(Å)	54.4	54.4	53.1	53.2	53.2	52.0
density(kg/m3)	809	808	866	862	862	922
Finite size corrected self-diffusion coefficients (10^{-10} m^2 s^{-1})						
Me$_2$O	63.6	68.2	41.1	42.1	41.4	21.6
TFE	5.0	4.6	2.8	2.9	2.2	1.4
PFE	5.0	4.6	2.8	2.9	2.2	1.4
FSI$^-$	24.2	24.0	14.7	14.8	13.8	7.6
Li$^+$	24.3	23.8	14.8	14.8	13.7	7.7
conductivity (mS cm^{-1})[a]	13.9	13.1	13.6	13.4	11.4	14.1
conductivity (mS cm^{-1})[b]	17.6	16.3	16.7	16.7	13.7	17.4
viscosity (mPa *s)	0.24	0.26	0.39	0.37		0.65
degree of dynamic dissociation (α_d)	0.098	0.092	0.125	0.125	0.11	0.2
fraction of free Li (no N(FSI) within 5 Å) 0.13		0.13	0.18	0.18	0.18	0.24

[a] before finite size correction

[b] after finite size correction

Table 4.5 A summary of MD simulations of 1 M LiFSI-Me$_2$O-TFE-PFE

Temp (K)	313	273	273	273	253	253
Non-bonded cutoff (Å)	14	14	14	12	14	12
Length of equilibration (ns)	50.3	36	28	46.7	66.8	90
Length of production runs (ns)	120	188	121.2	145	195	174
box(Å)	57.6	55.4	55.4	55.4	54.6	54.6
density(kg/m3)	1174	1323	1323	1323	1383	1383
Finite size corrected self-diffusion coefficients (10^{-10} m^2 s^{-1})						
Me$_2$O	22.1	9.0	9.3	9.0	5.1	5.3
TFE	65.8	33.6	33.7	33.3	23.1	23.3
PFE	62.4	32.6	32.9	32.5	22.2	22.3
FSI$^-$	9.6	5.9	6.0	5.8	3.5	3.9
Li$^+$	9.6	5.9	5.9	5.8	3.5	3.9
conductivity (mS cm^{-1})[a]	1.4	1.7	1.5	1.7	1.9	1.7
conductivity (mS cm^{-1})[b]	2.3	2.7	2.5	2.5	2.7	2.7
viscosity (mPa *s)	0.32	0.47	0.46	0.52	0.90	0.69
degree of dynamic dissociation (α_d)	0.038	0.057	0.052	0.056	0.086	0.075
fraction of Li with no O(FSI) anion <2.8 Å	0.003	0.003	0.003	0.005	0.009	0.007
fraction of Li with no anion <5 Å	0.003	0.003	0.003	0.005	0.009	0.007
The Li$^+$ cation coordination numbers						
Number of O from Me$_2$O within 2.8 Å	1.17	1.28	1.28	1.28	1.32	1.32
Number of O from FSI$^-$ within 2.8 Å	3.15	3.08	3.09	3.08	3.08	3.09
Number of N from FSI$^-$ within 5.0 Å	2.37	2.32	2.32	2.33	2.24	2.25

[a] before finite size correction

[b] after finite size correction

4.5 Conclusion

We rationally design LGE by adding the simplest (liquefied) ether to the non-flammable low solvating hydrofluorocarbon mixture. The resulting LGE is not only non-flammable but has a fire-extinguishing feature. It delivers high performance over a wide temperature range (–78 to +80°C) and enables a stable Li metal and Li/NMC cycling with high CEs. A practical electrolyte recycling process was demonstrated by using the vapor pressure-temperature relationship of liquefied gas solvents. The electrochemical, safety and recycling properties of the LGE are derived directly from their physical and chemical properties. This study provides an insight into designing multi-functional electrolytes and presents an encouraging path towards safer batteries with a wide operation temperature range and a feasible recycling process.

Chapter 4, in full, is a reprint of the material "Yin, Yijie*, Yangyuchen Yang*, Diyi Cheng, Matthew Mayer, John Holoubek, Weikang Li, Ganesh Raghavendran, Alex Liu, Bingyu Lu, Daniel M. Davies, Zheng Chen, Oleg Borodin & Y. Shirley Meng. "Fire-extinguishing, recyclable liquefied gas electrolytes for temperature-resilient lithium-metal batteries." Nature Energy 7, no. 6 (2022): 548-559". The dissertation author was the primary investigator and first author of the paper.

Chapter 5. Coulombic Condensation of Liquefied Gas Electrolytes for Li Metal Batteries at Ambient Pressure

Investigating diverse electrolyte formulations is considered a highly effective strategy for achieving Li-metal batteries with a cell-level energy density > 500 Wh/Kg. The concept of using highly concentrated electrolyte has been widely incorporated into electrolyte design, owing to their commendable passivation for Li-metal and improved oxidative stability compared to their diluted counterparts. However, challenges like high viscosity, sub-optimal wettability, and lack of thermal evaluation question their suitability for commercial use. Here, we present a highly concentrated dimethyl ether-based electrolyte that remains stable as a liquid phase at ambient conditions via Li^+ coulombic condensation. Thanks to its small size, ultra-low viscosity, excellent reductive stability, and weak Li+ solvation, the formulated electrolyte shows enhanced thermal stability, improved ionic conductivity at low temperatures, and an anion-rich solvation structure. These superior properties contribute to the formation of a salt-derived solid electrolyte interphase (SEI), enabling Li metal cycling with > 99.2% Coulombic efficiency over 1000 cycles. When combined with a SPAN electrode, the electrolyte mitigates the polysulfide cross-talk effect and supports stable cycling under both mild and high-speed charging currents up to 2 C. This research highlights a promising approach to formulating an anion-rich high concentration electrolyte with low viscosity, enabling Li/SPAN chemistry that demonstrates strong temperature resilience and fast-charging tolerance.

5.1 Introduction

As the transportation sector rapidly electrifies, the demand for high energy density energy storage system is significantly stimulated. However, the conventional Li-ion chemistry is reaching their limit, new chemistries must be implemented for the continued progress. Lithium (Li) metal is considered as the most promising candidates for the next-generation high-energy density batteries, given its highest theoretical specific capacity (3860 mAh g–1), exceedingly low standard reduction potential (−3.04 V relative to the standard hydrogen electrode), and one of the lowest solid densities (0.534 g cm–3). Yet it is inhibited from the poor cyclability and safety concerns caused by the incompatible SEI formation, significant volume change, dendritic Li and the "dead lithium" formation over cycling[107]. As the result, it will enhance cell overpotential, accelerate cell failure and easily cause thermal runaway.

In terms of cathode chemistry, S-based conversion cathodes are also desirable to pair with Li due to their high theoretical capacity up to 1675 mAh g–1, low cost and abundance of sulfur, and lack of expensive Co and Ni transition metals. However, elemental S rely on the polysulfide redox, which is difficult to chemically stabilize over long-term calendar and cycling periods[108]. When considering the high energy-density target for elemental S, the cathode loading and electrolyte loading should be carefully tuned and mostly require > 5 mAh/cm2 and < 2.5 g/Ah, respectively, due to the relatively lower nominal voltage. Such high cathode loading and electrolyte loading are barely achievable at the current stage. Sulfurized polyacrylonitrile (SPAN), which sulfur is covalently bonded to polymer PAN backbones, circumvents the need for polysulfide redox[109]. However, SPAN is sensitive to solvent types, salt concentrations, and thus require specific electrolyte design strategies[110].

From the perspective of the electrolyte design for enabling Li-metal anodes, carbonate solvents paired with lithium hexafluorophosphate (LiPF$_6$) salt was firstly borrowed from the commercially successful lithium-ion system, due to its effective formation of stable SEI towards graphite, good oxidative stability.

However, due to the incompatibility of carbonate solvents with Li metal, the low CE, and the generation of dendritic Li results in the failure of its application towards Li metal. Alternatively, ether solvents were systematically explored due to its more thermodynamically reductive stable compared with its carbonate counterparts. However, conventional (LCE) ether systems typically rely on lithium nitrate (LiNO$_3$) for reversible Li metal operation, which serves as a temporary solution with progressively consumed during cycling[111]. In addition, LCE also re-introduce polysulfide dissolution and those soluble polysulfide intermediates deposited on the Li metal. This will substantially exhaust the electrolyte, Li reservoir and thicken the SEI, which is further detrimental to the cyclability. The introduction of utilizing highly concentrated electrolytes (HCE) endow unusual features for ethers to overcome above challenges, benefit from the significant decrease of free solvent and reduction of solubility of polysulfide, and the generation of salt-derived SEI/CEI[112]. High bulk ion concentration is also beneficial to reduce the concentration gradient at the interface and maximize Sand's time. However, HCE also suffer from the reduced ionic conductivity owing to high viscosity, low ionicity from ion-pairing, which raise an issue for high current rate tolerance and low-temperature operation. The increased viscosity of the HCE might also impact the wettability with separators and electrodes, which complicate the cell formation process and sometimes do harm to the normal electrochemical cycling. By introducing non-coordinating diluent, localized highly concentrated electrolytes (LHCE) can significantly lower the bulk concentration and decrease the viscosity, but it still suffers from undesirable ionic conductivity due to ion-pairing effects.

Herein, we provide a route to HCE systems with improved ion conductivity by employing an ultra-low viscosity solvent dimethyl ether (Me$_2$O) that is typically under gas phase with 593 kPa at room temperature. We find that Me$_2$O can be condensed at ambient pressure by Li$^+$ coulombic effect from LiFSI salt, forming an ambient-pressure stable liquefied gas electrolyte. The saturated LiFSI concentration in Me$_2$O (Sat. LiFSI-Me$_2$O) can remain stable from –60 to 60 $^{\circ}$C and show improved thermal stability

compared with 4 M LiFSI in DME (4 M LiFSI-DME) which has similar LiFSI: ether molar ratio as 1:2.4. Such electrolyte also offers comparative viscosity and ionic conductivity > 5.5 mS/cm at +20 °C, but reduced viscosity and improved ionic at subzero temperature compared with 4 M LiFSI-DME. In addition, benefit from the good reductive stability of ethers and the salt-derived SEI formed SEI, the Li metal can stably cycle over 1000 cycles with > 99.2% Coulombic efficiency. When paired with SPAN electrode, the Li/SPAN half cells demonstrate > 90.1 % capacity retention over 200 cycles mostly due to the poor solubility of polysulfide and the salt-decomposed SEI/CEI stabilizing both Li/electrolyte and SPAN/electrolyte interfaces. The Sat. LiFSI-Me_2O electrolyte also show temperature resilience and withstand 2 C fast charging evaluation.

5.2 Results

5.2.1 Design of gas electrolyte stable at ambient condition

Dimethyl ether (Me2O), which exists at gaseous state at Standard temperature and pressure (STP) conditions (Boiling point: –28°C at STP), is demonstrated to act as a promising liquefied gas solvent for enabling next-generation lithium-ion batteries due to its superior physical properties and excellent lithium metal compatibility. Distinct to hydrofluorocarbon-based liquefied gas solvents, Me_2O exhibits improved solubility of different Li-salts due to more polar ether functional group. Given the propensity of Me_2O to solvate the Li^+, the high covalency of Li^+ and the high interaction energy of Li^+ and ether oxygen in the Me_2O molecule, Li salts are hypothesized to possibly hold dimethyl ether solvent even at near atmospheric pressures when salt concentration reach to certain point[46]. Due to the excellent Li-metal compatibility, more positively dissociation energy (easier to dissociate), and high thermal stability, LiFSI has been widely utilized in the Li-metal anode. To obtain a stable saturated LiFSI with Me_2O at around ~1atm,

LiFSI salt is preloaded in a high-pressure window cell followed by filling Me$_2$O gas to reach transparent low concentration solution (around 1M) (Figure 5.1a). Currently, the electrolyte still contains large number of contact ion pair under its vapor pressure at around 75 psi (Figure 5.1b). The LiFSI salt concentration of the solution increases as the pressure of the system is decreased by slowly releasing Me$_2$O gas from the cell. Once the gas is released completely, the equilibrium of the solution is reached at atmospheric pressure and the measured salt: ether molar ratio is 1: 2.36. The solvation structure is proposed to contain much less free Me2O solvent, but with substantial number of Li-FSI-Me2O aggregates, as shown in Figure 5.1b.
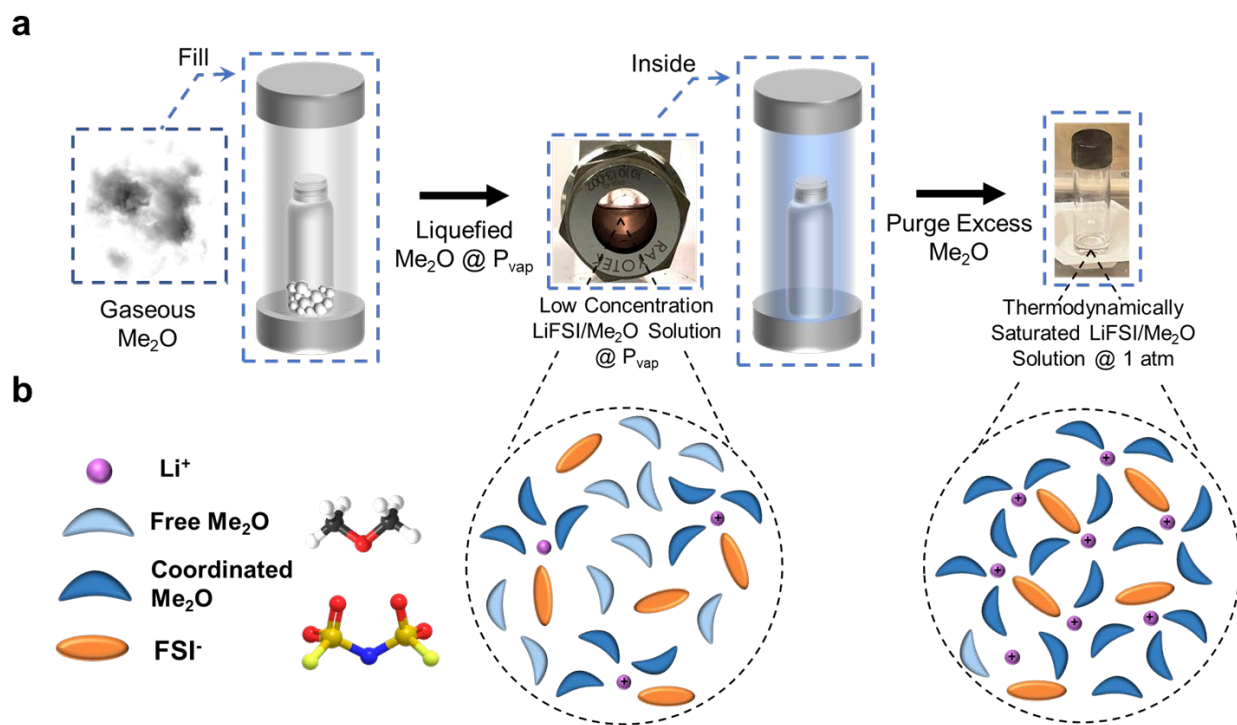
Figure 5.1 Design of the condensed electrolytes (a) The workflow of obtaining thermodynamically saturated LiFSI in Me2O electrolytes at ambient condition. (b) Proposed solvation structures for the low concentration LiFSI in Me2O and the saturated LiFSI in Me2O.

5.2.2 Thermal stabilities, electrochemical transport properties, and solvation structures

The thermal stabilities of the pure DME solvent, 4 M LiFSI in DME, Sat. LiFSI-DME and Sat. LiFSI-Me2O were evaluated through Thermogravimetric Analysis-Differential Scanning Calorimetry (TGA-DSC) methods. As illustrated in Fig.2a and b, pure DME is volatile and easily boils when temperature > 75 °C. With the increase of the salt concentration, the boiling point is postponed to higher temperature at > 125 °C and > 185 °C for 4 M salt concentration and saturation state, respectively. Whereas sat. LiFSI-Me2O does not show an obvious endothermic peak and the mass loss rate is slightly higher compared with 4 M LiFSI-DME before 172 °C. When temperature reach to > 210 °C, LiFSI will decompose and generate a significant exothermic peak. Based on the Fig.2b, we can observe the exothermic peak is delayed for the sat. LiFSI-Me2O system, indicating its improved thermal stability. To understand different electrolytes' fluidity, the viscosity is measured and shown in Fig. 2c and Supplementary Table.1. The measured viscosity of pure DME is around 0.42 mPa S^{-1}, which is consistent with literature report. With the increase of the LiFSI concentration, the viscosity is expected to increase significantly from 0.92 mPa S^{-1} for 1 M LiFSI-DME to 21.65 mPa S^{-1} 4 M LiFSI-DME and then reach to 140.29 mPa S^{-1} for sat. LiFSI-DME. In comparison, the viscosity of LiFSI-Me2O is slightly higher than 4 M LiFSI-DME. The ionic conductivities of the 1 M LiFSI-Me$_2$O, 4 M LiFSI-DME, Sat.LiFSI-Me$_2$O and Sat.LiFSI-DME electrolytes were measured and are shown in Fig 2d. The low mobility of the Li+ in the Sat.LiFSI-Me$_2$O, Sat.LiFSI-DME, and 4 M LiFSI-DME electrolytes due to their high concentrations is reflected in the lower conductivities across the wide temperature range (-60 ℃ to +60 ℃) compared to the relatively low concentration 1 M LiFSI-Me$_2$O.

In addition, the ionic conductivities of the highly concentrated systems drop with temperature although the saturated LiFSI Me$_2$O electrolyte demonstrates a more modest decline in conductivity with respect to reduced temperatures. Solvation structure analysis by Raman spectroscopy and NMR 7Li was

conducted. These spectra are displayed in Fig. 2e,f, where the LiFSI Me2O and LiFSI DME electrolytes are compared to the individual LiFSI salt and Me2O solvent, respectively. In Fig 2e. the characteristic S-N-S bending peak of the FSI- at 774 cm-1 can be observed for the LiFSI spectra which undergoes a significant shift to 720 cm-1 when dissolved in DME in 1 M LiFSI-DME.   Furthermore, an upshift is observed for higher concentrations of LiFSI as seen in the 4 M and saturated LiFSI DME Raman spectras, indicating an increase in the Li+/FSI- interactions characteristic of contact-ion pair (CIP) and aggregate (AGG) structures typically formed in high concentration electrolytes. Similarly, the characteristic FSI- peak is shifted upon LiFSI dissolution in the Me2O solvent, albeit a smaller shift from 774 cm-1 to 725 cm-1 was observed for 1 M LiFSI Me2O in comparison to 1 M LiFSI DME, suggesting a weakly Li+ solvating power of Me2O solvent, leading to a higher degree of cation-anion interactions in the LiFSI Me2O system at the same salt concentration. At saturated states, the S-N-S bending peak at 775 cm-1 is shifted to 750 cm-1 in both the LiFSI Me2O and LiFSI DME electrolytes which signifies comparable degrees of (Li+)n CIP and AGG formation. The Raman spectrum for the Me2O solvent is shown in Fig. 2f. The characteristic C-O-C stretching peak of Me2O centered at 918 cm-1 was found to be slightly redshifted to 916 cm-1 in the saturated state, due to the increasingly solvated Me2O from a relatively low concentration of 1 M to the saturated salt concentration. However, the peak shift of the solvated DME is more obvious when salt concentration increases (Supplementary Fig.3). The relatively solvating power behavior can also be dictated from the 7 Li NMR spectra. As shown in Fig. 2g, Sat. LiFSI-Me2O exhibited wider peak broadening compared with Sat. LiFSI-DME, indicating Me2O is a weakly solvating solvent.
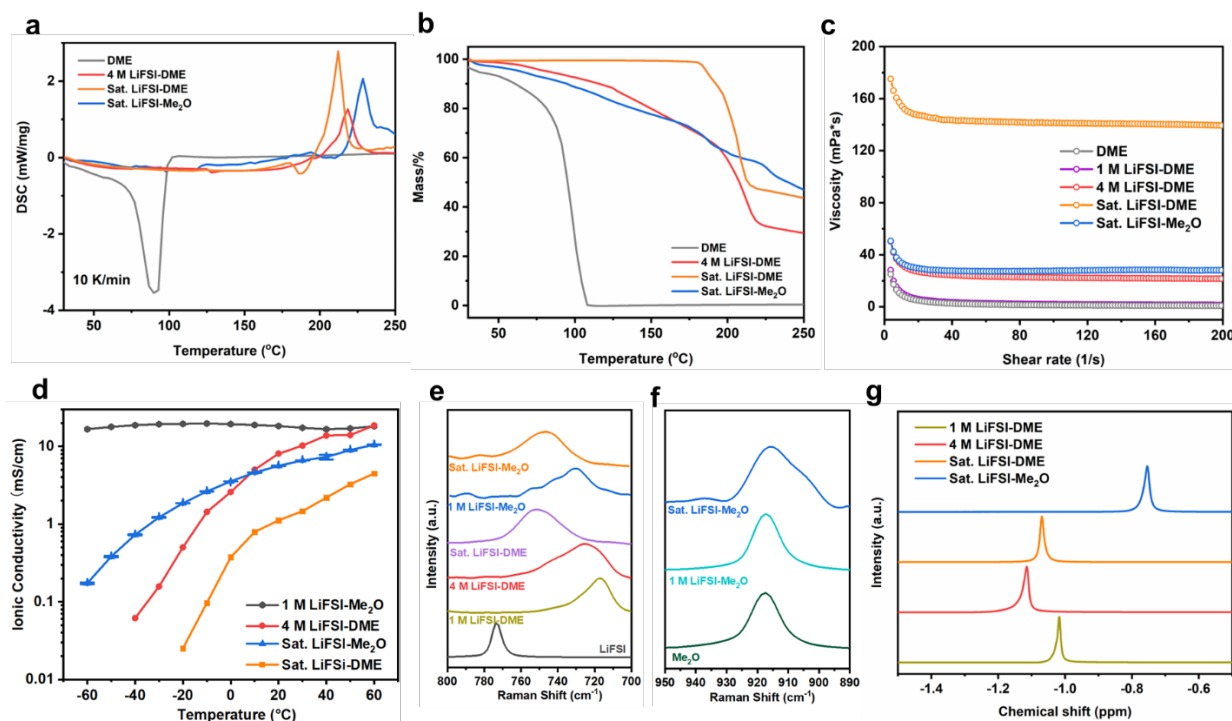
Figure 5.2 Physical and electrochemical properties of electrolytes (a-c) Summary of DSC, TGA, and viscosity results for different electrolytes (d) Summary of the ionic conductivities of different electrolytes (e-f) Summary of Raman spectra of FSI⁻ and Me₂O of different electrolytes (g) Summary of NMR spectra of different electrolytes

5.2.3 MD simulations

To gain a molecular understanding of the electrolytes of interest we employ molecular dynamics (MD) simulations of the various DME electrolytes of interest and Me$_2$O:LiFSI solutions at various molecular ratios (Figure 5.3a).   First, we predict the condensation behavior of various Me$_2$O: LiFSI systems at molar ratios ranging from 20:1 – 2:1. These systems are constructed such that a LiFSI agglomerate is placed in contact with gaseous Me$_2$O and then investigated at 1 bar of applied pressure as managed by an isothermal-isobaric Noose-Hoover barostat (computational methods). As shown in Figure 3b, we observe a sharp increase in system density at Me$_2$O:LiFSI to ~ 1.02 g mL^{-1} within 2 ns for system ratios ≤ 2.3, whereas every other system maintains total densities << 0.1 g mL^{-1}. When examining the trajectories (Figure 3a), this indicates a favorable condensation for Me$_2$O:LiFSI 2.3:1 into the liquid phase

driven by salt dissolution. The Me_2O:LiFSI 2.3:1 ratio is in good agreement with that measured experimentally, and indicates that coulombic condensation phenomena can be computationally predicted in future systems.

Next, to understand the local environment of Li^+ in the Sat. LiFSI-Me2O relative to the conventional DME-based systems, we conduct radial distribution function (RDF) analysis on the systems of interest over 10 ns (computational methods). As shown in Figure 5.3c and 5.3d, we predict a substantially reduced probability of Li^+/Me_2O coordination relative to Li^+/DME, whereas the probability of Li^+/FSI^- coordination in Sat. LiFSI-Me2O is comparable to that of 11 M LiFSI DME. Taking into account the relative number density of each coordinating species, we predict average solvation structures of $Li^+(DME)_{3.0}$, $Li^+(DME)_{2.7}$ $(FSI^-)_1$, and $Li^+(DME)_{0.85}$ $(FSI^-)_{3.1}$ for 1, 4 and 11 M LiFSI DME, respectively (note that 1 DME contains 2 oxygen atoms) (Figure 5.3e,f). The same analysis reveals an average structure of $Li^+(Me_2O)_{0.9}$ $(FSI^-)_{3.7}$ in Sat. LiFSI Me2O (Figure 3e,f). Such highly aggregated solvation structures are commonly associated with salt-derived SEI chemistries when applied in Li metal batteries, but are also typically associated with poor transport and elevated solution viscosity as previously discussed. In Sat. LiFSI Me2O, however, these negative externalities are substantially mitigated (Figure 5.3b) while maintaining such beneficial solvation properties.
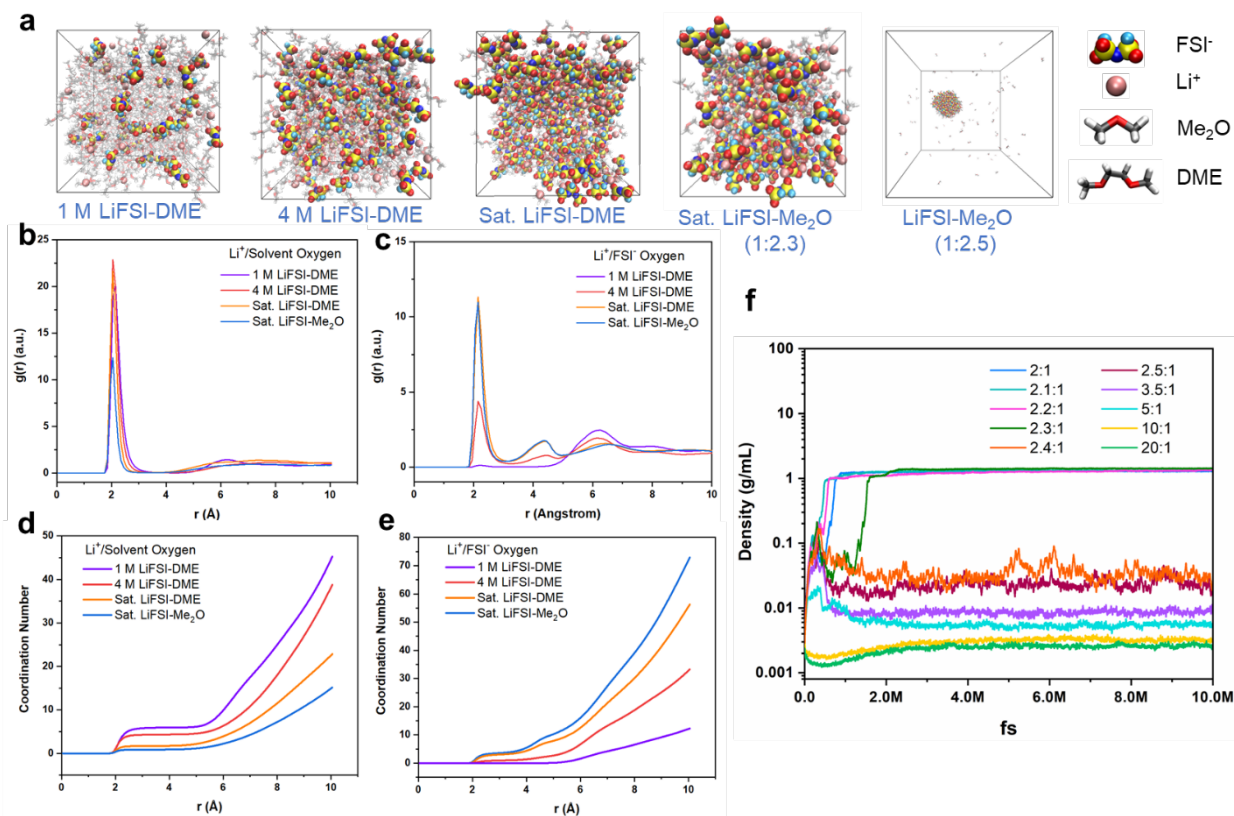
Figure 5.3 Solvation structure and MD simulation results of the formulated electrolytes (a) Snapshots of the MD simulation cell containing the representative Li+ solvates (b-e) Simulated RDF and coordination numbers for different electrolytes. (f) Calculated densities for different Me2O:LiFSI molar ratios

5.2.4 Electrochemical Performance

The stability of Li-metal cycling was assessed through Li/Cu half-cell plating and stripping tests. A control electrolyte, 4 M LiFSI DME, known for its high Coulombic efficiency (CE) values, was used alongside the saturated LiFSI Me2O and LiFSI DME systems. These electrolytes were tested in Li‖Cu cells at a current density of 0.5 mA cm-2. As depicted in Figure 5.4a, both the 4 M LiFSI DME system and saturated LiFSI Me2O systems show consistent Li metal anode cycling over 1000 cycles. However, the saturated LiFSI DME system exhibited more significant cycling fluctuations. To determine the wide-temperature operability of the electrolytes, Li-half cells using 4 M LiFSI DME and saturated LiFSI Me2O were cycled at -20℃, -40 ℃, and 50℃. The saturated LiFSI Me2O system maintained CE values of 98.4%,

98.4%, and 99.0% respectively at these temperatures (Figure 5.4b, e, h). Conversely, the 4 M LiFSI DME system showed extreme fluctuations at lower temperatures and only comparable Li metal performance to the saturated LiFSI Me2O system at 50℃ with a CE of 99.1%. We attribute this to higher Li-metal porosity at reduced temperatures, causing continual corrosion.

Despite the similar CE at room temperature between the 4 M LiFSI DME and saturated LiFSI Me2O systems, Li-metal deposition was carried out, depositing 3 mAh cm-2 at 3 mA cm-2 in both electrolytes at room temperature. After disassembly for characterization, the cross-section (Figure 5.4c, f) and surface morphology (Figure 5.4d, g) of the plated Li-metal were analyzed. While both systems exhibit a locally dense surface structure, the 4 M LiFSI DME system showed a greater thickness and porosity in the plated Li. On the contrary, the plated Li in the saturated LiFSI Me2O system exhibited fewer voids and an exceptionally dense morphology with a thickness closely matching the theoretical plated capacity ($t_{theoretical}$ = 14.55 μm).
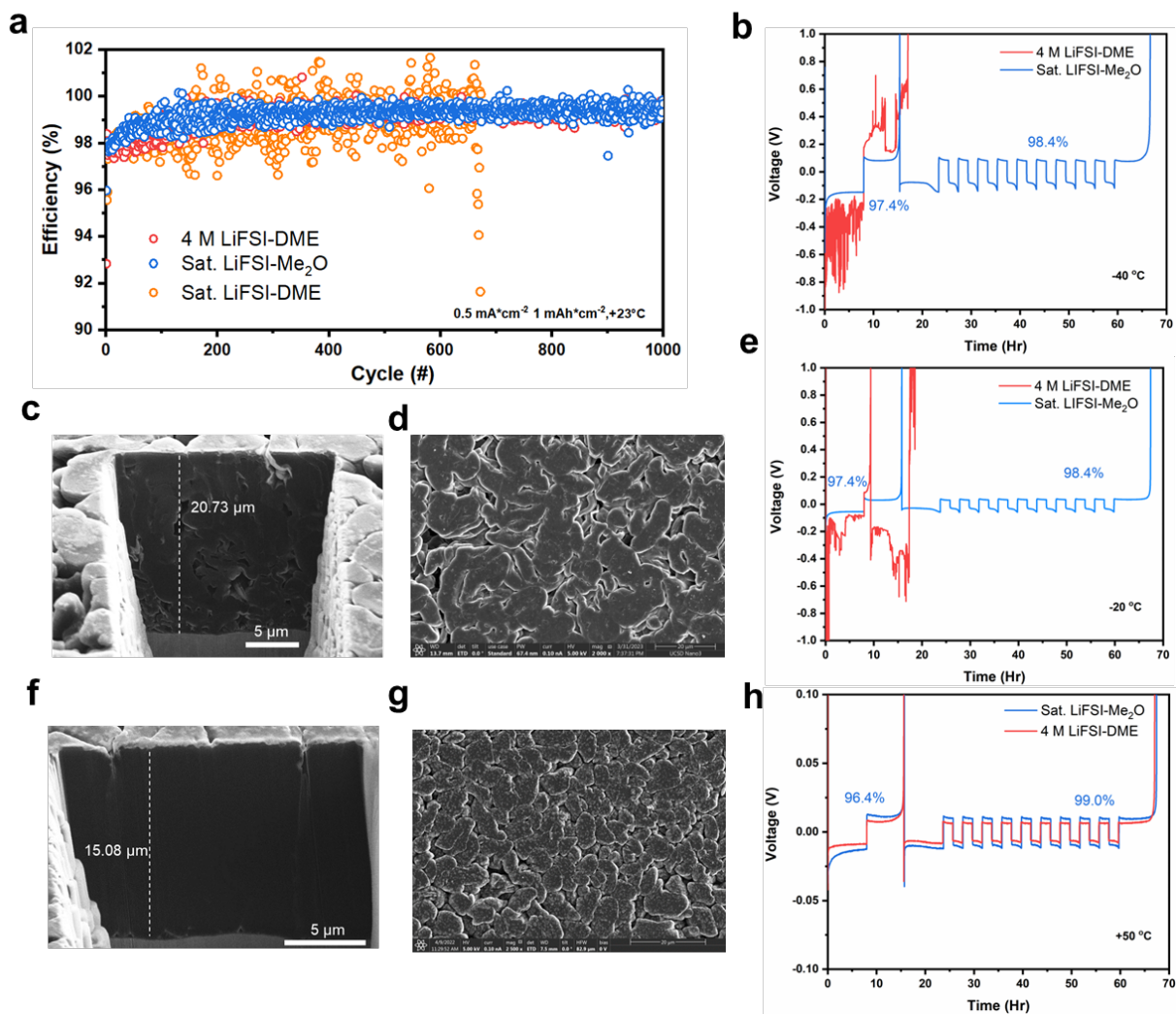
Figure 5.4 Electrochemical performance of Li plating and stripping and deposited morphology investigations in different electrolytes. (a) Long-term cycling stability of Li-metal in different electrolytes. (b,e,h) Temperature resilience evaluations. (c,d,f,g) Cross-sectional and top-view of plated Li.

To assess the electrochemical performance of the saturated LiFSI Me2O system, a SPAN (Sulfurized polyacrylonitrile) cathode was selected owing to its low-cost and modest voltage, which accommodate the limited oxidative stability of typical ether electrolytes. Although lithium polysulfide solubility is a major concern in ether electrolytes, the saturated LiFSI Me2O electrolyte shows limited polysulfide dissolution compared to the 4 M LiFSI DME electrolyte, as illustrated in Figure 5.5a. This decreased dissolution is further highlighted by the long-term cycling behavior of full-cells consisting of a SPAN

124

cathode with a high areal mass loading of 3 mAh cm-2 coupled with a 500 μm Li metal anode, equating to a one-fold surplus capacity (Figure 5.5b). While both systems show similar initial capacities of xx, the 4M LiFSI DME system nears a 90% capacity retention cutoff at 125 cycles, whereas the saturated LiFSI Me2O system maintains > 90% capacity retention even after 200 cycles. Conversely, the saturated LiFSI DME system fails to produce any notable capacity upon the initial C/10 charge and discharge (Figure 5.5c), indicating its poor transport properties.

The half-cells based on these two electrolytes were also cycled at 50 ℃, where the saturated LiFSI Me2O and 4 M LiFSI DME systems exhibit capacity retentions of 96 % and 45 % after 50 cycles, respectively (Figure 5.4d). This notable difference is credited to the heightened SPAN dissolution in the 4 M LiFSI DME system at high temperatures, in contrast to the limited polysulfide dissolution observed in the saturated LiFSI Me2O system. Moreover, the fast-charging evaluation of the Li∥SPAN full-cell using 4 M LiFSI DME similarly demonstrates severe capacity fade after 30 cycles, while the saturated LiFSI Me2O system manages to deliver consistent cycling performance across 100 cycles (Figure 5.5e). These results suggest that although the 4 M LiFSI DME system provides adequate Li CE, the substantial dissolution of SPAN impedes the cell's performance, particularly at higher temperatures and charging rates.
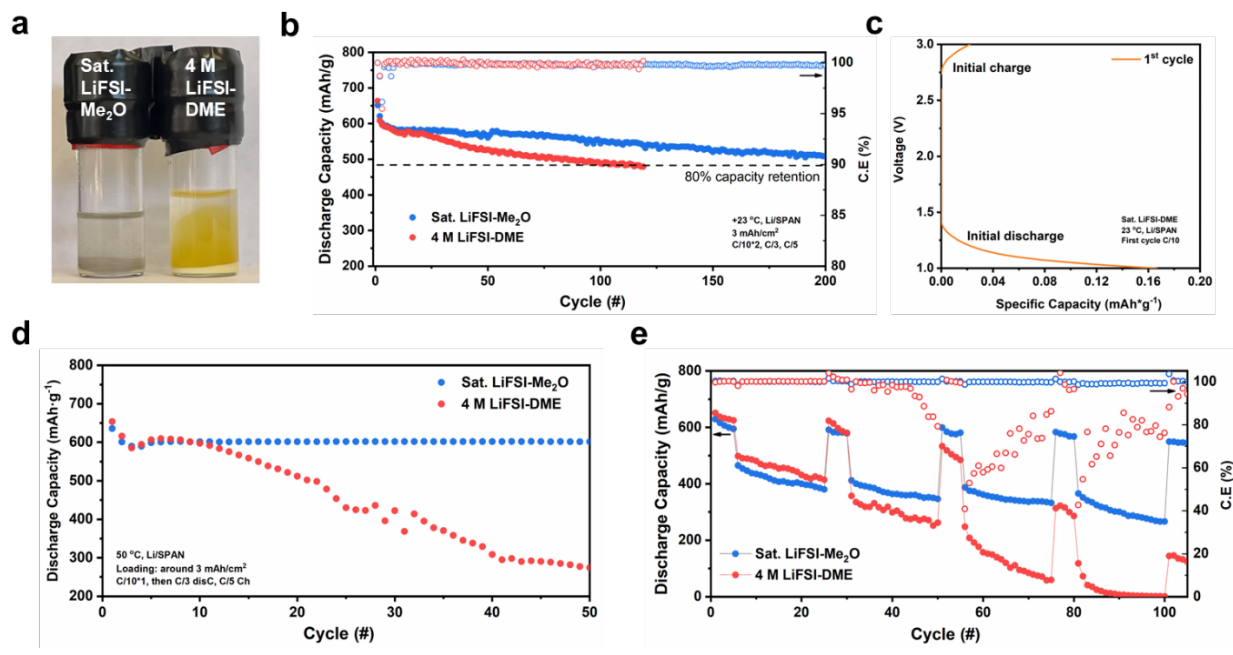
Figure 5.5 Electrochemical cycling evaluations of Li/SPAN cells (a) The images of polysulfide LixSy soak tests. (b) Electrochemical cycling of Li/SPAN half cells at room temperature. (c) Initial cycle of the Li/SPAN half-cell in saturated LiFSI in DME. (d) Electrochemical cycling of Li/SPAN half cells at 50 °C and (e) fast charging evaluations of Li/SPAN cells

5.2.5 Interfacial Analysis
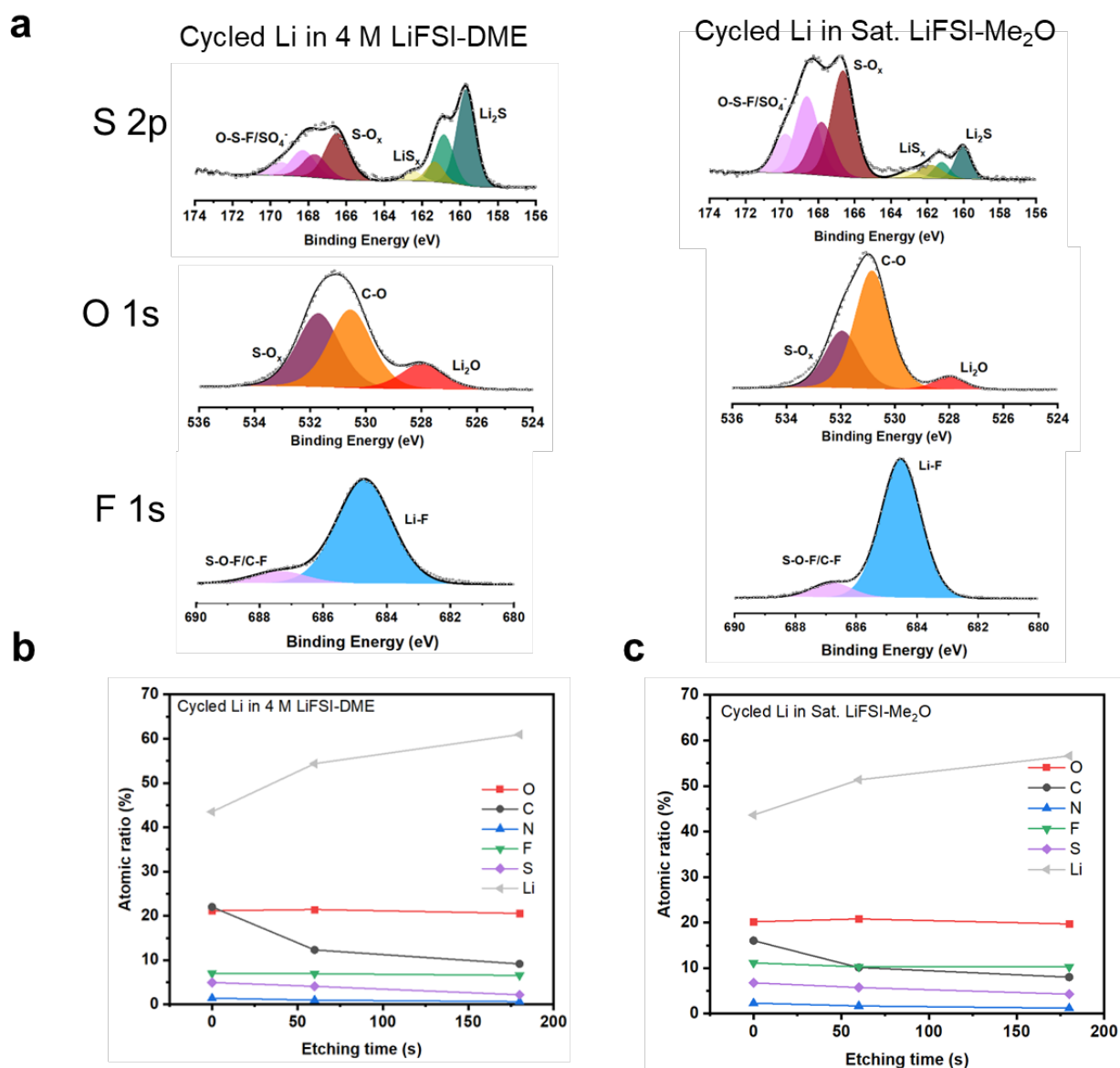
Figure 5.6 Interface analysis of the cycled Li from the fully charged Li/SPAN cells at 60th cycle (a) Local XPS spectra of cycled Li in the 4 M LiFSI-DME electrolyte and the sat. LiFSI-Me$_2$O electrolyte. (b-c) Depth profiling of global atomic ratio of cycled Li in the 4 M LiFSI-DME electrolyte and the sat. LiFSI-Me$_2$O electrolyte

The interface of cycled Li metal from Li/SPAN cells was characterized to investigate the interfacial influence. As depicted in Figure 5.6, a relatively higher proportion of Li2S was observed on the Li metal cycled in the 4 M LiFSI-DME system, while a lower amount was found in the saturated LiFSI-Me2O

system. This difference can be attributed to the dissolved polysulfide shuttle from SPAN to the lithium metal, facilitated by the higher solubility in the 4 M LiFSI-DME system. However, there was little disparity observed in the O 1s and F 1s spectra, indicating their overall similarity.

To further evaluate the effect of polysulfide shuttling, a parallel experiment involving Li/Cu cycling was conducted for 60 cycles. The deposited Li on Cu substrates was collected and prepared for XPS experiments. As illustrated in Figure 5.7, a higher amount of Li2S was observed on the cycled Li using the saturated LiFSI-Me2O electrolyte, indicating a greater degree of salt decomposition. This finding provides additional evidence that the improved performance of the Li/SPAN system is attributed to reduced polysulfide dissolution and the presence of a salt-derived SEI containing Li2S.
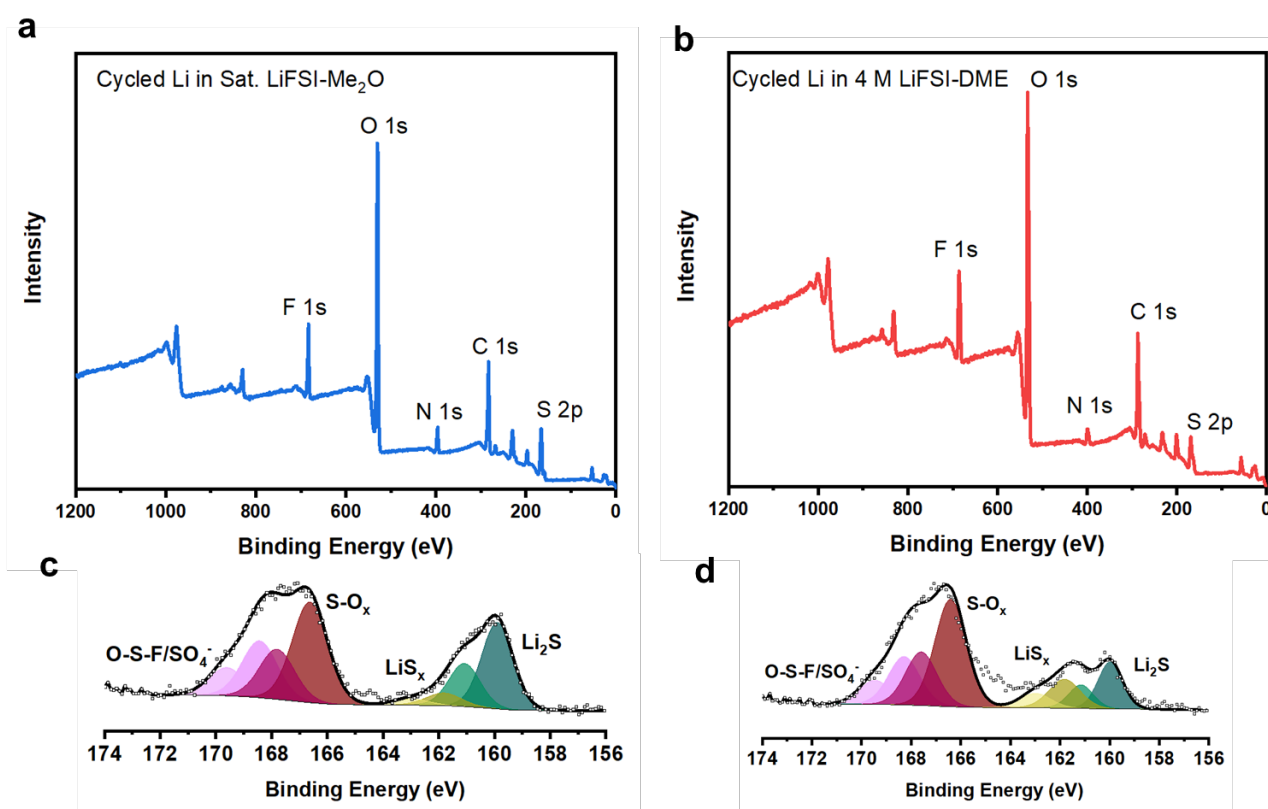
Figure 5.7 Interface analysis of the cycled Li from the Li/Cu cells at 60th cycle (a-b) Global XPS spectra of cycled Li in sat. LiFSI-Me2O and 4 M LiFSI-DME electrolyte. (c-d) S 2p spectra of cycled Li in sat. LiFSI-Me2O electrolyte and 4 M LiFSI-DME electrolyte

5.3 Methods

5.3.1 Materials

Dimethyl ether (99%) was obtained from Sigma-Aldrich. The salts Lithium bis(fluorosulfonyl)imide (99.9%) were purchased from Gotion. 1,2-dimethoxyethane (99.5%) was purchased from Sigma-Aldrich and stored over molecular sieves. The SPAN electrodes were made with an 8:1:1 ratio between active materials: PVDF and C65.

5.3.2 Electrochemical Testing

Electrolytic conductivity measurements were performed in custom fabricated high-pressure stainless-steel coin cells, using polished stainless-steel (SS 316L) as both electrodes. The cell constant was calibrated frequently from 0.447 to 80 mS cm-1 by using OAKTON standard conductivity solutions.

Electrochemical impedance spectroscopy was collected by a Biologic SAS (SP-200) system and the spectra were then fitted using ZView software.

Battery testing was performed by assembling 2032-type coin cells. A three-layer 25µm porous PP/PE/PP membrane (Celgard 2325) was used for all the electrochemical tests. For Li/SPAN discharge tests in different temperatures, the cells were soaked at the testing temperature in a temperature chamber (Espec) for at least 2 hours before cycling.

5.3.3 Characterizations

Differential Scanning calorimetry (DSC) was performed on Netzsch STA 449 Jupiter. The electrolyte/solvent (Approx. 25-30 uL) was injected and sealed in Cu-backed Aluminum pans. All sample preparations were done in an Argon-filled glovebox (<0.5 ppm O2, <0.5 ppm H2O). The Aluminum pan was pierced by a needle after loading into the DSC furnace chamber. The temperature was ramped up to 250 C from room temperature at the rate of 10 C/min. All DSC measurements were performed under a constant Ar flow rate of 40 ml/min.

5.4 Conclusion

Me$_2$O gas was demonstrated to be condensed at ambient condition with significant boost of boiling point by utilization of high salt concentration. Such electrolyte exhibits anion-pair solvation structure and moderate ionic conductivities over wide-temperature range. By formulating a saturated LiFSI-Me$_2$O electrolyte, we achieved excellent cyclability of lithium metal over 1000 cycles and the ability to withstand critical current densities up to 12 mA/cm^2. When combined with a SPAN electrode, the saturated LiFSI-Me2O electrolyte demonstrated superior performance compared to a 4 M LiFSI-DME electrolyte. This improvement can be attributed to the formation of a salt-derived solid electrolyte interphase (SEI) at the lithium metal anode and reduced dissolution of polysulfides, as verified by XPS and polysulfide soak tests. The study provides a new design strategy for high concentration electrolyte with low viscosity and low polysulfide solubilities for Li/Sulfur system.

Chapter 5, in full, is a draft of the manuscript of "Coulombic Condensation of Liquefied Gas Electrolytes for Li Metal Batteries at Ambient Pressure" under preparation. The manuscript is co-authored with John Holoubek, Prof. Ping Liu, Prof. Ying Shirley Meng, and Prof. Zheng Chen. The dissertation author was the primary investigator and first author of the paper.

Chapter 6 Future Plans

6.1. Fluorinated ethers for future liquefied gas electrolyte development.

Among all electrolyte designs aimed at enabling Li-metal batteries, ethers display favorable thermodynamic reductive stability compared to esters and carbonates. Ethers are both chemically and electrochemically more stable with Li-metal. However, their relatively poor oxidative stability raises questions about their compatibility with high-voltage cathodes. Consequently, a significant amount of electrolyte engineering research has been directed towards improving ethers, aiming not only to retain their superior Li-metal compatibility, but also to enhance their stability with high-voltage layered oxides.

In parallel with other liquid electrolyte engineering efforts, dimethyl ether (Me2O), which exists as a gas under ambient conditions and represents the simplest form of ether, has been shown to provide good Li-metal cycling stability, as reported in previous studies. However, as discussed in Chapter 4, its high-voltage stability with NMC electrodes doesn't rank among the best in current state-of-the-art chemistries. One possible strategy to further enhance the oxidative stability involves fluorination. The fluorine functional group exerts a strong electron-withdrawing effect, leading to the delocalization of the ether's oxygen and improving the oxidative stability of ethers. As shown in the Figure 6.1a, Me_2O has the lowest absolute HOMO (-7.2113 eV) value indicating its relatively potential reduced oxidative stability compared with its fluorinated counterparts, F2Me2O: -8.6882 eV, F3Me2O: -8.7879 eV, and F4Me2O: -10.3276 eV. As comparison, F4Me2O (TFDME) demonstrates highest HOMO absolute value owing to the symmetric structure and higher F to O ratio. In the meantime, TFDME also shows highest boiling point at 4.7 ºC, allowing for easier gas filling and electrolyte preparations.

Solvents	CAS	Melting point(℃)	Boiling point(℃)	LUMO(eV)	HOMO(eV)
Me2O	115-10-6	-141	-24	-0.2176	-7.2113
BTFE	333-36-8	-	63	-0.6321	-8.6882
F2Me2O	359-15-9	-	-4	-0.3436	-8.7879
F3Me2O	421-14-7	-149	-24	-0.3069	-9.3409
F4Me2O(TFDME)	1691-17-4	-107	4.7	-0.5353	-10.3276

b
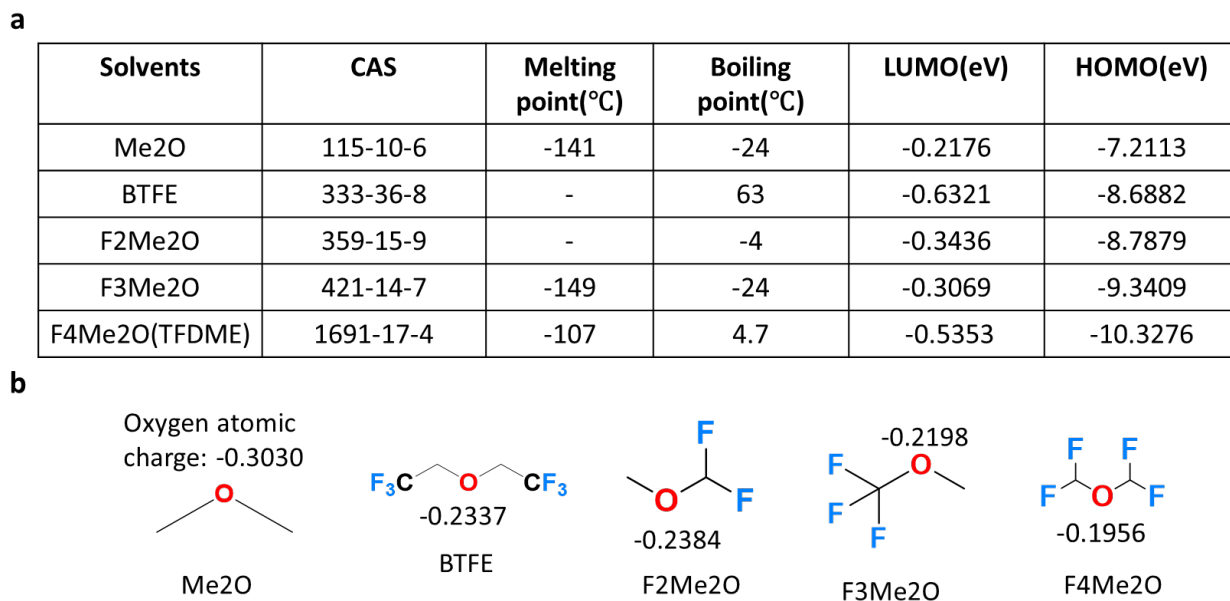
Figure 6.1 List of different fluorinated ethers (a) Summary of physical properties of different ethers. (b) Calculated oxygen atomic charge for different ethers.

While fluorination does enhance oxidative stability and results in the creation of F-rich solid/electrolyte interfaces, it also causes the delocalization of ether oxygen, which in turn reduces the Li+/O coordination and decreases the salt's solubility in the solution. This issue could potentially be mitigated through the partial tailoring of fluorination sites.

As depicted in Figure 6.1b, we simulated the central oxygen atomic charge across all ethers. Me2O exhibited the most negative atomic charge at -0.3030 eV, implying a particularly favorable Li+/Me2O coordination. In comparison, the widely studied BTFE diluent exhibits a negligible Li+ coordination with -0.2337 eV, suggesting a possible correlation between oxygen atomic charge and Li+/solvent coordination. When two methyl groups are partially replaced by -CF2, the central oxygen atomic charge is observed to be -0.1956 eV, even higher than that of the BTFE diluent. This suggests that F4Me2O is less likely to coordinate with Li+ compared to BTFE.

Interestingly, the introduction of an asymmetric fluorination structure results in F2Me2O and F3Me2O showing a more negative oxygen atomic charge than F4Me2O. In particular, F2Me2O, with its

higher absolute HOMO value than Me2O and increased oxygen atomic charge compared to BTFE, could potentially function as a weakly solvating solvent.

Considering TFDME has enhanced absolute value HOMO energy compared with BTFE, it might serve as a diluent with wide electrochemical stability window. To prove that, basic physical properties, salt solubility, electrochemical transport properties, and Li-metal compatibility were performed. As shown in Figure 6.2a, TFDME exhibits lower vapor pressure (25 psi at 20 °C) compared with FM (487 psi) and Me$_2$O (86 psi). Consistent with the hypothesis, TFDME can barely dissolve LiFSI salt. When adding excess 0.1 M LiFSI in TFDME, the ionic conductivity is below 0.1 mS/cm from -60 °C to 60 °C, making it unsuitable for providing sufficient Li+ diffusivity (Figure 6.2b, c). After soaking fresh Li metal in 0.1 M LiFSI in TFDME, there are some dots formed on the Li surface, indicating ineffective passivation.
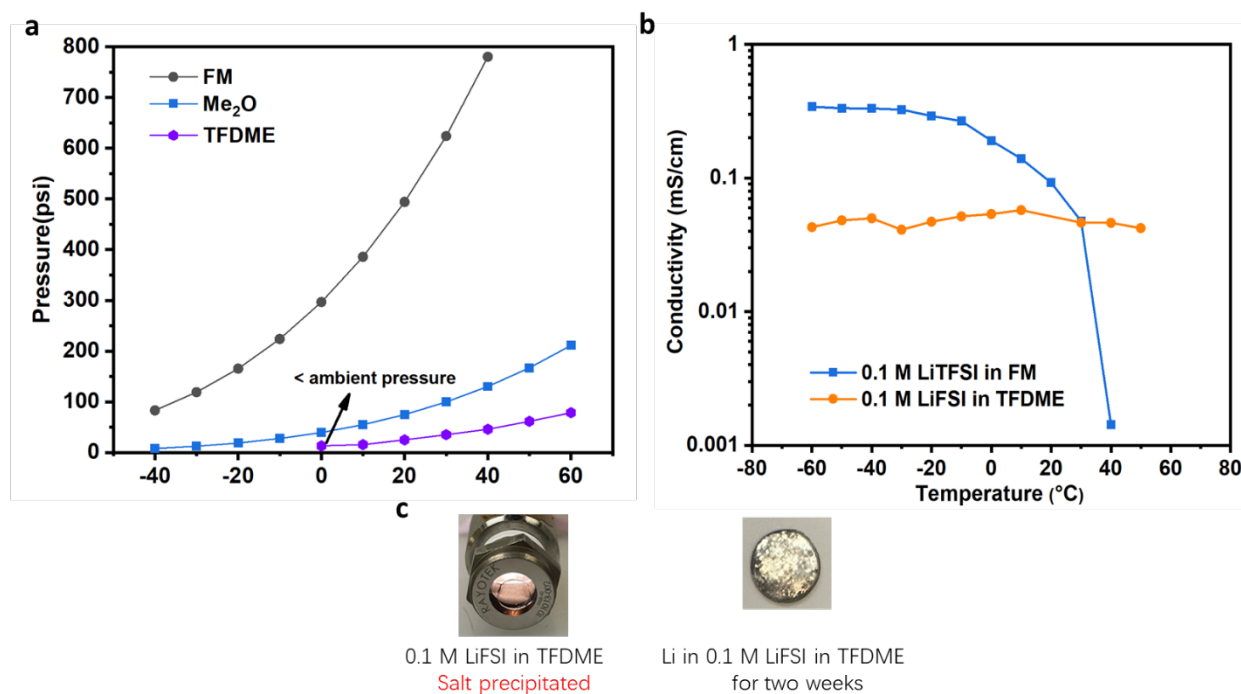
Figure 6.2 Physical and chemical properties of LGEs (a) Summary of pressure of different gases. (b) Ionic conductivities of TFDME and FM-based electrolytes. (c) Li-metal soak tests

To improve the ionic conductivities and Li metal compatibility, a higher salt concentration should be maintained with the assistance of co-solvents. Here, for the purpose of the demonstration, we select fluorinated carbonates as co-solvents owing to their improved oxidative stability, and high performance reported from literatures[50]. As illustrated in Figure 6.3a, high concentration LiFSI in FEC/FEMC solution was prepared before adding TFDME diluent.
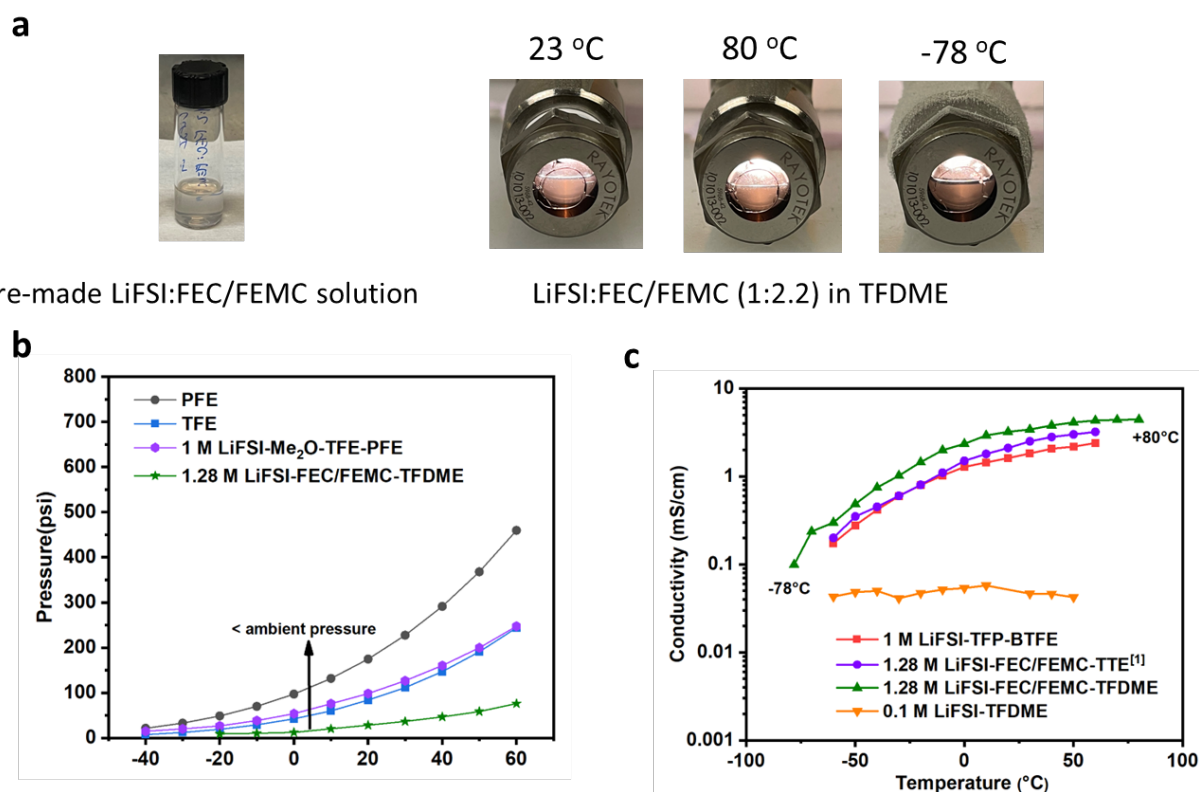
Figure 6.3 (a) Optical image of the pre-made LiFSI in FEC/FEMC liquid solution and the solubilities test of LiFSI-FEC/FEMC-TFDME at different temperatures. (b) Summary of pressure of different electrolytes and gases. (b) Ionic conductivities of TFDME-based electrolytes and other reference electrolytes

After adding TFDME, the formulated LiFSI-FEC/FEMC-TFDME maintains 1.28 M salt concentration and no obvious phase separation or salt precipitation is observed over wide temperature range, which demonstrates the successful formulation of the electrolyte. The 1.28 M LiFSI-FEC/FEMC-TFDME electrolyte also demonstrates significantly lower vapor pressure (21 psi at 20 °C) compared with previously developed fire-extinguishing TFE-based liquefied gas electrolytes (87 psi at 20 °C). The ionic

conductivity also benefits from the addition of FEC/FEMC, which increase from < 0.1 mS/cm (only TFDME containing electrolyte) to > 3 mS/cm at ambient condition. Compared with TTE diluent system, the TFDME-based system shows slightly improved ionic conductivity across large temperature range. Further evaluation of electrochemical performance of Li-metal and Li/NMC will be performed.

In addition to partial fluorination methodology, researchers also propose to chlorinate the ether molecule and thus retain the well-balance between Li+/solvent coordination and oxidative stabilities[113]. However, LiCl was shown to dissolve in the organic electrolyte, and it usually require to combine with other organic buffer layers to eliminate the direct contact with organic electrolytes[114]. Therefore, further evaluation on the chlorination will bring about more clear understanding.

In terms of environmental concerns, no matter fluorination or chlorination, they all pose harmful influence to our ecosystem without strict regulations[115]. For example, certain chlorofluorocarbons (CFCs) and halons used in industrial applications, such as refrigerants and fire extinguishers, have been found to contribute to the depletion of the ozone layer in the stratosphere. To address that, hydrofluorocarbons (HFCs), have been developed as alternatives to ozone-depleting substances. While they do not deplete the ozone layer, HFCs are potent greenhouse gases and have a high global warming potential (GWP). In addition, fluorine and chlorine compounds can exhibit varying degrees of environmental persistence, meaning they can remain in the environment for long periods. This persistence can lead to bioaccumulation in organisms, potentially causing ecological imbalances and adverse effects on wildlife.

In conclusion, the application of fluorination strategies to ethers has the potential to improve their oxidative stability. However, it is important to consider the impact on the coordination of Li+ ions with ether oxygen, as this can affect both ionic conductivity and salt solubility. Partial fluorination offers a possible solution by maintaining moderate Li+ solvation while expanding the electrochemical window compared to non-fluorinated ethers. Achieving the desired results requires careful consideration of

fluorination parameters, including the site and symmetry of fluorination, as well as controlling the fluorine/oxygen ratio. From an environmental perspective, it is crucial to implement strict regulations for monitoring the fluorination and chlorination processes. Furthermore, greater research efforts and resources should be dedicated to minimizing the influence of fluorinated and chlorinated compounds on our environment.

6.2 Future workflow of designing electrolytes for Li-metal batteries

The development of battery chemistry is crucial for supporting the widespread use of electric vehicles (EVs) and electric vertical takeoff and landing (EVTOL) applications in our daily lives. However, concerns regarding limited mileage and lower power output continue to create hesitation among both individuals and industries to fully embrace the transition to electrifying society. Li-metal anode, which offers high energy density, has gained significant attention as a potential solution. However, the reactive nature of Li-metal poses challenges for conventional electrolyte strategies, leading to issues such as dendritic growth, short cycle life, and safety concerns. More specifically, Li metal tends to preferentially reduce other battery electrolytes, resulting in the formation of a passivation layer upon contact. During the process of Li plating and stripping, dendritic Li structures tend to grow, which leads to the consumption of electrolyte and the thickening of the solid-electrolyte interphase (SEI) layer. This, in turn, forms an electrochemically insulated region known as "Dead Li" surrounded by SEI. Consequently, the impedance of the cell increases, and the cycle life is shortened.

To address these challenges, a key area of focus is electrolyte engineering for Li-metal batteries (LMBs). However, long-term electrochemical testing methods are often time-consuming and resource-intensive. Besides that, with the exploration of more complicated molecules, the cost and development timeline significantly increase accordingly. In light of this, I have developed and optimized a screening

protocol based on the experience during my PhD at the University of California, San Diego, and my internship at SolidEnergy System Inc. This protocol aims to expedite the screening process, allowing for more efficient evaluation of electrolyte performance. Furthermore, I propose considering other parameters that are currently overlooked but play a critical role in achieving effective electrolyte design. By identifying and assessing these overlooked factors, we can enhance the overall performance and durability of Li-metal batteries, addressing concerns related to dendritic growth, cycle life, and safety.

As shown in Figure 6.4, the screening process is composed of four steps before performing electrochemical long-term cycling: 1. Searching; 2. Sourcing; 3. Formulating; 4. Testing.

Step 1: Searching
- Literature search, and personal brainstorm based on different functional groups
- List basic physical properties(including toxicity, vapor pressure)
- DFT simulation on the potential electrochemical windows, Li$^+$ binding energy over large amount of chemicals
- Company patent

Step 2: Sourcing
- Purchase order or synthesis;
- Quality check on the received chemical (Water content, NMR, GC-MS)

Step 3: Formulating
- Salt solubility test, Li metal stabilities test;
- Electrochemical tests (Conductivities, CV, LSV on C-coated Al, LSV on platinum), voltage hold;
- Thermal analysis(DSC)
- Wettability towards different separators.

Step 4: Testing
- Standard Li-full cell E-chem C-rate testing and evaluation.
- Anode-free cell configurations.
- Advanced characterization tools to post-mortem analysis

Figure 6.4 Four-step workflow for electrolyte design

In Step 1, searching, we usually keep track of recent literature publications to gain a brief understanding of newly developed molecules. Then, we summarize the physical properties of promising molecules and utilize simulation tools to calculate their potential electrochemical window stability and Li+ binding energy. Sometimes, company patents offer novel ideas and disclose incomplete experimental

reports. In such cases, it is highly recommended to engage in further discussions with team members to narrow down the potential study molecules.
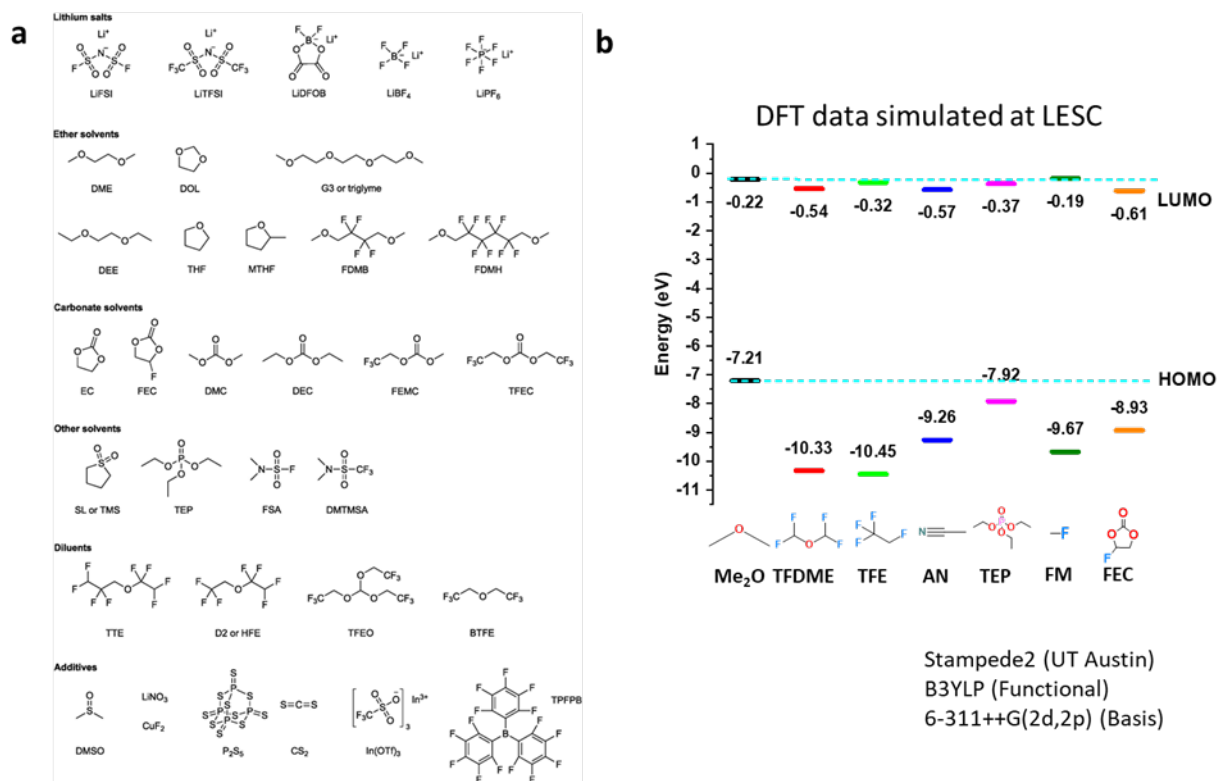
Figure 6.5 (a) Summary of different solvents, additives, and salts used for battery electrolytes. (b) Summayr of DFT calculations for battery solvents.

As depicted in Figure 6.5a, different categories of lithium salts, ethers, carbonates, diluents, and additives are searched and listed. Typically, parameters such as boiling points, melting points, dielectric constants, viscosities, flammability, and toxicity are of interest for preliminary evaluations. After the initial screening based on these parameters, density functional theory and molecular dynamics can be employed to calculate the potential LUMO and HOMO energy for each molecule. As shown in Figure 6.5b, fluorinated carbonate FEC (-8.93 eV), nitrile-based AN (-9.26 eV), and phosphate-based TEP (-7.92 eV) exhibited higher absolute values than ether-based Me2O (-7.21 eV). Additionally, simulating the potential Li+/solvent binding energy might be helpful in describing the potential salt solubility, although simulations cannot guarantee consistent experimental results.

In Step 2, sourcing, the goal is to obtain the proposed molecules with the lowest possible impurity from Step 1. Sometimes, these molecules may not be available from commercial vendors. In such cases, collaborating with other institutions, particularly those specializing in organic chemistry research, can expedite the sourcing process. Once the target molecules are received from a commercial vendor or synthesized in-house, quality control becomes essential to assess the purity of the obtained samples. Typically, moisture levels are measured using coulometric Karl Fischer titration. The purity of the sample is determined through nuclear magnetic resonance (NMR) and gas chromatography – mass spectrometry (GC-MS) tests. For liquefied gas systems, GC-MS can quantify the impurities of received gases and ensure the quality of all studied materials.

Regarding Step 3, formulation, the objective is to quantify salt solubility, assess Li-metal compatibility, and determine the optimal salt/solvent ratio to achieve desirable electrochemical transport properties, as well as improved oxidative stabilities and effective Li-metal passivation. As shown in Figure 6.6a, an example consists of LiFSI and DME is given to detailed demonstrate the working flow. We will tailor LiFSI and DME molar ratio to obtain (1) > 1 mS/cm ionic conductivity at room temperature with sufficient separator wetting. (2) Higher oxidative stability compared with Gen 2 carbonate or other related baseline electrolytes. (3) Effective passivation towards Li metal, which means the cathodic peaks will gradually decrease or even disappear over cyclic voltammetry cycling. As depicted in Figure 6.6b, the step will firstly start from the salt solubility, physical properties, and electrochemical transport characterizations. We will screen a wide molar ratio range of LiFSI and DME to obtain the ionic conductivity, viscosity, and bulk electrolyte solvation structure tendency with the change of salt concentration. After that, Li-metal soak tests should be performed to verify the formulated electrolyte's chemical stability with Li metal. Sometimes, SEM and XPS might be helpful tools to have a deep understanding on the surface morphology and chemical compositions.

With the enhancement of battery safety awareness, the thermodynamic stability of electrolytes has attracted increasing attention. Differential scanning calorimetry (DSC) testing is an accurate method for testing the thermodynamic stability of electrolyte systems. By matching with different charging and discharging states of Li metal and positive electrode, we can objectively characterize the heat release changes of these systems with electrolytes at different temperatures, thereby more accurately evaluating the safety of electrolytes.

After generating more understanding of fundamental chemical and physical properties of the electrolytes, we will apply different electrolytes towards real working electrodes, which are straightforward methodologies to quantify the electrolyte oxidative and reductive stability. Li/Cathodes (NMC) voltage-hold test can be utilized to monitor the leakage currents at the end of state-of-charge (SOC) state. Cyclic voltammetry can assess the SEI passivation at Li anode side. After fully understanding electrochemical stabilities, we can move on performing long-term cell cycling. By controlling the total Li reservoir (for example, utilizing anode-free and limited thickness of Li anode), we can significantly shorten the testing time and obtain the clear conclusion.
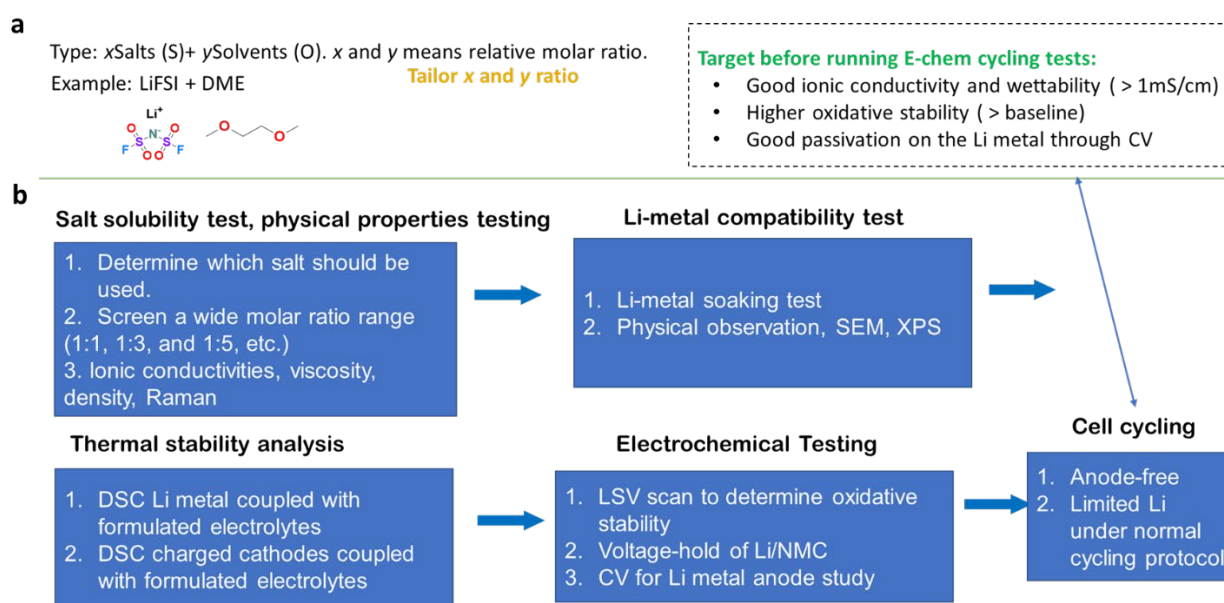
Figure 6.6 (a) Example of electrolyte formulations and the goal before running E-chem tests. (b) Detailed workflow for electrolyte formulations

In conclusion, the implementation of a four-step electrolyte screening process can serve as a standardized protocol for designing next-generation electrolytes specifically tailored for Li-metal batteries. This process stands out due to its rigorous experimental design, which considers the complexities associated with Li-metal anodes. Additionally, all the results generated from this screening process can be utilized to train machine learning tools. As a result, even the undesirable outcomes can contribute to the development of an extensive electrolyte database for the Li-metal system, further advancing research in this field.

6.3 Separator influence on the performance of LMBs

The successful realization of the lithium-ion system relies heavily on the adoption of advanced battery separators. These separators serve a primary function of physically isolating the positive and negative electrodes, preventing short circuits while facilitating the flow of lithium ions[116]. In addition to this vital role, battery separators also provide structural support to the electrodes, ensuring their physical integrity and safeguarding against deformation or damage during battery operation (Figure 6.7a)[116].

Coating the separator with a thermally responsive material is another way to enhance battery safety[117]. This coating triggers a shutdown mechanism when temperatures surpass a specific threshold, effectively preventing potential hazards. Moreover, the coating layer can be engineered to exhibit chemical stability and compatibility with the battery's electrolyte. This characteristic safeguards against separator material breakdown or decomposition in the presence of the electrolyte, minimizing the risk of internal short circuits or other safety concerns.
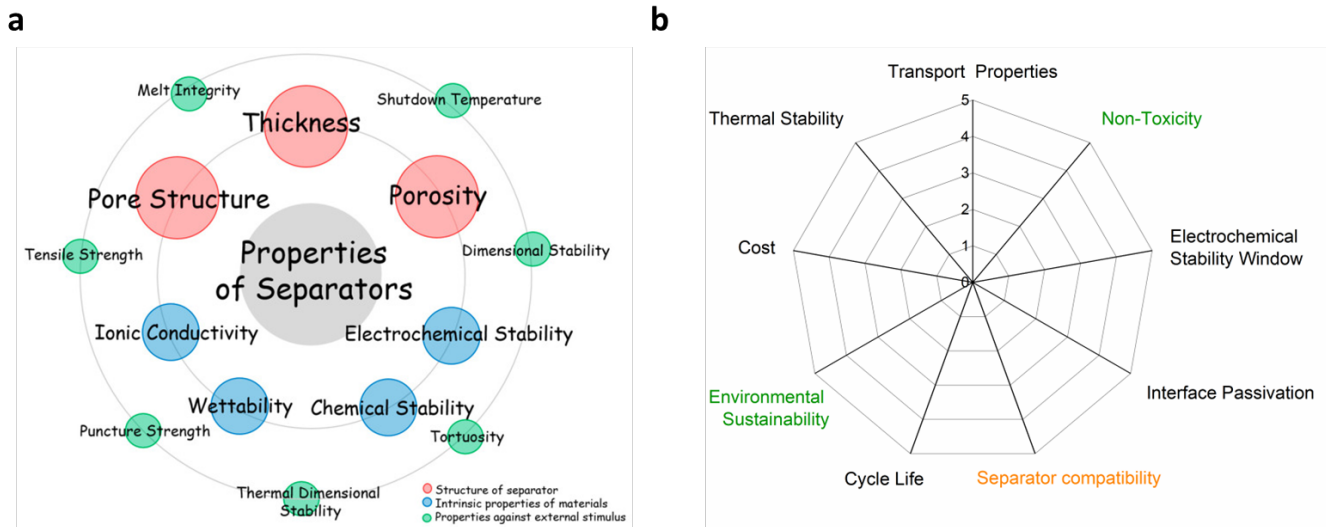
Figure 6.7 (a) Parameters to assess battery electrolytes. (b) List of properties of battery separators

However, when assessing various parameters to determine the suitability of an electrolyte for a Li-metal anode, separator compatibility is sometimes overlooked (Figure 6.7b). Consequently, when designing separators for Li metal batteries, careful consideration should be given to their ability to mitigate short circuits resulting from dendritic lithium growth[118]. As high concentration or localized highly concentrated electrolytes are developed mainly for Li-metal anodes, the electrolyte's wettability and compatibility with separators become crucial factors affecting effective Li+ diffusivity, rate-endurance, and overall cycle life.

Summary

Liquefied gas electrolytes have shown promise, owing to their desirable chemo-physical properties such as low melting point, low viscosity, and wide electrochemical stability. They have demonstrated excellent stability of Li-metal anodes, outstanding performance at low temperatures, and good oxidative stability. However, the further advancement of liquefied gas electrolytes has been impeded by safety concerns arising from moderate vapor pressure and flammability. In this study, we present a novel type of liquefied gas electrolyte that replaces fluoromethane with dimethyl ether.

In chapter 3, we formulated Me_2O-based electrolytes to improve the low-T performance of Li/CFx batteries. The Me_2O solvent delivers lower vapor pressure and higher salt solubility compared with FM-based LGE. The optimized Me_2O-PC electrolyte demonstrated > 3.5 mS cm-1 ionic conductivity through a wide temperature range of −70 to 60 ºC and excellent rate capability and low-T operation by forming anion-rich solvation structure and decent Li^+ transport. However, the oxidative stability and non-flammability of Me_2O solvent have not been addressed.

In chapter 4, we introduced two fire-extinguishing 1,1,1,2 tetrafloroethane and pentafluoroethane diluents into the Me_2O system. The optimized electrolyte not only maintains high Li-metal performance and excellent resilience at low temperatures but also exhibits promising characteristics in terms of improved battery safety and environmental sustainability. The development of these new liquefied gas electrolytes also enriches our fundamental understanding for designing safer battery electrolytes.

In chapter 5, we observed a unique condensation behavior when salt concentration increases, Me_2O gas can be captured and remain stable as liquid phase at ambient condition. The formulated sat. LiFSI-Me_2O electrolyte delivered excellent lithium-metal cyclability over 1000 cycles as well as withstanding critical current density up to 12 mA/cm^2. When paired with SPAN electrode, the sat. LiFSI-Me_2O showed

high performance compared with 4 M LiFSI-DME due to the salt-derived SEI formed at Li anode and less dissolution of polysulfides, verified by XPS and polysulfide soak tests.

In chapter 6, we propose that fluorinated ether gas might be promising for the next-generation LGE development due to its potentially enhanced oxidative stability. However, we should strike the balance between the fluorination and the salt solubility. The environmental concerns involve fluorine chemistry should be investigated and monitored. Everyone in this field should cooperate to minimize their impact on the ecosystem. In addition, we summarize the developed workflow for design new LGE and point out we previously overlook the electrolyte and other cell parts interactions. To comprehensively assess the electrolyte, the separator compatibility with electrolyte, current collector's compatibility with electrolyte should all be carefully considered.

In conclusion, by introducing Me_2O-based LGE, we present a promising direction for achieving high energy density, improved safety, ultra-low temperature operation, and sustainability in multiple Li-based batteries (Figure 7.1). During the development of new LGE, the methodology has been summarized and optimized. We should strictly follow the established workflow and perform more comprehensive evaluations to understand LGE's potential in enabling Li-metal technologies.
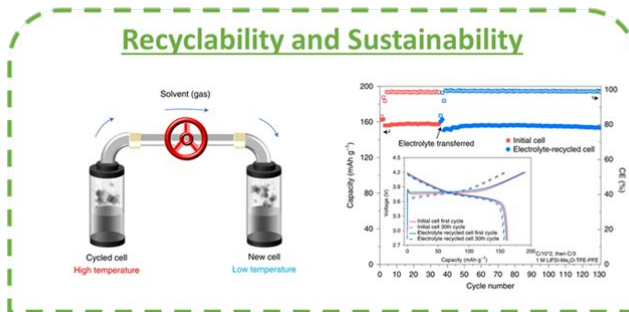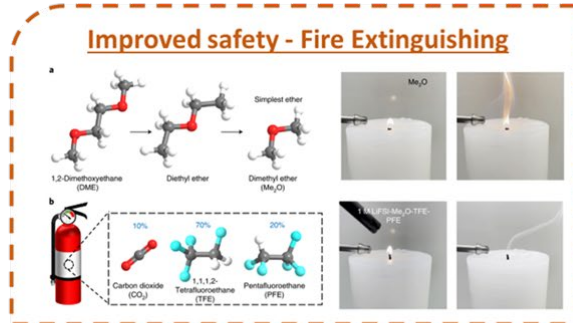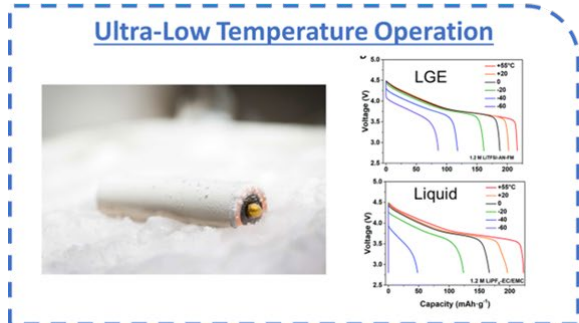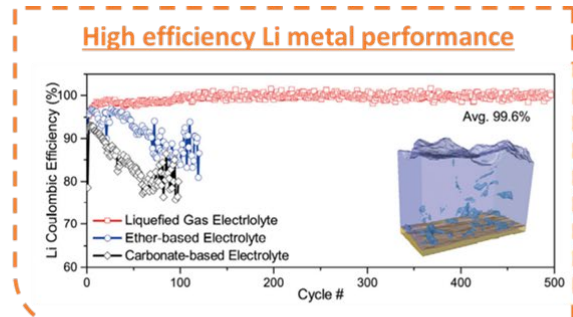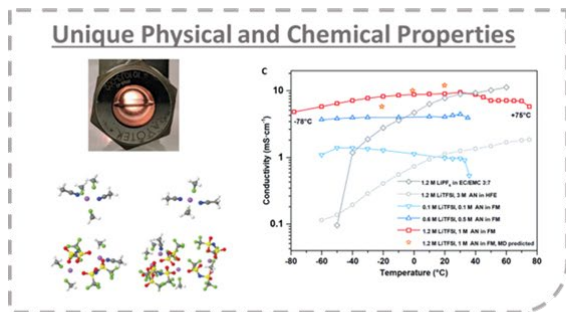
Figure 7.1 Summary of development of liquefied gas electrolytes with new features

References

1.   Lamb, W. F.; Wiedmann, T.; Pongratz, J.; Andrew, R.; Crippa, M.; Olivier, J. G.; Wiedenhofer, D.; Mattioli, G.; Al Khourdajie, A.; House, J., A review of trends and drivers of greenhouse gas emissions by sector from 1990 to 2018. *Environmental research letters* **2021,** *16* (7), 073005.

2.   Winter, M.; Brodd, R. J., What Are Batteries, Fuel Cells, and Supercapacitors? *Chemical Reviews* **2004,** *104* (10), 4245-4270.

3.   Fan, L.; Tu, Z.; Chan, S. H., Recent development of hydrogen and fuel cell technologies: A review. *Energy Reports* **2021,** *7*, 8421-8446.

4.   Frith, J. T.; Lacey, M. J.; Ulissi, U., A non-academic perspective on the future of lithium-based batteries. *Nature Communications* **2023,** *14* (1), 420.

5.   Meng, Y. S.; Srinivasan, V.; Xu, K., Designing better electrolytes. *Science* **2022,** *378* (6624), eabq3750.

6.   Xu, K., Nonaqueous liquid electrolytes for lithium-based rechargeable batteries. *Chemical reviews* **2004,** *104* (10), 4303-4418.

7.   Xu, K.; von Cresce, A., Interfacing electrolytes with electrodes in Li ion batteries. *Journal of Materials Chemistry* **2011,** *21* (27), 9849-9864.

8.   Xu, K.; Lam, Y.; Zhang, S. S.; Jow, T. R.; Curtis, T. B., Solvation Sheath of Li+ in Nonaqueous Electrolytes and Its Implication of Graphite/Electrolyte Interface Chemistry. *The Journal of Physical Chemistry C* **2007,** *111* (20), 7411-7421.

9.   Asenbauer, J.; Eisenmann, T.; Kuenzel, M.; Kazzazi, A.; Chen, Z.; Bresser, D., The success story of graphite as a lithium-ion anode material – fundamentals, remaining challenges, and recent developments including silicon (oxide) composites. *Sustainable Energy & Fuels* **2020,** *4* (11), 5387-5416.

10. Chung, D. D. L., Review Graphite. *Journal of Materials Science* **2002,** *37* (8), 1475-1489.

11. Lin, D.; Liu, Y.; Cui, Y., Reviving the lithium metal anode for high-energy batteries. *Nature Nanotechnology* **2017,** *12* (3), 194-206.

12. Armand, M.; Tarascon, J. M., Building better batteries. *Nature* **2008,** *451* (7179), 652-657.

13. Xin, S.; Chang, Z.; Zhang, X.; Guo, Y.-G., Progress of rechargeable lithium metal batteries based on conversion reactions. *National Science Review* **2016,** *4* (1), 54-70.

14. Whittingham, M. S., Electrical Energy Storage and Intercalation Chemistry. *Science* **1976,** *192* (4244), 1126-1127.

15. Mauger, A.; Julien, C. M.; Armand, M.; Zaghib, K., Tribute to John B. Goodenough: From Magnetism to Rechargeable Batteries. *Advanced Energy Materials* **2021,** *11* (2), 2000773.

16. Shen, X.; Zhang, X.-Q.; Ding, F.; Huang, J.-Q.; Xu, R.; Chen, X.; Yan, C.; Su, F.-Y.; Chen, C.-M.; Liu, X.; Zhang, Q., Advanced Electrode Materials in Lithium Batteries: Retrospect and Prospect. *Energy Material Advances* **2021,** *2021*.

17. Chebiam, R. V.; Kannan, A. M.; Prado, F.; Manthiram, A., Comparison of the chemical stability of the high energy density cathodes of lithium-ion batteries. *Electrochemistry Communications* **2001,** *3* (11), 624-627.

18. Cho, J.; Kim, Y. J.; Kim, T.-J.; Park, B., Zero-Strain Intercalation Cathode for Rechargeable Li-Ion Cell. *Angewandte Chemie International Edition* **2001,** *40* (18), 3367-3369.

19. Tsutomu, O.; Yoshinari, M., Layered Lithium Insertion Material of LiCo1/3Ni1/3Mn1/3O2 for Lithium-Ion Batteries. *Chemistry Letters* **2001,** *30* (7), 642-643.

20. Dutta, G.; Manthiram, A.; Goodenough, J. B.; Grenier, J. C., Chemical synthesis and properties of Li1−δ−xNi1+δO2 and Li[Ni2]O4. *Journal of Solid State Chemistry* **1992,** *96* (1), 123-131.

21. Choi, W.; Manthiram, A., Comparison of Metal Ion Dissolutions from Lithium Ion Battery Cathodes. *Journal of The Electrochemical Society* **2006,** *153* (9), A1760.

22. Manthiram, A.; Chemelewski, K.; Lee, E.-S., A perspective on the high-voltage LiMn1.5Ni0.5O4 spinel cathode for lithium-ion batteries. *Energy & Environmental Science* **2014,** *7* (4), 1339-1350.

23. Tarascon, J. M.; Armand, M., Issues and challenges facing rechargeable lithium batteries. *Nature* **2001,** *414* (6861), 359-367.

24. Doughty, D. H.; Roth, E. P., A General Discussion of Li Ion Battery Safety. *The Electrochemical Society Interface* **2012,** *21* (2), 37.

25. Hua, X.; Eggeman, A. S.; Castillo-Martínez, E.; Robert, R.; Geddes, H. S.; Lu, Z.; Pickard, C. J.; Meng, W.; Wiaderek, K. M.; Pereira, N.; Amatucci, G. G.; Midgley, P. A.; Chapman, K. W.; Steiner, U.; Goodwin, A. L.; Grey, C. P., Revisiting metal fluorides as lithium-ion battery cathodes. *Nature Materials* **2021,** *20* (6), 841-850.

26. Xu, K., Electrolytes and Interphases in Li-Ion Batteries and Beyond. *Chemical Reviews* **2014,** *114* (23), 11503-11618.

27. Qian, J.; Henderson, W. A.; Xu, W.; Bhattacharya, P.; Engelhard, M.; Borodin, O.; Zhang, J.-G., High rate and stable cycling of lithium metal anode. *Nature Communications* **2015,** *6* (1), 6362.

28. Zhang, C.; Gu, S.; Zhang, D.; Ma, J.; Zheng, H.; Zheng, M.; Lv, R.; Yu, K.; Wu, J.; Wang, X.; Yang, Q.-H.; Kang, F.; Lv, W., Nonflammable, localized high-concentration electrolyte towards a high-safety lithium metal battery. *Energy Storage Materials* **2022,** *52*, 355-364.

29. Cao, X.; Jia, H.; Xu, W.; Zhang, J.-G., Review—Localized High-Concentration Electrolytes for Lithium Batteries. *Journal of The Electrochemical Society* **2021,** *168* (1), 010522.

30. Rustomji, C. S.; Yang, Y.; Kim, T. K.; Mac, J.; Kim, Y. J.; Caldwell, E.; Chung, H.; Meng, Y. S., Liquefied gas electrolytes for electrochemical energy storage devices. *Science* **2017,** *356* (6345), eaal4263.

31. Yang, Y.; Davies, D. M.; Yin, Y.; Borodin, O.; Lee, J. Z.; Fang, C.; Olguin, M.; Zhang, Y.; Sablina, E. S.; Wang, X.; Rustomji, C. S.; Meng, Y. S., High-Efficiency Lithium-Metal Anode Enabled by Liquefied Gas Electrolytes. *Joule* **2019,** *3* (8), 1986-2000.

32. Yang, Y.; Yin, Y.; Davies, D. M.; Zhang, M.; Mayer, M.; Zhang, Y.; Sablina, E. S.; Wang, S.; Lee, J. Z.; Borodin, O.; Rustomji, C. S.; Meng, Y. S., Liquefied gas electrolytes for wide-temperature lithium metal batteries. *Energy & Environmental Science* **2020,** *13* (7), 2209-2219.

33. Davies, D. M.; Yang, Y.; Sablina, E. S.; Yin, Y.; Mayer, M.; Zhang, Y.; Olguin, M.; Lee, J. Z.; Lu, B.; Damien, D., A Safer, Wide-Temperature Liquefied Gas Electrolyte Based on Difluoromethane. *Journal of Power Sources* **2021,** *493*, 229668.

34. Yu, Z.; Wang, H.; Kong, X.; Huang, W.; Tsao, Y.; Mackanic, D. G.; Wang, K.; Wang, X.; Huang, W.; Choudhury, S.; Zheng, Y.; Amanchukwu, C. V.; Hung, S. T.; Ma, Y.; Lomeli, E. G.; Qin, J.; Cui, Y.; Bao, Z., Molecular design for electrolyte solvents enabling energy-dense and long-cycling lithium metal batteries. *Nature Energy* **2020,** *5* (7), 526-533.

35. Yu, Z.; Rudnicki, P. E.; Zhang, Z.; Huang, Z.; Celik, H.; Oyakhire, S. T.; Chen, Y.; Kong, X.; Kim, S. C.; Xiao, X.; Wang, H.; Zheng, Y.; Kamat, G. A.; Kim, M. S.; Bent, S. F.; Qin, J.; Cui, Y.; Bao, Z., Rational solvent molecule tuning for high-performance lithium metal battery electrolytes. *Nature Energy* **2022,** *7* (1), 94-106.

36. Suo, L.; Xue, W.; Gobet, M.; Greenbaum, S. G.; Wang, C.; Chen, Y.; Yang, W.; Li, Y.; Li, J., Fluorine-donating electrolytes enable highly reversible 5-V-class Li metal batteries. *Proceedings of the National Academy of Sciences* **2018,** *115* (6), 1156-1161.

37. Ma, X.; Arumugam, R. S.; Ma, L.; Logan, E.; Tonita, E.; Xia, J.; Petibon, R.; Kohn, S.; Dahn, J. R., A Study of Three Ester Co-Solvents in Lithium-Ion Cells. *Journal of The Electrochemical Society* **2017,** *164* (14), A3556.

38. Holoubek, J.; Yu, M.; Yu, S.; Li, M.; Wu, Z.; Xia, D.; Bhaladhare, P.; Gonzalez, M. S.; Pascal, T. A.; Liu, P.; Chen, Z., An All-Fluorinated Ester Electrolyte for Stable High-Voltage Li Metal Batteries Capable of Ultra-Low-Temperature Operation. *ACS Energy Letters* **2020,** *5* (5), 1438-1447.

39. Su, C.-C.; He, M.; Shi, J.; Amine, R.; Yu, Z.; Cheng, L.; Guo, J.; Amine, K., Principle in developing novel fluorinated sulfone electrolyte for high voltage lithium-ion batteries. *Energy & Environmental Science* **2021,** *14* (5), 3029-3034.

40. Wolfenstine, J.; Foster, D.; Behl, W.; Gilman, S. *Gas evolution and self-discharge in Li/MnO2 primary batteries*; Army Research Lab Adelphi Md Sensors and Electron Devices Directorate: 1998.

41. Whitacre, J.; Yazami, R.; Hamwi, A.; Smart, M. C.; Bennett, W.; Prakash, G. S.; Miller, T.; Bugga, R., Low operational temperature Li–CFx batteries using cathodes containing sub-fluorinated graphitic materials. *Journal of power sources* **2006,** *160* (1), 577-584.

42. Holoubek, J.; Kim, K.; Yin, Y.; Wu, Z.; Liu, H.; Li, M.; Chen, A.; Gao, H.; Cai, G.; Pascal, T. A., Electrolyte design implications of ion-pairing in low-temperature Li metal batteries. *Energy & Environmental Science* **2022,** *15* (4), 1647-1658.

43. Holoubek, J.; Baskin, A.; Lawson, J. W.; Khemchandani, H.; Pascal, T. A.; Liu, P.; Chen, Z., Predicting the Ion Desolvation Pathway of Lithium Electrolytes and Their Dependence on Chemistry and Temperature. *The Journal of Physical Chemistry Letters* **2022,** *13*, 4426-4433.

44. Li, Q.; Lu, D.; Zheng, J.; Jiao, S.; Luo, L.; Wang, C.-M.; Xu, K.; Zhang, J.-G.; Xu, W., Li+-desolvation dictating lithium-ion battery's low-temperature performances. *ACS applied materials & interfaces* **2017,** *9* (49), 42761-42768.

45. Hunter, E. P.; Lias, S. G., Evaluated gas phase basicities and proton affinities of molecules: an update. *Journal of Physical and Chemical Reference Data* **1998,** *27* (3), 413-656.

46. Yin, Y.; Yang, Y.; Cheng, D.; Mayer, M.; Holoubek, J.; Li, W.; Raghavendran, G.; Liu, A.; Lu, B.; Davies, D. M., Fire-extinguishing, recyclable liquefied gas electrolytes for temperature-resilient lithium-metal batteries. *Nature Energy* **2022**, 1-12.

47. Park, C.; Kanduč, M.; Chudoba, R.; Ronneburg, A.; Risse, S.; Ballauff, M.; Dzubiella, J., Molecular simulations of electrolyte structure and dynamics in lithium–sulfur battery solvents. *Journal of Power Sources* **2018,** *373*, 70-78.

48. Hesse, H. C.; Schimpe, M.; Kucevic, D.; Jossen, A., Lithium-ion battery storage for the grid—A review of stationary battery storage system design tailored for applications in modern power grids. *Energies* **2017,** *10* (12), 2107.

49. Chen, S.; Zheng, J.; Yu, L.; Ren, X.; Engelhard, M. H.; Niu, C.; Lee, H.; Xu, W.; Xiao, J.; Liu, J.; Zhang, J.-G., High-Efficiency Lithium Metal Batteries with Fire-Retardant Electrolytes. *Joule* **2018,** *2* (8), 1548-1558.

50. Fan, X.; Chen, L.; Borodin, O.; Ji, X.; Chen, J.; Hou, S.; Deng, T.; Zheng, J.; Yang, C.; Liou, S.-C.; Amine, K.; Xu, K.; Wang, C., Non-flammable electrolyte enables Li-metal batteries with aggressive cathode chemistries. *Nature Nanotechnology* **2018,** *13* (8), 715-722.

51. Hobold, G. M.; Lopez, J.; Guo, R.; Minafra, N.; Banerjee, A.; Shirley Meng, Y.; Shao-Horn, Y.; Gallant, B. M., Moving beyond 99.9% Coulombic efficiency for lithium anodes in liquid electrolytes. *Nature Energy* **2021,** *6* (10), 951-960.

52. Liu, Y.; Liu, Q.; Xin, L.; Liu, Y.; Yang, F.; Stach, E. A.; Xie, J., Making Li-metal electrodes rechargeable by controlling the dendrite growth direction. *Nature Energy* **2017,** *2* (7), 1-10.

53. Fang, C.; Li, J.; Zhang, M.; Zhang, Y.; Yang, F.; Lee, J. Z.; Lee, M.-H.; Alvarado, J.; Schroeder, M. A.; Yang, Y., Quantifying inactive lithium in lithium metal batteries. *Nature* **2019,** *572* (7770), 511-515.

54. Wang, J.; Huang, W.; Pei, A.; Li, Y.; Shi, F.; Yu, X.; Cui, Y., Improving cyclability of Li metal batteries at elevated temperatures and its origin revealed by cryo-electron microscopy. *Nature Energy* **2019,** *4* (8), 664-670.

55. Hess, S.; Wohlfahrt-Mehrens, M.; Wachtler, M., Flammability of Li-Ion Battery Electrolytes: Flash Point and Self-Extinguishing Time Measurements. *Journal of The Electrochemical Society* **2015,** *162* (2), A3084-A3097.

56. Xu, K.; Zhang, S.; Allen, J. L.; Jow, T. R., Evaluation of fluorinated alkyl phosphates as flame retardants in electrolytes for Li-ion batteries: II. Performance in cell. *Journal of the Electrochemical Society* **2003,** *150* (2), A170.

57. Xu, P.; Dai, Q.; Gao, H.; Liu, H.; Zhang, M.; Li, M.; Chen, Y.; An, K.; Meng, Y. S.; Liu, P.; Li, Y.; Spangenberger, J. S.; Gaines, L.; Lu, J.; Chen, Z., Efficient Direct Recycling of Lithium-Ion Battery Cathodes by Targeted Healing. *Joule* **2020,** *4* (12), 2609-2626.

58. Xu, P.; Tan, D. H.; Chen, Z., Emerging trends in sustainable battery chemistries. *Trends in Chemistry* **2021**.

59. Tan, D. H.; Banerjee, A.; Chen, Z.; Meng, Y. S., From nanoscale interface characterization to sustainable energy storage using all-solid-state batteries. *Nature nanotechnology* **2020,** *15* (3), 170-180.

60. Sun, H.; Zhu, G.; Zhu, Y.; Lin, M. C.; Chen, H.; Li, Y. Y.; Hung, W. H.; Zhou, B.; Wang, X.; Bai, Y., High‑Safety and High‑Energy‑Density Lithium Metal Batteries in a Novel Ionic‑Liquid Electrolyte. *Advanced Materials* **2020,** *32* (26), 2001741.

61. Banerjee, A.; Wang, X.; Fang, C.; Wu, E. A.; Meng, Y. S., Interfaces and Interphases in All-Solid-State Batteries with Inorganic Solid Electrolytes. *Chemical Reviews* **2020,** *120* (14), 6878-6933.

62. Wu, L.; Song, Z.; Liu, L.; Guo, X.; Kong, L.; Zhan, H.; Zhou, Y.; Li, Z., A new phosphate-based nonflammable electrolyte solvent for Li-ion batteries. *Journal of Power Sources* **2009,** *188* (2), 570-573.

63. Zeng, Z.; Wu, B.; Xiao, L.; Jiang, X.; Chen, Y.; Ai, X.; Yang, H.; Cao, Y., Safer lithium ion batteries based on nonflammable electrolyte. *Journal of Power Sources* **2015,** *279*, 6-12.

64. Shiga, T.; Kato, Y.; Kondo, H.; Okuda, C.-a., Self-extinguishing electrolytes using fluorinated alkyl phosphates for lithium batteries. *Journal of Materials Chemistry A* **2017,** *5* (10), 5156-5162.

65. Ota, H.; Kominato, A.; Chun, W.-J.; Yasukawa, E.; Kasuya, S., Effect of cyclic phosphate additive in non-flammable electrolyte. *Journal of Power Sources* **2003,** *119-121*, 393-398.

66. Wang, J.; Yamada, Y.; Sodeyama, K.; Watanabe, E.; Takada, K.; Tateyama, Y.; Yamada, A., Fire-extinguishing organic electrolytes for safe batteries. *Nature Energy* **2018,** *3* (1), 22-29.

67. Chen, S.; Zheng, J.; Mei, D.; Han, K. S.; Engelhard, M. H.; Zhao, W.; Xu, W.; Liu, J.; Zhang, J.-G., High-Voltage Lithium-Metal Batteries Enabled by Localized High-Concentration Electrolytes. *Advanced Materials* **2018,** *30* (21), 1706102.

68. Ren, X.; Chen, S.; Lee, H.; Mei, D.; Engelhard, M. H.; Burton, S. D.; Zhao, W.; Zheng, J.; Li, Q.; Ding, M. S.; Schroeder, M.; Alvarado, J.; Xu, K.; Meng, Y. S.; Liu, J.; Zhang, J.-G.; Xu, W., Localized High-Concentration Sulfone Electrolytes for High-Efficiency Lithium-Metal Batteries. *Chem* **2018,** *4* (8), 1877-1892.

69. Cao, X.; Xu, Y.; Zhang, L.; Engelhard, M. H.; Zhong, L.; Ren, X.; Jia, H.; Liu, B.; Niu, C.; Matthews, B. E.; Wu, H.; Arey, B. W.; Wang, C.; Zhang, J.-G.; Xu, W., Nonflammable Electrolytes for Lithium Ion Batteries Enabled by Ultraconformal Passivation Interphases. *ACS Energy Letters* **2019,** *4* (10), 2529-2534.

70. Niu, C.; Lee, H.; Chen, S.; Li, Q.; Du, J.; Xu, W.; Zhang, J.-G.; Whittingham, M. S.; Xiao, J.; Liu, J., High-energy lithium metal pouch cells with limited anode swelling and long stable cycles. *Nature Energy* **2019,** *4* (7), 551-559.

71. Fan, X.; Ji, X.; Chen, L.; Chen, J.; Deng, T.; Han, F.; Yue, J.; Piao, N.; Wang, R.; Zhou, X.; Xiao, X.; Chen, L.; Wang, C., All-temperature batteries enabled by fluorinated electrolytes with non-polar solvents. *Nature Energy* **2019,** *4* (10), 882-890.

72. Wang, Q.; Mao, B.; Stoliarov, S. I.; Sun, J., A review of lithium ion battery failure mechanisms and fire prevention strategies. *Progress in Energy and Combustion Science* **2019,** *73*, 95-131.

73. Rustomji, C. S.; Yang, Y.; Kim, T. K.; Mac, J.; Kim, Y. J.; Caldwell, E.; Chung, H.; Meng, Y. S., Liquefied gas electrolytes for electrochemical energy storage devices. *Science* **2017**.

74. Wu, J.; Liu, Z.; Bi, S.; Meng, X., Viscosity of saturated liquid dimethyl ether from (227 to 343) K. *Journal of Chemical & Engineering Data* **2003,** *48* (2), 426-429.

75. Wu, J.; Yin, J., Vapor pressure measurements of dimethyl ether from (213 to 393) K. *Journal of Chemical & Engineering Data* **2008,** *53* (9), 2247-2249.

76. Prince, J. C.; Williams, F. A., A short reaction mechanism for the combustion of dimethyl-ether. *Combustion and Flame* **2015,** *162* (10), 3589-3595.

77. Westmoreland, P. R.; Burgess, D. R. F.; Zachariah, M. R.; Tsang, W., Fluoromethane chemistry and its role in flame suppression. *Symposium (International) on Combustion* **1994,** *25* (1), 1505-1511.

78. Holcomb, C. D.; Magee, J. W.; Scott, J. L.; Outcalt, S. L.; Haynes, W. M., Selected Thermodynamic Properties for Mixtures of R-32 (Difluoromethane), R-125 (Pentafluoroethane), R-134a (1, 1, 1, 2-Tetrafluoroethane), R-143a (1, 1, 1-Trifluoroethane), R-41 (Fluoromethane), R-290 (Propane), and R-744 (Carbon Dioxide). **1997**.

79. Sun, L.-Q.; Zhu, M.-S.; Han, L.-Z.; Lin, Z.-Z., Viscosity of difluoromethane and pentafluoroethane along the saturation line. *Journal of Chemical & Engineering Data* **1996,** *41* (2), 292-296.

80. Wang, T.; Hu, Y.-j.; Zhang, P.; Pan, R.-m., Study on thermal decomposition properties and its decomposition mechanism of pentafluoroethane (HFC-125) fire extinguishing agent. *Journal of Fluorine Chemistry* **2016,** *190*, 48-55.

81. von Aspern, N.; Röschenthaler, G.-V.; Winter, M.; Cekic-Laskovic, I., Fluorine and Lithium: Ideal Partners for High-Performance Rechargeable Battery Electrolytes. *Angewandte Chemie International Edition 0* (0).

82. Holoubek, J.; Liu, H.; Wu, Z.; Yin, Y.; Xing, X.; Cai, G.; Yu, S.; Zhou, H.; Pascal, T. A.; Chen, Z.; Liu, P., Tailoring electrolyte solvation for Li metal batteries cycled at ultra-low temperature. *Nature Energy* **2021,** *6* (3), 303-313.

83. Cai, G.; Yin, Y.; Xia, D.; Chen, A. A.; Holoubek, J.; Scharf, J.; Yang, Y.; Koh, K. H.; Li, M.; Davies, D. M., Sub-nanometer confinement enables facile condensation of gas electrolyte for low-temperature batteries. *Nature communications* **2021,** *12* (1), 1-11.

84. Davies, D. M.; Yang, Y.; Sablina, E. S.; Yin, Y.; Mayer, M.; Zhang, Y.; Olguin, M.; Lee, J. Z.; Lu, B.; Damien, D.; Borodin, O.; Rustomji, C. S.; Meng, Y. S., A Safer, Wide-Temperature Liquefied Gas Electrolyte Based on Difluoromethane. *Journal of Power Sources* **2021,** *493*, 229668.

85. Dong, X.; Lin, Y.; Li, P.; Ma, Y.; Huang, J.; Bin, D.; Wang, Y.; Qi, Y.; Xia, Y., High‐energy rechargeable metallic lithium battery at− 70 C enabled by a cosolvent electrolyte. *Angewandte Chemie International Edition* **2019,** *58* (17), 5623-5627.

86. Wang, X.; Li, Y.; Meng, Y. S., Cryogenic electron microscopy for characterizing and diagnosing batteries. *Joule* **2018,** *2* (11), 2225-2234.

87. Cao, X.; Ren, X.; Zou, L.; Engelhard, M. H.; Huang, W.; Wang, H.; Matthews, B. E.; Lee, H.; Niu, C.; Arey, B. W., Monolithic solid–electrolyte interphases formed in fluorinated orthoformate-based electrolytes minimize Li depletion and pulverization. *Nature Energy* **2019,** *4* (9), 796-805.

88. Chen, H.; Pei, A.; Lin, D.; Xie, J.; Yang, A.; Xu, J.; Lin, K.; Wang, J.; Wang, H.; Shi, F., Uniform high ionic conducting lithium sulfide protection layer for stable lithium metal anode. *Advanced Energy Materials* **2019,** *9* (22), 1900858.

89. Kim, M. S.; Zhang, Z.; Rudnicki, P. E.; Yu, Z.; Wang, J.; Wang, H.; Oyakhire, S. T.; Chen, Y.; Kim, S. C.; Zhang, W., Suspension electrolyte with modified Li+ solvation environment for lithium metal batteries. *Nature materials* **2022**, 1-10.

90. Lain, M. J., Recycling of lithium ion cells and batteries. *Journal of power sources* **2001,** *97*, 736-738.

91. Georgi-Maschler, T.; Friedrich, B.; Weyhe, R.; Heegn, H.; Rutz, M., Development of a recycling process for Li-ion batteries. *Journal of power sources* **2012,** *207*, 173-182.

92. Sloop, S.; Crandon, L.; Allen, M.; Koetje, K.; Reed, L.; Gaines, L.; Sirisaksoontorn, W.; Lerner, M., A direct recycling case study from a lithium-ion battery recall. *Sustainable Materials and Technologies* **2020,** *25*, e00152.

93. Nowak, S.; Winter, M., The role of sub-and supercritical CO2 as "processing solvent" for the recycling and sample preparation of lithium ion battery electrolytes. *Molecules* **2017,** *22* (3), 403.

94. Hehre, W.; Radom, L., P. v R. Schleyer and JA Pople, Ab initio Molecular Orbital Theory. Wiley, New York: 1986.

95.	Laming, G. J.; Termath, V.; Handy, N. C., A general purpose exchange‑correlation energy functional. *The Journal of chemical physics* **1993,** *99* (11), 8765-8773.

96.	Borodin, O., Polarizable Force Field Development and Molecular Dynamics Simulations of Ionic Liquids. *J. Phys. Chem. B* **2009,** *113* (33), 11463-11478.

97.	Suo, L.; Borodin, O.; Gao, T.; Olguin, M.; Ho, J.; Fan, X.; Luo, C.; Wang, C.; Xu, K., "Water-in-salt" electrolyte enables high-voltage aqueous lithium-ion chemistries. *Science* **2015,** *350* (6263), 938-943.

98.	Borodin, O.; Smith, G. D., Quantum Chemistry and Molecular Dynamics Simulation Study of Dimethyl Carbonate: Ethylene Carbonate Electrolytes Doped with LiPF6. *The Journal of Physical Chemistry B* **2009,** *113* (6), 1763-1776.

99.	Ghosh, B., Assessment of the benefits of Fire Extinguishers as fire safety precautions in New Zealand Buildings. **2009**.

100.	Houghton, J. T.; Meira Filho, L. G.; Griggs, D. J.; Maskell, K., *An introduction to simple climate models used in the IPCC Second Assessment Report*. WMO: 1997; Vol. 410.

101.	Fan, X.; Chen, L.; Borodin, O.; Ji, X.; Chen, J.; Hou, S.; Deng, T.; Zheng, J.; Yang, C.; Liou, S.-C., Non-flammable electrolyte enables Li-metal batteries with aggressive cathode chemistries. *Nature nanotechnology* **2018,** *13* (8), 715-722.

102.	Fan, X.; Ji, X.; Chen, L.; Chen, J.; Deng, T.; Han, F.; Yue, J.; Piao, N.; Wang, R.; Zhou, X., All-temperature batteries enabled by fluorinated electrolytes with non-polar solvents. *Nature Energy* **2019,** *4* (10), 882-890.

103.	Zheng, J.; Ji, G.; Fan, X.; Chen, J.; Li, Q.; Wang, H.; Yang, Y.; DeMella, K. C.; Raghavan, S. R.; Wang, C., High‑fluorinated electrolytes for Li–S batteries. *Advanced energy materials* **2019,** *9* (16), 1803774.

104.	Chen, S.; Zheng, J.; Yu, L.; Ren, X.; Engelhard, M. H.; Niu, C.; Lee, H.; Xu, W.; Xiao, J.; Liu, J., High-efficiency lithium metal batteries with fire-retardant electrolytes. *Joule* **2018,** *2* (8), 1548-1558.

105.	Li, Y.; An, Y.; Tian, Y.; Wei, C.; Xiong, S.; Feng, J., High-safety and high-voltage lithium metal batteries enabled by a nonflammable ether-based electrolyte with phosphazene as a cosolvent. *ACS Applied Materials & Interfaces* **2021,** *13* (8), 10141-10148.

106.	Cho, S.-J.; Yu, D.-E.; Pollard, T. P.; Moon, H.; Jang, M.; Borodin, O.; Lee, S.-Y., Nonflammable lithium metal full cells with ultra-high energy density based on coordinated carbonate electrolytes. *Iscience* **2020,** *23* (2), 100844.

107.   Jia, H.; Xu, W., Electrolytes for high-voltage lithium batteries. *Trends in Chemistry* **2022,** *4* (7), 627-642.

108.   Lee, B.-J.; Zhao, C.; Yu, J.-H.; Kang, T.-H.; Park, H.-Y.; Kang, J.; Jung, Y.; Liu, X.; Li, T.; Xu, W.; Zuo, X.-B.; Xu, G.-L.; Amine, K.; Yu, J.-S., Development of high-energy non-aqueous lithium-sulfur batteries via redox-active interlayer strategy. *Nature Communications* **2022,** *13* (1), 4629.

109.   Zhang, S. S., Understanding of Sulfurized Polyacrylonitrile for Superior Performance Lithium/Sulfur Battery. *Energies* **2014,** *7* (7), 4588-4600.

110. Liu, H.; Holoubek, J.; Zhou, H.; Chen, A.; Chang, N.; Wu, Z.; Yu, S.; Yan, Q.; Xing, X.; Li, Y.; Pascal, T. A.; Liu, P., Ultrahigh coulombic efficiency electrolyte enables Li||SPAN batteries with superior cycling performance. *Materials Today* **2021,** *42*, 17-28.

111. Li, X.; Zhao, R.; Fu, Y.; Manthiram, A., Nitrate additives for lithium batteries: Mechanisms, applications, and prospects. *eScience* **2021,** *1* (2), 108-123.

112. Ren, X.; Zou, L.; Jiao, S.; Mei, D.; Engelhard, M. H.; Li, Q.; Lee, H.; Niu, C.; Adams, B. D.; Wang, C.; Liu, J.; Zhang, J.-G.; Xu, W., High-Concentration Ether Electrolytes for Stable High-Voltage Lithium Metal Batteries. *ACS Energy Letters* **2019,** *4* (4), 896-902.

113. Tan, L.; Chen, S.; Chen, Y.; Fan, J.; Ruan, D.; Nian, Q.; Chen, L.; Jiao, S.; Ren, X., Intrinsic Nonflammable Ether Electrolytes for Ultrahigh-Voltage Lithium Metal Batteries Enabled by Chlorine Functionality. *Angewandte Chemie International Edition* **2022,** *61* (32), e202203693.

114. Zhang, K.; Wu, F.; Zhang, K.; Weng, S.; Wang, X.; Gao, M.; Sun, Y.; Cao, D.; Bai, Y.; Xu, H.; Wang, X.; Wu, C., Chlorinated dual-protective layers as interfacial stabilizer for dendrite-free lithium metal anode. *Energy Storage Materials* **2021,** *41*, 485-494.

115. Han, J.; Kiss, L.; Mei, H.; Remete, A. M.; Ponikvar-Svet, M.; Sedgwick, D. M.; Roman, R.; Fustero, S.; Moriwaki, H.; Soloshonok, V. A., Chemical Aspects of Human and Environmental Overload with Fluorine. *Chemical Reviews* **2021,** *121* (8), 4678-4742.

116. Jang, J.; Oh, J.; Jeong, H.; Kang, W.; Jo, C., A review of functional separators for lithium metal battery applications. *Materials* **2020,** *13* (20), 4625.

117. Ji, W.; Jiang, B.; Ai, F.; Yang, H.; Ai, X., Temperature-responsive microspheres-coated separator for thermal shutdown protection of lithium ion batteries. *RSC Advances* **2015,** *5* (1), 172-176.

118. Chang, Z.; Yang, H.; Pan, A.; He, P.; Zhou, H., An improved 9 micron thick separator for a 350 Wh/kg lithium metal rechargeable pouch cell. *Nature Communications* **2022,** *13* (1), 6788.